



TECHNISCHE UNIVERSITÄT WIEN

DISSERTATION

**Open Quantum System Approach to
Transient Coherence in Ion-Solid Transport**

ausgeführt zum Zwecke der Erlangung des akademischen Grades
eines Doktors der technischen Wissenschaften

unter der Leitung von

O.Univ.Prof. Dipl.-Phys. Dr.rer.nat. Joachim Burgdörfer
Institut für Theoretische Physik (E136)

und

Prof. Dr. Carlos O. Reinhold

Department of Physics and Astronomy, University of Tennessee, Knoxville
and Physics Division, Oak Ridge National Laboratory, Tennessee, USA

eingereicht an der Technischen Universität Wien
Fakultät für Physik

von

Dipl.-Ing. Marek Seliger
Matrikelnummer: 9526101

Rienöflgasse 15/12
1040 Wien

Wien, am 5. Juni 2005

A handwritten signature in black ink, reading 'Marek Seliger'. The signature is written in a cursive style with a long horizontal stroke extending to the right.

Zusammenfassung

Der Durchgang von hochgeladenen Ionen durch Festkörper wird mit Hilfe von klassischer und quantenmechanischer Transporttheorie untersucht. Wir betrachten die Zeitentwicklung von elektronischen Zuständen von wasserstoffartigen Projektilionen während vielfacher Stöße im Festkörper. Die Dynamik der Elektronen in hoch angeregten Projektilzuständen und im Kontinuum wird durch eine klassische Transporttheorie beschrieben. Wir verwenden eine quantenmechanische Transporttheorie für die Beschreibung tief gebundener Zustände. Für die Zeitentwicklung von offenen Quantensystemen (OQS) haben wir eine verallgemeinerte nichtunitäre Lindblad Mastergleichung und deren Monte Carlo Lösung mittels Quantentrajektorien entwickelt. Diese Beschreibung nichtunitärer OQSs erlaubt es, Systeme zu beschreiben, die auch in Bezug auf Wahrscheinlichkeitsfluss (d.h. Elektroneneinfang und Ionisation) offen sind.

Mit Hilfe der klassischen Transporttheorie untersuchen wir Convoyelektronen im Spektrum der emittierten Elektronen. Mittels der quantenmechanischen Transporttheorie beschreiben wir die Entwicklung von tief gebundenen Zuständen. In einer ersten Anwendung der neuen Theorie untersuchen wir transiente Kohärenzen erzeugt durch Stoßanregung im Transport von Kr^{35+} Ionen durch Kohlenstofffolien. Gegenüber vorangegangenen Arbeiten konnte eine bessere Übereinstimmung mit experimentellen Daten erreicht werden.

Als eine zweite Anwendung untersuchen wir transiente Kohärenzen erzeugt im Elektroneneinfang durch ein anfänglich vollständig ionisiertes Argonion und Dekohärenz in weiterer Wechselwirkung mit dem Festkörper. Elektroneneinfang besetzt eine teilweise kohärente Superposition von wasserstoffartigen Projektilzuständen, während die Wechselwirkung mit der Umgebung (Targetatome und Elektronen, radiativer Zerfall) in stoßinduzierter und dynamischer Mischung von Populationen und Kohärenzen wie auch Ionisation resultiert. Wir können n_l Populationen während des Transports mit Messungen vergleichen. Im Grenzfall dünner Folien können wir direkt Einfangwirkungsquerschnitte gegen experimentelle Ergebnisse testen. Für dickere Targets haben wir die Möglichkeit die Dynamik des offenen Quantensystems in Wechselwirkung mit dem Festkörper als Funktion der Wechselwirkungszeit zu verfolgen. Die erhaltenen Resultate sind in guter Übereinstimmung mit den experimentellen Daten und bestätigen die Genauigkeit der Einfangwirkungsquerschnitte wie auch die Beschreibung der Zeitentwicklung innerhalb des OQS Ansatzes.

Abstract

We investigate the passage of highly charged ions through solids by means of classical and quantum transport theory. We focus on the time evolution of electronic states of hydrogenic projectile ions as they suffer multiple collisions and radiative decay inside the solid. We use a hybrid approach where the dynamics of electrons in highly excited projectile states and in the continuum is described by a classical transport theory while we adopt a quantum transport theory for the description of deeply bound states. For the evolution of open quantum systems (OQS) we have developed a generalized non-unitary Lindblad master equation and its quantum trajectory Monte Carlo implementation allowing for a description of non-unitary OQSs that are also open with respect to probability flux (i.e. electron capture and ionization).

We apply the classical transport theory to the emission of electrons and investigate properties of the convoy electron peak. Within the quantum transport theory we focus on the evolution of deeply bound states. In a first application of the new theory we investigate transient coherences created by collisional excitation in transport of Kr^{35+} ions through a carbon target. We find improved agreement of the non-unitary transport theory with experimental data.

In a second application we investigate transient coherences created in electron capture by an initially bare argon projectile and decoherence in further interaction with the solid. Electron capture populates a partially coherent superposition of hydrogenic projectile states while interaction with the environment (target atoms and electrons, radiative decay) results in collisional and dynamical mixing of populations and coherences as well as ionization. We compare nl populations during transport with measurements. In the limit of thin targets we can directly test electron capture cross sections against experimental findings while for thicker targets we have the opportunity to follow the dynamics of the open quantum system in interaction with the solid as a function of interaction time. The observed results are in close agreement with the experimental data confirming the accuracy of electron capture cross sections as well as the description of the time evolution within the OQS approach.

Contents

1	Introduction	1
2	Overview	6
2.1	Elementary processes	6
2.2	Experimental realization	10
2.3	Observation of solid state effects	13
3	Processes in ion-solid transport	16
3.1	Energy spectrum of hydrogenic ion	16
3.2	Collisional cross sections	18
3.2.1	Electron-core collisions	20
3.2.2	Electron-electron collisions	23
3.2.3	Radiative decay	25
3.3	Wake field	25
3.4	Electron capture	30
3.4.1	Classical description of electron capture	30
3.4.2	Continuum-distorted-wave approximation	32
3.4.3	Solving time-dependent Schrödinger equation on a lattice	34
3.4.4	Relativistic eikonal theory of electron capture	36
3.4.5	Comparison of electron capture cross sections	37
4	Classical transport theory	42
4.1	Introduction	42
4.2	Classical transport theory	43
4.3	Highly excited states	45
4.4	Convoy electron emission	46
4.4.1	Random walk	47
4.4.2	Convoy electron distribution	49
4.4.3	Comparison with experiment	51
4.5	Summary	52

5	Quantum transport theory	54
5.1	Introduction	54
5.2	Master equation	55
5.3	Unitary open quantum systems	58
5.3.1	Unitary Lindblad master equation	58
5.3.2	Quantum trajectory Monte Carlo solution	59
5.4	Non-unitary open quantum systems	64
5.4.1	Non-unitary Lindblad equation	65
5.4.2	Quantum trajectory Monte Carlo solution	68
5.4.3	Analytical equivalence	69
5.4.4	Test case: radiative cascade as sink	72
5.5	Alternative solution	75
5.5.1	Solving quantum master equation directly	75
5.5.2	Lindblad master equation for quasi-free electrons	75
5.6	Summary	76
6	Non-unitary decay operators	77
6.1	Introduction	77
6.2	Electron-core collisions	78
6.2.1	Closure approximation	79
6.2.2	Decay rates	80
6.2.3	Numerical results for core collisions	82
6.2.4	Convergence for high n	85
6.3	Electron-electron collisions	86
6.3.1	Closure approximation and decay rates	87
6.3.2	Numerical results for electron collisions	88
6.3.3	Convergence for high n	91
6.4	Summary	92
7	Application to Kr^{35+} transport	93
7.1	Introduction	93
7.2	Numerical results	97
7.2.1	Role of loss channel	98
7.2.2	Transient coherences	102
7.3	Decay of coherences: decoherence	105
7.3.1	A simple model for transient coherence	105
7.3.2	Numerical results for coherences	110
7.4	Comparison with experiment	116
7.5	Summary	118

8	Open quantum system with a source	120
8.1	Introduction	120
8.2	Source term in Lindblad master equation	120
8.3	Application to radiative cascade	126
8.3.1	Radiative cascade as source	127
8.3.2	Radiative cascade as source and sink	128
8.4	Summary	130
9	Application to Ar¹⁸⁺ transport	131
9.1	Introduction	131
9.2	Numerical simulation	133
9.2.1	Transient coherence	136
9.3	Relativistic effects in electron capture	137
9.3.1	Predictions by non-relativistic theories	137
9.3.2	Comparison with experiment	139
9.4	Comparison of populations	145
9.4.1	Dependence on capture density matrix	147
9.4.2	Effect of wake field	148
9.4.3	Comparison with alternative approaches	151
9.5	Summary	152
10	Summary and conclusions	153
	Bibliography	155
	List of figures	163
	List of tables	164
	Acknowledgments	165

Chapter 1

Introduction

The passage of an atom or ion through a solid represents a system with a variety of interesting physical phenomena that is, however, difficult to describe. We probe the effect of the solid on the internal degrees of freedom of the projectile by focusing on hydrogenic projectiles penetrating the target at moderately relativistic velocities. The complexity of a theoretical treatment of the projectile-solid interaction originates from the many-body nature of the solid. Additionally, the large Hilbert space of the hydrogenic projectile prohibits a full quantum mechanical solution within the entire Hilbert space. Different approaches have been developed in the past applicable for different collision systems.

A description within classical mechanics was successfully adopted for systems where the electron is weakly bound to the projectile nucleus. A classical transport theory (CTT) was developed [Bur88, Bur90a] describing the time evolution of an electron bound to the projectile ion during the transport through a solid. By a discretization of the electronic phase space individual classical electron trajectories can be followed according to a Langevin equation. Initially the studies of ion-solid transport were motivated by the application of stripping foils in a tandem accelerator scheme for spallation neutron sources [Ger96, Gul96] first accelerating H^- ions that get converted into H^+ in the foil and are then stored in an accumulation ring of a spallation neutron source. A detailed knowledge of the electron dynamics provided helpful information for the design of optimal foils such that stripping is effective but does not result in significant beam spreading and energy loss. The dynamics of the active electron can be followed during the excitation and in the continuum by a classical trajectory Monte Carlo (CTMC) simulation. First calculations based on classical dynamics were performed for ions with low nuclear charge.

Energy spectra of emitted continuum electrons exhibit a sharp peak in

forward direction at the same velocity as the projectile ion. Various aspects of this convoy electron peak were studied in the non-relativistic velocity regime in the past decades [Dre76, Bur83a, Els85]. The shape and intensity of this cusp reveals details not only about the dynamics in the low-energy continuum but also about excited state populations prior to ionization. The CTT is appropriate for the description of this electron emission process.

To access quantum effects a quantum transport theory (QTT) has been developed. The time evolution of the density matrix is described by a quantum master equation (QME). In a system with N_S states the direct solution of the QME involves N_S^4 couplings. Solving the QME for the density matrix directly [Ver01] is only possible for a reduced set of couplings due to the large projectile Hilbert space of a hydrogenic ion. Alternatively, the QME can be solved by means of a Monte Carlo discretization with quantum trajectories. The time evolution of each trajectory was in a first QTT determined by a stochastic Schrödinger equation [Arb99, Arb00, Min02a, Min02b]. The importance of this quantum trajectory Monte Carlo (QTMC) method [Car93, Min03a] and closely related techniques such as the Monte-Carlo wavefunction method [Dal92, Mol93, Dum92] lies in the reduction of dimensionality of the problem. Propagating states rather than the density operators leads to a scaling with N_S^2 . In both transport theories (CTT and QTT) the interaction of the projectile electron with the solid was taken into account in the quasi-free electron limit. As the QTT reduces to the CTT in the limit of highly excited states, the transition from the quantum regime to the classical domain could be studied [Arb99, Arb00].

Considerations beyond the quasi-free electron approximation are necessary for deeply bound states of highly charged ions. This step requires significant extensions of the QTT which was done by means of an open quantum system approach [Min03a]. The open quantum system (OQS) approach provides a useful theoretical framework for describing the time evolution of a system interacting with an environment representing a large number of degrees of freedom. The underlying concept of studying the partially coherent dynamics of the reduced “small” system under the influence of all other degrees of freedom of the problem to be traced out is at the core of the investigations of decoherence. For example, the coupling between an atom (the small system) and the vacuum fluctuations of the radiation field (the environment) results in spontaneous transitions in the atomic system (i.e. radiative decay) and thus in decoherence as well as in modifications of the eigenstates by shifting their eigenenergies (the Lamb shift).

The passage of an atomic system through solids under multiple-scattering conditions provides a typical example of the interaction of an open quantum system (the projectile) with a large environment (the solid). Studying such

transport problems has the advantage that the system-environment interaction is switched on suddenly when the projectile enters the solid and ceases suddenly after escaping from the solid, thus allowing the time-resolved study of the evolution of the density matrix on an attosecond to femtosecond time scale.

Starting point of a theoretical analysis of OQSs is, typically, the reduction of the master equation for the reduced density matrix to a Redfield equation by applying the Born-Markov approximation [Dal92, Mol93, Dum92, Car93, Min03a]. Even with such a drastic simplification which treats the coupling to the environment in first-order perturbation theory and neglects memory effects, a solution of the equation of motion for the density matrix is still a formidable task. Difficulties in describing OQSs in terms of the evolution of the reduced density matrix originate from the high dimensionality of the problem.

Solving the Redfield equation by QTMC techniques requires its reduction to a form strictly preserving positive definiteness of the reduced density matrix. This can be conveniently achieved by a reduction to a Lindblad form [Lin76a, Lin76b]. Alternatively, a solution of the Redfield equation by QTMC methods has been proposed [Kle02, Kon03] requiring, however, an extended state space. Depending on the physical system to be described, the reduction to the Lindblad form is not unique and is still an open problem. A form for this reduction that accounts for both the build-up of coherences as well as the decoherence [Min03a] was recently developed opening up a wide range of applications.

The first analysis was directly related to experimental studies of collisionally induced coherences in highly charged Kr^q ($q=35$) ions traversing carbon foils at high velocity ($v_p=47$ a.u.). While good agreement was found for thin foils corresponding to short interaction times, discrepancies for thicker distances ($\geq 10^4$ a.u.) corresponding to propagation times of ≥ 5 fs were observed [Min03a]. These discrepancies were particularly troubling as they only appeared within the formulation of quantum transport in terms of a Lindblad equation [Min03a] while with an earlier more phenomenological model [Min02a] better agreement could be obtained. Understanding and resolving these discrepancies was the starting point of the investigations leading to the results discussed in this thesis.

One key feature of the Lindblad equation is the unitarity of the evolution of the described reduced system, built in by construction. The point to be noted is that preservation of positivity does not necessarily require unitarity. In fact, the unitarity of the Lindblad equation is of limited value when dealing with any truncated Hilbert space of the reduced system in a realistic simulation. As flux out of this subspace into its outgoing complement

can and, in general, is bound to occur, enforcing unitarity means unphysical suppression of flux out of the system and thus distortion of the evolution within the truncated Hilbert space. A classic example is the propagation of wavepackets of continuum electrons. Within any basis expansion or finite elements (grid) representation of finite dimension, only a bounded region in coordinate space can be represented. The wavepacket will therefore be artificially reflected at the boundary unless absorbing boundary conditions, optical potentials or masking functions are introduced [Yos99]. All of these methods result in absorption of probability flux and thus in a manifestly non-unitary evolution. In analogy, we introduce in this thesis a generalized non-unitary Lindblad equation and its QTMC realization that accounts for probability flux out of the truncated Hilbert space to be explicitly treated. The class of open quantum systems discussed in the following are not only open with respect to energy transfer but also with respect to probability flux in analogy to a grand canonical ensemble in statistical mechanics. In the application to the projectile state evolution in the solid the present approach permits to treat explicitly the low-lying states of the ion within a finite Hilbert space of a size manageable within a numerical solution using a Monte Carlo method, while implicitly accounting for the flow of probability towards highly excited bound states and continuum states in the complement. This method significantly modifies the results and leads to better agreement with measurements. A shortcoming of this first extension of the Lindblad master equation to a non-unitary form is that while it can account for probability flux out of the system no flow into the system is considered.

To account for this deficiency we introduce a scheme that allows to solve a Lindblad master equation including a source term. This generalization enables to address the question of coherence in a system that has a continuous influx of probability. As an application we turn to the transport of projectiles entering the solid without an electron attached. The projectile degrees of freedom are subsequently populated by electron capture. The open quantum system approach renders the possibility to investigate the role of coherence populated by electron capture as well as by excitation. Furthermore, in comparison with measurements different methods for the calculation of capture cross sections can be tested.

Electron capture in ion-atom collisions is treated using a variety of sophisticated methods. Due to the complexity of the three-body dynamics, different methods often lead to different results. Capture cross sections can be reconstructed from single ion-atom collisions or from ion-solid interactions. The disentanglement of the single collision contributions from transport effects in the measured signal constitutes one of the aims of a theoretical description of the full transport problem. Recently an effort was made to resolve the

issue of electron capture [Min04a]. To provide an accurate description, the time-dependent Schrödinger equation has been solved on a lattice with the help of an up-to-date large scale computer facility. We present a comparison of cross sections in the single collision regime and during transport with other methods. We also present a study of transient coherences during different stages of the time evolution.

Outline

The thesis is organized as follows. After an overview of the elementary processes of ion-solid interaction we sketch the experiments that triggered our investigations of solid-state effects (chapter 2). In chapter 3 we provide the calculation of cross sections for the various scattering mechanisms such as collisions and electron capture. We describe the classical transport theory (CTT) and apply it to the emission of convoy electrons (chapter 4). We present a quantum transport theory (QTT) by means of an open quantum system (OQS) approach for ion-solid transport that describes also loss to an unobserved complement (chapter 5). The calculation of the modified collisional decay operators entering this non-unitary QTT is addressed in chapter 6. In a first application to $\text{Kr}^{35+}(1s)$ transport we investigate transient coherences in comparison with a simple model for decoherence (chapter 7). In chapter 8 we discuss an OQS approach describing systems with a source and present calculations of the radiative cascade of excited states feeding deeply bound states. In the application to Ar^{18+} transport we investigate transient populations and coherences created by electron capture (chapter 9). We discuss different models for electron capture and their performance in comparison with experimental data. Atomic units (a.u.), where $|e|=m_e=\hbar=1$ and $c=137$, will be used throughout this thesis unless otherwise stated.

Parts of this thesis have already been published [Sel05a, Sel03, Sel01, Tak03] are in print [Sel05b] and in preparation [Sel05c].

Chapter 2

Overview

The evolution of a projectile states through a solid is a very complicated issue due to the many-body dynamics. To get an insight into the dynamics we subdivide the target into its individual constituents and consider their interactions. The solid is composed of atomic cores and electrons bound to these cores. The relevant processes in ion-solid transport can be divided into two groups: exchange of energy with the solid and exchange of constituents. Collisions lead to transfer of energy and momentum while electron capture transfers electrons from the target to the projectile. Ionization is the effect in the opposite direction transferring electrons from the projectile to the target. In the following we present a brief overview over the processes relevant in the further discussion. In the next chapter we go into the details of the cross section calculations for these processes as they will be the input for the simulation of transport problems.

At the end of this overview we briefly sketch the setups of the experiments we will compare with. These experiments use fast highly charged ions to probe the interaction with the solid. The first setup was designed to measure electrons emitted during transport. In the second experiment emitted photons were recorded. For very short interaction times the projectile can only interact only once with the solid. The gradual shift from this single interaction picture to a multiple interaction scheme indicates the effects of the solid.

2.1 Elementary processes

Collisions

We shall consider the interaction of the projectile electron with the solid. The interaction with atomic cores and electrons exhibits different characteristic

features. The scattering at target atoms can be considered as electron scattering at a central potential. This potential is not a pure Coulomb potential because target electrons partially shield the atoms. The mass of the target atom is very large compared to the projectile electron mass. In a collision almost no energy is transferred to the target. Consequently the kinetic energy of the projectile electron in the target rest frame is not modified. Only the direction of the velocity vector is changed. Therefore the scattering at target atoms is sometimes referred to as elastic scattering. However, this process allows for the transformation of translational energy into excitation of internal projectile degrees of freedom. In other words, free electrons are scattered at target atoms elastically while electrons attached to projectiles can undergo state-to-state transitions within the hydrogenic Hilbert space. Henceforth we call this process scattering at atomic cores.

In scattering at target electrons also energy can be transferred. Therefore this scattering process is sometimes referred to as inelastic scattering. The valence electrons in the target can get excited easily and they are mobile. This has three consequences. First, the amount of momentum and energy transferred to the projectile electron can be small while core scattering is a more violent event. Secondly, the target electrons represent a strongly coupled ensemble where also collective oscillations can be excited. Thirdly, the mobility in combination with the projectile Coulomb potential causes the target electrons to move towards the projectile. This effect induces the so-called wake field we will focus on now.

Wake field

The highly charged projectile in the solid attracts target electrons. The electrons move as long as the projectile potential is not completely shielded. For an ion at rest the target electrons have enough time to adjust to the perturbation such that the ion is shielded. In case the ionic projectile is faster than the Fermi velocity of target electrons, complete shielding at small distances to the ion is not possible any more. Target electrons try to shield the projectile but are too slow to succeed. The perturbation introduces electron density fluctuations. The effective potential of these fluctuations has a maximum behind the projectile with respect to the moving direction. Figure 2.1 depicts an example of the potential of electron density fluctuations. Due to its structure it is called the “wake” potential.

This wake potential is responsible for a number of interesting effects. At the position of the ion the potential has a slope that results in an electric field. This field is slowing down the ion and therefore contributes to the “stopping power”. An electron attached to the projectile ion evolves in the

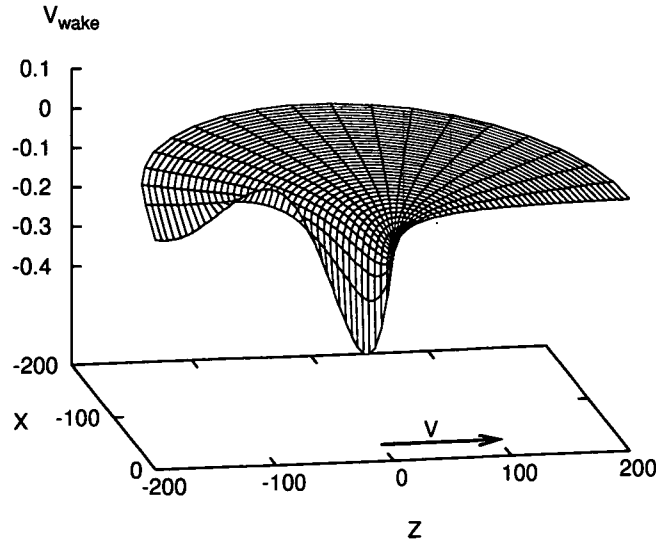


Figure 2.1: Wake potential of a bare argon ion during transport through a carbon foil with an energy of 13 MeV/amu. The direction of the projectile velocity is parallel to the z -coordinate.

vicinity of the combined potential of the ion and the wake potential. The presence of the wake potential modifies the hydrogenic Hamiltonian in two ways. (i) The energy levels are shifted according to the value of the potential at the ion position. (ii) The slope of the potential producing an electric field results in Stark mixing.

Electron capture

A highly charged ion in a solid attracts target electrons by its high nuclear charge. Consequently an ion at rest is neutralized very fast. A moving ion attracts target electrons as well, but the short interaction time prevents a fast neutralization. Nevertheless, a target electron can be captured by the projectile ion. If the final state is in the projectile continuum we speak of electron capture to continuum (ECC) [Luc80, Bur86]. Here we are interested in electron capture into hydrogenic bound states of highly charged ions at moderate relativistic velocities.

The dynamics of electron capture is complicated by the fact that the target electrons move in the potentials of both the target and the projectile.

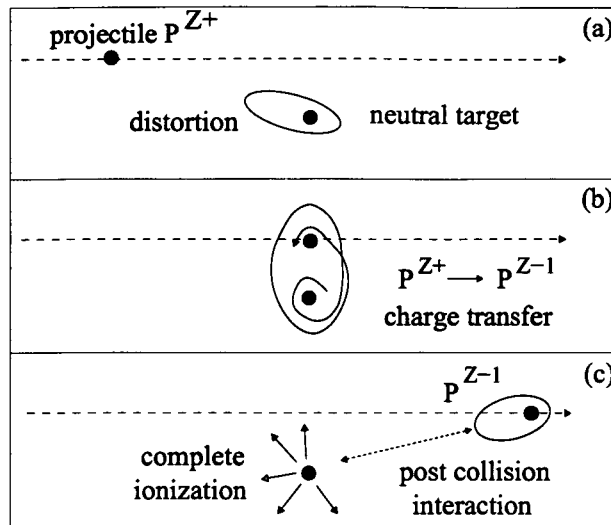


Figure 2.2: Classical picture of electron capture in a collision of a bare highly charged ion with a neutral atom. We show the different stages of the capture process; (a) distortion of initial state; (b) charge transfer; (c) post collision interaction.

To follow this many-body problem in time is a formidable task. First we would like to estimate which target electrons contribute most and what final states are to be expected to be predominantly populated.

Charge transfer cross sections are related to the overlap in phase space of the initial with the final state. To estimate the region of phase space the following “velocity matching” consideration has been proven to be useful. Electrons in target bound states have a certain velocity distribution centered around the Bohr velocity Z_T/n . A moderately relativistic projectile exhibits a velocity overlap in the tails of these velocity distributions. The overlap is larger for higher Bohr velocities. Consequently the velocity overlap is maximal for the 1s target electron. Capture from 2s is suppressed by the significantly larger velocity mismatch and hence less overlap in the tails. Therefore capture from 1s is the dominant channel. Most calculations consider the 1s target electron as the only active electron in the capture process at high projectile velocities.

After having identified the dominant initial state we can also make an estimation for the spatial region where charge transfer occurs. The 1s electron is initially localized close to the target nucleus. Therefore the major contribution to capture cross sections can be expected to originate from small impact parameters. At these distances the Coulomb potential of the pro-

jectile strongly acts on the electronic states making a theoretical description challenging.

To close in on the problem and in view of the complexity of the three-body dynamics we first identify the different stages of the time evolution. For simplicity we first choose a classical picture (figure 2.2). The nuclear motion is unaltered due to the high relative velocity. While the projectile approaches, the initial target state gets distorted as indicated by the elliptic orbit of the classical trajectory of the active electron (figure 2.2 (a)). In the region of closest approach the charge transfer occurs (figure 2.2 (b)). At this close distance the electron is strongly perturbed. After the internuclear distance has increased enough such that charge transfer has ceased the electron is attached to the projectile nucleus with a certain probability (figure 2.2 (c)). The long range Coulomb potential of the ionized target atom perturbs the final states of the projectile whilst its departure for the collision region. This effect is called the post collision interaction (PCI) and is in general significantly mixing the final projectile states. Previous investigations [Rei04] indicated that the target atom can get completely ionized as a result of the very close passing-by of the highly charged bare projectile ion. The remaining bare target ion with a high nuclear charge is responsible for a considerable amount of mixing of projectile states during the PCI.

2.2 Experimental realization

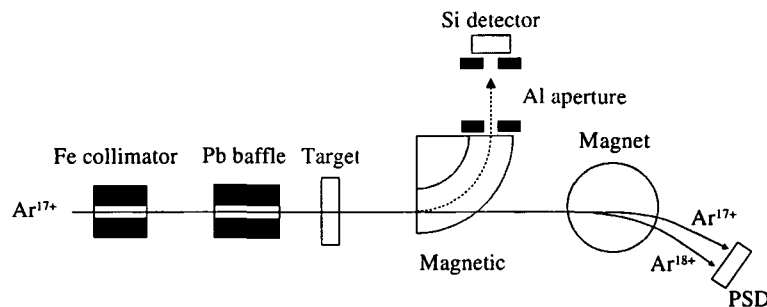


Figure 2.3: Schematic drawing of the experimental setup with the magnetic spectrometer for convoy electrons and the subsequent separation of ion charge states. Solid lines: trajectories of Ar ions; dotted line: convoy electron trajectory in the magnetic spectrometer [Tak99a].

For ion-atom collisions a variety of detector systems has been developed not only to measure the reaction products but also to obtain information

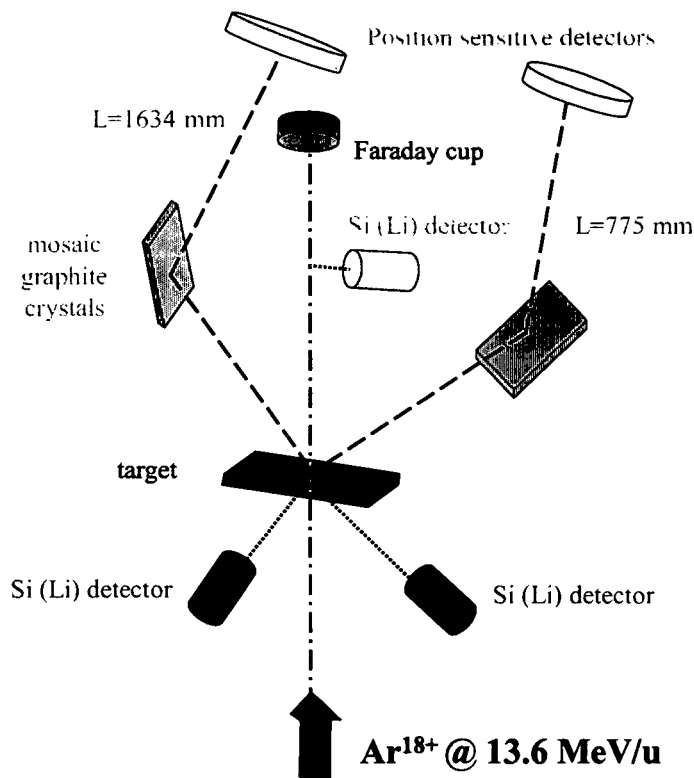


Figure 2.4: Schematic picture of the experimental setup for measurements of photons emitted in transport of Ar^{18+} and Kr^{36+} projectiles through a solid target [Lam97].

on differential cross sections. In the following we present two examples of detector systems that are relevant for measurements of ion-solid interactions. Later we will compare our simulation results with the measured data from these two experimental setups.

The first experiment performed at the Heavy Ion Medical Accelerator in Chiba (HIMAC) [Tak99a, Tak99b, Tak03] schematically depicted in figure 2.3 investigates the passage of relativistic hydrogenic ions through a solid target. For these measurements a beam of Ar^{17+} ions accelerated to an energy of 390 MeV/u corresponding to a velocity of $v_p=97 \text{ a.u.}$ has been used. The target is a self-supporting amorphous carbon foil. The final charge state of the projectile is observed by a magnetic spectrometer. Putting an energy dispersive detector at the end of the beam line (for example a semiconductor detector) allows to measure the kinetic energy of the transmitted projectiles. As the projectile undergoes inelastic collisions depositing energy in the solid

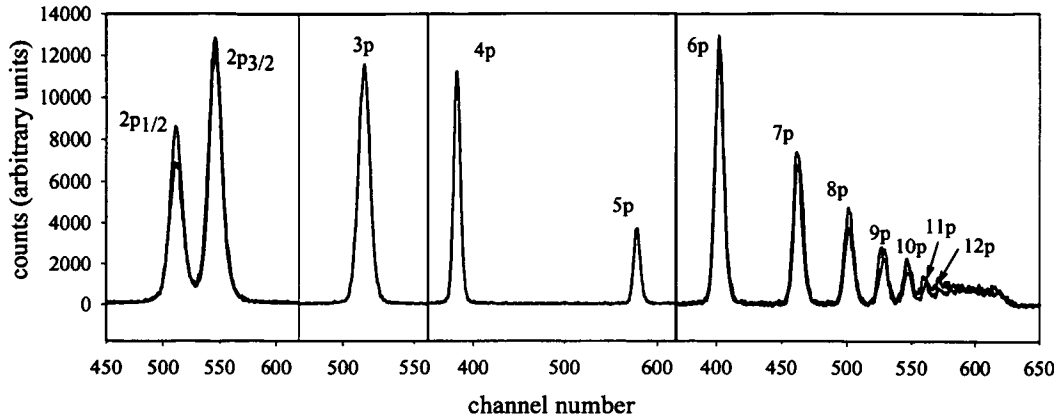


Figure 2.5: Spectrum of emitted photons from Ar^{17+} in the transport of initially Ar^{18+} as a function of channel number in arbitrary units, i.e. counts [Lam05]. Black line: gaseous CH_4 target; red line: amorphous carbon target of $47.2 \mu\text{g}/\text{cm}^2$ thickness. The scaling is chosen individually for each part of the spectrum separated by vertical lines. The counting rate decreases with increasing n , i.e. from left to right.

its kinetic energy is reduced. Thick targets can even stop the projectile. The amount of stopping, the stopping power, gives information about the material or about the actual thickness of the target. The thickness is typically denoted in units of mass per area like $\mu\text{g}/\text{cm}^2$ ($1\mu\text{g}/\text{cm}^2 \approx 94 \text{ a.u.}$).

To get a deeper insight into the dynamics of the projectile in the solid the state of the attached electron has to be analyzed. One possibility is to observe the continuum state of the electron by means of a magnetic spectrometer where a semi-conductor detector counts all electrons in $\Delta E = \pm 9 \text{ keV}$ centered around the nominal kinetic energy (figure 2.3). Momentum spectra of electrons can be accumulated by scanning the magnetic field strength of the spectrometer. Electron spectra recorded by this setup will be later discussed. The differential electron spectra provide in combination with a simulation insight into the electron emission process as well as information about excited states prior to ionization.

Detailed information on the dynamics of deeply bound states can be acquired by measurements of emitted photons. The detection of the emitted characteristic photons allows the determination of excited state populations. These experiments were performed at GANIL (Grand Accélérateur National d'Ions Lourde) on the LISE (Ligne d'Ions Super Epluchés) facility [Ver98, Lam97, Fou00]. The projectiles used were hydrogenic Kr^{35+} at an energy of $60 \text{ MeV}/\text{amu}$ corresponding to a collision velocity of $v_p=47 \text{ a.u.}$

and Ar^{18+} at 13.6 MeV/amu ($v_p=23$ a.u.). Photons emitted during and after interaction of the projectile with the target (carbon foil) were measured by different detectors (figure 2.4). Spectra of Balmer and Lyman lines can be recorded by semiconductor photo-detectors based on Ge and Si(Li). In order to separate individual components a high-resolution high-transmission Bragg-crystal spectrometer has been developed. A mosaic graphite crystal reflects the high energy photons onto a position sensitive detector allowing to achieve a resolving power of 2.2×10^{-2} which corresponds to a linewidth of 7 eV for 3.1 keV photons. The arm length of the spectrometer determines the acceptance window of photon energies. Modification of this length allows to adapt each detector to a certain energy range and thus to cover the whole spectrum of Lyman and Balmer lines as will be later shown for the example of fully stripped argon ions. The first spectrometer with a long arm length of 1634 mm could resolve individual fine-structure components of the Lyman α -line as displayed in figure 2.5. With the second spectrometer with a short arm length of 775 mm Lyman lines from $n>2$ were recorded up to $n=12$.

The 2s state does not relax to the ground states by a single photon transition but via a 2-photon decay with a lifetime much longer than, for example, the lifetime of the 2p state. A long lifetime implies a decay far behind the target in contrast to the dipole photon transitions emitting photons only millimeters after the foil. To this end a Si(Li) detector was placed downstream from the target extending the acceptance region up to 127 mm behind the foil. As energy conservation has to be satisfied only for the sum of the two photon energies the linewidth of a two-photon decay is much broader than that of a single-photon transition. Therefore the resolving power of a semiconductor detector was efficient for this purpose.

2.3 Observation of solid state effects

The available carbon foils can be very thin such that the projectile interacts at most only once corresponding to single collision conditions. These conditions are experimentally also realizable by dilute gaseous targets such as CH_4 . When we consider a certain observable measured under single collision conditions, the interesting question is how this observable will change with increasing target thickness. For longer interaction times with the target modifications of the measured data can be expected.

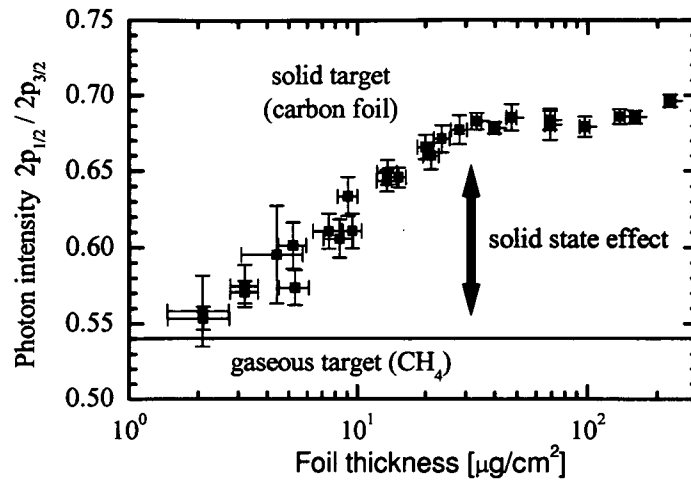


Figure 2.6: Experimental ratio of photon intensities $(2p_{1/2} \rightarrow 1s)/(2p_{3/2} \rightarrow 1s)$ as a function of carbon foil thickness emitted by an Ar^{17+} projectile with a velocity of $v_p = 23$ a.u. initially in the Ar^{18+} state [Lam97]. Data obtained by a gaseous target plotted as reference line.

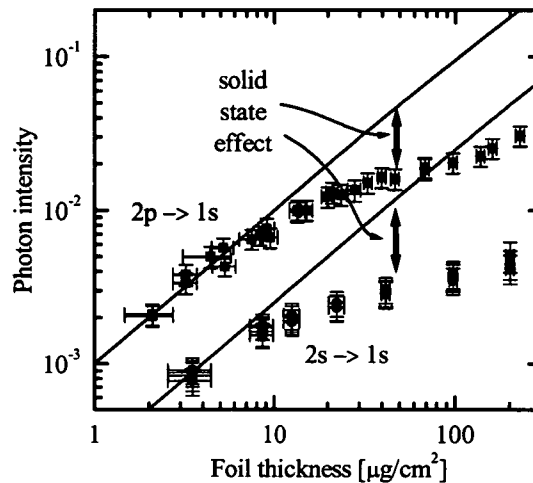


Figure 2.7: Experimental photon intensities as a function of foil thickness emitted by an Ar^{17+} projectile in transmission through an amorphous carbon foil with a velocity of $v_p = 23$ a.u. initially in the Ar^{18+} state [Lam97]. Extrapolation of single collision values to thicker targets according to $1 - \exp(-\alpha x)$ indicated as lines. The parameter α was fitted to measurements for thinnest foils.

To verify this assumption the integrated peak intensities of the spectrum (figure 2.5) are compared for different transitions. As an example, in figure 2.6 the ratio between two transitions is depicted. Measurements with a gaseous target as well as measurements with the thinnest carbon foils yield the same value. However, for thicker solid targets we observe a dramatic increase of the measured ratio as a result of the interaction with the solid.

In figure 2.7 individual integrated peak intensities of Lyman transitions for different target thicknesses are displayed. The clear deviation from the extrapolation to thicker targets based on single-collision data reveals the presence of solid state effects. These measurements provide direct information on excited state populations during the interaction of the projectile with the solid. The exploration of these solid state effects is the major goal of this thesis.

After a qualitative description of the different processes in the solid and the experimental realization to measure these solid state effects we focus in the next chapter on the explicit calculation of the various cross sections. We will describe collisions with constituents of the target, i.e. atomic cores and electrons, presenting calculations of the collision cross sections for state-to-state transitions as well as for free electrons. We provide a description of the wake potential and the calculation of matrix elements entering the Hamiltonian. Finally we turn to electron capture as treated within different approximations.

Chapter 3

Processes in ion-solid transport

In this chapter we describe the calculation of cross sections as they enter the simulation of transport problems. We first discuss the properties of the unperturbed hydrogenic Hamiltonian and its eigen-energies. Then we give a description of the calculation of collisional cross sections for the interaction with atomic target cores and with electrons (section 3.2). The matrix elements of the wake field and the modification of the Hamiltonian is discussed (section 3.3). Models for electron capture are presented followed by a comparison of capture cross section (section 3.4).

3.1 Energy spectrum of hydrogenic ion

The hydrogenic Hamiltonian

$$H_S^{(\text{non rel})} = -\nabla_r^2/2 - Z_p/r \quad (3.1)$$

with the kinetic and potential energy terms exhibits bound state eigen-energies as a function of the principal quantum number n according to

$$E(n) = -Z_p^2/(2n^2) \quad (3.2)$$

with the nuclear charge Z_p . In vacuum the eigen-spectrum is degenerate with respect to the angular momentum l and its projection onto the quantization axis m_l . By including relativistic corrections ΔH_{rel} , i.e. fine structure and Lamb shift, the Hamiltonian becomes

$$H_S = -\nabla_r^2/2 - Z_p/r + \Delta H_{rel} . \quad (3.3)$$

The eigenstates of H_S can be quantified by the quantum numbers n , l , j and m_j . Considering the electron spin and the fine-structure the energy spectrum

is given as a function of the total angular momentum $\vec{j} = \vec{l} + \vec{s}$ as

$$E = \mu c^2 \left(\left(1 + \left(\frac{\alpha Z_p}{n - j - \frac{1}{2} + \sqrt{(j + \frac{1}{2})^2 - (\alpha Z_p)^2}} \right)^2 \right)^{-\frac{1}{2}} - 1 \right) + E_{LS} \quad (3.4)$$

with the fine-structure constant $\alpha = 1/c$ and the reduced mass $\mu = M_p/(M_p + 1)$ (M_p : mass of projectile).

The only l dependent term is the Lamb shift correction E_{LS} . The Lamb-shift can be parameterized by [Pal98]

$$E_{LS} = (\alpha Z_p)^4 \frac{1}{\pi n^3} \frac{1}{\alpha} \Lambda \quad (3.5)$$

with Λ listed in table 3.1. As a result of the Lamb shift the energy of the $p_{1/2}$

	argon	krypton
$\Lambda(1s_{1/2})$	3.2302	2.0975
$\Lambda(ns_{1/2})$	3.4832	2.3949
$\Lambda(np_{1/2})$	-0.0980	-0.0486
$\Lambda(np_{3/2})$	0.1402	0.1707

Table 3.1: Lamb-shift parameter Λ for argon and Krypton according to (3.5)

state lies below the energy of the $s_{1/2}$ state and analogously $d_{3/2}$ is slightly below $p_{3/2}$. The resulting eigen-energies are listed in table 3.2.

	n=1	n=2	n=3	n=4
$s_{1/2}$	-162.66	-40.714	-18.0763	-10.15989
$p_{1/2}$		-40.720	-18.0781	-10.16062
$p_{3/2}$		-40.543	-18.0256	-10.13850
$d_{3/2}$			-18.0257	-10.13852
$d_{5/2}$			-18.0084	-10.13122
$f_{5/2}$				-10.13122
$f_{7/2}$				-10.12758

Table 3.2: Eigen energies (a.u.) of an electron bound to an argon nucleus including fine-structure and Lamb shift corrections.

The important point for the later investigation of coherences is that the energy spectrum has three classes of energy spacings between two levels. The

large inter-shell energy spacings according to equation (3.2) are of the order of magnitude of 10 a.u.. The intra-shell energy spacings are determined by fine-structure (equation (3.4)) and Lamb-shift (equation (3.5)). Both scale to first order as n^{-3} . In combination with the n^{-2} scaling of the inter-shell energy this leads to a decreasing role of intra-shell energy splittings compared to inter-shell splittings with increasing value of n . Nevertheless, the dominant fine-structure splitting is always one order of magnitude larger than energy spacings due to Lamb-shift.

3.2 Collisional cross sections

After having given a qualitative description of the scattering processes in solids in section 2.1 we now tackle the explicit calculation of the corresponding cross sections. In perturbation theory scattering cross sections are obtained by Fermi's Golden Rule in first order Born approximation. This implies the assumption of linear response of the target which is valid for weak perturbations of the target. Within linear response theory the target is always found in its ground state prior to interaction. This assumption is certainly valid for the fast projectiles we are studying throughout this thesis.

As the projectile moves through the solid it induces a perturbation. This perturbation is quantified by means of a momentum transfer \vec{k} and an energy transfer ω . The strength of the response of the target to this perturbation determines the differential cross section for \vec{k} and ω . Therefore the target response has to be quantified in order to obtain the scattering cross sections. The response of the target to the perturbation given by momentum \vec{k} and energy ω consists of fluctuations of target particle density $\rho_T(\vec{x}_T)$. In coordinate space the target density is represented by a sum over the positions \vec{r}_j of all interacting particles $\rho_T(\vec{x}_T) = \sum_j \delta(\vec{x}_T - \vec{r}_j)$ while $\tilde{\rho}_T(\vec{k})$ denotes the Fourier transform of the target particle density. Evaluating the sum over transitions from the initial ground state to all possible final states of the target is demanding due to the exceedingly large sum over the target states. Since target particles interact with each other as well as with the projectile, excitations of collective resonances become possible making the evaluation of the response even more challenging. In many-body physics [Pin89] the response of a target to a perturbation \vec{k}, ω is described by the susceptibility denoted as $\chi(\vec{k}, \omega)$. In this context the imaginary part of $\chi(\vec{k}, \omega)$ (denoted as $\chi''(\vec{k}, \omega)$) describes the dissipative part of the response. The sum over transitions from the initial target ground state $|0_T\rangle$ to all possible final states of

the target $|f_T\rangle$ can be assigned to [Pin89]

$$\chi''(\vec{k}, \omega) = \pi \sum_{f_T} |\langle f_T | \tilde{\rho}_T(\vec{k}) | 0_T \rangle|^2 \delta(\omega_T - \omega). \quad (3.6)$$

where ω_T describes the energy difference between the states $|f_T\rangle$ and $|0_T\rangle$ and $\tilde{\rho}_T(\vec{k})$ denotes the Fourier transform of the target particle density. The convenience of (3.6) is that while the details on the dynamics of target particles may be inaccessible, $\chi''(\vec{k}, \omega)$ can be determined by other means, theoretically or experimentally. Later we will discuss the evaluation of $\chi''(\vec{k}, \omega)$ for different scattering mechanisms.

With the approximation (3.6) we can express the differential scattering cross section for a transition from the initial projectile state $|i\rangle$ to the final state $|f\rangle$ by [Min03a]

$$\frac{d\sigma_{fi}(\vec{k})}{d\vec{k}} = \frac{2}{v_p} \tilde{V}_{PT}^2(\vec{k}) |\langle f | e^{i\vec{k}\vec{r}} | i \rangle|^2 \chi''(\vec{k}, \omega_{if} - \vec{k}\vec{v}_p) \quad (3.7)$$

where $\tilde{V}_{PT}(\vec{k})$ is the Fourier transform of the interaction potential and $e^{i\vec{k}\vec{r}}$ the Fourier transform of the projectile density for a point-like particle at position \vec{r} . The energy transfer ω in equation (3.6) is shifted (due to the transformation from the projectile to the target rest frame) by the translational energy parallel to the projectile velocity $\vec{k}\vec{v}_p$. The cross section in (3.7) is of the form

$$\frac{d\sigma_{fi}(\vec{k})}{d\vec{k}} = |S_{if}(\vec{k})|^2 \quad (3.8)$$

with the transition operator

$$S_{if}(\vec{k}) = \sqrt{\frac{2}{v_p}} \chi''(\vec{k}, \omega_{if} - \vec{k}\vec{v}_p) \tilde{V}_{PT}(\vec{k}) \langle f | e^{i\vec{k}\vec{r}} | i \rangle. \quad (3.9)$$

For the calculation of state-to-state cross sections for scattering of a hydrogenic projectile, we have to evaluate the scattering form factor $\langle f | e^{i\vec{k}\vec{r}} | i \rangle$ in (3.9) in the hydrogenic basis. This implies that $|i\rangle$ and $|f\rangle$ are to be taken as hydrogenic bound state wave functions.

To obtain scattering cross sections for free electron scattering we choose the wave functions of free electrons. These are plane waves in coordinate space given by $\phi_i(\vec{r}) = \exp(i\vec{k}_i\vec{r})/(2\pi)^{3/2}$ with the electron momentum \vec{k}_i . We consider the momentum \vec{k}_i of $|i\rangle$ and \vec{k}_f of $|f\rangle$ in the rest frame of the target. Evaluation of the scattering form factor leads to

$$\langle f | e^{i\vec{k}\vec{r}} | i \rangle = \frac{1}{(2\pi)^3} \int d^3r e^{-i\vec{k}_f\vec{r}} e^{i\vec{k}\vec{r}} e^{i\vec{k}_i\vec{r}} = \delta(\vec{k}_i + \vec{k} - \vec{k}_f) \quad (3.10)$$

with the initial and final momentum, \vec{k}_i and \vec{k}_f , respectively. The resulting delta function expresses momentum conservation or, in other words, the final momentum as $\vec{k}_f = \vec{k}_i + \vec{k}$. The differential cross section is

$$\frac{d\sigma_{fi}(\vec{k}, \omega)}{dkd\omega} = \frac{2}{v_p} \tilde{V}_{PT}^2(\vec{k}) \chi''(\vec{k}, \omega) \delta(\vec{k}_i + \vec{k} - \vec{k}_f). \quad (3.11)$$

In transport theory it has proven useful to consider mean free paths rather than cross sections. The mean free path (MFP) is the path length that the projectile, on average, travels through the target between two subsequent scattering events. The MFP λ is related to the cross section σ as $\lambda = 1/(n_A\sigma)$ with the number density of the scattering particles per unit volume as n_A . In case the cross section has been calculated as scattering at an ensemble of particles, the number density is already contained in σ . Also the inverse MFP (IMFP) is frequently used. From (3.11) we can construct the differential IMFP for free electron scattering as

$$\frac{d^2\lambda^{-1}(k, \omega)}{d\omega dk} = \frac{k}{2\pi^2 v_p^2} \tilde{V}_{PT}^2(\vec{k}) \chi''(\vec{k}, \omega) \quad (3.12)$$

being differential with respect to energy and momentum transfer. From the point of view of scattering a target consists of two constituents: the atomic cores and the electrons. We first consider the core scattering and later describe electron scattering.

3.2.1 Electron-core collisions

The atoms in the target attract the target electrons that partly shield the pure nuclear Coulomb potential. A useful approximation of this shielding is a Yukawa type potential as $V_{PT}(\vec{r}) = -(Z_T/r) \exp(-r/a_{TF})$ with the Thomas-Fermi screening length $a_{TF} = 0.885Z_T^{-1/3}$ and the nuclear charge of the target atoms Z_T . At close distances $V_{PT}(\vec{r})$ resembles the unscreened core potential while it vanishes at large distances due to screening. The Fourier transform is $\tilde{V}_c(\vec{k}) = -(4\pi Z_T)/(k^2 + a_{TF}^{-2})$. The density $\rho_T(\vec{x}_T) = \sum_j \delta(\vec{x}_T - \vec{r}_j)$ is a sum over target atomic positions \vec{r}_j . In this case the susceptibility in (3.6) describes the response of the target atomic cores to a perturbation. Collective excitations of atomic cores are called phonons. Estimating the relation between \vec{k} and ω in $\chi''(\vec{k}, \omega)$ we can use the simple free-particle dispersion relation

$$\omega = \frac{k^2}{2M_c}, \quad (3.13)$$

where M_C is the mass of a target atom. In view of the large atomic mass compared to the electron mass no phonon excitation can occur, since the scattering does not transfer a significant amount of energy to the target. Consequently, for free-electron scattering the kinetic energy of the projectile electron and thus the absolute value of the momentum vector remains constant, $|\vec{k}_f| = |\vec{k}_i|$, while only the direction is changed. Under these conditions we can consider free-electron-core scattering as elastic. Assuming the target to remain in the ground state $|0_T\rangle$, the susceptibility can be evaluated as

$$\chi''(\vec{k}, \omega) = \pi \left| \langle 0_T | \sum_j e^{i\vec{k}\vec{r}_j} | 0_T \rangle \right|^2 = \pi \sum_j = \pi n_A \quad (3.14)$$

with the number density n_A of target atoms per unit volume.

Neglecting phonon effects implies that the system transitions are solely driven by the translational projectile motion with the energy transfer $k_z v_p$. This requirement fixes the parallel component of the momentum transfer for a certain state-to-state system transition as $k_z = \omega_{fi}/v_p$ reducing the dispersion to the perpendicular component \vec{k}_\perp . The corresponding transition operator is written as

$$S_{fi}^{(c)}(\vec{k}_\perp) = \sqrt{\frac{2\pi n_A}{v_p}} \tilde{V}_{PT}(k) \langle f | e^{i\vec{k}\cdot\vec{r}} | i \rangle \quad (3.15)$$

with $\vec{k} = \vec{k}_\perp + \hat{z}\omega_{fi}/v_p$. The differential IMFP reads

$$\frac{d^2 \lambda_c^{-1}(k, \omega)}{d\omega dk} = \frac{8\pi n_A Z_T^2}{v_p^2} \frac{k}{(k^2 + a_{TF}^{-2})^2} \delta(\omega). \quad (3.16)$$

The inverse mean free path (IMFP) is obtained by integration of (3.16) over all possible momentum transfers. The maximum momentum transfer is limited by the incident projectile momentum $p = \gamma_p v_p$ with $\gamma_p = (1 - v_p^2/c^2)^{-1/2}$ carried into the collision. In the case of backscattering the maximum momentum transfer $k_{\max} = 2p = 2\gamma_p v_p$ is delivered. In this limit the IMFP can be written as

$$\lambda_c^{-1} = \int_0^{k_{\max}} \frac{d\lambda_c^{-1}(k)}{dk} dk = \frac{4\pi n_A Z_T^2}{v_p^2 a_{TF}^{-2}} \frac{1}{1 + (2v_p \gamma_p a_{TF})^{-2}}. \quad (3.17)$$

If the integration is performed from zero to infinity we obtain an inverse mean free path (IMFP) of

$$\lambda_c^{-1} = \int_0^\infty \frac{d\lambda_c^{-1}(k)}{dk} dk = \frac{4\pi n_A Z_T^2}{v_p^2 a_{TF}^{-2}}. \quad (3.18)$$

In a Monte Carlo simulation the momentum transfer k has to be randomly distributed with a random number $r_c \in [0, 1]$ according to

$$r_c(k) = \frac{\int_0^k \frac{d\lambda_c^{-1}(k')}{dk'} dk'}{\int_0^{k_{\max}} \frac{d\lambda_c^{-1}(k')}{dk'} dk'} = \frac{1 + (2v_p \gamma_p a_{\text{TF}})^{-2}}{1 + (k a_{\text{TF}})^{-2}}. \quad (3.19)$$

Accordingly, the momentum transfer k for a given realization can be expressed in terms of the random number r_c as

$$k = \frac{1}{a_{\text{TF}}} \left(\frac{1}{r_c} (1 + (2v_p \gamma_p a_{\text{TF}})^{-2}) - 1 \right)^{-\frac{1}{2}}. \quad (3.20)$$

An analytical expression for the distribution $P_c(k)$ of the momentum transfer k can be obtained from (3.19) by calculating the derivative of r_c with respect to k

$$P_c(k) = \frac{dr_c(k)}{dk} = \frac{2}{k^3 a_{\text{TF}}^2} \frac{1 + (2v_p \gamma_p a_{\text{TF}})^{-2}}{(1 + (k a_{\text{TF}})^{-2})^2}. \quad (3.21)$$

Since the velocity-dependent term in the enumerator is negligible for the ve-

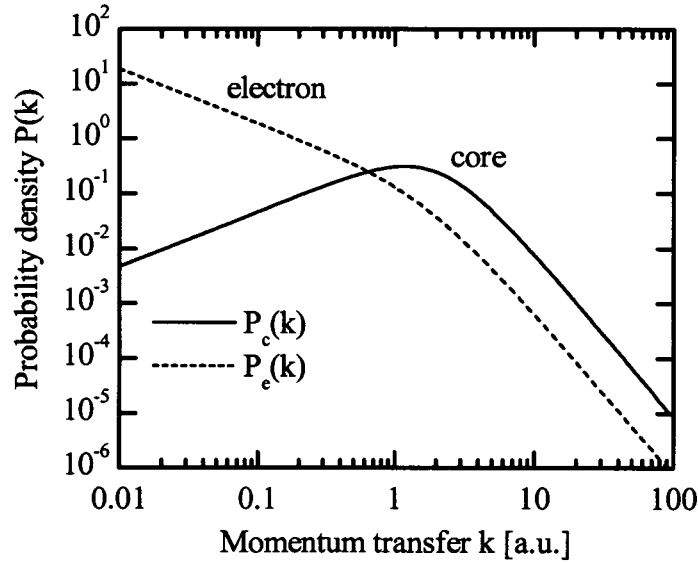


Figure 3.1: Momentum transfer distribution for free electron scattering in amorphous carbon. Solid line: core scattering $P_c(k)$; dashed line: electron-electron interaction $P_e(k)$.

locities considered here ($1 + (2v_p \gamma_p a_{\text{TF}})^{-2} = 1.002 \simeq 1$ for $v_p = 23$ a.u.) we obtain a momentum transfer distribution irrespective of the projectile velocity

$$P_c(k) = \frac{2}{k^3 a_{\text{TF}}^2} \frac{1}{(1 + (ka_{\text{TF}})^{-2})^2}. \quad (3.22)$$

This limit corresponds to neglecting the maximum momentum that can be transferred and taking $k_{\text{max}} \rightarrow \infty$ as we have done to derive the IMFP in equation (3.18). This momentum transfer distribution has a maximum at about $k=1$ a.u. as shown in figure 3.1.

The direction of the momentum transfer supplied in a core scattering event is determined by $\delta(\omega)$ in the differential IMFP in equation (3.16) leading to conservation of kinetic energy in the rest frame of the target. This means that the momentum after the scattering event points into another direction with the same absolute magnitude on a circle. This circle is called the ‘‘Newton circle’’. For $|\vec{k}| \ll |\vec{k}_i|$ this condition implies that the momentum transfer \vec{k} is perpendicular to the initial momentum \vec{k}_i .

3.2.2 Electron-electron collisions

The second constituent of the target the projectile interacts with are the target electrons. The interaction V_{PT} is a pure Coulomb potential with the Fourier transform given by $\tilde{V}_{PT}(\vec{k}) = 4\pi/k^2$. The density $\rho_T(\vec{x}_T)$ contains the positions of all target electrons. Unlike for core scattering, the dispersion relation $\omega = k^2/2$ favors excitations of the target. To be more specific, the small mass of the target electrons allows for a certain value of momentum transfer k also to transfer a relevant amount of energy ω . Target electrons in the outer shells are loosely bound and can thus be considered as quasi-free from the point of view of the fast projectile. Collective excitations of the electron gas are called plasmons.

For an electron gas $\chi''(\vec{k}, \omega)$ is related to the negative imaginary part of the dielectric response function $\varepsilon(k, \omega)$ as

$$\chi''(\vec{k}, \omega) = \frac{k^2}{4\pi} \text{Im} \left[\frac{-1}{\varepsilon(k, \omega)} \right]. \quad (3.23)$$

In the present approach $\varepsilon(k, \omega)$ is parameterized in terms of a sum of n Drude-type functions introduced by Ashley [Ash79]. The parameters are determined from the optical limit ($k = 0$) where experimental optical data for the loss function $\text{Im}[-1/\varepsilon(k = 0, \omega)]$ is available for many materials. For carbon the loss function can be fitted by a sum of five Drude-type functions

[Wil72, Ash79]

$$\text{Im} \left[\frac{-1}{\varepsilon(k, \omega)} \right] = \sum_{j=1}^n \frac{\omega_{pj}^2 \eta_j \omega}{(\omega_{0j}^2(k) - \omega^2)^2 + \eta_j^2 \omega^2} \quad (3.24)$$

fixing the parameters ω_{pj} , ω_{0j} and η_j ($j = 1..5$) for $k = 0$. The use of the relativistic free particle dispersion relation for the resonance frequency $\omega_{0j}(k) = \omega_{0j} + c^2 \left(\sqrt{1 + k^2/c^2} - 1 \right)$ allows to access regions with $k > 0$. The advantage of such a parameterization is that $\varepsilon(k, \omega)$ accounts not only for collective effects but also for single-particle-single-hole excitations. As also internal degrees of freedom of the reservoir can be excited, system transitions are not only driven by the translational motion but also by direct energy exchange. This leads, unlike for core collisions, only to an upper bound of the energy transfer and thus to $k_z \leq \omega_{fi}/v_p$ for a certain transition $i \rightarrow f$. The resulting transition operator is given by

$$S_{if}^{(e)}(\vec{k}) = \sqrt{\frac{8\pi}{k^2}} \text{Im} \left[\frac{-1}{\varepsilon(k, \omega_{fi} - k_z v_p)} \right] \langle i | e^{i\vec{k} \cdot \vec{r}} | f \rangle \quad (3.25)$$

leading to a differential IMFP (3.12) of

$$\frac{d^2 \lambda_e^{-1}(k, \omega)}{d\omega dk} = \frac{2}{\pi v_p^2 k} \text{Im} \left[\frac{-1}{\varepsilon(k, \omega)} \right]. \quad (3.26)$$

The total mean free path is obtained by integration of (3.26) over the momentum and energy transfer as

$$\lambda_e^{-1} = \int dk \int d\omega \frac{d^2 \lambda_e^{-1}(k, \omega)}{d\omega dk}, \quad (3.27)$$

where the integration limits are determined by the kinematics.

The momentum transfer is chosen via a random number $r_e \in (0, 1)$ that is given by

$$r_e(k) = \lambda_e \int dk' \int d\omega \frac{d^2 \lambda_e^{-1}(k', \omega)}{d\omega dk'} \quad (3.28)$$

with the derivative

$$P_e(k) = \frac{dr_e(k)}{dk}. \quad (3.29)$$

Figure 3.1 shows the momentum transfer distribution $P_e(k)$ in comparison with the distribution for core scattering $P_c(k)$.

Although the DIMFP for e-e scattering in (3.26) is proportional to v_p^{-2} , the normalized momentum transfer distribution $P_e(k)$ is independent of the electron velocity. Fig. 3.1 displays the qualitative difference between core and electron scattering. Transitions of bound electrons induced by core scattering transfer a considerable amount of momentum while electron scattering transfers only a small amount of energy and momentum. The direction of the momenta transferred in interaction of free electrons with the electron gas is oriented predominantly antiparallel to the initial electron momentum.

3.2.3 Radiative decay

The cross section for a radiative transition of a hydrogenic ion from an initial state i to a final state f is given in the electric dipole approximation by [Bet77]

$$\sigma_{if} = \frac{4\omega_{if}^3}{3c^3} |\langle i|\vec{r}|f\rangle|^2 \quad (3.30)$$

with the energy difference ω_{ij} between the initial and final state corresponding to the energy of the emitted photon. From (3.30) the transition operator can be constructed according to [Min03a] as

$$S_{if}^{(\tau)}(\gamma) = \frac{2}{\sqrt{3c^3}} \omega_{fi}^{3/2} \langle i|r_\gamma|f\rangle \theta(\omega_{fi}), \quad (3.31)$$

where $\gamma=x,y$ and z denotes the polarization direction of the photon and the step function accounts for transitions from energetically higher states to lower ones in order to consider radiative decay processes only.

3.3 Wake field

The passage of the highly charged swift projectile ion induces density fluctuations of the target electrons that, in turn, produce an electric potential. In figure 2.1 an example of this potential is illustrated. In linear response theory we can approximate it by [Ech79, Ech86]

$$V^{(w)}(\vec{r}) = \frac{Z_p}{2\pi^2} \int d^3\vec{q} \frac{1}{q^2} \left(\frac{1}{\varepsilon(q, \omega = \vec{q} \cdot \vec{v}_p)} - 1 \right) e^{i\vec{q} \cdot \vec{r}} \quad (3.32)$$

with the dielectric response function $\varepsilon(q, \omega)$ of the target electron gas.

The resulting shape of $V^{(w)}$ resembles that of a wake, i.e. the ion moves in front of the center of the induced potential. Since the projectile velocity is larger than the Fermi velocity of target electrons, the perturbation is effective

only in a narrow cone around the projectile path resembling the shape of a supersonic (Mach) cone. The fluctuations form a wave pattern behind the ion that is constant in the rest frame of the projectile. The strength of the wake potential scales proportional to the projectile charge Z_p (prefactor in (3.32)) and inversely proportional to the projectile velocity v_p entering via the dielectric response function.

At the position of the projectile ion the potential exhibits a slope parallel to the projectile velocity v_p resulting in an effective electric field. We choose the coordinate system such that the z-axis is parallel to the direction of v_p and the quantization axis to coincide with this direction. The slope is, in first order, constant at the scale of deeply bound states resulting in a constant electric field F .

The presence of the electric field has two consequences for the projectile. First, it exerts an electric force on the projectile pulling it backwards resulting in a slowing down. This effect is called the electronic stopping power. In view of the thin targets this stopping power is negligible compared to the projectile kinetic energy for the collision systems investigated throughout this thesis.

The second effect of the wake field is the Stark splitting of states

$$E_{ij}^{(w),(\text{dipole})} = -F \langle i|z|j \rangle \quad (3.33)$$

with the dipole matrix elements $\langle i|z|j \rangle$. More sophisticated approximations account for the non-linearity of the wake potential by a state dependent wake field

$$E_{ij}^{(w)} = -F_{ij} \langle i|z|j \rangle \quad (3.34)$$

as for example Ponce [Roz99]

$$F_{ij}^{(\text{Ponce})} = Z_p \left(\frac{1.07}{v_p} \right)^2 \ln \left(\frac{2v_p^2}{1.07} \right) e^{-\alpha^{(w)} n_i \sqrt{1.0228/Z_p}} \quad (3.35)$$

with the parameter

$$\alpha^{(w)} = 0.71 + (0.02 \delta_{l_{\max,1}} - 0.13 \delta_{l_{\max,2}}) \delta_{m_i,0} + 0.27 \delta_{l_{\max,2}} \delta_{m_i,1} \quad (3.36)$$

where $l_{\max} = \max(l_i, l_j)$. $\alpha^{(w)}$ describes intra-shell mixing ($n_i=n_j$) while conserving the projection of angular momentum ($m_i=m_j$).

Contributions beyond the dipole approximation up to all orders can be obtained by calculating the expectation values for the full potential as given in equation (3.32)

$$V_{ij}^{(w)} = \langle i|V^{(w)}(\vec{r})|j \rangle = \frac{Z_p}{2\pi^2} \int d^3\vec{q} \frac{1}{q^2} \left(\frac{1}{\varepsilon(q, \omega = \vec{q} \cdot \vec{v}_p)} - 1 \right) \langle i|e^{i\vec{q} \cdot \vec{r}}|j \rangle. \quad (3.37)$$

As seen from the Taylor series expansion of the boost operator

$$e^{ikz} = 1 + ikz + O(k^2) \quad (3.38)$$

for negligible momentum transfers the boost has no effect. The zero-order component in (3.38) leads to a constant energy shift of all eigenstates. This energy shift can be observed, for example, in spectra of emitted photons in radiative electron capture. The first-order term kz corresponds to the dipole approximation in (3.34) with a state selective wake field. The description of the wake potential by the dipole operator leads to a coupling obeying the dipole selection rule $l_i = l_j \pm 1$. Higher-order components described by the full boost operator account for the coupling beyond the dipole.

The main ingredient of the calculation is the boost operator $\langle i | e^{i\vec{k}\cdot\vec{r}} | j \rangle$ describing a transition from the state j into the state i by the transfer of a momentum \vec{k} to the system in an arbitrary direction. It can be expressed in terms of the boost where the momentum is transferred parallel to the quantization axis z as

$$\begin{aligned} \langle i | e^{i\vec{k}\cdot\vec{r}} | j \rangle &= \langle n_i l_i m_i | e^{i\vec{k}\cdot\vec{r}} | n_j l_j m_j \rangle \\ &= \sum_{m' = -\min(l_i, l_j)}^{m' = \min(l_i, l_j)} (R_{m' m_i}^{l_i}(\theta, \phi))^* \langle n_i l_i m' | e^{ikz} | n_j l_j m' \rangle R_{m' m_j}^{l_j}(\theta, \phi) \end{aligned} \quad (3.39)$$

with the rotation operator $R_{m' m_i}^{l_i}(\theta, \phi)$. The Euler angles θ and ϕ denote the angles between the vector \vec{k} and the quantization axis z . The third Euler angle is not required for the rotation of a one dimensional structure. The rotation of the azimuthal angle ϕ corresponds to a complex phase and simplifies the rotation operator to

$$R_{m' m_i}^{l_i}(\theta, \phi) = r_{m' m_i}^{l_i}(\theta) e^{-im_i \phi}, \quad (3.40)$$

where the matrix elements for the remaining rotation $r_{m' m_i}^{l_i}(\theta)$ are given by the Wigner formula in reference [Mes86].

The overall dependence of the boost operator on the azimuthal angle ϕ is given by $\exp(-i(m_j - m_i)\phi)$ whose integration over all possible values of $\phi = (0, 2\pi)$ leads to a Kronecker-delta function

$$\frac{1}{2\pi} \int_0^{2\pi} d\phi e^{-i(m_j - m_i)\phi} = \delta_{m_j m_i} \quad (3.41)$$

implying that the boost operator only couples states with the same quantum number m .

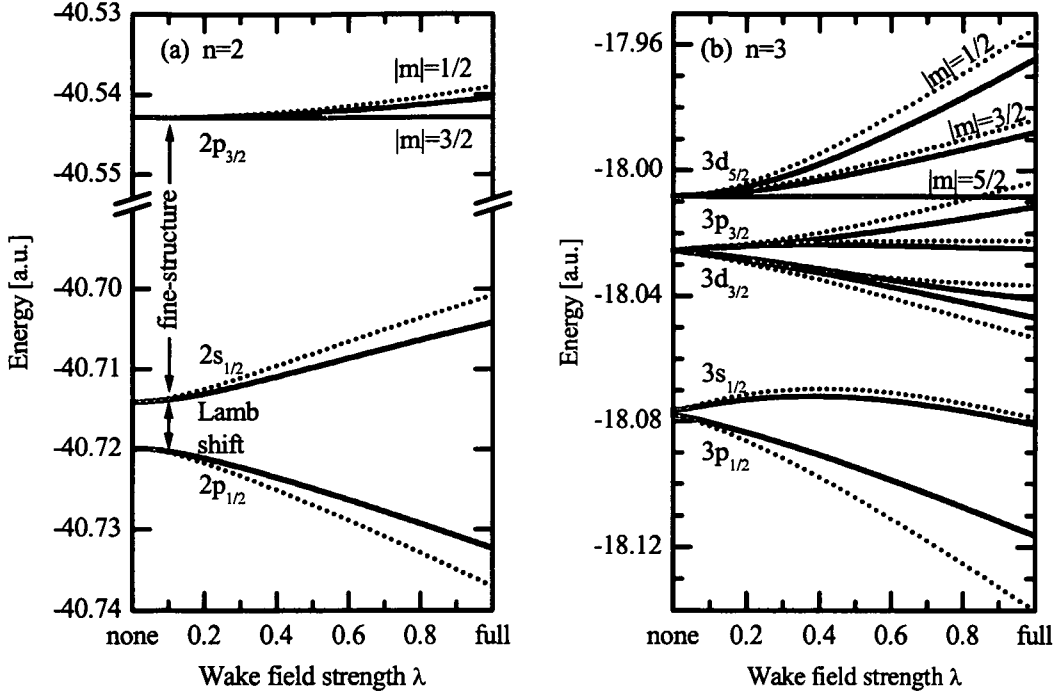


Figure 3.2: Stark map of wake field for $n=2$ (a) and $n=3$ (b) as a function of field strength in an adiabatic turn-on of the field. Solid lines: results obtained with the full potential (equation (3.37)); dashed lines: approximation of Ponce (equation (3.35)).

The matrix elements of the boost operator $\langle n_i l_i m' | e^{ikz} | n_j l_j m' \rangle$ can be evaluated analytically in the parabolic Sturmian basis set (n_1, n_2, m, ϵ) where ϵ is the Sturmian parameter [Mel92, Mel93, Bur83a]. By setting $\epsilon = Z_P/n$ we obtain the matrix elements in the hydrogenic basis.

$V_{ij}^{(w)}$ is added to the unperturbed Hamiltonian (equation (3.3))

$$H^{(\text{solid})} = H_S + V^{(w)}. \quad (3.42)$$

The diagonal elements of $V_{ij}^{(w)}$ result from the zero-order term of the boost operator and account for the overall energy shift. For an argon projectile launched through a carbon target with a velocity of $v_p=23$ a.u. this shift amounts to 0.73 a.u.. Since it affects all states equally we can omit this contribution and only consider the off-diagonal elements of $V_{ij}^{(w)}$. Each eigenvector of the combined Hamiltonian (3.42) contains an admixture of states coupled by the wake field, i.e. intra-shell states with same m_j . In figure 3.2 we show the eigenvalues as a function of the strength of the wake field, i.e.

$H_{ij}^{(\text{solid})} = H_{S,ij} + \lambda V_{ij}^{(w)}$ for $\lambda \in (0, 1)$. In the unperturbed system ($\lambda=0$) the states are separated in energy by the Lamb shift and by the fine-structure. When adiabatically turning on the wake field, the degeneracy with respect to $|m_j|$ is lifted. This Stark effect is well observed, for example, in $2p_{3/2}$ in figure 3.2 (a) as the eigenenergy of the $2p_{3/2,1/2}$ state increases due to an admixture of $2p_{1/2,1/2}$ and $2s_{1/2,1/2}$. For two states with same j and same m_j the eigenvalue of the component with smaller l is increased while the one with larger l is reduced (see figure 3.2 (b)). States with the maximum angular momentum $j=n-1+1/2$ parallel to the quantization axis $|m_j|=j$ have no other state within their shell to be coupled with by the wake potential. Correspondingly, this group of states remains unchanged as can be seen in figure 3.2 (a) for $2p_{3/2,3/2}$ and in figure 3.2 (b) for $3d_{5/2,5/2}$.

3.4 Electron capture

The strong perturbation during charge transfer requires a detailed description of the close collision event. Different techniques have been developed for this purpose. What most of these sophisticated methods have in common is that the computation is very time consuming restricting the described part of the capture event to the closest distance between projectile and target. This is the region where the actual charge transfer occurs.

Most of these approaches describing the charge transfer at the close-collision region cannot be utilized to describe the PCI on the long time scale and vast spatial distances. On the other hand, during the PCI the Coulomb interaction is not so strong any more and a less sophisticated solution may still give accurate results. Therefore usually a hybrid approach [Bur81b] is chosen describing the close-collision region accurately and solving the PCI with a different method.

In the following we briefly discuss a selection of theoretical approaches for electron capture. First we stay within the classical picture and describe the calculation of cross sections by means of a classical trajectory Monte Carlo (CTMC) method (section 3.4.1). Then we discuss two quantum mechanical non-relativistic methods: the continuum-distorted wave (CDW) method (section 3.4.2) and the solution of the time-dependent Schrödinger equation on the lattice (LTDSE) in section 3.4.3. The CDW calculation makes use of a hybrid approach by evaluating the cross sections in a distorted basis in the charge transfer region while the PCI is accounted for by Stark mixing in a parabolic basis set. In the LTDSE method the PCI is evaluated by an atomic orbital coupled channel (AOCC) calculation.

Motivated by the experimental measurements that could resolve differences in capture cross sections for fine structure states (see measurements in figure 2.6), we briefly discuss the description of electron capture in a relativistic framework applying the eikonal approximation in section 3.4.4. We compare the resulting cross sections in section 3.4.5 for capture by a bare Ar^{18+} projectile with a velocity of 23 a.u. in transport through amorphous carbon

3.4.1 Classical description of electron capture

In this section we consider a classical description of the electron capture process. This method has been introduced by Abrines and Percival [Abr66]. A full description can be found in reference [Per75, Ols77]. We solve the time evolution of the distribution function ρ of the electron probability in the vicinity of the projectile and target Coulomb potential, $V_P(\vec{r})$ and $V_T(\vec{r}, t)$,

respectively. In the rest frame of the projectile V_T is time dependent. The phase-space master equation describing the phase-space flow is

$$\frac{\partial}{\partial t} \rho(\vec{r}, \vec{v}, t) = \left(-\vec{v} \cdot \vec{\nabla}_r + \vec{\nabla} (V_P(\vec{r}) + V_T(\vec{r}, t)) \cdot \nabla_v \right) \rho(\vec{r}, \vec{v}, t), \quad (3.43)$$

with the kinetic part in the first term and the gradient of the combined potential in the second term. In a classical simulation we discretize the initial phase space density with classical test particles. In this case with electrons. Then we propagate each test particle according to its equation of motion which is Newton's equation of motion involving both Coulomb potentials as

$$\dot{\vec{p}} = -\vec{\nabla} (V_P(\vec{r}) + V_T(\vec{r}, t)). \quad (3.44)$$

The equation of motion can be integrated with the help of a standard method as for example the Runge-Kutta integration scheme [Pre86].

The final phase space distribution is constructed out of the ensemble of propagated test particles. The larger the number of propagated trajectories is, the smaller is the statistical uncertainty of the result which scales as the inverse square root of the number of trajectories.

We can divide the solution of the capture problem by terms of classical trajectories into three stages. In the first stage the quantum mechanical initial state is represented with a classical electron distribution. This generation of initial conditions is only approximate. The phase space distribution of the microcanonical ensemble of classical electron can be constructed such that it agrees with the quantum mechanical momentum distribution of the 1s ground state while the spatial distribution differs from the exact quantum mechanical result [Sch92]. This is mainly due to the fact, that unlike a quantum mechanical wave function, the classical particle ensemble can extend only up to a maximum radius which is determined by the balance of potential and kinetic energy. This deficiency of the classical particle discretization to reproduce the phase space properties of the unperturbed atomic wave function may introduce a significant source of uncertainty into the result for charge transfer [Sch92].

In the second stage of the calculation of electron capture each test particle is propagated in time along a classical trajectory according to its equation of motion (3.44). Therefore this method is referred to as the classical trajectory Monte Carlo (CTMC) method. Here lies the convincing advantage of a classical description. The numerical integration of the three-body system subject to Coulomb forces takes all the interactions into account exactly.

To obtain state-to-state charge transfer cross sections the final classical phase space density is mapped onto quantum numbers in the third stage of

the calculation. A method developed by Becker and McKeller [Bec84] based on the proportionality of quantum and classical weights provides a good description of the n,l capture distribution [Men90, Sch92]. This is achieved by mapping the classical principal number $n_c = Z_p/\sqrt{-2E_e}$ where E_e is the binding energy of the electron in the rest frame of the projectile onto the principal quantum number n as

$$n(n - 1/2)(n - 1) \leq n_c^3 \leq n(n + 1/2)(n + 1) \quad (3.45)$$

Similarly, the classical angular momentum l_c is mapped onto its quantum equivalent as

$$l \leq \frac{n}{n_c} l_c \leq l + 1 \quad (3.46)$$

The coherences between two states with different angular momentum can be extracted from a classical calculation through their correspondence to the expectation values of combinations of the Runge-Lenz vector and the angular momentum [Bur83b].

To summarize, a classical calculation allows for a test particle discretization of the initial condition and to propagate each test particle according to the corresponding equation of motion in the time dependent combined electron field of the target and projectile nucleus. This Monte Carlo technique is quite robust and is also suitable to calculate efficiently capture into higher excited states. The deficiency is not only the lack of quantum effects in the dynamics but also the incapability of exactly reproduce the initial quantum phase space distribution.

3.4.2 Continuum-distorted-wave approximation

In the following we discuss two non-relativistic quantum mechanical models for electron capture. The solution of the full Schrödinger equation for the long time evolution and the large number of states is prohibitively difficult. Only recently computing facilities that can handle the problem became available as we will discuss in the next section.

An efficient method to simplify the calculation of electron capture cross sections is to include the effect of the core potentials in the unperturbed basis functions and consider the kinetic electron energy as perturbation. This continuum-distorted-wave (CDW) model [Che64] can be adopted for bare targets and projectiles, i.e. for unscreened Coulomb potentials. Cross sections are obtained as an integral over the perpendicular momentum transfer \vec{k}_\perp as

$$C_{\alpha\beta} = (2\pi v_p)^{-2} \int d^2 k_\perp T_{i \rightarrow \alpha}(\vec{k}) T_{i \rightarrow \beta}^*(\vec{k}) \quad (3.47)$$

with the overall momentum transfer $\vec{k} = \vec{k}_\perp + \hat{z}k_z$. The parallel component of the momentum transfer is fixed by the amount of energy brought into the collision as $-k_z v_p = E_{kin} + \Delta E_{bind}$ where E_{kin} is the initial kinetic energy of the electron in the projectile rest frame as $E_{kin} = v^2/2$ and ΔE_{bind} is the difference in binding energy of the electronic initial and final state. The transition amplitudes $T_{i \rightarrow \alpha, \beta}(\vec{k})$ denote transition matrix elements for the initial state i to a final state α or β as a function of momentum transfer. Due to the velocity matching argument (see section 2.1) the largest contribution to the cross section comes from the 1s projectile ground state. To account for the presence of other electrons of the neutral carbon projectile atom we use for the initial wave function parameterized Roothaan-Hartree-Fock atomic wave functions tabulated, among others, also for carbon in reference [Cle74].

Since the interaction strength varies strongly between very strong in the close-collision region to vanishingly small in asymptotic far distance a hybrid approach is utilized [Bur81a, Bur81b]. At close projectile-target distance, the transition amplitudes are evaluated in the basis of continuum-distorted waves and then projected onto a parabolic basis set. $T_{i \rightarrow \alpha, \beta}$ contain higher order scattering contributions in the perturbation expansion and are therefore able to account for capture into higher angular momentum states. The CDW method is suitable for collision systems with similar projectile and target charge since it treats deformation of initial and final states in the distorted wave functions on the same footing.

A projection of $T_{i \rightarrow \alpha, \beta}$ onto parabolic states has the advantage of an easy inclusion of subsequent post collision interaction (PCI) with the Coulomb field $\vec{F}(\vec{r})$ of the residual target ion resulting in Stark mixing of final states. This combined approach, the CDW-PCI model, considers long range Stark mixing as well as multiple-scattering contributions in the close-collision region [Bur81b, Bur84]. The time evolution operator for PCI is given as an integral over the remaining path

$$U^{(PCI)} = \exp \left(\frac{i}{v} \int_{\langle r \rangle_n}^{\infty} dr \vec{F}(\vec{r}) \cdot \vec{d} \right) \quad (3.48)$$

with the dipole operator \vec{d} . The size of the close-collision region where charge transfer takes place is determined by the region of significant overlap of initial and final wave functions. This border line can be approximately drawn at a distance between target and projectile that is of the size of the final state $\langle r \rangle_n$. In a parabolic basis $U^{(PCI)}$ results in an additional phase, the so-called PCI-phase, that can be evaluated in closed form [Bur81a, Bur81b, Bur85] under certain assumption. A detailed comparison with a first order (single

scattering) theory on excited states cross sections and their sensitivity to PCI is discussed in references [Bur84, Bur85] where it has been demonstrated that this post collisional Stark interaction modifies the final state populations significantly.

To summarize, the extension of the unperturbed wave functions by the distortion of the core potentials makes the calculation significantly faster than a solution of the underlying time-dependent Schrödinger equation. The non-relativistic quantum mechanical CDW method allows to calculate cross sections of higher angular momentum states and is most suitable for symmetric collision systems. By the implementation of the hybrid approach the long range interaction is also accounted for.

3.4.3 Solving time-dependent Schrödinger equation on a lattice

The charge transfer in electron capture is determined by the time-dependent Schrödinger equation (TDSE). Accounting numerically for the large Hilbert space including the large quasi-continuum with a considerable number of bound-continuum transition channels open, poses a formidable task. One effective method of resolution is to solve the TDSE on a 3D lattice discretizing the continuous space centered around the projectile ion at the distance of closest approach. Very recently such a calculation for electron capture has been implemented by Minami et. al. and first promising results were reported [Min04a]. This non-perturbative method gives a complete description of the collision problem within non-relativistic quantum mechanics.

The size of this lattice (and thus the calculation effort) is mainly determined by two considerations. First, all described bound states shall be contained within the lattice as is indicated in figure 3.3 (a). The second criterion for the lattice extension is determined by the internuclear distance at which the probability of the captured electron is not exchanged between target and projectile any more, i.e. charge transfer ceases. For further propagation the electron probability attached to the projectile is projected onto a basis of atomic-orbital coupled-channels (AOCC) at this distance. From there on the AOCC are propagated in the time (i.e. distance) dependent electronic field $\vec{F}(\vec{r})$ of the residual target as indicated in figure 3.3 (b). This calculation has to be performed until the projectile has reached a distance from the target ion where the post collision interaction (PCI) is not effective for mixing any more.

With this hybrid approach, the multi-center dynamics at the distance of closest approach can be treated accurately while the dynamics of single-center

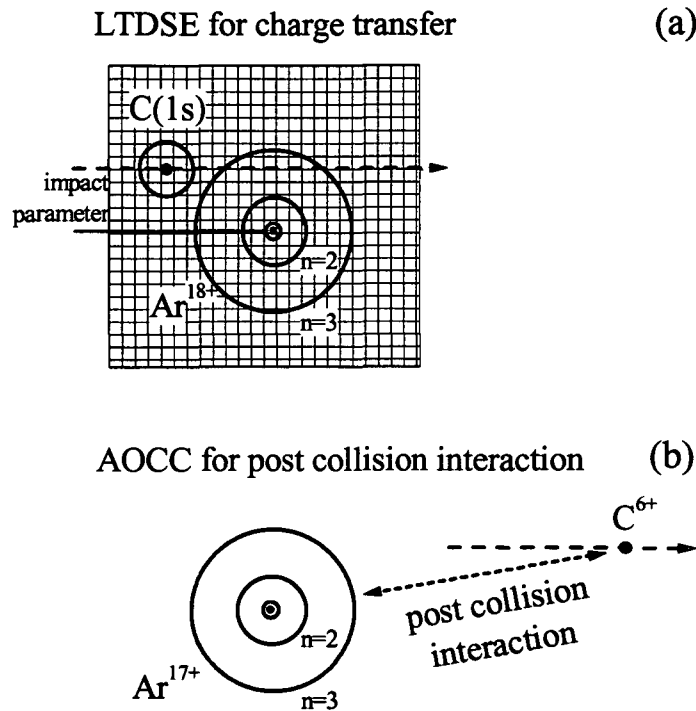


Figure 3.3: Schematic picture of the calculation of electron capture in a collision of a bare argon with a neutral carbon atom performed by Minami et. al. [Min04a]: (a) lattice (mesh not to scale) in the region of closest approach centered around the argon ion for the solution of the time-dependent Schrödinger equation (LTDSE); (b) atomic-orbital coupled-channels (AOCC) calculation for the post ionization interaction at large distances. Bohr radii for $n=1,2,3$ for argon and $n=1$ for carbon are indicated to scale as orbits.

projectile states during the departure from the region of charged transfer can be treated effectively as well. It has to be pointed out that while the AOCC calculation of the PCI is relatively fast from the point of view of computational effort, the solution of the TDSE on a 3D lattice for a series of impact parameters is very extensive requiring large scale computing resources.

The method was first applied by Minami et. al. to calculate electron capture by a proton out of a helium atom [Min04a] solving the TDSE in a grid of 320^3 points. For this collision system a series of experimental studies covering a wide range of impact energies is available. Results of other theoretical calculations are also available for this collision system. Comparison with results obtained by LTDSE demonstrated the accuracy of the method.

To summarize, the LTDSE provides a complete description of the close-

collision interaction within non-relativistic quantum mechanics and is therefore expected to be the most accurate method for the calculation of capture cross sections available. The price to pay is the large amount of computing time needed to solve the TDSE on a relatively large 3D grid for different impact parameters. As in the CDW method, the hybrid approach allows to spend this computing power for the important close-collision region while adopting a less computing time intensive method to account for the asymptotic Stark mixing.

3.4.4 Relativistic eikonal theory of electron capture

In the collision system we consider $v_p = 23$ a.u. such that $\beta = v_p/c \approx 0.17$ which is moderately relativistic. To probe possible relativistic effects we consider a theory that predicts cross sections in the relativistic energy regime. A method to consider relativistic effects in electron capture is the relativistic eikonal approximation [Eic85, Eic90]. This relativistic eikonal theory is suitable for collisions where the kinetic energy of a free electron (traveling with the speed of the projectile) brought into the collision by far exceeds the binding energy of the initial target state as well as of the final projectile state. The energies involved in the collision system considered here just satisfy this requirement. Since we use this theory on the border line of its applicability accuracy of the resulting cross sections may be not guaranteed. However, we expect ratios between cross sections of different fine structure states to be still reliable and account for possible relativistic effects.

State-to-state capture cross sections are calculated as an integral over the impact parameter b as

$$C_{fi} = \frac{1}{2j+1} \sum_{m_f m_i} \int d^2b \left| A_{fi}^{m_f m_i}(\vec{b}) \right|^2 \quad (3.49)$$

with the statistical weighting of initial projection of total angular momentum m_i and the transition amplitudes A . The cross sections obtained are summed over final m_f . The transition amplitudes are constructed as

$$A_{fi}^{m_f m_i} = i \int dt \int d^3r \Psi_f'^{\dagger}(\vec{r}'_P, t') S \frac{Z_T}{r_T} \Psi_i(\vec{r}_T, t) \quad (3.50)$$

with the electron-target interaction entering in first order which is of Coulomb form in the projectile system and is subsequently transformed into the target frame by the spinor transformation S . A Dirac eigenfunction is Lorentz transformed by S from the target to the projectile frame as $\Psi'(\vec{r}'_P, t') = S \Psi(\vec{r}_T, t)$. We denote space-time coordinates in the projectile frame with a prime.

	Ar (2p _{1/2})	Ar (2p _{3/2})
C (1s _{1/2})	6.699	6.437
C (2s _{1/2})	1.112	1.072

Table 3.3: Electron capture cross sections evaluated within the relativistic eikonal theory for charge transfer from carbon 1s and 2s into the fine structure manifold of 2p in argon in units of 10^{-22} cm² [Eic05].

The initial time-dependent wave function in the transition amplitude consists of the stationary target wave function ψ_i and the phase as a function of the relativistic eigen energy E_i as

$$\Psi_i(\vec{r}_T, t) = \psi_i(\vec{r}_T) e^{-iE_i t} e^{i(Z_P/v_P) \ln(r_P + \vec{r}_P \cdot \hat{z})} \quad (3.51)$$

containing the eikonal phase as phase-distortion by the electron-projectile interaction in the last term. In this way, in a certain approximation, the electron-projectile interaction is treated non-perturbatively, while the electron-target interaction enters in first order in equation (3.50). By contrast the final wave function is $\Psi_f(\vec{r}'_P, t') = \psi_f(\vec{r}'_P) \exp(-iE_f t)$. Since the eikonal approximation is an asymptotic theory the effect of the higher charge should be described more accurately. In the collision system considered, $Z_P > Z_T$ making the use of the so-called *post form* appropriate.

Electron capture cross sections solving equation (3.49) within the relativistic eikonal theory are tabulated for a wide range of relativistic energies and collision systems in reference [Ich93]. Additional data for the collision system considered here were provided by these authors [Eic05]. The results for capture into 2p are listed in table 3.3 showing two interesting aspects. (i) The capture from carbon 2s is less effective as from 1s. This we expect as a result from the “velocity matching” consideration made before in section 2.1. Interestingly the relativistic eikonal approximation predicts contributions from the 2s initial state to be of the order of 15 %. (ii) Capture into the fine structure final states 2p_{1/2} and 2p_{3/2} is not exactly equal giving a hint on a relativistic effect.

3.4.5 Comparison of electron capture cross sections

Here we compare electron capture cross sections under single collision conditions obtained by the methods described above for the collision of a bare Ar¹⁸⁺ with a neutral carbon atom at a velocity of 23 a.u.. CTMC results (C^{CTMC}) were calculated by Reinhold as described in [Rei00] and references therein. C^{CDW} was obtained from the program presented in [Bur84]. C^{LTDSE}

final state	CTMC	CDW	LTDSE
1s ₀	163.00	106.20	123.18
2s ₀	73.94	66.27	68.24
2p ₀	117.16	49.36	68.24
2p ₁	34.78	9.95	15.55
3s ₀	29.65	30.44	29.32
3p ₀	53.46	22.09	29.88
3p ₁	13.92	4.49	5.86
3d ₀	8.07	3.15	5.64
3d ₁	2.59	1.86	2.47
3d ₂	0.14	0.35	0.23
4s ₀	13.27	15.63	
4p ₀	26.31	10.52	
4p ₁	6.47	2.30	
4d ₀	5.88	1.82	
4d ₁	1.81	1.13	
4d ₂	0.06	0.25	
4f ₀	0.00	0.18	
4f ₁	0.01	0.11	
4f ₂	0.00	0.13	
4f ₃	0.00	0.04	

Table 3.4: Electron capture cross section for a bare Ar¹⁸⁺ ion colliding with a carbon atom at a velocity of 23 a.u. in units of 10⁻²² cm² as a function of final state calculated by CTMC 3.4.1, CDW 3.4.2, and LTDSE 3.4.3.

was calculated by adapting the method introduced in [Min04a] to this collision system by the same authors [Min04b].

All the methods consider capture from the 1s ground state of the target. To account for the contribution of the second electron in the 1s state we have multiplied the cross sections by two. In table 3.4 we list the capture cross sections calculated of the three described methods while in figure 3.4 we visualize this data for a better comparison. The overall observation is that capture into p-states is the dominant channel while capture into higher angular momentum states is rare. Within a fixed angular momentum, $m_l=0$ -states are predominantly populated.

Generally speaking, these features of the cross sections are reproduced by all methods. Nevertheless, at a closer look we observe differences in magnitude and structure. Overall, CTMC cross sections are larger than those obtained by LTDSE. This difference is most pronounced for p-states.

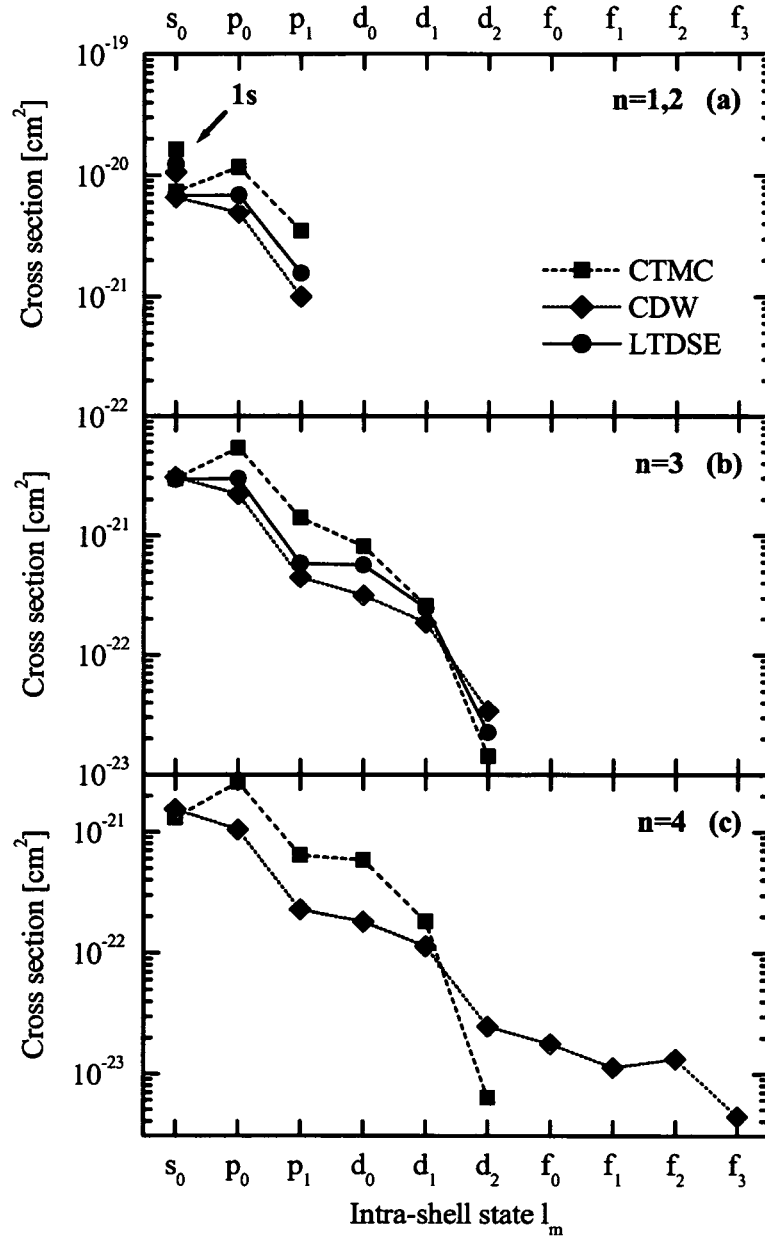


Figure 3.4: Electron capture cross section for $\text{Ar}^{18+} + \text{C} \rightarrow (\text{Ar}^{17+})^* + \text{C}^{1+}$ ($v_p = 23$ a.u.) for different shells: $n=1$ and $n=2$ (a); $n=3$ (b); and $n=4$ (c) calculated within different approximations: CTMC (■); CDW (◆); and LTDSE (●).

CTMC predicts much larger - about a factor of 2 - cross sections for p-states. CDW gives results slightly below values calculated by LTDSE. For capture into s-states the three methods give very similar results, except for capture into 1s. CDW seems to overestimate capture into states with $l > 2$ (figure 3.4 (c)). Capture into $n=2$ is strongest and drops off rapidly for higher shells (figure 3.5). This decrease is first for lower n proportional to n^{-2} and n^{-3} for higher n . This feature is reproduced by all three approaches. The off-diagonal elements of the capture density matrix are very similar in the comparison of CDW and LTDSE results in table 3.5. In accordance with the higher cross sections for populations (diagonal elements) of C^{LTDSE} also the magnitude of coherences of C^{LTDSE} is slightly higher than C^{CDW} . Nevertheless, the complex phase is comparable in both methods.

The cross section for capture into any projectile is given by the trace over the capture density matrix C_{ij} as $\text{Tr}[C]$. For the three methods discussed here we obtain

$$\begin{aligned} \text{Tr}[C^{CTMC}] &= 6.1 \times 10^{-20} \text{cm}^2 \\ \text{Tr}[C^{CDW}] &= 3.5 \times 10^{-20} \text{cm}^2 \\ \text{Tr}[C^{LTDSE}] &= 3.7 \times 10^{-20} \text{cm}^2 \end{aligned} \quad (3.52)$$

where the discrepancy between classical and quantum methods is most evident. In [Min04a] p-He capture cross sections were obtained by the LTDSE method. In comparison with a CTMC calculation and the CDW approach it was found that for p-He the LTDSE gives results agreeing reasonably well with results obtained by the CTMC calculation while considerable differences with CDW results have been found. This is especially remarkable since for the argon-carbon system the agreement is exactly the opposite.

In summary, the two quantum results are comparable in magnitude and structure while C^{CTMC} is higher and overestimates the dipole character of charge transfer, i.e. capture for the initial s-state into p-states. In the present transport simulation we consider the time evolution of the density matrix up to $n=4$, but cross sections from LTDSE are available only for $n \leq 3$. In view of the similarities between CDW and LTDSE results we construct C^{LTDSE} such that for $n \leq 3$ LTDSE values remain and for $n=4$ we adopt CDW results. In the experiment we will compare with, populations of p-states for $n \leq 4$ and of 2s have been measure. The comparison of results of the present simulation of transport enables us to bench mark the different methods for calculation of electron capture cross sections.

	CDW	LTDSE
2s ₀ 2p ₀	7.07 +i 48.01	6.28 +i 56.12
3s ₀ 3p ₀	4.07 +i 22.03	3.93 +i 25.02
3p ₀ 3d ₀	0.88 +i 7.19	1.33 +i 11.75
3s ₀ 3d ₀	-5.33 +i 1.99	-7.23 +i 2.21
3p ₋₁ 3d ₋₁	0.15 +i 2.32	0.06 +i 3.57
3p ₁ 3d ₁	0.15 +i 2.32	0.06 +i 3.57

Table 3.5: Intra-shell coherences of electron capture density matrix for a bare Ar¹⁸⁺ ion colliding with a carbon atom ($v_p = 23$ a.u.) in units of 10^{-22} cm² calculated by different methods (CDW and LTDSE) for $n=2$ and $n=3$.

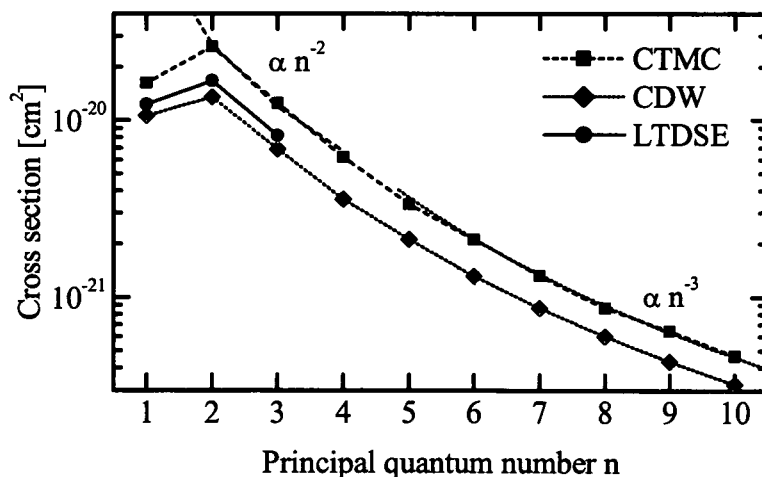


Figure 3.5: Electron capture cross section $\text{Ar}^{18+} + \text{C} \rightarrow (\text{Ar}^{17+})^* + \text{C}^{1+}$ for $v_p = 23$ a.u. into different shells within different approximations (CTMC (■); CDW (◆); and LTDSE (●)). The scaling with n for results obtained with CTMC is indicated for small n as $\propto n^{-2}$ (dashed line) and in the limit of high n as $\propto n^{-3}$ (dotted line).

Chapter 4

Classical transport theory

4.1 Introduction

We first consider a classical picture of the ion transport through solids. Following the electron on a classical path provides insight into different aspects of the complex problem that are helpful for the understanding of a quantum mechanical description. A classical theory is suitable for the treatment of highly excited Rydberg states and also electrons in the continuum. It fails to account for quantum effects and is therefore less suitable for a description of deeply bound electrons in highly charged ions. Consequently, the electronic Hilbert space of a hydrogenic ion covers a region where a classical description is appropriate but also a region where only a description within quantum mechanics can lead to reliable results. None of the methods can be used to describe the whole Hilbert space accurately. In this work we choose a pragmatic approach. We describe the time evolution of electrons deeply bound to highly charged ions within a quantum approach, while we switch to a classical model for highly excited states. To be more specific, we calculate the time evolution of the reduced density matrix for core states according to the quantum mechanical master equation and extrapolate towards higher excited states using scaling properties learned with the help of a classical simulation. This is the first application of a classical theory in this thesis. As a second example we apply a classical description to the emission of electrons into the low-lying continuum of the projectile ion in section 4.4 and discuss an extension to multi-electron projectiles. Before presenting these applications we briefly outline the classical description of the time evolution of an electron attached to a projectile ion in transport through a solid.

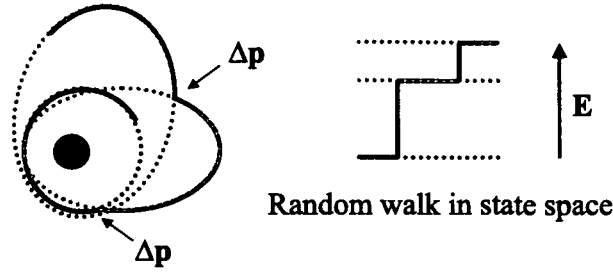


Figure 4.1: Random walk along a Kepler orbit. Momentum transfer of collisions indicated by $\Delta\vec{p}$.

4.2 Classical transport theory

The evolution of the state of an electron is represented within the classical transport theory (CTT) [Bur90a, Kur98, Rei92] by a probability density in phase space $\rho(\vec{r}, \vec{p})$. $\rho(\vec{r}, \vec{p})$ is initially given either by a microcanonical ensemble with the binding energy of the active electron in the initial state or the phase space distribution obtained in a separate electron capture calculation 3.4.1. For hydrogenic 1s states, the momentum distribution $\rho(p)$ agrees with its quantum mechanical counterpart while the spatial distribution has a maximum at the point of balance between potential and kinetic electron energy.

The time evolution of the electron is given by a reduced Liouville equation

$$\frac{\partial}{\partial t} \rho(\vec{r}, \vec{v}, t) = \left(-\vec{v} \cdot \vec{\nabla}_r + \vec{\nabla} V_P(\vec{r}) \cdot \nabla_v + \hat{R} \right) \rho(\vec{r}, \vec{v}, t), \quad (4.1)$$

where the relaxation operator \hat{R} contains the interaction with the solid in all its complexity. This master equation can be solved by test particle discretization (i.e. classical trajectory Monte Carlo (CTMC) sampling). Microscopically, the dynamics of each test particle is governed by a Langevin equation involving both a deterministic Coulomb force and a stochastic force acting on the electron

$$\dot{\vec{p}} = -\vec{\nabla} V_P(\vec{r}) + \sum_i \Delta\vec{p}_i \delta(t - t_i), \quad (4.2)$$

where V_P denotes the interaction potential between the active electron and the projectile. For hydrogenic ions, $V_P(\vec{r}) = -Z_P/r$, with the projectile charge Z_P . The interaction with the solid enters in the last term of (4.2). At high velocities, the electron-solid interaction can be treated in the impulsive

momentum transfer approximation, i.e. momenta $\Delta\vec{p}_i$ are transferred instantaneously at collision times t_i reducing the transport problem to a random walk of the projectile electron along Kepler orbits subject to a stochastic sequence of momentum transfers (figure 4.1). The collisional cross sections are obtained in the quasi-free electron limit as described in section 3.2. The distribution of momentum transfers $\Delta\vec{p}_i$ is discussed in section 3.2.1 and 3.2.2. An individual $\Delta\vec{p}_i$ is chosen randomly according to the corresponding differential MFP. The flight times between two collisions Δt are obtained according to the Poisson distribution

$$P(\Delta t) = \lambda_{c,l,t}^{-1} e^{-\Delta t/\lambda_{c,l,t}} \quad \text{as} \quad \Delta t = -\ln(r)\lambda_{c,l,t} \quad (4.3)$$

with a random number $r \in (0, 1)$ for the individual scattering processes. Those are core collisions (c), longitudinal (l) and transverse (t) electron-electron interactions.

For deeply bound electrons, the quasi-free electron approximation is poorly justified. In a quantum mechanical treatment of the projectile electronic system, the final state after a collision is restricted by the discrete level structure of bound states leading to suppression of small momentum transfers in soft collisions for deeply bound electrons. Considering the transition operators in (6.4) for core collisions and (6.23) for electron-electron interaction, the parallel component of the momentum transfer, k_y , is restricted by the energy spacing between the considered states leading to a lower bound of the amount of transferred momentum. A classical description of the transport problem does not provide such a feature. To partly account for this inadequacy we introduce the requirement of a minimum energy transfer ω_{min} in the rest frame of the projectile ion which is determined by the energy gap between the binding energy before and after the collision. Accordingly, we introduce a minimum momentum transfer k_{min} as a lower cut-off for the momentum transferred by the collision in the modified differential inverse mean free path (DIMFP)

$$\left(\frac{d^2 \lambda_{c,l,t}^{-1}(k, \omega)}{d\omega dk} \right)_m = \frac{d^2 \lambda_{c,l,t}^{-1}(k, \omega)}{d\omega dk} \theta(k - k_{min}) \quad (4.4)$$

through the Heaviside step function $\theta(k - k_{min})$. In the limit of highly excited states the modified DIMFP in Eq. (4.4) resembles the free electron DIMFP. We thus partly include the quantum mechanical suppression of small momentum transfers in the classical treatment of collisions of bound electrons.

The relative importance of the cut-off is largest for electron-electron scattering while the comparatively large amount of momentum transferred in core collisions mostly exceeds the cut-off k_{min} . As a consequence, core states

are excited by core scattering while excited states are subject to both interactions. In section 4.4 we discuss an application where this sequential fading plays an important role.

4.3 Transport of bound states populated by capture

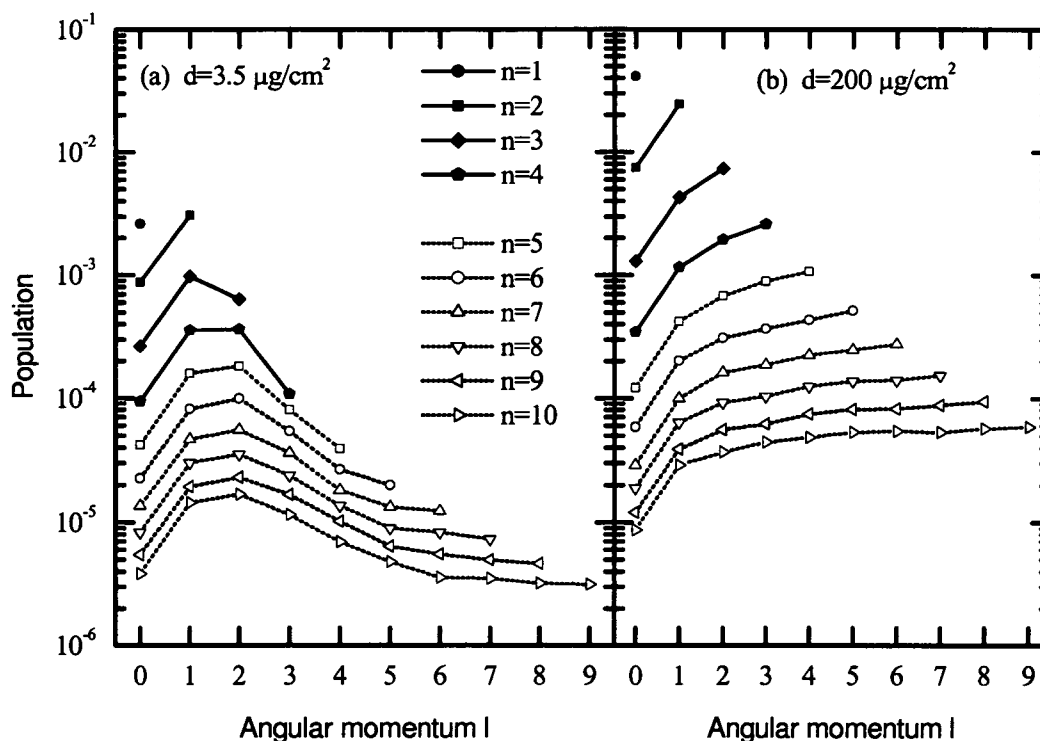


Figure 4.2: Populations obtained with a classical calculation for the transport of an Ar^{17+} ion through amorphous carbon of thickness $3.5 \mu\text{g}/\text{cm}^2$ (a) and $200 \mu\text{g}/\text{cm}^2$ (b) as a function of angular momentum l with the principal quantum number n as parameter. Solid lines: populations with $n \leq 4$; dotted lines populations with $n > 4$. The initial state is Ar^{18+} .

In this section we discuss results obtained within the classical transport theory for the transport of an Ar^{18+} ion ($v_p = 23$ a.u.) through amorphous carbon. The initial conditions are determined by the phase space distribution of electrons captured according to the description in section 3.4.1. Further propagation through the solid is calculated as a random walk along Kepler

orbits (section 4.2). The resulting classical phase space is mapped onto the principal quantum number n and the angular momentum quantum number l according to (3.45) and (3.46) respectively.

For thin foils the populations resemble the initial conditions produced by electron capture (see section 3.4.5). The overall probability to find an electron in a given shell scales with n^{-3} (figure 3.5). The angular momentum distribution of the initial condition shown in figure 3.4 corresponds to the limit of infinitesimal short propagation length through the solid. There electron capture into p-states is the dominant feature of the l -distribution. In figure 4.2 (a) we show the distribution of Ar^{17+} populations for a propagation length of 322 a.u. corresponding to a foil thickness of $3.5 \mu\text{g}/\text{cm}^2$. The angular momentum distributions peak for small values of l and rapidly subside for large values of l . Unlike the initial distribution we can observe after short propagation angular momentum diffusion towards higher values of l . At short propagation paths as $d=3.5 \mu\text{g}/\text{cm}^2$ (figure 4.2 (a)) d-states become dominant while higher angular momentum states are still less pronounced. After a long interaction time, i.e. propagation length, the picture is considerably different as shown in figure 4.2 (b) for $d=200 \mu\text{g}/\text{cm}^2=18400$ a.u.. A large number of collisions has redistributed the probability towards a statistical mixture of states resulting in a linear $2l+1$ scaling with l .

4.4 Convoy electron emission

In this section we present an application of the classical transport theory and put the emphasis on disentangling contributions from different collision mechanisms onto the spectra of emitted electrons. The angular and energy distributions of electrons emitted in ion-atom and ion-solid collisions have been studied extensively [Bre82, Gib91] during the last few decades. In ion-atom collisions one of the most prominent features of these emission spectra is that in the forward direction they exhibit a cusp-shaped peak at the energy corresponding to the velocity of the incident ion. In ion-solid collisions this feature is commonly referred to as convoy electron peak (CEP)[Bre82]. Its origin is far more complex than in ion-atom collisions as a multitude of collision processes opens alternative pathways for populating these low-lying continuum states. Recently, measurements of the CEP for relativistic projectiles have become available [Tak99a]. Due to the vanishingly small cross section for electron capture to continuum (ECC)[Luc80] at very high velocities loss from the projectile by stepwise excitation (electron loss to continuum (ELC))[Bur83a] and multiple scattering of liberated electrons are the main source of the CEP in this case.

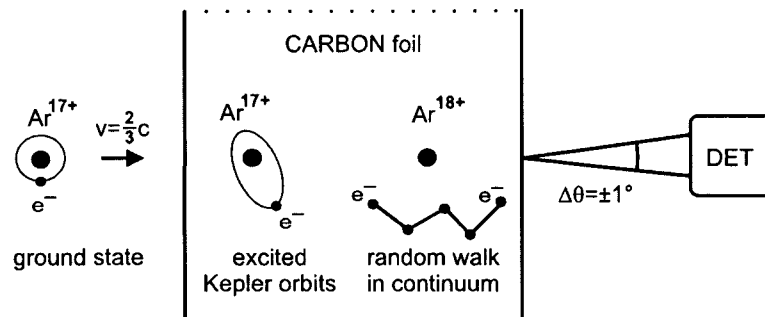


Figure 4.3: Schematic picture of the convoy emission process within a classical transport theory.

We investigate the convoy electron emission by (moderately) relativistic projectiles. Here we briefly sketch the main results while a detailed discussion can be found in [Sel03, Tak03]. In line with the experiment [Tak99a], we focus on Ar^{17+} ions with an energy of 390 MeV/amu ($v_p=97$ a.u.) traversing thin self-supporting amorphous carbon foils of thickness varying from 25 to 9190 $\mu\text{g}/\text{cm}^2$. This collision system has several attractive features: In the relativistic velocity regime the average distance between two collisions, the mean free path, is long. The thinnest carbon foils available have a thickness of the order of the collisional mean free path, thus providing a testing ground for the limit of single collisions. By varying the foil thickness we have the opportunity to follow the time evolution of the projectile for up to several hundred collisions.

4.4.1 Random walk

We follow the evolution of the electron initially attached to the projectile by means of a CTMC calculations. The process is schematically depicted in figure 4.3. The multi-step ionization of transient highly excited states leaves a clear mark on the charge state probability for different regions of propagation length. Figure 4.4 shows the charge state distribution as a function of carbon foil thickness for 390 MeV/u incident Ar^{17+} ions. Since at very high collision energies the electron capture process is negligible, only Ar^{17+} and Ar^{18+} ions were observed. The fraction of Ar^{18+} ions was 0.8% at 25 $\mu\text{g}/\text{cm}^2$, and increased to more than 99% at ~ 10000 $\mu\text{g}/\text{cm}^2$. The charge state distribution is still not fully equilibrated even at ~ 10000 $\mu\text{g}/\text{cm}^2$. The

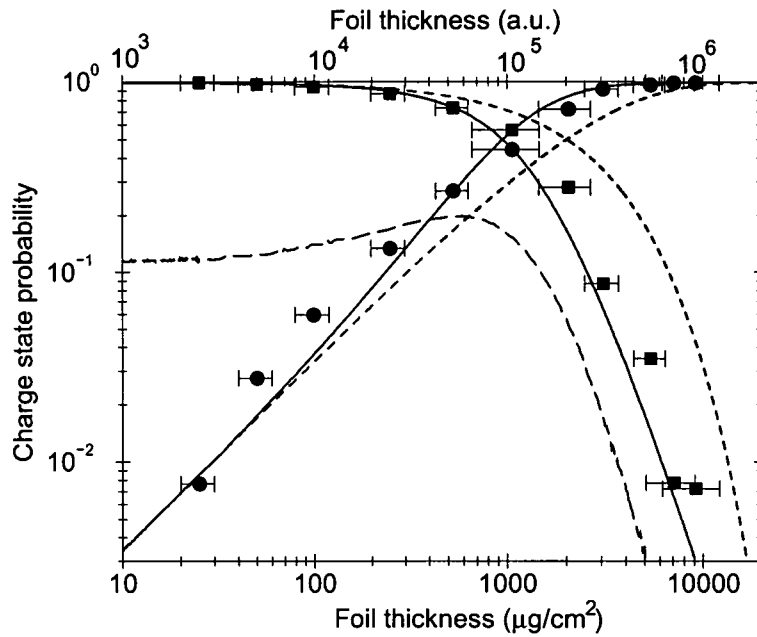


Figure 4.4: Outgoing fractions of Ar^{17+} and Ar^{18+} ions as a function of foil thickness resulting from the transmission of 390 MeV/u Ar^{17+} ions through amorphous carbon foils. Experimental data for Ar^{17+} (squares) and Ar^{18+} (circles); short dashed line: simulation neglecting multiple excitation (i.e. single collision ionization from ground state); solid line: full CTT simulation; long dashed line: electron emission probability per 10^6 a.u. path length. The thickness of $1\mu\text{g}/\text{cm}^2$ of amorphous carbon with a density of $2\text{g}/\text{cm}^3$ corresponds to a propagation length of 92 a.u..

agreement with the simulation based on the CTT is excellent over orders of magnitude in thickness and probability. We also show the calculated charge state probabilities when only direct ionization from the ground state is taken into account, i.e. when stepwise excitation in multiple collisions prior to ionization is neglected. The charge state probability $P_{17}(d)$ (d : foil thickness) for the initial state (Ar^{17+}) obeys in this case a simple exponential decay law $P_{17}(d) = \exp(-d/\lambda_{1s})$ with the MFP for ionization of the $1s$ ground state $\lambda_{1s} \simeq 3000\mu\text{g}/\text{cm}^2$. The fact that we observe clear deviations from such a simple exponential decay provides direct evidence for the random walk in state space prior to ionization. The probability per atomic unit path length for emitting an electron is proportional to the slope of the ionization probability and is also shown in figure 4.4. For very thin foils the

emission rate of electrons is constant at a value of $w = 1.1 \times 10^{-7}$, because ionization from ground state is the dominant electron loss process. With increasing foil thickness other processes start contributing thereby enhancing the emission rate and reaching a maximum around a propagation distance of $d = 1000 \mu\text{g}/\text{cm}^2 \sim 10^5 \text{ a.u.}$ before rapidly decreasing. This multi-step ionization determines the spectra of emitted electrons at different propagation path lengths.

4.4.2 Convoy electron distribution

The velocity distribution $P(\vec{v})$ of emitted electrons carry signatures of different pre- and post-ionization processes. Detailed information about the convoy electron emission and the post-ionization interactions can be obtained from the two-dimensional distribution of the parallel (v_{\parallel}) and a perpendicular (v_{\perp}) component of the velocity with respect to the beam direction (figure 4.5). The propagation distances considered in figure 4.5 vary from the single-collision regime to the multiple scattering regime involving up to hundreds of collisions. The direct ionization from the ground state results in a near-isotropic distribution with a weak enhancement in the transverse direction ($d = 25 \mu\text{g}/\text{cm}^2$). For thicknesses $d \leq 250 \mu\text{g}/\text{cm}^2$ the distribution becomes increasingly squeezed in both (v_{\parallel}) and (v_{\perp}) directions reflecting the growth of ionization from excited states built-up in preceding collisions. This is due to the fact that electrons emitted via a step-wise excitation provide a measure of the momentum distribution (Compton profiles) immediately before ionization. As the momentum distribution of the excited states scales as Z_P/n , the velocity distribution of electrons directly ionized from such states becomes narrower with increasing n .

Up to a foil thickness of $d = 250 \mu\text{g}/\text{cm}^2$ post-ionization transport is not yet important. The velocity distribution resembles that of ion-atom collisions, more specifically, that of an ensemble of initial states with increasing weight of excited states. The distribution $P(\vec{v})$ becomes increasingly oblate ellipsoidal [Sel03, Sza93] with a pronounced dominance of transverse components. During the transport through thicker foils, post-ionization collisions have a significant effect on the angular velocity distribution: Core collisions of the free electrons transfer a momentum perpendicular to the electron velocity in the rest frame of the target. Additionally the kinetic energy in the target rest frame is preserved. Since the change of velocity is relatively small compared to the velocity in the target restframe, core collisions therefore effectively modify the electron velocity along a circle. The velocity of an ensemble of electrons initially with the same velocity vector is by spread along this Newton circle. On the other hand, electron-electron post-ionization collisions

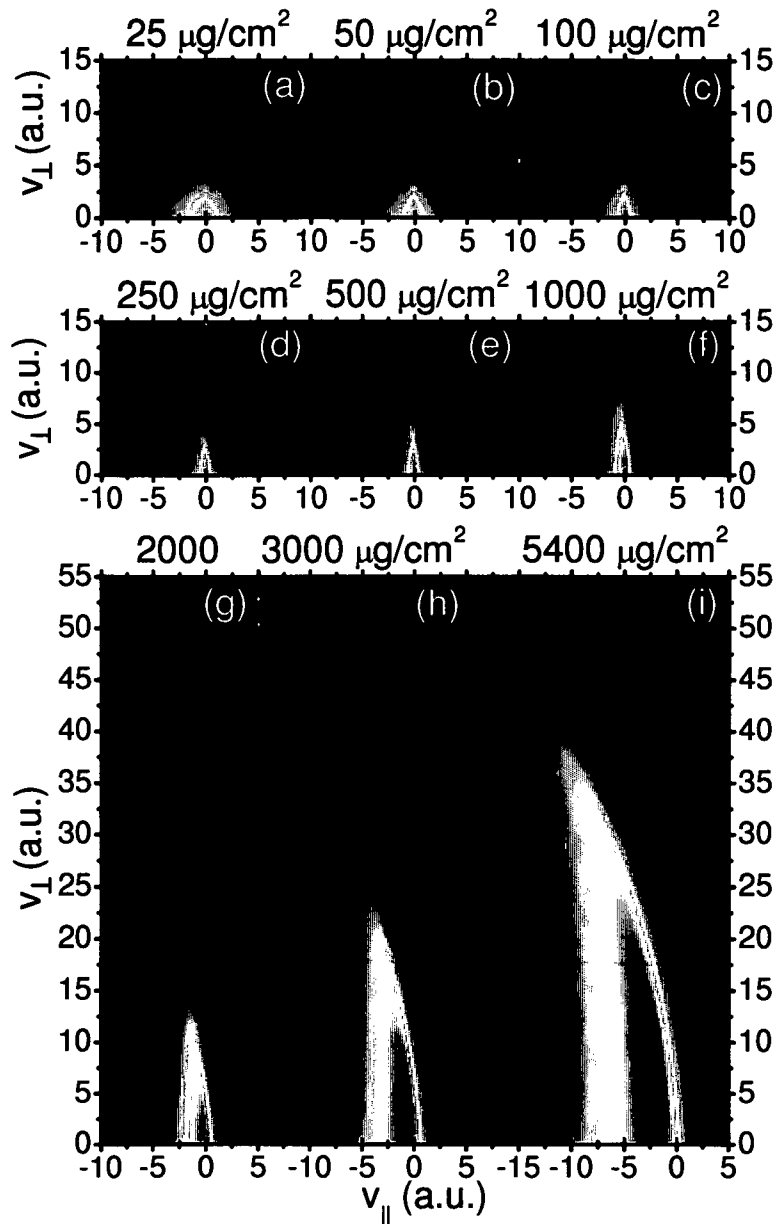


Figure 4.5: Contour plot of the velocity distribution $P(\vec{v})$ of convoy electrons emitted by an Ar^{17+} (390 MeV/u) traversing carbon foils of different thickness. The foil thickness is denoted in each graph and the intensities are normalized to one and taken on a logarithmic scale. We show the distribution of the parallel (v_{\parallel}) and one perpendicular ($v_{\perp} = v_x$ or v_y) velocity component.

transfer, on average, a smaller amount of momentum to the free electron and therefore modify the v_{\parallel} distribution in two ways while leaving v_{\perp} almost unaffected: v_{\parallel} is broadened and also shifted towards lower energies due to an overall energy loss (stopping) becoming noticeable after propagation through foils thicker than $d = 1000 \mu\text{g}/\text{cm}^2$. Since core and e-e collisions have different strengths (compare momentum transfer distributions in figure 3.1), they effectively modify the continuum distribution at different propagation distances. We thus have the opportunity to disentangle the contributions of these two collisional interactions in figure 4.5.

4.4.3 Comparison with experiment

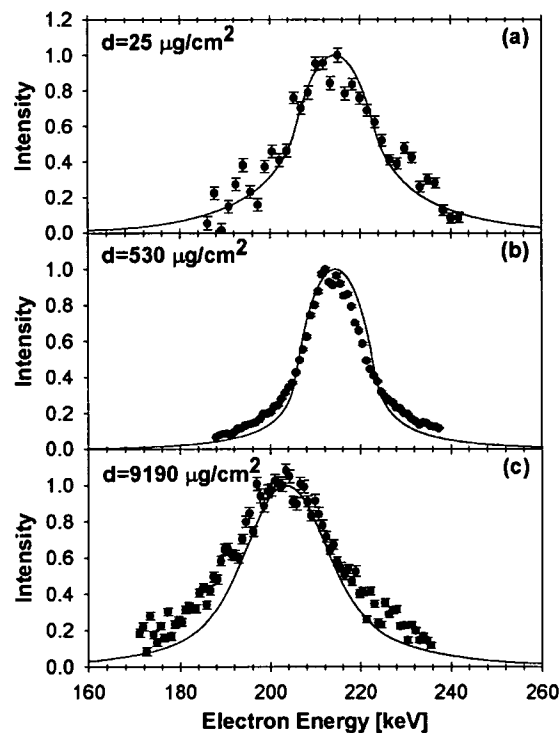


Figure 4.6: Comparison of the theoretical calculation (solid line) with experimental data (symbols) for convoy electrons emitted by the transport of an Ar^{17+} ion (390 MeV/amu) through a carbon foil of following thickness: (a) $25 \mu\text{g}/\text{cm}^2$ (2500 a.u.); (b) $530 \mu\text{g}/\text{cm}^2$; (c) $9190 \mu\text{g}/\text{cm}^2$. Theoretical data has been convoluted with the experimental resolution ($\Delta\theta = \pm 1^\circ$, $\Delta E = \pm 9$ keV). Intensity has been normalized to one.

The experimental setup was described in section 2.2. In order to compare the theoretical findings with the measurements, simulated electron spectra with $\Delta\theta = \pm 1^\circ$ are convoluted with the detector resolution of $\Delta E = \pm 9$ keV. The three different frames in figure 4.6 pertain to the three different regimes accessible: figure 4.6(a) displays the convoy electron peak in the (approximate) single-collision regime. Figure 4.6(b) is a much narrower CEP reflecting the oblate spheroidal distributions analyzed in the previous section. Finally figure 4.6(c) displays a drastically broadened and shifted CEP that is subject to a large number of slowing collisions subsequent to ionization. For all three cases we find excellent agreement with experimental data confirming, among other properties, the highly anisotropic emission pattern at intermediate propagation distances.

In summary, study of convoy electron emission induced by moderately relativistic highly charged ions allows the study of the evolution of the CEP from the near single-collision limit to the true multiple scattering regime involving up to hundreds of electron-ion core and electron-electron collisions. The discussed classical transport theory (CTT) based on a Monte Carlo solution of a microscopic Langevin equation is capable to describe this complex evolution process, including the transient build-up of a high degree of anisotropy, quite well.

4.5 Summary

In this chapter we have taken a first glance at ion transport through solids by a classical approach. While a description within the quantum transport theory (QTT) is suitable for (and is also limited by the increasing size of the Hilbert space to) deeply bound core states, the classical transport theory (CTT) enables us to follow the electron in a highly excited state and in the continuum.

In order to partly account for the discrete structure of quantum eigenstates we have introduced a minimum momentum transfer requirement for collisions of the quasi-free electron effectively suppressing electron-electron collisions of core states (section 4.2). We investigate this effect for the example of multi-step convoy electron emission (section 4.4) by illustrating its consequences on the velocity distribution of convoy electrons in the emission process as well as in further transport in the continuum. Because of the high charge, high projectile energies, and a wide range of thicknesses the path of sequential excitation and ionization of an initially bound electron could be followed in, - for ion solid collisions - unprecedented detail. The build-up of excited states is, through the narrowing of the Compton profile, clearly

reflected in the narrowing of the convoy peak. The width of the convoy peak evolves non-monotonically as a function of the foil thickness: narrowing due to the generation of projectile excitation by multiple scattering is followed by broadening in both energy and angle due to further multiple scattering of the liberated electrons. The charge state distributions of the transmitted ions and the convoy electron spectra calculated by the CTT simulation are in good agreement with the experiment over a wide range of target thicknesses, i.e., from a single collision regime to a multiple collision regime.

Chapter 5

Quantum transport theory

5.1 Introduction

We present a quantum transport theory based on the solution of quantum master equation. We discuss the Lindblad master equation and its solution by a quantum trajectory Monte Carlo method. We first briefly review the open quantum system approach while a detailed description can be found in [Min03a]. Starting from the underlying Liouville-von Neumann equation we discuss the reduction to a master equation of the Redfield form by means of the Born-Markov approximation. A further mapping onto a master equation of the Lindblad form allows for a significant simplification of the solution. This is that the Lindblad master equation can be transformed to a non-linear stochastic Schrödinger equation without further approximation. The advantage of this additional step is that the latter can be solved by means of a quantum trajectory Monte Carlo method making a large number of problems accessible to a numerical solution. In the following applications of this method we will explore this fact.

We present the extension for a system with a net flux out into a complement and discuss the quantum trajectory Monte Carlo implementation. This modification of the Lindblad master equation is necessary since the standard Lindblad formalism is strictly unitary and does not account, actually forbids, for outgoing as well as for incoming probability flux. We show its validity of the Monte Carlo solution by an analytical proof and by a numerical test considering the comparison with an exact system. As we will see in this chapter, for collisions this generalization implies certain approximations that will be discussed in detail in the next chapter before we can apply this method to the calculation of ion-solid transport. In chapter 8 we present a more general form of the Lindblad framework that accounts for incoming flux as well.

5.2 Master equation

Consider a system (S) of interest with Hamiltonian H_S with the reduced density matrix σ interacting with an environment referred to in the following as reservoir (R) with Hamiltonian H_R and σ_R through a coupling interaction V_{SR} (Fig. 5.2(a)). The time evolution of the density matrix $\rho(t) = \sigma(t) \otimes \sigma_R(t)$ of the entire interacting system is given by the Liouville-von Neumann equation

$$\frac{d}{dt}\rho(t) = -i[H, \rho(t)], \quad (5.1)$$

including the total Hamiltonian $H = H_S + H_R + V_{SR}$.

Clearly, the solution of the full Liouville-von Neumann equation is out of reach for realistic systems involving a large number of degrees of freedom. Instead, the focus is on a master equation, an equation of motion for the reduced density matrix of the system of interest $\sigma(t)$, which is obtained by tracing out all degrees of freedom of the reservoir by $\sigma(t) = \text{Tr}_R[\rho(t)]$. One requirement for the reservoir is that it has a large number of degrees of freedom compared to those of the system such that the energy spacing of reservoir states is much smaller than that of the system providing a quasi-continuous excitation spectrum. The reduction entails usually a number of additional approximations such as the Born-Markov approximation which neglects memory effects, treats the coupling V_{SR} in first-order perturbation theory, and yields a master equation of the Redfield type [Min03a].

The Born-Markov approximation is valid for systems that are initially disentangled. This means that the interaction is initially switched off and we can write the tensor product for $t=0$ as

$$\rho(0) = \sigma(0) \otimes \sigma_R(0). \quad (5.2)$$

In a beam-foil setup the interaction is effective only during the passage of a projectile through the target. There system and reservoir variables get entangled. This entanglement has to be weak from the point of view of the reservoir such that σ_R is unaffected by the interaction and remains approximately in its ground state as $\sigma_R(t) \approx \sigma_R(0)$. This corresponds to the assumption of linear response in reservoir variables. Obviously this assumption is only valid on a certain time scale. The fluctuations in σ_R destroy the entanglement of system and reservoir variables such that this perturbation is dissipated on a time scale t_c that is the reservoir correlation time. Consequently, when we restrict ourself to observables changing slower than t_c , i.e. $\sigma(t + t_c) \approx \sigma(t)$, we can assume

$$\rho(t) = \sigma(t) \otimes \sigma_R(0) \quad (5.3)$$

to be valid on this longer time scale.

Considering a swift projectile moving through a solid the correlation time t_c is of the order of the inverse projectile velocity. On the other hand the secular motion of projectile electronic observables occurs on a longer time scale making the Born-Markov approximation applicable for the description of projectile observables. In other words, it is the projectile velocity that ensures a fast dissipation of fluctuations of reservoir variables and that the projectile experience a reservoir in its ground state.

Within the Born-Markov approximations the Liouville-von Neumann equation can be reduced to the Redfield equation which is a master equation for the time evolutions of the reduced density matrix of the system as

$$\frac{d}{dt}\sigma(t) = -i[H_S, \sigma(t)] + R^{(R)}\sigma(t) \quad (5.4)$$

with the relaxation operator $R^{(R)}$

$$R^{(R)}\sigma(t) = -\frac{1}{2} \int d^3k \left[X^\dagger(\vec{k})Y(\vec{k})\sigma(t) + \sigma(t)X^\dagger(\vec{k})Y(\vec{k}) - X(\vec{k})\sigma(t)Y^\dagger(\vec{k}) - Y(\vec{k})\sigma(t)X^\dagger(\vec{k}) \right]. \quad (5.5)$$

$R^{(R)}$ describes transitions induced by the interaction with the environment. $R_{ijkl}^{(R)}$ maps each element of the matrix σ_{kl} on the time derivative of each element of σ_{ij} making it a rank four tensor. The product XY is determined according to (3.7)

$$X^\dagger(\vec{k})Y(\vec{k}) = \frac{2}{v_p} \tilde{V}_{PT}^2(\vec{k}) |\langle f|e^{i\vec{k}\vec{r}}|i\rangle|^2 \chi''(\vec{k}, \omega_{if} - \vec{k}\vec{v}_p) \quad (5.6)$$

splitting up into the individual components

$$X_{ij}(\vec{k}) = \sqrt{\frac{2}{v_p}} \tilde{V}_{PT}(\vec{k}) \langle i|e^{i\vec{k}\vec{r}}|j\rangle \chi''(\vec{k}, \omega_{ji} - \vec{k}\vec{v}_p) \quad (5.7)$$

and

$$Y_{ij}(\vec{k}) = \sqrt{\frac{2}{v_p}} \tilde{V}_{PT}(\vec{k}) \langle i|e^{i\vec{k}\vec{r}}|j\rangle \quad (5.8)$$

Hence in the Redfield master equation the bra and ket wave vectors of the density matrix $\sigma_{ij} = |\Psi_i\rangle\langle\Psi_j|$ are described by different operators, i.e X and Y . This extra complexity makes the solution of the Redfield master equation (5.4) cumbersome.

Lindblad proposed an alternative form of a master equation that describes the time evolution of bra and ket wave vectors by means of the same operator S . This is achieved by the following form of R which is called the Lindblad form

$$R\sigma(t) = -\frac{1}{2} \int d^3k \left[S^\dagger(\vec{k})S(\vec{k})\sigma(t) + \sigma(t)S^\dagger(\vec{k})S(\vec{k}) - 2S(\vec{k})\sigma(t)S^\dagger(\vec{k}) \right] \quad (5.9)$$

with the transition operator S . Mapping the Redfield transition operators X and Y on the Lindblad transition operator S is not unique and requires additional approximations. All terms in equation 5.4 carry oscillatory phase factors of the form $\exp(i\omega_{ij}t)$ in the interaction picture. The usually applied secular approximation assumes that for long interaction times the phases average out. Only those terms survive where $\omega_{ij}=0$ leading to the mapping

$$S_{ij}^{sec}(\vec{k}) = \delta_{ij} \sqrt{\frac{2}{v_p}} \chi''(\vec{k}, -\vec{k}\vec{v}_p) \tilde{V}_{PT}(\vec{k}). \quad (5.10)$$

A diagonal transition operator as S^{sec} can only account for decay of off-diagonal elements of the density matrix, but no build-up of off-diagonal elements can occur.

By taking the geometric mean of X and Y [Min03a]

$$S_{ij}(\vec{k}) = \sqrt{X_{ij}(\vec{k})Y_{ij}(\vec{k})} = \sqrt{\frac{2}{v_p}} \chi''(\vec{k}, \omega_{if} - \vec{k}\vec{v}_p) \tilde{V}_{PT}(\vec{k}) \langle f | e^{i\vec{k}\vec{r}} | i \rangle \quad (5.11)$$

we obtain a symmetrical form that is applicable in the Lindblad form of the master equation. Since S_{ij} contains also off-diagonal elements, a build-up of off-diagonal elements of the density matrix is possible. The transition operators S describing state-to-state transitions can be calculated for different environments as shown in section 3.2.

The two particularly important properties of the Lindblad form of the master equation are first the possibility to solve it by means of a Monte Carlo technique opening up a wide range of applications. In this thesis we will explore this feature. The second important point is that due to the specific choice of the transition operators (5.11) the Lindblad master equation can account for the build-up of diagonal elements of the reduced density matrix, i.e. coherences. To be more specific, the application of the transition operator S simultaneously from the left and also from the right on σ allows for transitions from one initial state to more than one final state. These final states have at that point a certain phase relation, that is, they form a coherent superposition. In [Min03a] it was shown that the mapping allows to account for the phase information on the time scale of the secular motion of system observables.

5.3 Unitary open quantum systems

In this section we consider the case of a Lindblad master equation that describes an open quantum system that is open with respect to energy exchange but closed for probability flux. The master equation describes a unitary transformation. Therefore we name this version of master equation the "unitary" Lindblad equation in contrast to the later discussed "non-unitary" version that describes open quantum systems that are also open with respect to probability flux.

5.3.1 Unitary Lindblad master equation

The unitary Lindblad master equation is written as

$$\frac{d}{dt}\sigma(t) = -i[H_S, \sigma(t)] + R\sigma(t) \quad (5.12)$$

with the relaxation superoperator

$$R\sigma(t) = -\frac{1}{2V} \sum_{\vec{k}} \left[S^\dagger(\vec{k})S(\vec{k})\sigma(t) + \sigma(t)S^\dagger(\vec{k})S(\vec{k}) - 2S(\vec{k})\sigma(t)S^\dagger(\vec{k}) \right], \quad (5.13)$$

that describes the interaction of the system with the reservoir and involves a sum containing the transition operator $S(\vec{k})$. The transition operator represents transitions between states of \mathbb{H}_S due to the coupling with the reservoir determined by V_{SR} . The physical meaning of the summation label k and quantization volume V depends on the system under consideration. In the following k represents the wavenumber vector of the momentum exchange between system and reservoir but may also include polarization indices etc. The time evolution of the reduced density matrix $\sigma(t)$ in this formalism is governed by H_S , the part of the total Hamiltonian acting on the system solely, and by the Lindblad transition operator $S(\vec{k})$. With this decomposition we separate the description of the dynamics into an unperturbed part of the small system without an environment (H_S) and put all effects of the presence of an environment (i.e. driving transitions within the open quantum system) into the relaxation superoperator (R). In the quantum Monte Carlo trajectory realization the first term of (5.12) and the first two terms of (5.13) of the Lindblad master equation result in a continuous time evolution while the last terms in (5.13) is responsible for discontinuous ("jump") processes. Built into Eq. (5.12) is the strict positivity of $\sigma(t)$ for all times ,

i.e. $\sigma_{ii}(t) \geq 0$ for all i and t . The Lindblad Eq. describes an open quantum system (OQS) allowing for energy exchange

$$\frac{d}{dt}\langle H_S \rangle = \frac{d}{dt}\text{Tr}[\sigma(t)H_S] \neq 0 \quad (5.14)$$

while preserving the total probability

$$\frac{d}{dt}\text{Tr}_S[\sigma(t)] = 0. \quad (5.15)$$

The latter follows from the explicitly built-in unitarity of the evolution into the relaxation operator (Eq. (5.13)). Eq. (5.12) describes a unitary mapping of the Hilbert space of the system, \mathbb{H}_S , onto itself.

5.3.2 Quantum trajectory Monte Carlo solution

The popularity of the Lindblad equation is, in part, due to the fact, that it can be mapped onto a nonlinear stochastic Schrödinger equation (NLSSE) without further assumptions or approximations. The advantage of such a mapping is that the NLSSE can be solved by propagating a Monte Carlo ensemble of state vectors: i.e. using the quantum trajectory Monte Carlo (QTMC) or Monte Carlo wavefunction (MCWF) method. In analogy to classical statistical mechanics, where the Boltzmann equation can be solved using test particle discretization following the trajectories of an ensemble of test particles in time according to a Langevin equation 4.2, the Lindblad form of the master equation can be solved by an ensemble of quantum trajectories. The dynamics of the classical trajectories in phase space is governed by the Langevin equation while in the quantum version each realization corresponds to a stochastically propagated state vector (quantum “trajectory” in Hilbert space) according the NLSSE.

Within the QTMC method the density matrix of a pure state is obtained as

$$\sigma(t) = \frac{1}{N_{traj}} \sum_{\eta=1}^{N_{traj}} |\Psi^\eta(t)\rangle\langle\Psi^\eta(t)| \quad (5.16)$$

where η is one stochastic realization and N_{traj} is the number of quantum trajectories controlling the statistical uncertainty. In the limit $N_{traj} \rightarrow \infty$, the ensemble average can be shown to be strictly equivalent to the solution of the original Lindblad equation [Gar99]. The time evolution of each trajectory

is governed by the NLSSE

$$|d\Psi^\eta(t)\rangle = \left[-iH_S dt - \frac{dt}{2V} \sum_{\vec{k}} \left(S^\dagger(\vec{k})S(\vec{k}) - \langle S^\dagger(\vec{k})S(\vec{k}) \rangle_{t,\eta} \right) + \frac{1}{V} \sum_{\vec{k}} dN_{\vec{k}}^\eta(t) \left(\frac{S(\vec{k})}{\sqrt{\langle S^\dagger(\vec{k})S(\vec{k}) \rangle_{t,\eta}}} - 1 \right) \right] |\Psi^\eta(t)\rangle \quad (5.17)$$

The differential, also called Ito differential, $dN_{\vec{k}}^\eta(t) = N_{\vec{k}}^\eta(t+\delta t) - N_{\vec{k}}^\eta(t)$ takes for a given quantum trajectory η for an infinitesimally short time interval δt the value 1 when a jump happened and 0 for no jump. This stochastic element generates different stochastic realizations of quantum trajectories labeled by η . We show in 5.4.3 that the reduced density matrix calculated as the Monte Carlo average (5.16) yields the Lindblad equation (5.12) when the expectation value of the Ito differentials for the system in state $|\Psi^\eta\rangle$ at time t are chosen as

$$\overline{dN_{\vec{k}}^\eta(t)dN_{\vec{k}'}^\eta(t)} = \overline{dN_{\vec{k}}^\eta(t)\delta_{\vec{k}\vec{k}'}} = dt \langle S^\dagger(\vec{k})S(\vec{k}) \rangle_{t,\eta} \delta_{\vec{k}\vec{k}'}. \quad (5.18)$$

Because the right hand side of the NLSSE (5.17) explicitly depends on the expectation value of the transition operator S the NLSSE is nonlinear leading to a non-Hamiltonian form.

Solving the NLSSE the time evolution of each quantum trajectory is constructed by applying the time evolution operator onto the initial wave function as $|\Psi^\eta(t)\rangle = U^\eta(t,0)|\Psi^\eta(0)\rangle$. The time evolution operator $U^\eta(t,0)$ is constructed as a sequence of continuous time evolution operators and discontinuous jump operators as

$$U^\eta(t,0) = U_{cont}^\eta(t,t_n) \prod_{j=1}^n U_{jump}^\eta(\vec{k}_j, t_j) U_{cont}^\eta(t_j, t_{j-1}) \quad (5.19)$$

with $t_0 = 0$. The application of the continuous time evolution operator results in

$$\begin{aligned} |\Psi^\eta(t_j)\rangle &= U_{cont}^\eta(t_j, t_{j-1}) |\Psi^\eta(t_{j-1})\rangle \\ &= \frac{e^{-iH_{eff}(t_j-t_{j-1})} |\Psi^\eta(t_{j-1})\rangle}{\|e^{-iH_{eff}(t_j-t_{j-1})} |\Psi^\eta(t_{j-1})\rangle\|}, \end{aligned} \quad (5.20)$$

with the effective Hamiltonian

$$H_{eff} = H_S - \frac{i}{2V} \sum_{\vec{k}} S^\dagger(\vec{k})S(\vec{k}) \quad (5.21)$$

including the unperturbed atomic Hamiltonian of the system (H_S) and the modification of the eigenstates due to the presence of the environment making the effective Hamiltonian non-Hermitian. In the last term we identify the decay operator Γ as

$$\Gamma = \frac{1}{V} \sum_{\vec{k}} \Gamma(\vec{k}) = \frac{1}{V} \sum_{\vec{k}} S^\dagger(\vec{k}) S(\vec{k}) \quad (5.22)$$

The discontinuous transitions

$$|\Psi^\eta(t_j + \delta t)\rangle = U_{jump}^\eta(\vec{k}_j, t_j) |\Psi^\eta(t_j)\rangle = \frac{S(\vec{k}_j) |\Psi^\eta(t_j)\rangle}{\|S(\vec{k}_j) |\Psi^\eta(t_j)\rangle\|} \quad (5.23)$$

are specified by a transition time (jump time) t_j and the parameter \vec{k}_j which are determined by the coupling to the reservoir degrees of freedom. In spite of the non-Hermitian nature of H_{eff} , the evolution (Eq. 5.20-5.23) remains unitary as the renormalization of the kets (Eq. 5.20 and 5.23) restores the norm at each step.

The time between two jumps is determined by the stochastic variable $dN_{\vec{k}}^\eta(t)$ whose average is defined by the expectation value of the decay operator Γ (see equation (5.18)). From (5.18) we can define a probability density for jump times per unit time as

$$\int_t^{t+\delta t} p^\eta(t') dt' = \delta t \langle \Gamma \rangle_{\eta t} = \delta t \langle \Psi^\eta(t) | \Gamma | \Psi^\eta(t) \rangle \quad (5.24)$$

which is constant in an infinitesimal time interval with the length δt .

A possible choice is to consider the decay of norm determined by the continuous time evolution operator when omitting the normalization in the denominator in equation (5.20)

$$p^\eta(t') = \frac{d}{dt} \|e^{-iH_{\text{eff}} t} |\Psi^\eta(t)\rangle\|^2 \quad (5.25)$$

with the normalization

$$\int_0^\infty p^\eta(t') dt' = 1 \quad (5.26)$$

such that the integral over the probability density $p^\eta(t)$ is in the interval between 0 and 1 for each positive upper time.

In order to find for a certain trajectory the next random jump time based on the probability density $p^\eta(t)$ we chose a random number r in the interval $(0, 1)$ and find the next jump time t' that fulfills the implicit equation

$$r = 1 - \|e^{-iH_{\text{eff}} t'} |\Psi^\eta(t)\rangle\|^2 \quad (5.27)$$

This means that we have to propagate the wavefunction in time until equation (5.27) is satisfied. The Newton iteration method for root-finding proved to be very efficient and converges to a satisfactory level within less than five iterations [Pre86].

It has to be pointed out that equation (5.27) describes a multi-exponential decay determined by the decay operator Γ . In a special case when we would consider only single-exponential decay, i.e. only one channel that can decay, we can use the expectation value of the decay operator directly to simplify the implicit equation (5.27) to

$$r = 1 - e^{-i\langle\Gamma\rangle_{\eta}t'} \quad (5.28)$$

giving a jump time as

$$t' = -\ln(1 - r) / \langle\Gamma\rangle_{\eta} \quad (5.29)$$

Since in the general case we are confronted with a multi-exponential decay, we have to solve (5.27) using the Newton iteration.

In a special case when the subspace \mathbb{H}_S contains states for which $\Gamma_{ii} = 0$ (i.e., states that do not decay at all) the integrated probability density for jump times adopts the form

$$\int_0^{\infty} p^n(t') dt' = Tr [\sigma_{ii}^n(t) \theta(\Gamma_{ii})] \quad (5.30)$$

where the step function θ selects only states that contribute to the reduction of norm in (5.27). A hydrogenic ion that can only radiatively decay by emitting one photon represents such a special case where the 2s metastable and the 1s ground state are such a probability sink.

After the jump time has been determined the value of \vec{k} is chosen according to the conditional probability density

$$p^n(\vec{k})|_{t=t'} = \frac{\left\| S(\vec{k}) |\Psi^n(t')\rangle \right\|^2}{\frac{1}{V} \sum_{\vec{k}'} \left\| S(\vec{k}') |\Psi^n(t')\rangle \right\|^2}. \quad (5.31)$$

In Figure 5.1 we show an example trajectory within the QTMC method. The left side shows the initial density matrix $\sigma(0)$ with an initial state denoted as an entry in the bottom left corner of the matrix with a red square while the other elements are 0 (empty entries). For this example we have chosen a hydrogenic Krypton in the 1s ground state as initial state. We show only a subspace of 16 states. The initial density matrix is decomposed according to $\sigma(0) = |\Psi(0)\rangle\langle\Psi(0)|$ into the bra and ket wavevectors indicated next to the matrix. Then we take the ket wavevector and propagate

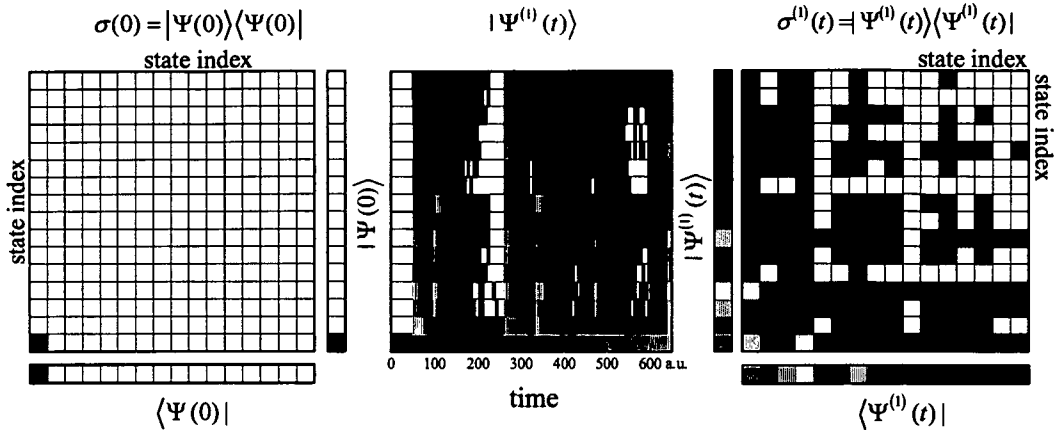


Figure 5.1: Example trajectory of the QTMC method for a Kr^{35+} ion initially in the $1s$ ground state. Left side shows the initial density matrix and its decomposition into a bra and ket wavevector. Middle segment shows the next step of one stochastic realization of the time propagation of the ket wavevector $|\Psi(0)\rangle \rightarrow |\Psi^{(1)}(t)\rangle$. We show one stochastic realization as a function of time for a subspace. On the right side the density matrix of the first quantum trajectory is put together.

it in time according to its equation of motion, the NLSSE (5.17). Since the NLSSE has a stochastic element we will create one stochastic realization of the time evolution. This is shown in the middle section of Figure 5.1 as a function of time. What happens in detail is that until the first quantum jump at $t_1 \approx 50 \text{ a.u.}$ the probability stays in the ground state. Then at t_1 the jump operator spreads the probability into higher excited states. Further interaction redistributes the probability that partly decays into the ground state or goes into higher excited states that are not displayed in the figure (at time $\approx 250 \text{ a.u.}$). Then a sequence of continuous and discontinuous time evolutions redistributes the probability. The final density matrix at a certain time t ($t = 650 \text{ a.u.}$ in this example) is reconstructed according to $\sigma^{(1)} = |\Psi^{(1)}\rangle\langle\Psi^{(1)}|$. In the right side of Figure 5.1 we show the density matrix for one stochastic realization. The solution of the underlying Lindblad master equation is a sum over a sufficiently large number of stochastic realizations as is written in equation (5.16).

The advantage of the QTMC method is the lower-order scaling of the solution with the basis size N_S . A direct solution of the Lindblad master equation scales with N_S^4 which makes larger systems inaccessible for a theoretical description. The solution of the NLSSE by means of the QTMC

method scales with N_S^2 because we obtain the time evolution of the density matrix by propagating wavefunctions in time. The additional scaling with the number of stochastic realizations (N_{traj}) controls the statistical uncertainty.

5.4 Non-unitary open quantum systems

In this section we introduce a generalized version of the Lindblad master equation that describes an open quantum system that is open not only with respect to energy exchange but also with respect to probability flux.

The unitarity constraint, Eq. (5.15), built into the Lindblad equation, poses a hurdle for realistic numerical simulations as it remains in force when the Hilbert space is truncated to dimension N_S . For realistic high, but finite, dimensional systems which include continuum states a strictly unitary evolution is unphysical. Only a subspace \mathbb{P} of the Hilbert space \mathbb{H}_S can be represented in a numerical simulation by a truncated basis of dimension $N_{\mathbb{P}}$ (see Fig. 5.2(b)). The subspace \mathbb{P} is coupled to its complement \mathbb{Q} by V_{SR} . The flow of probability between \mathbb{P} and \mathbb{Q} is therefore not an artifact but real for any computationally feasible truncated basis set. The point to be noted is that \mathbb{Q} refers to a subspace of the system Hilbert space, not to the reservoir.

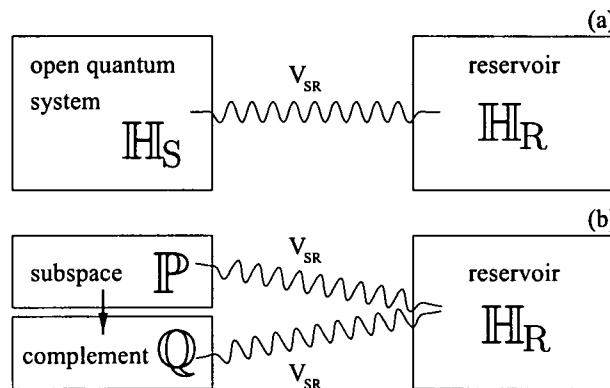


Figure 5.2: Schematic picture of the open quantum system \mathbb{H}_S interacting with the reservoir \mathbb{H}_R via the interaction V_{SR} . (a) full system \mathbb{H}_S and (b) decomposition into subspace \mathbb{P} and complement \mathbb{Q} .

In practice, numerical simulations take this effect into account by optical potentials or masking functions [Yos99]. Their purpose is to prevent “reflection” of wavepackets, i.e. the artificial confinement within \mathbb{P} rather than the

flow into \mathbb{Q} . Such approximations can account for a flow from \mathbb{P} into \mathbb{Q} while neglecting the backcoupling from \mathbb{Q} to \mathbb{P} . Their consequence is the violation of unitarity within $\mathbb{P} \subset \mathbb{H}_S$. In the application to the excited state evolution in the solid (see chapter 7), \mathbb{P} will represent the hydrogenic bound-state space up to $n \leq n_c$ where the cut-off quantum number is typically $n_c \approx 4$. (The dimension of \mathbb{P} is $N_S = 60$). Accordingly, \mathbb{Q} represents higher-lying bound states ($n > 4$) and the continuum spectrum of ionized electrons. Our goal is therefore to go beyond the restriction (5.15) and to develop a new master equation that accounts for the probability flow from \mathbb{P} into \mathbb{Q} as is indicated in Fig. 5.3.

5.4.1 Non-unitary Lindblad equation

The time evolution of the density matrix describing the full Hilbert space \mathbb{H}_S is unitary and is determined - in case it is fully contained in the basis - by the previously described unitary version of the Lindblad master equation. We label it $\sigma^U(t)$. The density matrix describing the subspace \mathbb{P} is labeled as $\sigma^{NU}(t)$ since the time evolution is not unitary within \mathbb{P} any more. We obtain the non-unitary density matrix by tracing out of $\sigma^U(t)$ all degrees of freedom associated with the complements \mathbb{Q} as

$$\sigma^{NU}(t) = \text{Tr}_{\mathbb{Q}} [\sigma^U(t)] \quad (5.32)$$

The next step is to construct a Lindblad master equation for $\sigma^{NU}(t)$ from the one governing the time evolution of the unitary density matrix

$$\frac{d}{dt} \sigma^U(t) = -i [H_S, \sigma^U(t)] - \frac{1}{2} [\Gamma, \sigma^U(t)]_+ + \frac{1}{V} \sum_{\vec{k}} S(\vec{k}) \sigma^U(t) S^\dagger(\vec{k}). \quad (5.33)$$

Formally we can write it as

$$\frac{d}{dt} \sigma^{NU}(t) = \text{Tr}_{\mathbb{Q}} \left[\frac{d}{dt} \sigma^U(t) \right] \quad (5.34)$$

which means that we have to consider $\sigma_{ij}^{NU}(t)$ for states that are only from the subspace \mathbb{P} . Since the subspace \mathbb{P} is not a closed system the time evolution for $\sigma^{NU}(t)$ is written as

$$\begin{aligned} \frac{d}{dt} \sigma_{ij}^{NU}(t) &= -i [H_{S,i\alpha}, \sigma_{\alpha j}^U(t)] - \frac{1}{2} [\Gamma_{i\beta}, \sigma_{\beta j}^U(t)]_+ \\ &+ \frac{1}{V} \sum_{\vec{k}} S_{i\mu}(\vec{k}) \sigma_{\mu\nu}^U(t) S_{\nu j}^\dagger(\vec{k}). \end{aligned} \quad (5.35)$$

Since we consider the density matrix in the basis where the system Hamiltonian H_S is diagonal, we can set $i = \alpha$ and can leave the first term in (5.35) unchanged.

The second term in equation (5.35) describes for $\beta \neq j$ the decay of coherences. In the case $\beta \in \mathbb{P}$ those coherences are contained in the subspace \mathbb{P} . For $\beta \in \mathbb{Q}$ the density matrix $\sigma_{\beta j}^U(t)$ describes coherent superpositions between two states where one of them is included in $\sigma^{NU}(t)$ and the other is not. Those coherences are very short-lived. For the systems we consider in this work, i.e. hydrogenic ions, the borderline between the subsystems \mathbb{P} and \mathbb{Q} is usually realized by a certain cut-off quantum number n_c . Therefore the energy spacing between two states, one in \mathbb{P} and the other \mathbb{Q} is at least of the order of the inter-shell energy spacing between n_c and $n_c + 1$, which is considerably large. As we will discuss below in section 7 in more detail, these inter-shell coherences dephase very fast and thus play no role on the time scales we consider here. We can neglect those coherences and consider only

$$\beta \in \mathbb{P}. \quad (5.36)$$

Because of the definition of the decay operator Γ as

$$\Gamma_{i\beta \in \mathbb{P}} = \frac{1}{V} \sum_{\vec{k}} S_{im}^\dagger(\vec{k}) S_{m\beta}(\vec{k}) \quad (5.37)$$

the state index m also covers states in the complement \mathbb{Q} .

In the third term and last term in equation (5.35) the states μ and ν are elements of $\mathbb{P} \oplus \mathbb{Q}$. For $\mu, \nu \in \mathbb{Q}$ this term describes coupling from the complement \mathbb{Q} back to the subspace \mathbb{P} . Because we are not able to describe the time evolution of the complement we are thus not able to account for its coupling back to the described subsystem \mathbb{P} . We consider only

$$\mu, \nu \in \mathbb{P}. \quad (5.38)$$

Here we also have to neglect cross coherences between \mathbb{Q} and \mathbb{P} as it was the case for the second term in equation (5.35).

Using the approximations (5.36) and (5.38) we introduce a generalized Lindblad equation

$$\frac{d}{dt} \sigma^{NU}(t) = -i[H_S, \sigma^{NU}(t)] + R^{NU} \sigma^{NU}(t), \quad (5.39)$$

in which the relaxation superoperator R^{NU} is replaced by

$$R^{NU} \sigma^{NU}(t) = -\frac{1}{2V} \sum_{\vec{k}} \left(P^{\mathbb{P}} S^\dagger(\vec{k}) S(\vec{k}) P^{\mathbb{P}} \sigma^{NU}(t) + \sigma^{NU}(t) P^{\mathbb{P}} S^\dagger(\vec{k}) S(\vec{k}) P^{\mathbb{P}} \right. \\ \left. - 2S^{\mathbb{P}}(\vec{k}) \sigma^{NU}(t) S^{\mathbb{P}\dagger}(\vec{k}) \right). \quad (5.40)$$

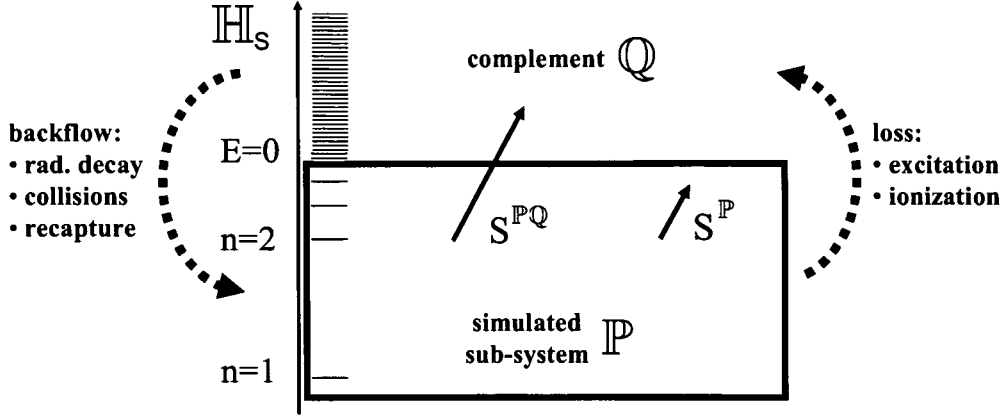


Figure 5.3: Schematic picture showing the decomposition of the full Hilbert space H_S into the subspace \mathbb{P} and the complement \mathbb{Q} in the energy space of hydrogenic eigenstates. We indicate the mechanism responsible for probability flux between these two subspaces.

In (5.40) S is defined in the entire Hilbert space \mathbb{H}_S while $S^{\mathbb{P}}$ is the submatrix of S mapping \mathbb{P} onto itself. That is, $S^{\mathbb{P}} = P^{\mathbb{P}} S P^{\mathbb{P}}$, where $P^{\mathbb{P}} = \sum_{\alpha \in \mathbb{P}} |\alpha\rangle\langle\alpha|$ is the projector operator onto the subspace \mathbb{P} . This gives rise to the decomposition

$$\Gamma^{\mathbb{P}\mathbb{P}} = \frac{1}{V} \sum_{\vec{k}} S^{\mathbb{P}\dagger}(\vec{k}) S^{\mathbb{P}}(\vec{k}) = \frac{1}{V} \sum_{\vec{k}} \Gamma^{\mathbb{P}\mathbb{P}}(\vec{k}) \quad (5.41a)$$

$$\Gamma^{\mathbb{P}} = \frac{1}{V} \sum_{\vec{k}} P^{\mathbb{P}} S^{\dagger}(\vec{k}) S(\vec{k}) P^{\mathbb{P}} = \frac{1}{V} \sum_{\vec{k}} \Gamma^{\mathbb{P}}(\vec{k}), \quad (5.41b)$$

where the former describes the decay matrix within \mathbb{P} while the latter also includes the decay from \mathbb{P} to \mathbb{Q} . In other words, (5.41b) involves the submatrix $S^{\mathbb{P}\mathbb{Q}}(\vec{k})$ mapping \mathbb{P} onto \mathbb{Q} (see Fig. 5.3). This allows us to write the non-unitary relaxation operator in a compact form as

$$R^{NU} \sigma^{NU}(t) = -\frac{1}{2} [\Gamma^{\mathbb{P}}, \sigma^{NU}(t)]_+ + \sum_{\vec{k}} S^{\mathbb{P}}(\vec{k}) \sigma(t) S^{\mathbb{P}\dagger}(\vec{k}). \quad (5.42)$$

Consequently the norm of $\sigma(t)$ is no longer conserved but decays according to

$$\begin{aligned} \frac{d}{dt} \text{Tr}_S [\sigma(t)] &= -\text{Tr}_S [\Gamma^{\mathbb{P}} \sigma(t)] + \text{Tr}_S [\Gamma^{\mathbb{P}\mathbb{P}} \sigma(t)] \\ &= -\frac{1}{V} \sum_{\vec{k}} \sum_{\alpha, \beta \in \mathbb{P}} \sum_{\nu \in \mathbb{Q}} S_{\alpha\nu}^{\dagger}(\vec{k}) S_{\nu\beta}(\vec{k}) \sigma_{\beta\alpha} \end{aligned} \quad (5.43)$$

where $S_{\alpha\nu}^\dagger$ and $S_{\nu\beta}$ in this equation correspond only to matrix elements of the submatrix $S^{\mathbb{P}\mathbb{Q}}$.

5.4.2 Quantum trajectory Monte Carlo solution

This non-unitary extension of the Lindblad equation has the advantageous feature that the positive-definiteness requirement remains satisfied within \mathbb{P} . Consequently it can be solved using a QTMC algorithm as well provided that a modified NLSSE and generalized versions of the continuous and jump operators

$$\begin{aligned} |\Psi^\eta(t_j)\rangle &= U_{cont}^\eta(t_j, t_{j-1}) |\Psi^\eta(t_{j-1})\rangle \\ &= \|\Psi^\eta(t_{j-1})\| \frac{e^{-iH_{eff}^{\mathbb{P}}(t_j-t_{j-1})} |\Psi^\eta(t_{j-1})\rangle}{\left\| e^{-iH_{eff}^{\mathbb{P}\mathbb{P}}(t_j-t_{j-1})} |\Psi^\eta(t_{j-1})\rangle \right\|}. \end{aligned} \quad (5.44)$$

is used. The non-hermitian effective Hamiltonians entering Eq.(5.44) are

$$H_{eff}^{\mathbb{P}} = H_S - \frac{i}{2}\Gamma^{\mathbb{P}} \quad \text{and} \quad H_{eff}^{\mathbb{P}\mathbb{P}} = H_S - \frac{i}{2}\Gamma^{\mathbb{P}\mathbb{P}}. \quad (5.45)$$

The interesting point to be noted is that the flow of probability from \mathbb{P} to \mathbb{Q} is realized by the continuous time evolution operator $U_{cont}^\eta(t_j, t_{j-1})$ in (5.44) where we use different effective Hamiltonians in the nominator and denominator which is due to the different decay operators $\Gamma^{\mathbb{P}}$ and $\Gamma^{\mathbb{P}\mathbb{P}}$ entering there. Since in (5.42) the loss of norm is only realized by $\Gamma^{\mathbb{P}}$ in the anti-commutator and because this part of the Lindblad master equation corresponds to continuous propagations in time, only $U_{cont}^\eta(t_j, t_{j-1})$ accounts for the probability flow out of \mathbb{P} . The jump operator describes only transitions within \mathbb{P} as

$$|\Psi^\eta(t_j + \delta t)\rangle = U_{jump}^\eta(\vec{k}_j, t_j) |\Psi^\eta(t_j)\rangle = \|\Psi^\eta(t_j)\| \frac{S^{\mathbb{P}}(\vec{k}_j) |\Psi^\eta(t_j)\rangle}{\|S^{\mathbb{P}}(\vec{k}_j) |\Psi^\eta(t_j)\rangle\|}. \quad (5.46)$$

by leaving the norm unchanged which is achieved by the prefactor $\|\Psi^\eta(t)\|$.

In contrast to (5.20), the continuous operator ((5.44)) does not preserve the norm of the wavefunction. The corresponding NLSSE now becomes

$$\begin{aligned} |d\Psi^\eta(t)\rangle &= \left\{ -i H_S^\mathbb{P} dt - \frac{dt}{2} \left(\Gamma^{\mathbb{P}} - \langle \Gamma^{\mathbb{P}\mathbb{P}} \rangle_{t,\eta} \right) \right. \\ &\quad \left. + \frac{1}{V} \sum_{\vec{k}} dN_{\vec{k}}^\eta(t) \left(\frac{S^{\mathbb{P}}(\vec{k})}{\sqrt{\langle \Gamma^{\mathbb{P}\mathbb{P}}(\vec{k}) \rangle_{t,\eta}}} - 1 \right) \right\} |\Psi^\eta\rangle, \end{aligned} \quad (5.47)$$

where the expectation values are now defined as

$$\langle \Gamma^{\text{PP}} \rangle_{\eta t} = \frac{\langle \Psi^\eta(t) | \Gamma^{\text{PP}} | \Psi^\eta(t) \rangle}{\langle \Psi^\eta(t) | \Psi^\eta(t) \rangle}. \quad (5.48)$$

In order to yield the generalized Lindblad form (5.40), the expectation value of the Ito differentials when the system is in state $|\Psi^\eta\rangle$ at time t is chosen as

$$\overline{dN_{\vec{k}}^\eta(t)} = dt \left\langle \Gamma^{\text{PP}}(\vec{k}) \right\rangle_{t,\eta} \quad (5.49)$$

In this case, the jump times dt till the next jump can be obtained from the implicit equation

$$r = \frac{1}{\|\Psi^\eta(t)\|} \left(1 - \left\| e^{-iH_{\text{eff}}^{\text{PP}} dt} |\Psi^\eta(t)\rangle \right\|^2 \right), \quad (5.50)$$

where r is a uniformly distributed random number, $r \in [0, 1]$.

In this section we have introduced an extension of the unitary Lindblad master equation to a non-unitary generalized Lindblad master equation. This formalism enables us to describe open quantum systems that are open with respect to probability flux out of the system. We have presented a solution algorithm by means of an adapted quantum trajectory Monte Carlo method. In the following we show that the Monte Carlo technique solves the generalized non-unitary Lindblad master equation. First we discuss the analytical equivalence in the next section and close this chapter with a numerical test in section 5.4.4.

5.4.3 Analytical equivalence

In this section we briefly show the correspondence of the solution of the QTMC method with the solution of the Lindblad master equation. Our analysis applies to both the unitary and non-unitary QTMC method. The derivation below is done for the more general case of a non-unitary system. In the unitary case the difference between Γ^{P} and Γ^{PP} vanishes and H^{P} becomes H^{PP} . The Lindblad master equation is a relation for the time derivative of the density matrix. Therefore we consider the short time behavior of the QTMC method and show that it solves the Lindblad master equation.

The wavevector is propagated in time according to a time evolution operator $U^\eta(t_j, t_{j-1})$ from time t_{j-1} to t_j . We decompose the time evolution into a continuous part from time t_{j-1} to t_j and a discontinuous part with a jump at the time t_j . Then $U^\eta(t_j, t_{j-1})$ becomes

$$|\Psi^\eta(t_j)\rangle = U^\eta(t_j, t_{j-1}) |\Psi^\eta(t_{j-1})\rangle = U_{\text{jump}}^\eta(\vec{k}, t_j) U_{\text{cont}}^\eta(t_j, t_{j-1}) |\Psi^\eta(t_{j-1})\rangle \quad (5.51)$$

where η labels the stochastic realization. We define a variable $N_{\vec{k}}^{\eta}(t)$ that counts the number of jumps up to a time t for a given quantum trajectory η and index \vec{k} of the transition.

When we consider the time evolution of the wavefunction not for a time interval given by the jump time t_{j-1} and t_j , but for an infinitesimal short time δt we have

$$|\Psi^{\eta}(t + \delta t)\rangle = \left(\frac{1}{V} \sum_{\vec{k}} dN_{\vec{k}}^{\eta}(t + \delta t) U_{\text{jump}}^{\eta}(\vec{k}, t + \delta t) \right) U_{\text{cont}}^{\eta}(t + \delta t, t) |\Psi^{\eta}(t)\rangle + \left(1 - \frac{1}{V} \sum_{\vec{k}} dN_{\vec{k}}^{\eta}(t + \delta t) \right) U_{\text{cont}}^{\eta}(t + \delta t, t) |\Psi^{\eta}(t)\rangle \quad (5.52)$$

where the first term corresponds to the case when a jump happens in the time interval δt weighted with probabilities $V^{-1} dN_{\vec{k}}^{\eta}(t)$. The continuous time evolution operator is applied to the wave function first and afterwards the jump operator acts on the evolved quantum trajectory. When no jump happens (second term with the complementary probability of $1 - V^{-1} \sum_{\vec{k}} dN_{\vec{k}}^{\eta}(t)$) only the continuous time evolution contributes via $U_{\text{cont}}^{\eta}(t + \delta t, t)$.

For an infinitesimally short time interval δt we set in the argument of the Ito differential and the jump operator $t + \delta t \rightarrow t$. Since $U_{\text{cont}}^{\eta}(t + \delta t, t)$ is applied in both cases we can simplify (5.52) to

$$|\Psi^{\eta}(t + \delta t)\rangle = \left[1 + \frac{1}{V} \sum_{\vec{k}} dN_{\vec{k}}^{\eta}(t) \left(U_{\text{jump}}^{\eta}(\vec{k}, t) - 1 \right) \right] U_{\text{cont}}^{\eta}(t + \delta t, t) |\Psi^{\eta}(t)\rangle \quad (5.53)$$

We make the following ansatz for the continuous time evolution operator $U_{\text{cont}}^{\eta}(t + \delta t, t)$ as

$$U_{\text{cont}}^{\eta}(t + \delta t, t) |\Psi^{\eta}(t)\rangle = \frac{e^{-iH_{\text{eff}}^{\text{P}} \delta t} |\Psi^{\eta}(t)\rangle}{\left\| e^{-iH_{\text{eff}}^{\text{PP}} \delta t} |\Psi^{\eta}(t)\rangle \right\|}, \quad (5.54)$$

Since we are interested in the short time behavior we expand the exponentials in (5.54) using the Taylor series

$$e^{-iH_{\text{eff}}^{\text{PP}} dt} = 1 - iH_{\text{eff}}^{\text{PP}} dt + O(dt^2) \quad (5.55)$$

up to first order in dt leading to

$$U_{\text{cont}}^{\eta}(t + dt, t) |\Psi^{\eta}(t)\rangle = \frac{(1 - iH_{\text{eff}}^{\text{P}} dt) |\Psi^{\eta}(t)\rangle}{\left[\langle \Psi^{\eta}(t) | (1 + iH_{\text{eff}}^{\text{PP} \dagger} dt) (1 - iH_{\text{eff}}^{\text{PP}} dt) | \Psi^{\eta}(t) \rangle \right]^{1/2}}. \quad (5.56)$$

By inserting the definition of the effective Hamiltonian $H_{eff}^{\mathbb{P},\mathbb{P}\mathbb{P}} = H_S - \frac{i}{2}\Gamma^{\mathbb{P},\mathbb{P}\mathbb{P}}$ the denominator of Eq. (5.56) simplifies to $(\langle \Psi^\eta(t) | 1 - \Gamma^{\mathbb{P}\mathbb{P}} dt | \Psi^\eta(t) \rangle)^{1/2}$, so that we obtain in first order of dt

$$U_{\text{cont}}^\eta(t + \delta t, t) | \Psi^\eta(t) \rangle = \left[1 - iH_S \delta t - \frac{\delta t}{2} (\Gamma^{\mathbb{P}} - \langle \Gamma^{\mathbb{P}\mathbb{P}} \rangle_{t,\eta}) \right] | \Psi^\eta(t) \rangle, \quad (5.57)$$

using the definition of the expectation value as

$$\langle \Gamma^{\mathbb{P}\mathbb{P}} \rangle_{t,\eta} = \frac{\langle \Psi^\eta(t) | \Gamma^{\mathbb{P}\mathbb{P}}(t) | \Psi^\eta(t) \rangle}{\langle \Psi^\eta(t) | \Psi^\eta(t) \rangle} = \frac{\langle \Psi^\eta(t) | \Gamma^{\mathbb{P}\mathbb{P}} | \Psi^\eta(t) \rangle}{\| \Psi^\eta(t) \|^2} \quad (5.58)$$

omitting all higher order terms on δt .

We insert the explicit form of $U_{\text{cont}}^\eta(t + dt, t)$ from equation (5.57) into equation (5.53). By considering the differential change of the wave function as $|d\Psi^\eta(t)\rangle = -|\Psi^\eta(t)\rangle + |\Psi^\eta(t + \delta t)\rangle$ we obtain

$$|d\Psi^\eta(t)\rangle = \left[-iH_S dt - \frac{dt}{2} (\Gamma^{\mathbb{P}} - \langle \Gamma^{\mathbb{P}\mathbb{P}} \rangle_{t,\eta}) + \frac{1}{V} \sum_{\vec{k}} dN_{\vec{k}}^\eta(t) (U_{\text{jump}}^\eta(\vec{k}, t) - 1) \right] | \Psi^\eta(t) \rangle. \quad (5.59)$$

All terms proportional to $dN_{\vec{k}}^\eta(t)dt$ vanish to first order in dt when we take the average over all stochastic realizations of a quantum trajectory. Also the product of two Ito differentials for the same time is $\overline{dN_{\vec{k}}^\eta(t)dN_{\vec{k}'}^\eta(t)} = \overline{dN_{\vec{k}}^\eta(t)}\delta_{\vec{k},\vec{k}'}$ because only one jump can occur in an infinitesimal short time interval dt .

For the jump operator we make the following ansatz

$$U_{\text{jump}}^\eta(\vec{k}, t) | \Psi^\eta(t) \rangle = \| \Psi^\eta(t) \| \frac{S^{\mathbb{P}}(\vec{k}) | \Psi^\eta(t) \rangle}{\| S^{\mathbb{P}}(\vec{k}) | \Psi^\eta(t) \rangle \|} \quad (5.60)$$

leading directly to the NLSSE

$$|d\Psi^\eta(t)\rangle = \left\{ -iH_S^\mathbb{P} dt - \frac{dt}{2} (\Gamma^{\mathbb{P}} - \langle \Gamma^{\mathbb{P}\mathbb{P}} \rangle_{t,\eta}) + \frac{1}{V} \sum_{\vec{k}} dN_{\vec{k}}^\eta(t) \left(\frac{S^{\mathbb{P}}(\vec{k})}{\sqrt{\langle \Gamma^{\mathbb{P}\mathbb{P}}(\vec{k}) \rangle_{t,\eta}}} - 1 \right) \right\} | \Psi^\eta \rangle. \quad (5.61)$$

Finally, the differential change of the reduced density matrix for a stochastic realization $d\sigma^\eta(t) = |d\Psi^\eta(t)\rangle\langle d\Psi^\eta(t)|$ is given by

$$d\sigma^\eta(t) = -i[H_S, \sigma^\eta(t)]dt + \frac{dt}{2} [\Gamma^{\mathbb{P}}, \sigma^\eta(t)]_+ + \langle \Gamma^{\mathbb{P}\mathbb{P}} \rangle_{t,\eta} \sigma^\eta(t) dt + \frac{1}{V} \sum_{\vec{k}} dN_{\vec{k}}^\eta(t) \left(\langle \Gamma_{\vec{k}}^{\mathbb{P}\mathbb{P}} \rangle_{t,\eta}^{-1} S^{\mathbb{P}}(\vec{k}) \sigma^\eta(t) S^{\mathbb{P}\dagger}(\vec{k}) - \sigma^\eta(t) \right).$$

With the ansatz for the averaged Ito differential

$$\overline{dN_{\vec{k}}^\eta(t)} = dt \langle \Gamma^{\mathbb{P}\mathbb{P}}(\vec{k}) \rangle_{t,\eta} \quad (5.62)$$

we relate the average time between two stochastic quantum jumps to the expectation value of the decay operator. Using this definition for an ensemble of stochastic realizations $\sigma(t) = N_{traj}^{-1} \sum_{\eta=1}^{N_{traj}} \sigma^\eta(t)$ we directly obtain the generalized Lindblad form of the master equation

$$\frac{d\sigma(t)}{dt} = -i[H_S, \sigma(t)] + \frac{1}{2} [\Gamma^{\mathbb{P}}, \sigma(t)]_+ + \frac{1}{V} \sum_{\vec{k}} S^{\mathbb{P}}(\vec{k}) \sigma(t) S^{\mathbb{P}\dagger}(\vec{k}). \quad (5.63)$$

The equivalence of equation (5.42) and equation (5.63) shows that the QTMC method solves the Lindblad master equation.

5.4.4 Test case: radiative cascade as sink

In this section we illustrate accuracy of the non-unitary QTMC method in comparison with an exactly solvable model problem: the multilevel time evolution of an excited hydrogenic atom subject to spontaneous radiative decay. Since spontaneous decay leads only to transitions to lower lying levels (unlike collisional excitation) truncation of the bound-state Hilbert space does not introduce errors and thus allows for an exact solution by directly integrating the Lindblad equation.

We consider a highly charged hydrogenic ion, Kr^{35+} , in the vacuum. The only interaction with the environment is the coupling to the vacuum fluctuations of the radiation field manifesting itself in two ways: the coupling driven by this interaction is the spontaneous radiative decay of the electron from an excited state and also the modification of the eigenenergies of the system by the Lamb shift [Bra83, Joh85]. Since radiative decay is an exothermic process, i.e. the final state energy of the electron is always below its initial energy, the Hilbert space necessary for a representation of all possible final states is restricted. For example, the time evolution of an electron initially

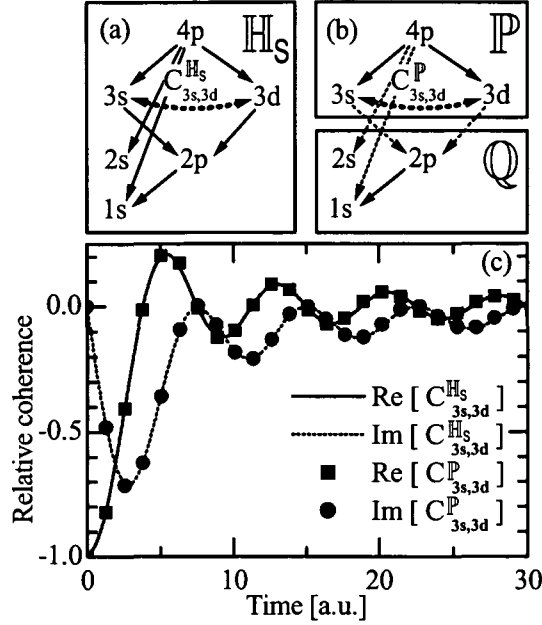


Figure 5.4: Test model for a free Kr^{35+} ion under the influence of radiative decay only. (a) Full Hilbert space \mathbb{H}_S with the initial state 4p. (b) Decomposition into the subspace \mathbb{P} and the complement \mathbb{Q} . (c) Comparison of the real and imaginary parts of the relative coherence between the $3s_{\frac{1}{2},\frac{1}{2}}$ and the $3d_{\frac{3}{2},\frac{1}{2}}$ states calculated exactly for the entire Hilbert space \mathbb{H}_S ($C_{3s,3d}^{\mathbb{H}_S}$) and using the non-unitary reduction for the subspace \mathbb{P} ($C_{3s,3d}^{\mathbb{P}}$).

in the 4p state is completely represented in the Hilbert space covering the first four shells of the electronic states rendering the unitary system within a finite Hilbert space \mathbb{H}_S , as is schematically shown in Fig. 5.4a.

We can now test the non-unitary QTMC evolution by arbitrarily dividing this finite system into two subspaces consisting, e.g., of the third and fourth shells representing \mathbb{P} containing the initial state 4p (Fig. 5.4b). Accordingly, the complement \mathbb{Q} contains the first and second shells. This system features now a net flux from \mathbb{P} to \mathbb{Q} (e.g. by a direct Ly_γ transition or a radiative cascade) and is thus open with respect to probability flux. Moreover, there is no probability flowing back from the energetically lower lying complement \mathbb{Q} to the subspace \mathbb{P} . Therefore, for this model system, a properly constructed non-unitary QTMC should exactly reproduce the results from the full unitary simulation of the whole system for any observables in \mathbb{P} .

Using the dipole approximation $\langle \alpha | \vec{\nabla}_{\vec{r}} | \beta \rangle = \omega_{\beta\alpha} \langle \alpha | \vec{r} | \beta \rangle$ with $\omega_{\beta\alpha} = \omega_\beta -$

ω_α we obtain the transition operator S for the radiative (r) decay as

$$S_{\alpha\beta}^{(r)}(\mathfrak{J}) = \frac{2}{\sqrt{3c^3}} \omega_{\beta\alpha}^{3/2} \langle \alpha | r_{\mathfrak{J}} | \beta \rangle \theta(\omega_{\beta\alpha}), \quad (5.64)$$

where the index \mathfrak{J} indicates the polarization of the emitted photon. The unperturbed Hamiltonian of the system including relativistic corrections is

$$H_S = -\nabla_{\vec{r}}^2/2 - Z_p/r + \Delta H_{rel} \quad (5.65)$$

where ΔH_{rel} represents relativistic and Lamb shift corrections. The transition operator $S_{\alpha\beta}^{(r)}(\mathfrak{J})$ is defined in the entire Hilbert space \mathbb{H}_S of the electronic states of a hydrogenic atom. By allowing the state indices α and β to cover only the subspace \mathbb{P} we obtain $S_{\alpha\beta}^{(r)\mathbb{P}}(\mathfrak{J}) = S_{\alpha\beta}^{(r)}(\mathfrak{J})$. The construction of the decay operators is straightforward,

$$\Gamma_{\alpha\beta}^{\mathbb{P}\mathbb{P}} = \sum_{\nu \in \mathbb{P}} \sum_{\mathfrak{J}} S_{\alpha\nu}^{(r)\dagger}(\mathfrak{J}) S_{\nu\beta}^{(r)}(\mathfrak{J}) \quad (5.66)$$

considering only transitions within the subspace \mathbb{P} . The decay operator accounting for the loss is

$$\Gamma_{\alpha\beta}^{\mathbb{P}} = \sum_{\gamma \in (\mathbb{P} \oplus \mathbb{Q})} \sum_{\mathfrak{J}} S_{\alpha\gamma}^{(r)\dagger}(\mathfrak{J}) S_{\gamma\beta}^{(r)}(\mathfrak{J}) \quad (5.67)$$

where the complete Hilbert space $\mathbb{H}_S = \mathbb{P} \oplus \mathbb{Q}$ is represented as a direct sum over the subspace \mathbb{P} and the complement \mathbb{Q} . The sum of the state index γ over the subspace \mathbb{P} corresponds to $\Gamma^{\mathbb{P}\mathbb{P}}$ as defined in the previous equation (5.67) while the sum over the complement \mathbb{Q} remains as

$$\Gamma_{\alpha\beta}^{\mathbb{P}} = \Gamma_{\alpha\beta}^{\mathbb{P}\mathbb{P}} + \sum_{\gamma \in \mathbb{Q}} \sum_{\mathfrak{J}} S_{\alpha\gamma}^{(r)\dagger}(\mathfrak{J}) S_{\gamma\beta}^{(r)}(\mathfrak{J}). \quad (5.68)$$

The unique feature of this test system is that the sum over \mathbb{Q} extends over a small number of states and therefore can be performed without further approximation. On the contrary, for an ion in a collisional environment collisions couple to higher excited states and to the continuum. In the latter case, the sum over γ (states in \mathbb{Q}) has an infinite number of terms. Approximating this sum introduces an additional source of discrepancies which is not the case for the present system using radiative decay.

In Figure 5.4(c) we show the time evolution of the reduced density matrix starting initially from a 4p state. A remarkable and often overlooked aspect of the radiative decay is that unless the wave packet is projected, i.e. a measurement is taken to determine the state of the emitted photon, the

spontaneous decay generates a partially coherent superposition of states. The relative coherence depicted in Fig. 5.4(c) is defined by

$$C_{\alpha\beta}(t) = \frac{\sigma_{\alpha\beta}(t)}{\sqrt{\sigma_{\alpha\alpha}(t)\sigma_{\beta\beta}(t)}} \quad (5.69)$$

for $\alpha=3s_{\frac{1}{2},\frac{1}{2}}$ and $\beta=3d_{\frac{3}{2},\frac{1}{2}}$. Because of $|\sigma_{\alpha\beta}| \leq \sqrt{\sigma_{\alpha\alpha}\sigma_{\beta\beta}}$, the absolute magnitude of the relative coherence, $|C_{\alpha\beta}|$, takes values in the interval $0 \leq |C_{\alpha\beta}| \leq 1$. $|C_{\alpha\beta}| = 1$ if the system is in a pure state while relative coherences smaller than one imply that the system is in a partially coherent state.

The near-perfect agreement between the exact result calculated in \mathbb{H}_S and the one calculated with the non-unitary QTMC method employing the split into the \mathbb{P} and \mathbb{Q} subspaces demonstrates the validity of the non-unitary dynamics in \mathbb{P} . Clearly this level of agreement is, in part, due to the fact that the back-coupling from \mathbb{Q} to \mathbb{P} , which is neglected in our approach, vanishes exactly in this problem.

5.5 Alternative solution

5.5.1 Solving quantum master equation directly

Alternative the Lindblad master equation can be solved directly. When we consider a system with N_S eigenstates, the direct solution of the full master equation scales with N_S^4 . For a projectile in transport through a solid with typically $N_S \approx 10^2$ necessary the direct solution is infeasible. However, when using a limited set of couplings a numerical solution is feasible. Recently this method was adopted for ion-solid transport [Ver01] calling this approach the master equation approach (MEA). The collisional transition rates are calculated in plane-wave first Born approximation (PWBA) thus adopting a quasi-free electron approximation. The effect of the wake field is described within the approximation provided by Ponce [Roz99] shown in equation (3.34). Convergence is reached for calculations involving all sub states up to $n=6$. Electron capture cross section are obtained by CDW calculations 3.4.2. This method shows good agreement with experimental findings for the transport of highly charged ions through carbon foils [Ver01].

5.5.2 Lindblad master equation for quasi-free electrons

When considering electrons in the continuum or in highly excited Rydberg states the open quantum system approach can be significantly simplified. The energy difference between two states ω_{ij} becomes small compared to the

Doppler shift $k_z v_p$. Setting ω_{ij} to zero in the calculation of the transition operators leads to

$$S_{ij}(\vec{k}) = \sqrt{\chi''(\vec{k}, -k_z v_p)} \tilde{V}_c(\vec{k}) \langle i | e^{i\vec{k}\cdot\vec{r}} | j \rangle \quad (5.70)$$

where the imaginary part of the susceptibility is state independent. The decay operator is then

$$\Gamma_{ij} = \int d^3k \chi''(\vec{k}, -k_z v_p) \left| \tilde{V}_c(\vec{k}) \right|^2 \sum_{\mu} \langle i | e^{-i\vec{k}\cdot\vec{r}} | \mu \rangle \langle \mu | e^{i\vec{k}\cdot\vec{r}} | j \rangle \quad (5.71)$$

where the sum over μ is 1 for $i=j$ and vanishes else.

The non-linear stochastic Schrödinger equation in (5.17) reduces in this limit to a linear stochastic Schrödinger equation (LSSE). In previous quantum transport theories [Arb99, Arb00, Min02a, Min02b] the LSSE was solved by means of a QTMC method.

5.6 Summary

We have presented an extension of the standard unitary Lindblad formalism by considering only a subspace of the system Hilbert space by excluding parts of it as the complement. The dynamics is modified by this projection in a way that it does not apply to the complement any more but still probability flux into the complement is accounted for. An analytical equivalence of the quantum trajectory Monte Carlo solution of the dynamics could be shown.

A prerequisite for an exact equivalence of the solution is the knowledge of the decay operator $\Gamma^{\mathbb{P}}$ that contains also contributions from transitions from \mathbb{P} to \mathbb{Q} . We could demonstrate the accuracy of the numerical solution for a system where $\Gamma^{\mathbb{P}}$ can be calculated, in a certain approximation, exactly. We point out that for an ion in a collisionary environment an infinite number of $\mathbb{P} \rightarrow \mathbb{Q}$ transitions exist and that additional approximations are required in order to evaluate $\Gamma^{\mathbb{P}}$ in equation (5.41b). Before applying the method on ion-solid transport we discuss these approximations in the next chapter.

Chapter 6

Collisional decay operators for non-unitary approach

6.1 Introduction

In the last chapter we have introduced a Lindblad master equation where the probability is not confined in the simulated subspace. In a first application we tested the method for a radiative cascade (section 5.4.4). The comparison with the exact solution confirmed the validity of the non-unitary approach. The non-unitary Lindblad master equation could describe the problem exactly only because the transition operators describing the probability flux out of the subspace are exactly known.

The decay operator for a non-unitary system is according to (5.41b) is given by

$$\Gamma^{\mathbb{P}} = \frac{1}{V} \sum_{\vec{k}} P^{\mathbb{P}} S^{\dagger}(\vec{k}) S(\vec{k}) P^{\mathbb{P}} = \frac{1}{V} \sum_{\vec{k}} \Gamma^{\mathbb{P}}(\vec{k}), \quad (6.1)$$

defining $\Gamma^{\mathbb{P}}(\vec{k})$ as

$$\Gamma_{\alpha\beta}^{\mathbb{P}}(\vec{k}) = \sum_{\mu \in (\mathbb{P} \oplus \mathbb{Q})} S_{\alpha\mu}^{\dagger}(\vec{k}) S_{\mu\beta}(\vec{k}) = \Gamma_{\alpha\beta}^{\mathbb{P}\mathbb{P}}(\vec{k}) + \Gamma_{\alpha\beta}^{\mathbb{P}\mathbb{Q}}(\vec{k}) \quad (6.2)$$

where $\alpha, \beta \in \mathbb{P}$. Probability flux outwards is described by the decay operator for loss

$$\Gamma_{\alpha\beta}^{\mathbb{P}\mathbb{Q}}(\vec{k}) = \sum_{\mu \in \mathbb{Q}} S_{\alpha\mu}^{\dagger}(\vec{k}) S_{\mu\beta}(\vec{k}). \quad (6.3)$$

The evaluation of $\Gamma_{\alpha\beta}^{\mathbb{P}\mathbb{Q}}(\vec{k})$ contains a sum over states in the complement \mathbb{Q} . For the radiative cascade (section 5.4.4) this sum could be evaluated without

any further approximation. For collisions the situation is different. Since the number of degrees of freedom in \mathbb{Q} is infinite for an ion in a collisional environment, we have to make an additional approximation when calculating $\Gamma^{\mathbb{P}\mathbb{Q}}$.

In section 3.2 we have described the construction of the transition operator S for the collisional environments, namely $S^{(c)}$ for core collisions (3.15) and $S^{(e)}$ for electron-electron interaction (3.25). In the present chapter we perform the calculation of $\Gamma^{\mathbb{P}\mathbb{Q}}$ for these interactions. The result will complete the non-unitary QTMC method enabling us to perform numerical calculations of ion-solid transport (chapter 7).

6.2 Electron-core collisions

In section 3.2.1 we have calculated the cross sections for core scattering. The Lindblad transition operator for the interaction with the reservoir of screened ionic cores of the solid (3.15) was found to be

$$S_{\alpha\beta}^{(c)}(\vec{k}_\perp) = \sqrt{\frac{2\pi n_A}{v_p}} \tilde{V}_c \left(\vec{k}_\perp + \hat{z} \frac{\omega_{\beta\alpha}}{v_p} \right) \langle \alpha | e^{i(\vec{k}_\perp + \hat{z} \frac{\omega_{\beta\alpha}}{v_p}) \cdot \vec{r}} | \beta \rangle \quad (6.4)$$

with the number density n_A of the ions in the solid and the Fourier transform of the screened Coulomb potential

$$V_c(\vec{r}) = -(Z_T/r)e^{-r/a_{TF}} \quad \text{as} \quad \tilde{V}_c(\vec{k}) = -(4\pi Z_T)/(k^2 + a_{TF}^{-2}) \quad (6.5)$$

with the Thomas-Fermi screening length $a_{TF} = 0.885 Z_T^{-1/3}$ and the nuclear charge of the target atoms Z_T . The component of momentum transfer parallel to the projectile velocity, k_z , is fixed by the requirement $\omega_{\beta\alpha} = \vec{k} \cdot \vec{v}_p$, while the component \vec{k}_\perp specifies the perpendicular momentum transferred.

The transition operator $S^{(c)}$ (equation (6.4)) can be expressed in the form

$$S_{\alpha\beta}^{(c)}(\vec{k}_\perp) = f^{(c)}(\omega_{\beta\alpha}, \vec{k}_\perp) \langle \alpha | e^{i(\vec{k}_\perp + \hat{z} \frac{\omega_{\beta\alpha}}{v_p}) \cdot \vec{r}} | \beta \rangle \quad (6.6)$$

with the prefactor $f^{(c)}(\omega_{\beta\alpha}, \vec{k}_\perp)$ given by equation (6.4). This factorization of $S^{(c)}$ will be used below. The decay operator for loss in core collisions (6.3) is

$$\Gamma_{\alpha\beta}^{(c)\mathbb{P}\mathbb{Q}}(\vec{k}_\perp) = \sum_{\mu \in \mathbb{Q}} S_{\alpha\mu}^{(c)\dagger}(\vec{k}_\perp) S_{\mu\beta}^{(c)}(\vec{k}_\perp), \quad (6.7)$$

where the states α and β are elements of \mathbb{P} .

6.2.1 Closure approximation

For the further evaluation of equation (6.7) we employ the approximate factorization (equation (6.6))

$$\Gamma_{\alpha\beta}^{(c)\mathbb{P}\mathbb{Q}}(\vec{k}_\perp) \simeq f^{(c)*}(\bar{\omega}_\alpha, \vec{k}_\perp) f^{(c)}(\bar{\omega}_\beta, \vec{k}_\perp) \sum_{\mu \in \mathbb{Q}} \langle \alpha | e^{-i\vec{k}_\alpha(\vec{k}_\perp) \cdot \vec{r}} | \mu \rangle \langle \mu | e^{i\vec{k}_\beta(\vec{k}_\perp) \cdot \vec{r}} | \beta \rangle \quad (6.8)$$

with $\vec{k}_\alpha(\vec{k}_\perp) = \vec{k}_\perp + \hat{z}\bar{\omega}_\alpha/v_p$ and $\vec{k}_\beta(\vec{k}_\perp) = \vec{k}_\perp + \hat{z}\bar{\omega}_\beta/v_p$ where we have approximated the energy transfer $\omega_{\alpha\mu}$ ($\omega_{\beta\mu}$) by an average excitation energy $\bar{\omega}_\alpha$ ($\bar{\omega}_\beta$) independent of the state μ . The latter is a prerequisite for using the closure relation

$$\sum_{\mu \in \mathbb{H}_S} \langle \alpha | e^{-i\vec{k}_\alpha(\vec{k}_\perp) \cdot \vec{r}} | \mu \rangle \langle \mu | e^{i\vec{k}_\alpha(\vec{k}_\perp) \cdot \vec{r}} | \beta \rangle = \delta_{\alpha\beta} . \quad (6.9)$$

Consequently, we obtain the decay operator for loss $\Gamma^{\mathbb{P}\mathbb{Q}}$

$$\Gamma_{\alpha\beta}^{(c)\mathbb{P}\mathbb{Q}}(\vec{k}_\perp) \simeq |f^{(c)}(\bar{\omega}_\alpha, \vec{k}_\perp)|^2 \times \left(\delta_{\alpha\beta} - \sum_{\mu \in \mathbb{P}} \langle \alpha | e^{-i\vec{k}_\alpha(\vec{k}_\perp) \cdot \vec{r}} | \mu \rangle \langle \mu | e^{i\vec{k}_\alpha(\vec{k}_\perp) \cdot \vec{r}} | \beta \rangle \right) \quad (6.10)$$

valid for all diagonal elements ($\alpha=\beta$) and the most important subset of off-diagonal elements $\alpha \neq \beta$ between nearly degenerate states with $\omega_\alpha = \omega_\beta$, $\bar{\omega}_\alpha = \bar{\omega}_\beta$ and consequently $\vec{k}_\alpha(\vec{k}_\perp) = \vec{k}_\beta(\vec{k}_\perp)$.

With the closure approximation (6.9) we reduce the infinite sum over the complement \mathbb{Q} in (6.7) to sums in the finite Hilbert subspace \mathbb{P} of the system. The price we have to pay is the approximation of the energy transfer $\omega_{\alpha\mu}$ ($\omega_{\beta\mu}$) by an average excitation energy $\bar{\omega}_\alpha$ ($\bar{\omega}_\beta$) so that the prefactor can be pulled out of the sum over $\mu \in \mathbb{Q}$ in equation (6.8). A proper choice of $\bar{\omega}_\alpha$ ($\bar{\omega}_\beta$) determines significantly the quality of the closure approximation for $\Gamma^{(c)\mathbb{P}}(\vec{k}_\perp)$. For fast collisional excitations in a solid it has been shown [Ino71] that the generalized oscillator strength distribution (“Bethe ridge”) peaks around the ionization threshold, i.e. a highly excited state or a low-lying continuum state. These considerations suggest the choice of the ionization energy for the average excitation energy

$$\bar{\omega}_\alpha = \epsilon_\alpha \quad (6.11)$$

implying $\omega_\mu \rightarrow 0$.

6.2.2 Decay rates

The total decay matrix for loss $\Gamma_{\alpha\beta}^{(c)\text{PQ}}$ is obtained from equation (6.10) by the integration over all possible perpendicular momentum transfers \vec{k}_\perp as

$$\Gamma_{\alpha\beta}^{(c)\text{PQ}} = \frac{1}{(2\pi)^3} \int d^2 k_\perp \Gamma_{\alpha\beta}^{(c)\text{PQ}}(\vec{k}_\perp) = D_\alpha^{(c)} \delta_{\alpha\beta} - M_{\alpha\beta}^{(c)}, \quad (6.12)$$

while the parallel component k_z is fixed according to equation (6.4). We label the integral over the second term in equation 6.10 as

$$M_{\alpha\beta}^{(c)} = \int d^2 k_\perp |f^{(c)}(\bar{\omega}_\alpha, \vec{k}_\perp)|^2 \sum_{\mu \in \mathbb{P}} \langle \alpha | e^{-i\vec{k}_\alpha(\vec{k}_\perp) \cdot \vec{r}} | \mu \rangle \langle \mu | e^{i\vec{k}_\alpha(\vec{k}_\perp) \cdot \vec{r}} | \beta \rangle, \quad (6.13)$$

while we denote the integration over the first term in equation (6.10) by

$$D_\alpha^{(c)} = \frac{1}{(2\pi)^3} \int d^2 k_\perp |f^{(c)}(\bar{\omega}_\alpha, \vec{k}_\perp)|^2, \quad (6.14)$$

which depends only on the state index α because of the Kronecker-delta function $\delta_{\alpha\beta}$. After inserting $f^{(c)}$ from (6.4) we have to solve the integral

$$D_\alpha^{(c)} = \frac{4n_A Z_T^2}{v_p} \int_0^\infty dk_\perp k_\perp \left(k_\perp^2 + \left(\frac{\bar{\omega}_\alpha}{v_p} \right)^2 + a_{TF}^{-2} \right)^{-2} \int_0^{2\pi} d\phi_k, \quad (6.15)$$

where the ϕ_k integration gives an additional factor of 2π and only a one-dimensional integration remains. This integration can be solved analytically according to reference [Bro97] so that (6.15) reduces to

$$D_\alpha^{(c)} = \frac{4\pi n_A Z_T^2}{\frac{\bar{\omega}_\alpha^2}{v_p} + v_p a_{TF}^{-2}}. \quad (6.16)$$

The only state dependence of $D_\alpha^{(c)}$ is contained in $\bar{\omega}_\alpha$. Taking $\bar{\omega}_\alpha = \epsilon_\alpha$ in equation (6.11) means that $\bar{\omega}_\alpha$ is mainly determined by the shell-energy $\epsilon_\alpha = -Z_p^2/(2n^2)$ whereas other corrections (discussed in section 3.1) are relatively small and therefore can be neglected in the calculation of $D_\alpha^{(c)}$. Hence $D_\alpha^{(c)}$ is only a function of the shell n . In table 6.1 we have summarized values of $D_\alpha^{(c)}$ for the two collision systems considered in this work. For deeply bound states the correction is small and saturates for highly excited states. As we will see in section 3.2.1, the expression for $D_\alpha^{(c)}$ for $\bar{\omega}_\alpha \rightarrow 0$ is the same as for the decay rate in the limit of quasi-free electron scattering.

	Ar ¹⁸⁺ , $v_p=23$ a.u.	Kr ³⁵⁺ , $v_p=47$ a.u.
n=1	5.36×10^{-3}	7.26×10^{-4}
n=2	3.94×10^{-2}	8.76×10^{-3}
n=3	5.97×10^{-2}	2.15×10^{-2}
n=4	6.54×10^{-2}	2.85×10^{-2}
$n \rightarrow \infty$	6.84×10^{-2}	3.35×10^{-2}

Table 6.1: Values of $D_\alpha^{(c)}$ calculated according to equation (6.16) as a function of principal quantum number n with $\omega_\alpha = -Z_p^2/(2n^2)$ for the two relevant collision systems, namely Ar¹⁸⁺ ($v_p=23$ a.u.) and Kr³⁵⁺ ($v_p=47$ a.u.) on amorphous carbon. To obtain the value for $n \rightarrow \infty$ we set $\bar{\omega}_\alpha = 0$ in equation (6.16).

Next we consider the second term $M_{\alpha\beta}^{(c)}$ in the decay operator for loss 6.12. By transforming it into polar coordinates and considering the ϕ_k dependence of the boost operator (see section 3.3) we see that the ϕ_k -integration yields $2\pi\delta_{m_\alpha, m_\beta}$ (see equation (3.41)). The integral we have to solve can be written as

$$M_{\alpha\beta}^{(c)} = \frac{8\pi n_A Z_T^2}{v_p} \int_0^\infty dk_\perp k_\perp \left(k_\perp^2 + \left(\frac{\bar{\omega}_\alpha}{v_p} \right)^2 + a_{TF}^{-2} \right)^{-2} \times \sum_{\mu \in \mathbb{P}} \langle \alpha | e^{-i(k_\perp \hat{x} + \frac{\bar{\omega}_\alpha}{v_p} \hat{z}) \cdot \vec{r}} | \mu \rangle \langle \mu | e^{i(k_\perp \hat{x} + \frac{\bar{\omega}_\alpha}{v_p} \hat{z}) \cdot \vec{r}} | \beta \rangle. \quad (6.17)$$

The diagonal element $M_{\alpha\alpha}^{(c)}$ contains the elastic scattering in the term $\mu = \alpha$ which can be the dominant part of the sum. The Taylor expansion of diagonal elements of the boost

$$\langle \alpha | e^{ikr} | \alpha \rangle = \langle \alpha | 1 + ikr + O(k^2) | \alpha \rangle = 1 + O(k^2) \quad (6.18)$$

is 1 for small k . The second term, the dipole element is zero while higher order terms $\sim k^2$ provide the leading corrections. To first order the elastic component of $M_{\alpha\alpha}^{(c)}$ exactly cancels $D_\alpha^{(c)}$ (6.16) in (6.10) It is worth mentioning, that this is not a correction of the elastic component of core scattering in $\Gamma_{\alpha\alpha}^{(c)\text{PP}}$ because in the original sum in equation (6.7), that the closure relation approximates, an elastic term ($\mu = \alpha$) is not included. The only contribution to elastic scattering is contained in $\Gamma^{(c)\text{PP}}$ and is given by

$$\gamma_\alpha^{(c)} = \frac{1}{V} \int d^3k S_{\alpha\alpha}^\dagger(\vec{k}) S_{\alpha\alpha}(\vec{k}). \quad (6.19)$$

It is, as expected, not affected by the coupling to the complement \mathbb{Q} .

For off-diagonal elements between non-degenerate states ($\epsilon_\alpha \neq \epsilon_\beta$) we invoke the additional approximation that the degree of coherence $\Gamma_{\alpha\beta}^{(c)}/\sqrt{\Gamma_{\alpha\alpha}^{(c)}\Gamma_{\beta\beta}^{(c)}}$ is the same for $\Gamma_{\alpha\beta}^{(c)\mathbb{P}\mathbb{P}}$ and $\Gamma_{\alpha\beta}^{(c)\mathbb{P}}$. We thus calculate $\Gamma_{\alpha\beta}^{(c)\mathbb{P}}$ by rescaling $\Gamma_{\alpha\beta}^{(c)\mathbb{P}\mathbb{P}}$ for $\alpha \neq \beta$ as

$$\Gamma_{\alpha\beta}^{(c)\mathbb{P}} = \Gamma_{\alpha\beta}^{(c)\mathbb{P}\mathbb{P}} \sqrt{\frac{\Gamma_{\alpha\alpha}^{(c)\mathbb{P}}\Gamma_{\beta\beta}^{(c)\mathbb{P}}}{\Gamma_{\alpha\alpha}^{(c)\mathbb{P}\mathbb{P}}\Gamma_{\beta\beta}^{(c)\mathbb{P}\mathbb{P}}}}. \quad (6.20)$$

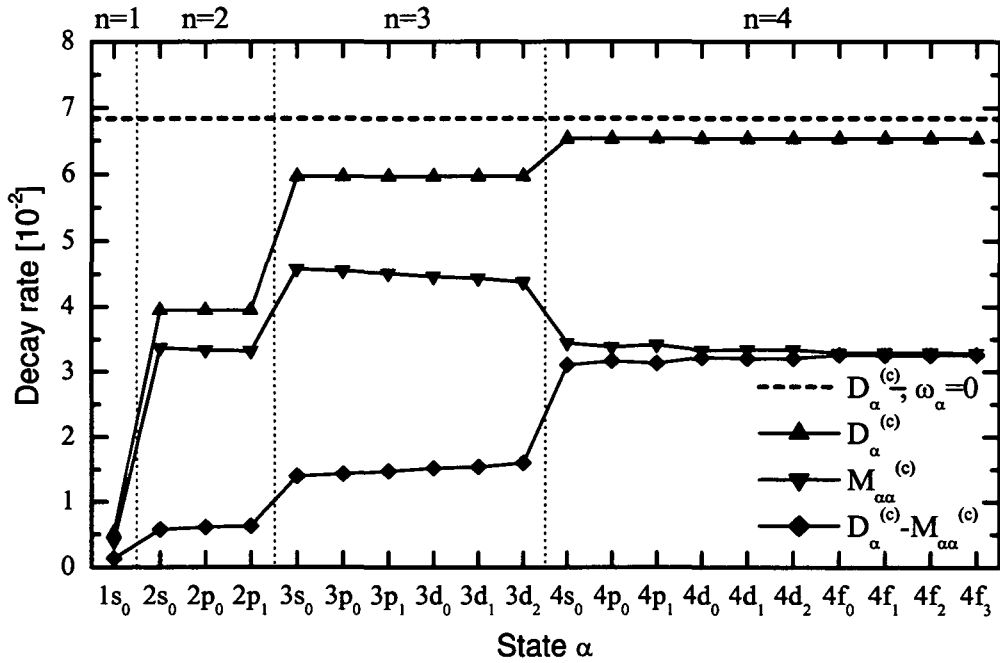


Figure 6.1: Correction terms to the closure approximation for different states within the subspace \mathbb{P} for core scattering of Ar^{17+} in carbon with $v_p = 23$ a.u.. The correction term $D_\alpha^{(c)}$ is calculated according to equation (6.16) (tabulated in table 6.1) while $M_{\alpha\alpha}^{(c)}$ is the result of numerical evaluation of the integral in equation (6.17). The overall correction $D_\alpha^{(c)} - M_{\alpha\alpha}^{(c)}$ is entering equation (6.12). We omit states with $m < 0$.

6.2.3 Numerical results for core collisions

In figure 6.1 we illustrate $D_\alpha^{(c)}$ and $M_{\alpha\alpha}^{(c)}$ for all $\alpha \in \mathbb{P}$ within the first four shells in the unperturbed n, l, m_l -basis. $D_\alpha^{(c)}$ exhibits a shell dependent step

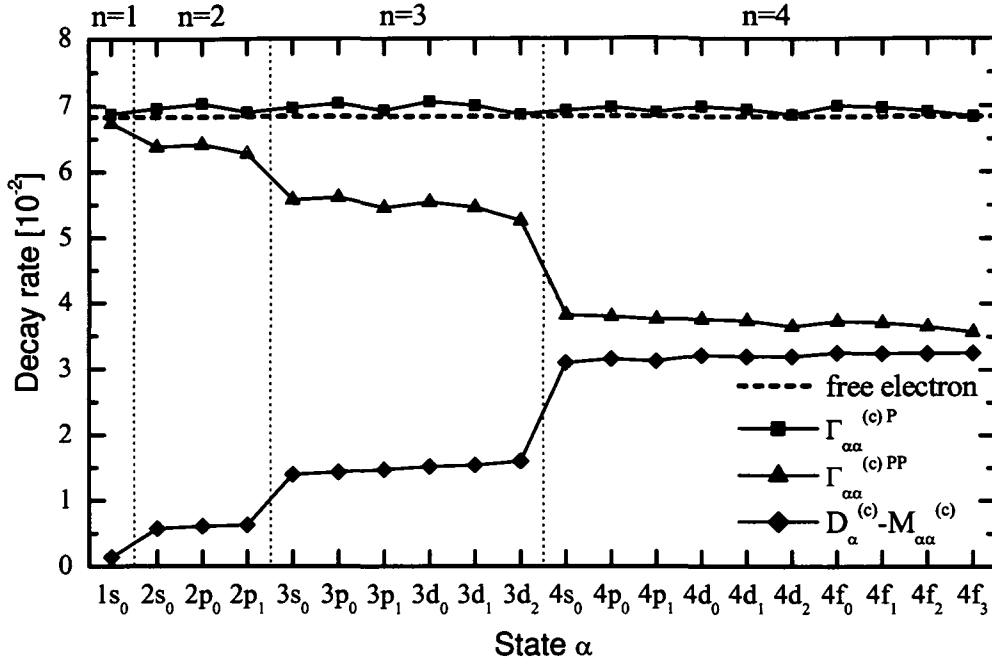


Figure 6.2: Decay rates for $\text{Ar}^{17+} \rightarrow \text{C}$ ($v_p = 23$ a.u.) as a function of state α ($m \geq 0$). $\Gamma_{\alpha\alpha}^{(c)\text{PP}}$ considers only transitions within \mathbb{P} while $\Gamma_{\alpha\alpha}^{(c)\text{P}}$ contains the correction ($D_{\alpha}^{(c)} - M_{\alpha\alpha}^{(c)}$) for flow of probability flux out of \mathbb{P} . The decay rate for free electrons (equation (6.21)) is shown for comparison.

structure as indicated in table 6.1. $M_{\alpha\alpha}^{(c)}$ shows large inter-shell variations and a smaller intra-shell state dependence. Since the interaction depends only on the magnitude of the angular momentum projection m , we do not show entries for $m < 0$ in the following figures. Figure 6.1 also shows the convergence of $D_{\alpha}^{(c)}$ towards the value for $\bar{\omega}_{\alpha} \rightarrow 0$ for higher principal quantum numbers n . For comparison the decay rate in the quasi-free electron limit obtained by

$$\Gamma_{\text{free}}^{(c)} = v_p \lambda_c^{-1} \quad (6.21)$$

from equation (3.18) is also displayed.

After having calculated the correction terms for the decay operator we can calculate $\Gamma_{\alpha\alpha}^{(c)\text{P}}$ by inserting the results for $D_{\alpha}^{(c)}$ (from equation (6.16)) and for $M_{\alpha\alpha}^{(c)}$ (from equation (6.17)) into equation (6.12). This step is visualized in figure 6.2 where we present the diagonal elements of $\Gamma_{\alpha\alpha}^{(c)\text{PP}}$ and $\Gamma_{\alpha\alpha}^{(c)\text{P}}$ with the correction term $D_{\alpha}^{(c)} - M_{\alpha\alpha}^{(c)}$. The decay rate $\Gamma_{\alpha\alpha}^{(c)\text{PP}}$ accounting for transitions within \mathbb{P} is lowest for states in the fourth shell while it is largest for those states resulting in a decay rate $\Gamma_{\alpha\alpha}^{(c)\text{P}}$ that is almost independent of the state

α . To be more precise, $\Gamma_{\alpha\alpha}^{(c)\mathbb{P}}$ resembles for all states $\alpha \in \mathbb{P}$ the value of the transition rate of a free electron under the same collision conditions

$$\Gamma_{\text{free}}^{(c)} \simeq \Gamma_{\alpha\alpha}^{(c)\mathbb{P}} \quad \forall \alpha \in \mathbb{P}. \quad (6.22)$$

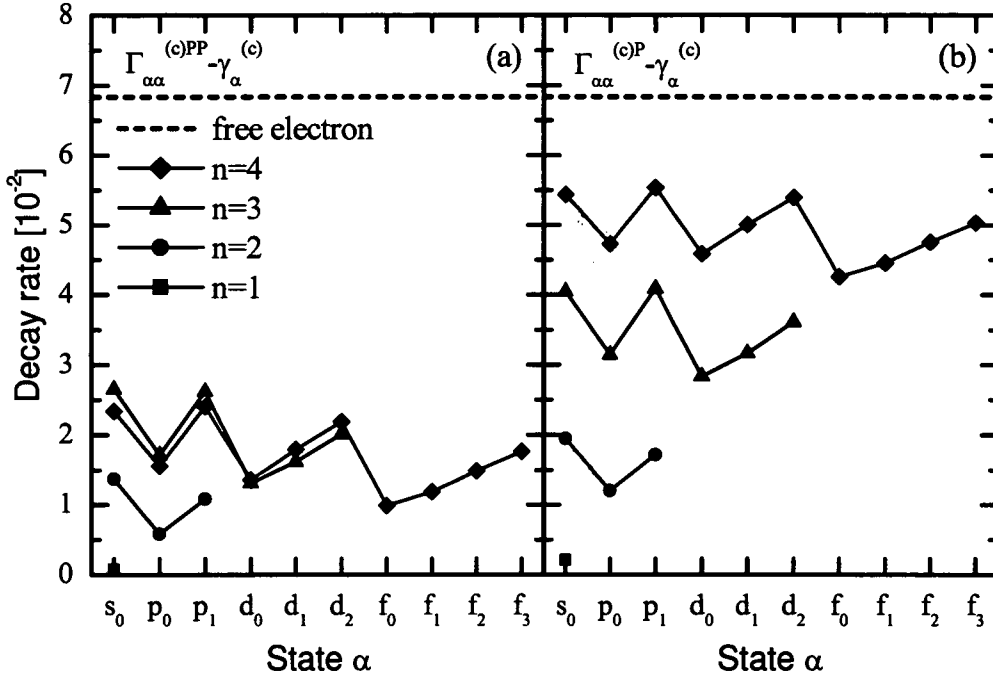


Figure 6.3: Decay rates for $\text{Ar}^{17+} \rightarrow \text{C}$ ($v_p = 23$ a.u.) as a function of intra-shell angular momentum states omitting the elastic component $\gamma_{\alpha}^{(c)}$ for the confined system ($\Gamma_{\alpha\alpha}^{(c)\mathbb{P}\mathbb{P}} - \gamma_{\alpha}^{(c)}$) and open system ($\Gamma_{\alpha\alpha}^{(c)\mathbb{P}} - \gamma_{\alpha}^{(c)}$) for principal quantum numbers $n = 1, 2, 3$ and 4 . For comparison the decay rate for free electrons (equation (6.21)) is also shown.

The small deviation from (6.22) is a measure for the accuracy of our calculation justifying the choice of an average excitation energy as $\bar{\omega}_{\alpha} = \epsilon_{\alpha}$ (see equation (6.11)). It is important to note that the result $\Gamma_{\text{free}}^{(c)} \simeq \Gamma_{\alpha\alpha}^{(c)\mathbb{P}}$ is valid for the complete decay operator $\Gamma_{\alpha\alpha}^{(c)\mathbb{P}}$ also containing the elastic component $\gamma_{\alpha}^{(c)}$ (as described in equation (6.19)) that accounts for transitions from the state α to itself. This elastic transition influences the phase and thus the coherence, but has no effect on transition probabilities to other states.

By subtracting the elastic component $\gamma_{\alpha}^{(c)}$ from $\Gamma_{\alpha\alpha}^{(c)\mathbb{P}\mathbb{P}}$ and $\Gamma_{\alpha\alpha}^{(c)\mathbb{P}}$ we obtain the decay rates of populations in the state α which are visualized in figure 6.3. The decay rates in the confined system for $n = 3$ and $n = 4$ are of the same

strength whereas $\Gamma_{\alpha\alpha}^{(c)\mathbb{P}} - \gamma_{\alpha}^{(c)}$ approaches the quasi-free electron limit for high principal quantum numbers n . The consequence for the time evolution of electron probability during transport is, that in the confined system the high shells ($n = 3, 4$) are depleted too slowly and we can expect to observe a pile-up of probability there. The intra-shell structure of variations of the decay rates is very similar for all shells while the overall magnitude is increasing with n . Another interesting point is that for a certain state (n, l) the decay rate increases linearly with m_l . This feature is reproduced in both systems.

6.2.4 Convergence for high n

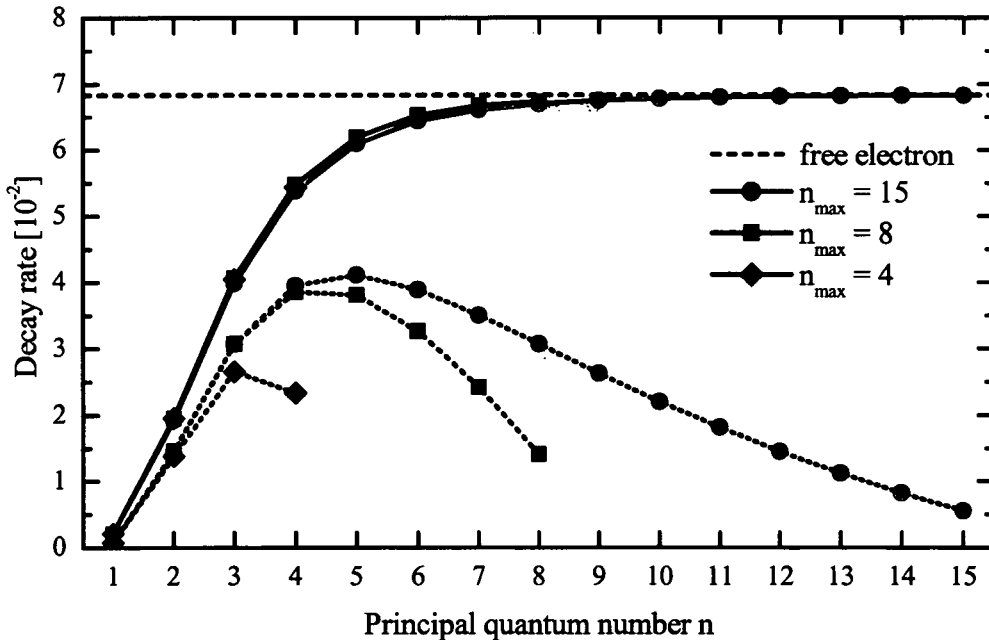


Figure 6.4: Decay rates of s-states for $\text{Ar}^{17+} \rightarrow \text{C}$ ($v_p = 23$ a.u.) as a function of shell n for different sizes (n_{max}) of the subspace \mathbb{P} . Dotted lines: confined system ($\Gamma_{\alpha\alpha}^{(c)\mathbb{P}\mathbb{P}} - \gamma_{\alpha}^{(c)}$); solid lines: open system ($\Gamma_{\alpha\alpha}^{(c)\mathbb{P}} - \gamma_{\alpha}^{(c)}$) accounting for loss to the complement \mathbb{Q} ; dashed line: quasi-free electron limit (equation (6.21))

In figure 6.4 we compare decay rates for core collisions up to a principal quantum number of $n_{max} = 15$. We depict only the s-states and subtract the elastic component $\gamma_{\alpha}^{(c)}$ such that we compare the decay rates governing the populations. Considering the decay rate within the confined system ($\Gamma_{\alpha\alpha}^{(c)\mathbb{P}\mathbb{P}} - \gamma_{\alpha}^{(c)}$) (dotted lines in figure 6.4) we observe a maximum around

$n = 5$. This is due to the fact that the momentum transfer distribution peaks around 1 a.u. (see section 3.2.1) with a vanishing probability for small momentum transfers making a collisional transfer between two near-degenerate states improbable. Considering the difference between $\Gamma_{\alpha\alpha}^{(c)\mathbb{P}\mathbb{P}} - \gamma_{\alpha}^{(c)}$ and $\Gamma_{\alpha\alpha}^{(c)\mathbb{P}} - \gamma_{\alpha}^{(c)}$ we see that a large fraction of deeply bound electrons scatters into the subspace \mathbb{P} while for higher excited electrons loss to the complement \mathbb{Q} becomes dominant. The fact that the effective decay rate $\Gamma_{\alpha\alpha}^{(c)\mathbb{P}} - \gamma_{\alpha}^{(c)}$ is identical for different sizes of the subspace \mathbb{P} indicates the accuracy of the numerical integration of the corrections $M_{\alpha\alpha}^{(c)}$.

6.3 Electron-electron collisions

In this section we turn to electron-electron (e-e) scattering. The Lindblad operator for the reservoir of quasi-free electrons was given in equation (3.25) by

$$S_{\alpha\beta}^{(e)}(\vec{k}) = \sqrt{\frac{8\pi}{k^2} \text{Im} \left[\frac{-1}{\varepsilon(k, \omega_{\beta\alpha} - \vec{k} \cdot \vec{v}_p)} \right]} \times \theta(\omega_{\beta\alpha} - \vec{k} \cdot \vec{v}_p) \langle \alpha | e^{i\vec{k} \cdot \vec{r}} | \beta \rangle \quad (6.23)$$

with the dielectric response function of the electron gas $\varepsilon(k, \omega)$ and the momentum \vec{k} transferred in the transition. Since the projectile moves with a velocity \vec{v}_p through the electron gas, the frequency spectrum of the response is Doppler shifted by $\vec{k} \cdot \vec{v}_p$ introducing a minimum energy transfer given by the step function θ in (6.23). The transition operator $S^{(e)}$ (equation (6.23)) can be expressed in the form

$$S_{\alpha\beta}^{(e)}(\vec{k}) = f^{(e)}(\omega_{\beta\alpha}, \vec{k}) \langle \alpha | e^{i\vec{k} \cdot \vec{r}} | \beta \rangle \quad (6.24)$$

with the prefactors $f^{(e)}(\omega_{\beta\alpha}, \vec{k})$ given by equation (6.23). The decay operator for loss in scattering at the electron gas is calculated as

$$\Gamma_{\alpha\beta}^{(e)\mathbb{P}\mathbb{Q}}(\vec{k}) = f^{(e)*}(\bar{\omega}_{\alpha}, \vec{k}) f^{(e)}(\bar{\omega}_{\beta}, \vec{k}) \sum_{\mu \in \mathbb{Q}} \langle \alpha | e^{-i\vec{k} \cdot \vec{r}} | \mu \rangle \langle \mu | e^{i\vec{k} \cdot \vec{r}} | \beta \rangle \quad (6.25)$$

with the transition operator $S_{\alpha\beta}^{(e)}(\vec{k})$ specified in (6.23). α and β denote states in \mathbb{P} .

	Ar ¹⁸⁺ , $v_p=23$ a.u.	Kr ³⁵⁺ , $v_p=47$ a.u.
n=1	5.33×10^{-4}	7.74×10^{-5}
n=2	7.65×10^{-3}	1.40×10^{-3}
n=3	2.01×10^{-2}	4.87×10^{-3}
n=4	3.18×10^{-2}	9.50×10^{-3}
n $\rightarrow \infty$	9.33×10^{-2}	5.67×10^{-2}

Table 6.2: Values of $D_\alpha^{(e)}$ calculated according to equation (6.30) as a function of principal quantum number n with $\omega_\alpha = -Z_p^2/(2n^2)$ for the two relevant projectiles in amorphous carbon. To obtain the value for $n \rightarrow \infty$ we set $\bar{\omega}_\alpha = 0$ in equation (6.30).

6.3.1 Closure approximation and decay rates

Unlike the corresponding equation for core collisions (6.8), the momentum transfers \vec{k} of the boost operators in (6.25) are identical in $\langle \alpha | e^{-i\vec{k}\cdot\vec{r}} | \mu \rangle$ and $\langle \mu | e^{i\vec{k}\cdot\vec{r}} | \beta \rangle$. Hence we can apply the closure approximation without restricting the resulting $\Gamma_{\alpha\beta}^{(e)\text{P}}(\vec{k})$ to near-degenerate states with $\epsilon_\alpha = \epsilon_\beta$ as for core scattering and obtain

$$\Gamma_{\alpha\beta}^{(e)\text{PQ}}(\vec{k}) \simeq f^{(e)*}(\bar{\omega}_\alpha, \vec{k}) f^{(e)}(\bar{\omega}_\beta, \vec{k}) \left(\delta_{\alpha\beta} - \sum_{\mu \in \text{P}} \langle \alpha | e^{-i\vec{k}\cdot\vec{r}} | \mu \rangle \langle \mu | e^{i\vec{k}\cdot\vec{r}} | \beta \rangle \right) \quad (6.26)$$

The total transition matrix for loss $\Gamma_{\alpha\beta}^{(e)\text{PQ}}$ is then obtained by the integration

$$\Gamma_{\alpha\beta}^{(e)\text{PQ}} = \frac{1}{(2\pi)^3} \int d^3k \Gamma_{\alpha\beta}^{(e)\text{PQ}}(\vec{k}) = D_\alpha^{(e)} \delta_{\alpha\beta} - M_{\alpha\beta}^{(e)} \quad (6.27)$$

without any further approximation. We label the integration over the first part of (6.26) as

$$D_\alpha^{(e)} = \int d^3k \left| f^{(e)}(\bar{\omega}_\alpha, \vec{k}) \right|^2 \quad (6.28)$$

and the second part as

$$M_{\alpha\beta}^{(e)} \int d^3k f^{(e)*}(\bar{\omega}_\alpha, \vec{k}) f^{(e)}(\bar{\omega}_\beta, \vec{k}) \sum_{\mu \in \text{P}} \langle \alpha | e^{-i\vec{k}\cdot\vec{r}} | \mu \rangle \langle \mu | e^{i\vec{k}\cdot\vec{r}} | \beta \rangle. \quad (6.29)$$

The θ -function in the transition operator $S^{(e)}$ in equation (6.23) restricts the component of the momentum transfer parallel to the projectile velocity to an upper limit of $k_z \leq \min(\bar{\omega}_\alpha, \bar{\omega}_\beta)/v_p$. The Doppler shift of the frequency

spectrum of the dielectric response function ε is due to the projectile motion that serves as a heat bath. This means that excitations of the target electron gas are driven to a large extent by the kinetic energy of the projectile rather than by the internal degrees of freedom of the projectile. Performing the integration in cylindrical coordinates the ϕ_k -integration for $D^{(e)}$ gives 2π and we have

$$D_{\alpha}^{(e)} = \frac{2}{\pi} \int_0^{\infty} dk_{\perp} k_{\perp} \int_{-\infty}^{\bar{\omega}_{\alpha}/v_p} dk_z \frac{1}{k_z^2 + k_{\perp}^2} \text{Im} \left(\frac{-1}{\varepsilon(\sqrt{k_z^2 + k_{\perp}^2}, \bar{\omega}_{\alpha} - k_z v_p)} \right). \quad (6.30)$$

Since the loss function $\text{Im}(-1/\varepsilon(k, \omega))$ is a bounded function, the integrand of (6.30) is also bounded and the two-dimensional integration can be performed numerically within finite integration limits.

As it was the case for $D_{\alpha}^{(c)}$, also $D_{\alpha}^{(e)}$ is to a good approximation only shell dependent. The values of $D_{\alpha}^{(e)}$ are listed in table 6.2 for different shells for the two relevant collision systems including the limit of $n \rightarrow \infty$. Similar as for core collisions, this correction is small for deeply bound states and saturates for highly excited states although in this case for the considered shells ($n \leq 15$) $D_{\alpha}^{(e)}$ has still not converged to the value calculated for $n \rightarrow \infty$.

The last integration in (6.27) is calculated as

$$M_{\alpha\beta}^{(e)} = \frac{2}{\pi} \int_0^{\infty} dk_{\perp} k_{\perp} \int_{-\infty}^{\min(\bar{\omega}_{\alpha}, \bar{\omega}_{\beta})/v_p} dk_z \frac{1}{k_z^2 + k_{\perp}^2} \times \sqrt{\text{Im} \left(\frac{-1}{\varepsilon(\sqrt{k_z^2 + k_{\perp}^2}, \bar{\omega}_{\alpha} - k_z v_p)} \right)} \sqrt{\text{Im} \left(\frac{-1}{\varepsilon(\sqrt{k_z^2 + k_{\perp}^2}, \bar{\omega}_{\beta} - k_z v_p)} \right)} \times \sum_{\mu \in \mathbb{P}} \langle \alpha | e^{-i(k_{\perp} \hat{x} + k_z \hat{z}) \cdot \vec{r}} | \mu \rangle \langle \mu | e^{i(k_{\perp} \hat{x} + k_z \hat{z}) \cdot \vec{r}} | \beta \rangle. \quad (6.31)$$

6.3.2 Numerical results for electron collisions

The two-dimensional integrals for $D_{\alpha}^{(e)}$ and $M_{\alpha\beta}^{(e)}$ in equation (6.30) and (6.31) have to be solved numerically. In figure 6.5 we show the integrand for $M_{\alpha\beta}^{(e)}$ which corresponds to the momentum transfer distribution of the selected decay rate. The shape is a result of the convolution of the loss function along a circle centered around $k_z = -v_p = -23$ a.u.. Since the integrand varies by several orders of magnitude (see figure 6.5) we adopt the following numerical

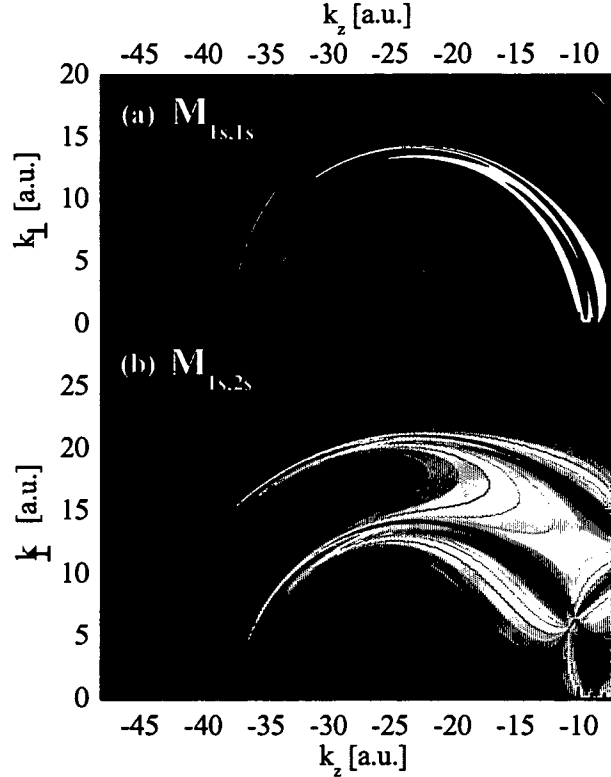


Figure 6.5: Absolute magnitude of the integrand of $M_{\alpha\beta}^{(e)}$ in equation (6.31) for Ar^{17+} in carbon with $v_p = 23$ a.u.. In the upper figure (a) we show the integrand for $\alpha=\beta=1s$ and each contour line corresponds to one order of magnitude. Blue is lowest and red highest. In the lower figure (b) $\alpha=1s$ and $\beta=2s$ and four contour lines represent one order of magnitude.

integration scheme. We divide the 2D-plane into a grid of 100×100 points and evaluate the integrand at these points. In case any of these values is higher than a certain threshold, we subdivide the corresponding 2D-interval into 5×5 points. If the integrand at any of the new points exceeds a second threshold a next step of refining is issued. By repeating this refinement for two more times we obtain a combined search and integration algorithm with a very fine mesh at the significant regions of the integrand only. The three adaptive thresholds for refinement are chosen such that the total number of mesh points for the calculation of each $D_\alpha^{(e)}$ and $M_{\alpha\beta}^{(e)}$ is 2×10^5 leading to a converged result.

The resulting decay rates are displayed in figure 6.6 for all states within the first four shells with $m \geq 0$. For electron-electron scattering we make the

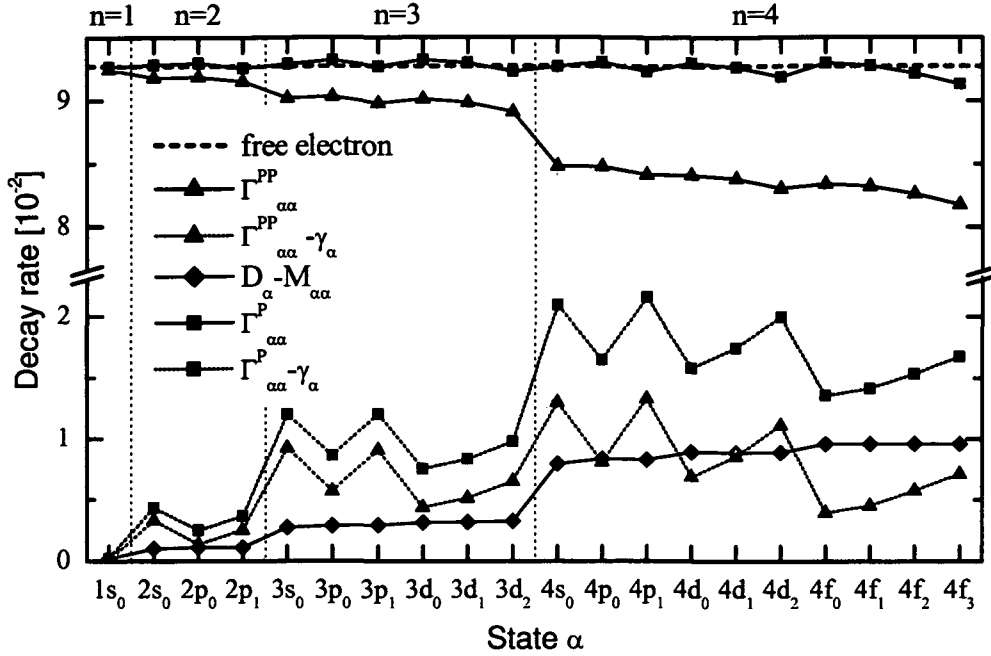


Figure 6.6: Decay rates for electron-electron collisions of $\text{Ar}^{17+} \rightarrow$ in carbon ($v_p = 23$ a.u.) as a function of state α for $m \geq 0$. We show the decay rates for the confined (red lines) and for the open (blue lines) system with respect to probability flux. The corrections $D_\alpha^{(e)}$ and $M_{\alpha\beta}^{(e)}$ are calculated according equation (6.30) and (6.31) respectively. Solid lines: full decay rate; dotted lines: effective decay rates omitting the elastic component $\gamma_\alpha^{(e)}$. The decay rate for free electrons (6.32) is shown for comparison.

same qualitative observations as for core scattering in the previous section. The decay rates that allow only for transitions within the confined subspace \mathbb{P} with n_{\max} ($\Gamma^{(e)\mathbb{P}\mathbb{P}}$) are highest for $\alpha = 1s$ and decrease with increasing principal quantum number n . The corrections ($D_\alpha^{(e)} - M_{\alpha\beta}^{(e)}$) accounting for loss to the complement \mathbb{Q} are mainly shell dependent with small intra-shell variations leading to a corrected decay rate $\Gamma^{(e)\mathbb{P}}$ that is almost constant and resembles the decay rate of a free electron that is obtained by

$$\Gamma_{\text{free}}^{(e)} = v_p \lambda_e^{-1} \quad (6.32)$$

from equation (3.27). A comparison of effective decay rates (without the elastic component $\gamma_\alpha^{(e)}$) reveals that for electrons in $n = 4$ the loss to \mathbb{Q} is of the same intensity as scattering into \mathbb{P} .

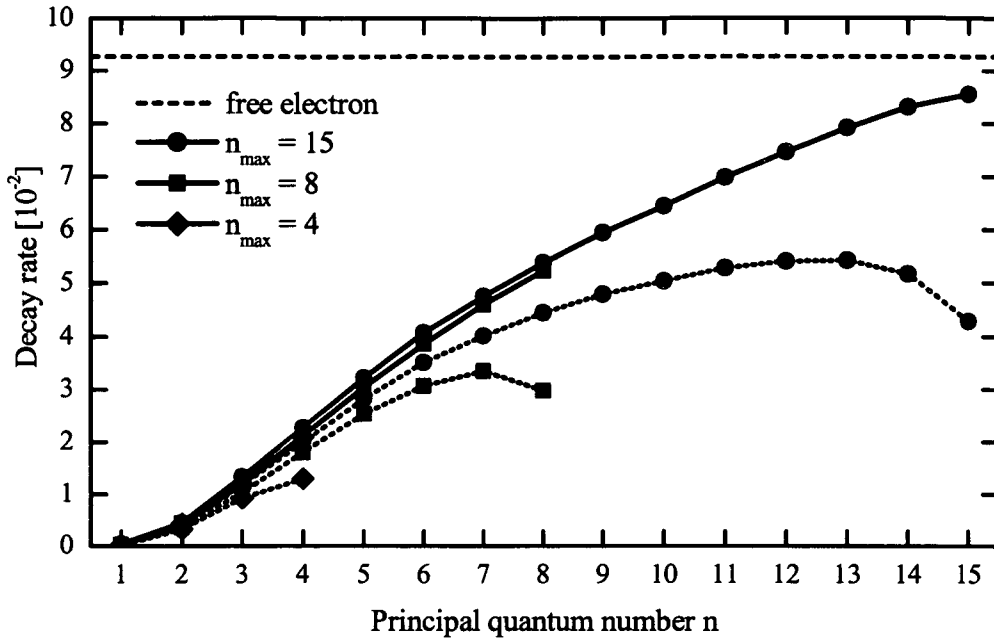
6.3.3 Convergence for high n 

Figure 6.7: Effective electron-electron decay rates of s-states for $\text{Ar}^{17+} \rightarrow \text{C}$ ($v_p = 23$ a.u.) as a function of shell n for different sizes (n_{\max}) of the subspace \mathbb{P} . Dotted lines: confined system ($\Gamma_{\alpha\alpha}^{(e)\mathbb{P}\mathbb{P}} - \gamma_{\alpha}^{(e)}$); solid lines: open system ($\Gamma_{\alpha\alpha}^{(e)\mathbb{P}} - \gamma_{\alpha}^{(e)}$) accounting for loss to the complement \mathbb{Q} ; dashed line: free electron limit (6.32).

Increasing the size of the subspace \mathbb{P} to $n_{\max} = 8$ and 15 respectively we observe the highest difference between $\Gamma^{(e)\mathbb{P}\mathbb{P}}$ and $\Gamma^{(e)\mathbb{P}}$ always for $n = n_{\max}$. The convergence towards the limit of quasi-free electron scattering is much slower with increasing n as it is the case for core scattering (figure 6.4) where $\Gamma^{(c)\mathbb{P}} = \Gamma_{\text{free}}^{(c)}$ for $n = 10$. The reason for the slow convergence is that the momentum transfer distribution for electron-electron collisions peaks at $k \rightarrow 0$ (see figure 3.1). The deviations of the effective decay rates $\Gamma_{\alpha\alpha}^{(e)\mathbb{P}} - \gamma_{\alpha}^{(e)}$ for different sizes of the subspace \mathbb{P} are due to the numerical inaccuracy in the calculation of $M_{\alpha\alpha}^{(e)}$ because for $n_{\max}=15$ we deal with matrices of size 1240×1240 .

6.4 Summary

In this chapter we have discussed details of the calculation of the decay operators as they enter the non-unitary QTMC method. For core collisions and electron-electron interaction transitions to the infinitely large complement cannot be evaluated exactly necessitating an approximative approach. We have used a closure approximation with an average excitation energy to estimate the contribution of the subspace to transitions into the complement. We have shown that for high n the transition rates converge towards the quasi-free electron limit.

After having calculated the decay operators for the non-unitary subspace, we have accumulated all ingredients to apply the non-unitary QTMC method to a realistic transport problem. In the next chapter we use it to investigate transient coherences during transport. In chapter 9 we extend the non-unitary QTMC method to account also for probability flux into the subspace and explore transient coherences by electron capture and collisions simultaneously in transport of initially bare projectile ions.

Chapter 7

Application to Kr^{35+} transport

7.1 Introduction

In this chapter we study the transport of a hydrogenic projectile ion through a solid. The projectile is a $\text{Kr}^{35+}(1s)$ ion with a velocity of 47 a.u. penetrating amorphous carbon foils of varying thickness, corresponding to varying evolution times. We investigate the build-up of transient coherences and decoherence of electronic states in this collisional environment. Before entering the solid the projectile electron is assumed to be in the $1s$ ground state. Therefore the reduced density matrix of the projectile electronic degrees of freedom is initially in a pure state. The primary source for build-up of excited states and transient coherences during transport is the collisional excitation of the $1s$ electron. In chapter 9 we will go one step further and consider transient coherences built-up by electron capture.

The experiment we compare with has been performed on the LISE (Ligne d'Ions Super Epluchés) facility at GANIL (Grand Accélérateur National d'Ions Lourde). Details of the experimental setup are described in the references [Ver98, Lam97, Fou00]. A schematic picture can be found in figure 2.4. We consider the ratio of emitted photons by $3p_{1/2} \rightarrow 2s_{1/2}$ and $3s_{1/2} \rightarrow 2p_{1/2}$ which shows a significant solid state effect as a function of target thickness (see figure 7.1). The ratio is initially approximately 2 and increases for thick targets. Several models have been employed to explain this solid state effect. A direct solution of the Lindblad master equation with a reduced number of couplings (see section 5.5.1) is able to describe the experimental findings [Ver01]. The couplings describe transitions induced by collisions and radiative decay. Collisional rates have been calculated using a plane-wave first order Born approximation (PWBA). We refer to this approach as the master equation approach (MEA).

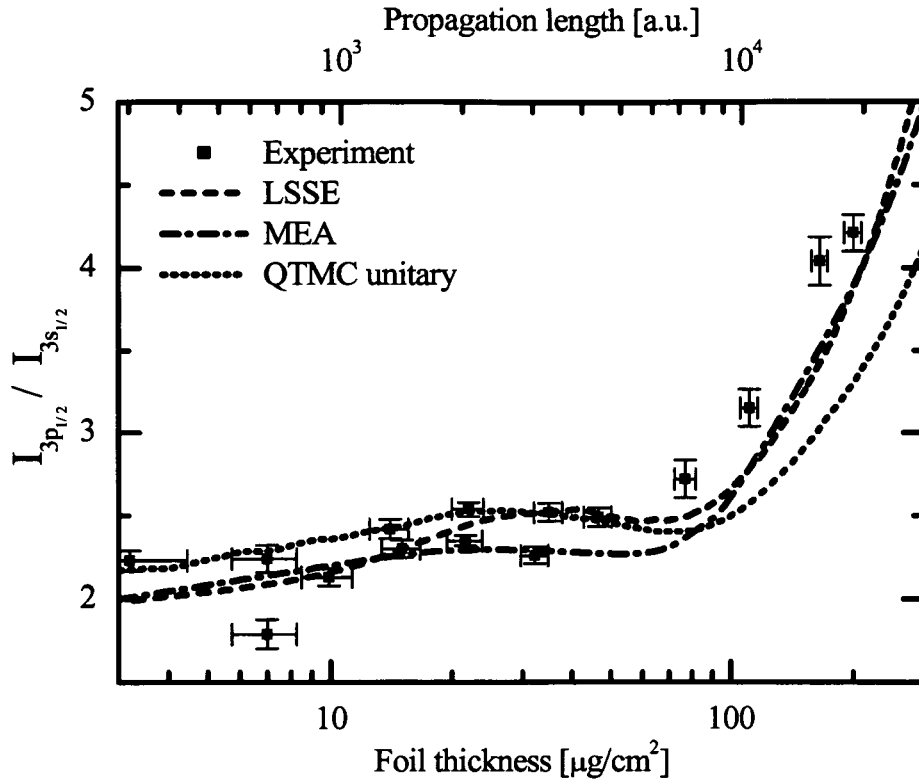


Figure 7.1: Relative line emission intensities $I_{3p_{1/2}}/I_{3s_{1/2}}$ resulting from the transmission of a $Kr^{35+}(1s)$ ion through amorphous carbon at a velocity of 47 a.u. as a function of target thickness. Symbols: experimental data from ref. [Ver98]; Lines: theoretical calculations; dashed line: linear stochastic Schrödinger equation (LSSE) [Min02a]; dash-dotted line: master equation approach (MEA) [Ver01]; solid line: unitary QTMC [Min03a].

The first quantum transport theories mapped the Lindblad master equation on a linear stochastic Schrödinger equation (LSSE) that could be solved by a quantum trajectory Monte Carlo (QTMC) method [Min02a]. In this approximation the projectile electron is treated in the quasi-free electron limit. The obtained results are in good agreement with the measurements (compare figure 7.1). They also agree with the MEA results for thin as well as for thick targets. In the region of intermediate thicknesses, however, differences can be observed. The collisional mean free path (MFP) is approximately 500 a.u. (chapter 6). Therefore results obtained for much thinner targets resemble single collision conditions. Since both methods treat collisions in the quasi-free electron limit they give same results in the single collision regime.

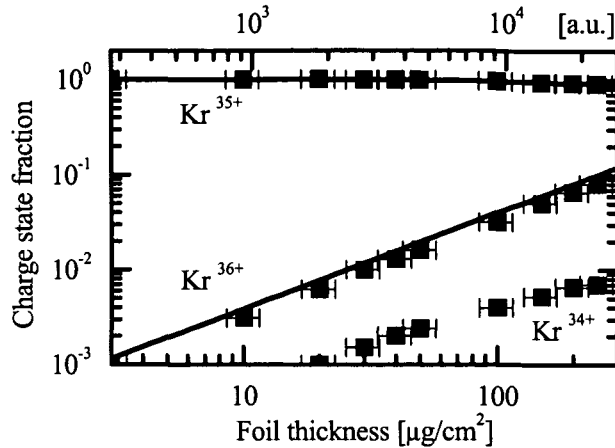


Figure 7.2: Charge state fraction of a $Kr^{35+}(1s)$ ion in transport through amorphous carbon at a velocity of $v_p = 47$ a.u. as a function of foil thickness. Symbols: experimental data from ref. [Ver98]; lines: results of the non-unitary QTMC simulation.

At propagation paths of the order of the collisional MFP different results can be observed resulting from the different description of the dynamics.

To further analyze this issue Minami et. al. [Min03a] mapped the Lindblad master equation on a non-linear stochastic Schrödinger equation (NLSSE) and solved it by a QTMC method. It turned out that the LSSE is the limiting case of the NLSSE when the quasi-free electron approximation can be applied (see section 5.5.2). Remarkably, the comparison with experimental findings shows a significant discrepancy for thick targets although the NLSSE is expected to describe the transport problem more accurately. To resolve this difference was the motivation for the investigations presented in this chapter.

The method presented in [Min03a] describes the time evolution of the reduced density matrix within a reduced Hilbert space. A manageable basis contains typically deeply bound states up to the fourth shell. One limitation of this method is that probability is artificially confined within this Hilbert space and hence ionization cannot be accounted for. We refer to this method as the unitary QTMC method. The application of a unitary QTMC description was motivated by measurements of outgoing charge state fractions after transport (see figure 7.2). They show that ionization is very slow for this collision system and only for the thickest targets about 10 percent of the projectile ions are ionized.

In this work we have derived a non-unitary Lindblad master equation

and its QTMC solution that allows for probability flux out of the reduced Hilbert space and thus can describe ionization. To explore the effect of the ionization channel we compare the newly developed non-unitary Lindblad master equation with a simulation using the unitary version from [Min03a].

The Hamiltonian of the system outside the foil is the unperturbed hydrogenic Hamiltonian (see section 3.1)

$$H_S = -\nabla_r^2/2 - Z_p/r + \Delta H_{rel} \quad (7.1)$$

including relativistic corrections ΔH_{rel} , i.e. fine structure and Lamb shift. An eigenstate of H_S can be quantified by the quantum numbers n , l , j and m_j . The unperturbed Hamiltonian inside the solid contains additionally the contribution from the wake field (section 3.3)

$$H_S^{(\text{solid})} = H_S + V^{(w)}. \quad (7.2)$$

Depending on the approximation we use for $V^{(w)}$, the eigenstates of this Hamiltonian $H_S^{(\text{solid})}$ are different. We employ a sudden approximation at the foil entrance at which the wake field in the Hamiltonian is switched on. Likewise, we project onto atomic final states in vacuum (eigenstates of H_S) at the exit surface invoking, again, a sudden approximation. If not stated otherwise, we use for $V^{(w)}$ the approximation given in equation (3.37).

The interaction with the environment contains scattering at the atomic cores $\Gamma^{\mathbb{P}(c)}$, interaction with the electron gas $\Gamma^{\mathbb{P}(e)}$ and radiative decay $\Gamma^{(r)}$ (see chapter 3). The total decay operator is the sum of these three contributions

$$\Gamma^{\mathbb{P}} = \Gamma^{\mathbb{P}(c)} + \Gamma^{\mathbb{P}(e)} + \Gamma^{(r)} \quad (7.3)$$

entering the effective Hamiltonian

$$H_{eff} = H_S^{(\text{solid})} - \frac{i}{2} \Gamma^{\mathbb{P}}. \quad (7.4)$$

First, we consider the unitary QTMC method within the subspace \mathbb{P} spanned by the hydrogenic basis set with the quantum numbers n , l , j and m_j . This method has been described in section 5.3. We label the resulting time evolved unitary density matrix as $\sigma^U(t)$. We choose \mathbb{P} as the Hilbert space represented by the first four shells of the hydrogenic basis set ($n_{\text{max}} = 4$) limiting the size of $\sigma^U(t)$ to 60×60 . We note, however, that extensions to larger subspaces are computationally feasible. Increasing the dimension of \mathbb{P} , for example to 182×182 (corresponding to $n_{\text{max}} = 6$), does not significantly modify the results. The time evolution is governed by the decay operator $\Gamma^{\mathbb{P}\mathbb{P}}$ (describing only transitions within \mathbb{P}) rather than $\Gamma^{\mathbb{P}}$ (containing also

ionization) in the effective Hamiltonian in equation (7.4). This calculation reproduces the results of the previous simulation in [Min03a].

We perform a second calculation using the non-unitary QTMC method describing not only the time evolution within the subspace \mathbb{P} but also ionization (section 5.4). This calculation involves $\Gamma^{\mathbb{P}}$ in (7.4). All other parameters are unchanged. The resulting non-unitary density matrix will be denoted by $\sigma^{NU}(t)$.

The interaction of the projectile nucleus with the solid is weak due to the high velocity and mass of the projectile. For the considered propagation lengths the ion follows approximately a straight line trajectory with constant velocity v_p . We use time t in the projectile rest frame and distance d in the laboratory frame interchangeably with $d(t=0) = 0$ at the entrance of the foil and $d(t) = v_p t / \sqrt{1 - (v_p/c)^2}$.

7.2 Numerical results

The charge state fraction shown in figure 7.2 is an approximate measure of the loss of probability of the one-electron bound-state Hilbert space due to transitions to the continuum. More precisely, all high-lying bound states with $n > n_{max}$ also belong to \mathbb{Q} thus overestimating this fraction somewhat. In addition, capture of a second electron leading to the formation of Kr^{34+} would represent a further loss channel corresponding to the transition from a one-electron to a two-electron Hilbert space. Figure 7.2 indicates that this channel is for the system under consideration a slow process leading to only 1% Kr^{34+} for the thickest foil and is neglected in the description of this collision system. Loss due to ionization dominates. By comparing the experimental findings with the results of the non-unitary QTMC we find that the trace of the density matrix, $\text{Tr}[\sigma^{NU}(d)]$ and $1 - \text{Tr}[\sigma^{NU}(d)]$, agree well with the charge state probability for Kr^{35+} and Kr^{36+} , respectively.

While the population in $1s$ decreases very slowly, excited states populations first grow relatively fast and saturate at long propagation paths as displayed in figure 7.3. We can identify three characteristic regions with respect to the propagation path lengths. (i) For very thin foils interaction time with the solid is so short that excited states populations result from a single interaction proportional to the transition probability from $1s$. (ii) In the intermediate region of propagation lengths between 10^3 and 10^4 a.u. the populations deviate strongly from a simple linear increase. In this region mixing by multiple collisions starts playing an important role. (iii) At longer propagation paths the populations in figure 7.3 saturate indicating a dynamical balance between populating by excitation from the ground state, mixing

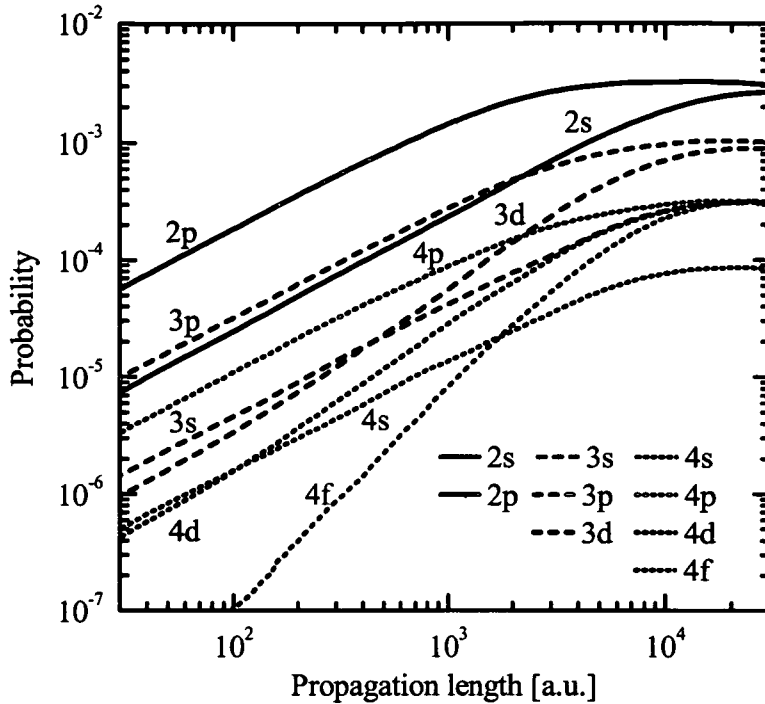


Figure 7.3: Excited states populations of Kr^{35+} ions in transport through carbon ($v_p = 47$ a.u.) as a function of propagation length. Results of the non-unitary simulation are summed over fine structure quantum numbers j and m_j .

in further transport and loss. We note that this equilibrium is transient as the feeding by excitation from 1s is still considered to be a constant source and capture of electrons is neglected.

7.2.1 Role of loss channel

As a next step we discuss the role of the loss channel in the time evolution of individual elements of the reduced density matrix. The shell population ratios $P(n)/P(n')$ show drastic modifications when loss into Q is taken into account (figure 7.4). For small propagation lengths the ratios between shell populations are controlled by single collisions and remain constant. They are identical in the unitary and non-unitary QTMC simulation. In the multiple collision regime the unitary simulation accumulates the electron probability in the higher-lying shells while in the non-unitary simulation the ratios approach saturation. In this regime the flow of probability among states in \mathbb{P}

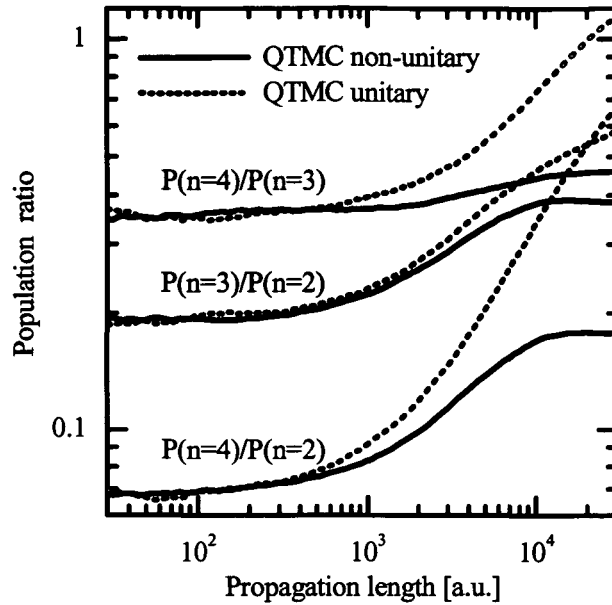


Figure 7.4: Evolution of shell population ratios as a function of propagation length for the non-unitary QTMC (solid lines) and a unitary QTMC simulation (dotted lines) with $n_{\max} = 4$.

balances the flow of flux from \mathbb{P} to \mathbb{Q} and back to the $1s$ state.

The relative subshell populations of states with different angular momenta within a shell resemble for thin targets the final state distribution of single collision excitation of the $1s$ state. Since dipole transitions are the dominant component of the boost operator (compare Taylor expansion of boost in (6.18)) predominantly p-states are initially occupied. In subsequent transport these populations are redistributed. High angular momentum states are populated for long propagation times. We briefly discuss the combined effect of collisions and wake field on the angular momentum distribution first described in [Rei00]. Collisions deliver a momentum transfer \vec{k} perpendicular to the quantization axis z hence they are distributed in the x - y -plane. For an electron with an angular momentum vector \vec{l} in the x - y -plane a series of momentum transfers \vec{k} in the x - y direction results in a change of the angular momentum vector \vec{l} towards the z -axis. For collisions in the solid this implies an increase of m_l towards l . The wake potential exerts an electric field parallel to z and hence mixes states with the same value of the projection of the angular momentum m_l but different values of l . The combination of these two mixing mechanisms leads to a mixing of angular momenta as well as of the projections. The remarkable point is that none of the interactions

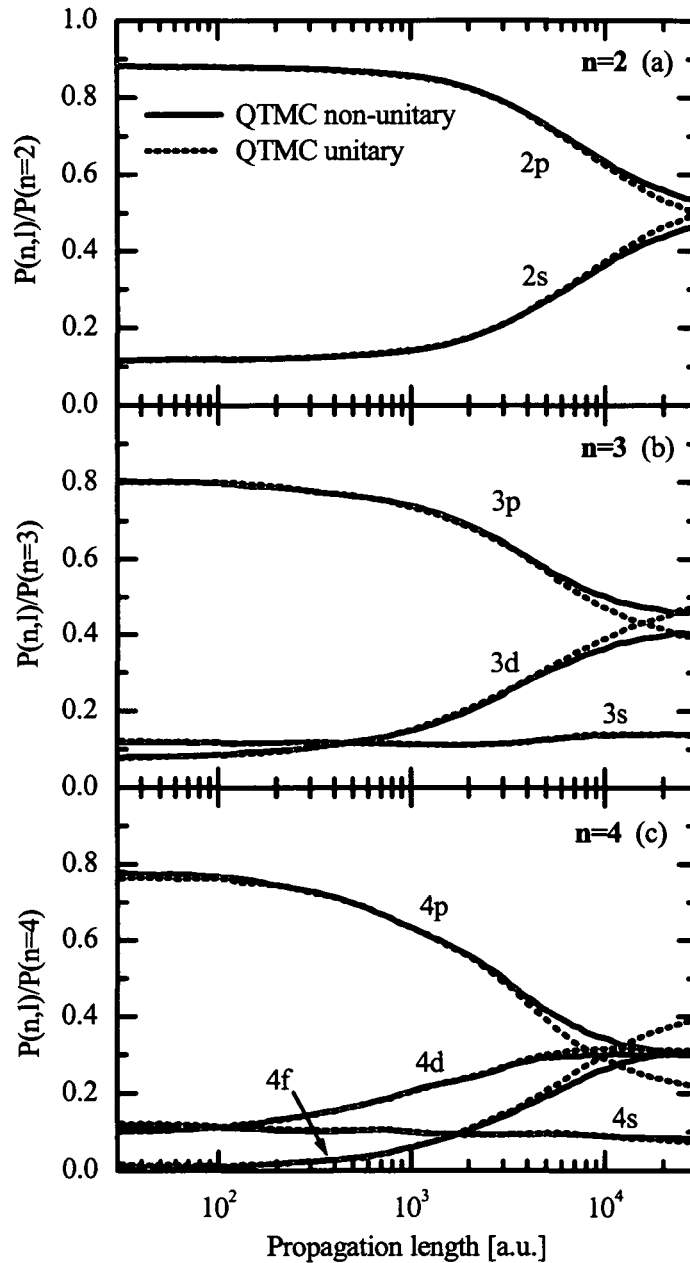


Figure 7.5: Evolution of relative populations of Kr^{35+} states as a function of propagation length for the full non-unitary QTMC (solid lines) and a unitary QTMC simulation (dotted lines) with $n_{\max} = 4$. The results are shown as a function of the principal quantum number n and the angular momentum l . The populations are normalized to the overall probability in the corresponding shell. (a) $P(n=2,l)$ for $n=2$, (b) $P(n=3,l)$ for $n=3$ and (c) $P(n=4,l)$ for $n=4$.

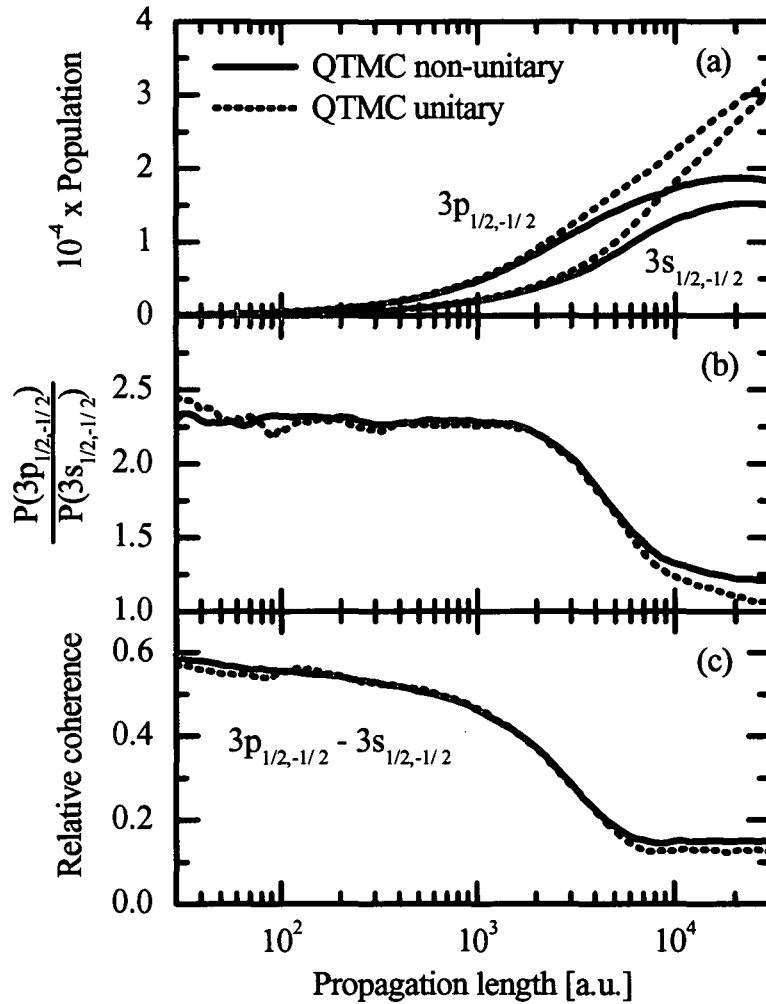


Figure 7.6: Evolution of selected populations and coherences of the internal state of a Kr^{35+} ion traversing an amorphous carbon foil with velocity $v_p=47$ a.u. as a function of propagation length. The system is initially prepared in the $1s$ ground state. We compare results of the non-unitary simulation (solid lines) with results obtained in a unitary simulation (dotted lines) with $n_{\max} = 4$. (a) Populations of the $3s_{1/2,-1/2}$ and $3p_{1/2,-1/2}$ states, (b) ratio of these populations, and (c) relative coherence between these two states.

could populate these high l -states on its own but only the combined effect results in an effective angular momentum diffusion from the initial distribution peaking at $l=1$ towards higher values of l .

The relative subshell populations as a function of propagation length agree for the unitary and non-unitary QTMC calculations for short distances (figure 7.5). However, differences become noticeable at large distances. Relative to the non-unitary QTMC result, the unitary transport enhances the probability for higher angular momentum states. The effect of the non-unitary evolution on individual state populations and coherences is shown in figure 7.6 for the $3s_{1/2,-1/2}$ and $3p_{1/2,-1/2}$ subspace. The most pronounced difference is observed for the populations of these states. While in a unitary calculation the feeding from low-lying states remains dominant even for long propagation lengths, in the non-unitary simulation loss from higher excited states into the complement Q leads to a depletion and thus to a dynamical equilibrium of the populations shown in figure 7.6(a) following closely the findings for shell populations in figure 7.4. Remarkably, the population ratio between states of different angular momenta within the same shell (figure 7.6(b)) is very similar in both calculations, the non-unitary QTMC results showing a slightly higher ratio for thick targets. Also for the relative coherence (equation (5.69)) only a slight increase is observed.

7.2.2 Transient coherences

The build-up and decay of coherences is most directly observed in the reduced density matrix $|\sigma_{ij}^{NU}(d)|$, which displays, on one hand, the excitation to excited states in the diagonal elements $\sigma_{ii}^{NU}(d)$ and, on the other hand, the coherences in the off-diagonal elements of $\sigma_{ij}^{NU}(d)$ ($i \neq j$). The absolute magnitude of the elements of σ^{NU} for excited states is given in figure 7.7 while the matrix of relative coherences is shown in figure 7.8 for different propagation distances d . While figure 7.7(a) and (b) reflect the excitation from single collisions, figure 7.7(c) and (d) reflect the multiple collision regime, where we can observe not only the initially generated coherences by excitation from the $1s$ ground state but also coherences generated by deexcitation. Coherences most robust against decoherence and still visible after a propagation length of 3×10^4 a.u. (~ 15 fs) are intra-shell coherences between different angular momentum states.

The matrix of relative coherences (equation (5.69)) displayed in figure 7.8 shows the gradual shift and decay of coherences as a function of propagation distance (or foil thickness). The intra-shell coherences between the $2s$ and $2p$ states survive longest.

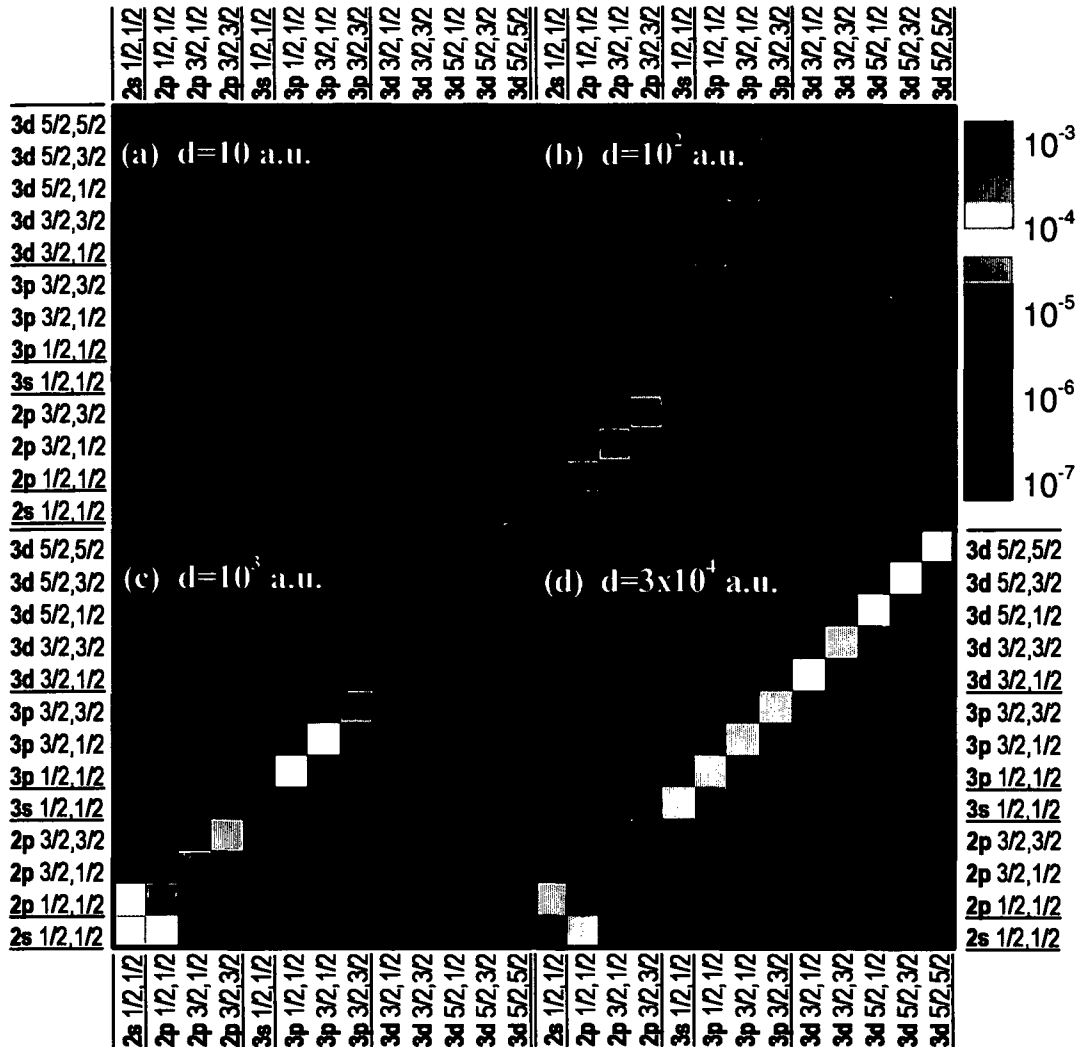


Figure 7.7: Reduced density matrix $\sigma^{NU}(d)$ of a Kr³⁵⁺ ion in transport through amorphous carbon at a velocity of $v_p = 47$ a.u. at various propagation lengths. (a) $d=10$ a.u., (b) $d=10^2$ a.u., (c) $d=10^3$ a.u. and (d) $d=3 \times 10^4$ a.u.. Absolute magnitude of excited states matrix elements $|\sigma_{ij}^{NU}(d)|$ from $n=2$ and $n=3$ involving $m_j > 0$ is shown.

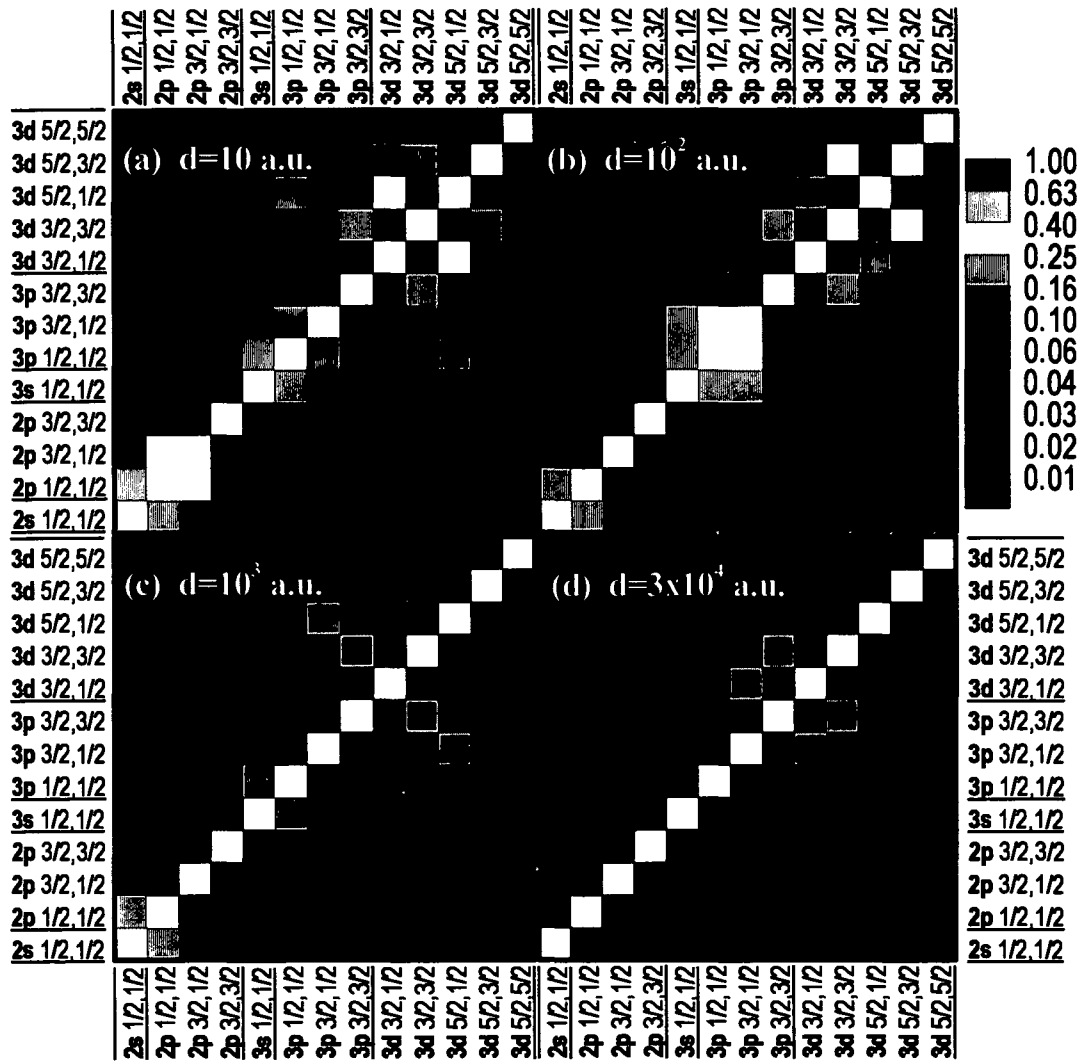


Figure 7.8: Relative coherences $|C_{ij}^{NU}(d)|$ (5.69) of the reduced density matrix of a Kr^{35+} ion in transport through amorphous carbon at a velocity of $v_p = 47$ a.u. at various propagation lengths. (a) $d=10$ a.u., (b) $d=10^2$ a.u., (c) $d=10^3$ a.u. and (d) $d=3 \times 10^4$ a.u.. Only matrix elements from $n=2$ and $n=3$ involving $m_j > 0$ are shown.

7.3 Decay of coherences: decoherence

We would like to obtain a qualitative estimate of the time evolution of off-diagonal elements of the reduced density matrix σ . For this purpose we consider the Lindblad master equation (LME) for only one off-diagonal element ($\sigma_{ij}(t)$) and assume the remaining elements of $\sigma(t)$ to be constant in time

$$\sigma_{mn}(t) = \sigma_{mn}(t=0) \quad \text{for } m \neq i \text{ and } n \neq j. \quad (7.5)$$

This allows us to simplify the LME such that we can find closed expressions for $\sigma(t)$. We can identify certain characteristic patterns in the time evolution of the coherence. Later in the application to a complex system we can try to classify the numerical results with respect to the findings for a simple system as it is discussed in this section.

7.3.1 A simple model for transient coherence

In the Lindblad master equation (LME) we can identify a damping term and a gain term as

$$\frac{d}{dt}\sigma(t) = -i\omega\sigma(t) - \underbrace{\frac{1}{2}(\Gamma\sigma(t) + \sigma(t)\Gamma)}_{\text{damping}} + \underbrace{\sum_k S(k)\sigma(t)S^\dagger(k)}_{\text{gain}}. \quad (7.6)$$

For the damping term we consider only direct coupling from $\sigma_{ij}(t)$ to $d\sigma_{ij}(t)/dt$ and can hence make the following approximation

$$\frac{1}{2}(\Gamma_{i\mu}\sigma_{\mu j}(t) + \sigma_{i\mu}(t)\Gamma_{\mu j}) \rightarrow \frac{1}{2}(\Gamma_{ii} + \Gamma_{jj})\sigma_{ij}(t) \rightarrow \bar{\Gamma}_{ij}\sigma_{ij}(t) \quad (7.7)$$

In order to estimate the qualitative time evolution of $\sigma_{ij}(t)$ we consider the gain term in (7.6) as constant and denote it by G in the following

$$\sum_k S(k)\sigma(t)S^\dagger(k) \rightarrow G. \quad (7.8)$$

With these approximations we can write the Lindblad master equation for $\sigma_{ij}(t)$ as

$$\frac{d}{dt}\sigma_{ij}(t) = -i\omega_{ij}\sigma_{ij}(t) - \bar{\Gamma}_{ij}\sigma_{ij}(t) + G \quad (7.9)$$

which is an inhomogeneous first-order differential equation. We first investigate the homogeneous solution for $G = 0$ which corresponds to the case of a coherence that is only decaying and no build-up occurs.

Homogeneous solution (G=0)

For $G = 0$ the solution is an exponential function

$$\sigma_{ij}(t) = \sigma_{ij}(0) e^{-i\omega_{ij}t} e^{-\bar{\Gamma}_{ij}t} \quad (7.10)$$

with the initial condition $\sigma_{ij}(0)$ at $t=0$. The first exponential in the time evolution is responsible for rotation in the complex plane

$$\sigma_{ij}(t) = \sigma_{ij}(0) e^{-i\omega_{ij}t} \quad (7.11)$$

with the time constant for one revolution given by

$$e^{-i\omega_{ij}t} = e^{-i2\pi t/T_{ij}^{2\pi}} \quad \text{with} \quad T_{ij}^{2\pi} = 2\pi/\omega_{ij}. \quad (7.12)$$

The second exponential in equation (7.10) results in damping $\exp(-t/T_{ij}^{\text{damp}})$ with the time constant

$$T_{ij}^{\text{damp}} = \frac{1}{\bar{\Gamma}_{ij}}. \quad (7.13)$$

The overall time evolution of the coherence is a revolution in the complex plane with ω_{ij} with the center at the origin. The radius $\sigma_{ij}(0)$ is damped by $\bar{\Gamma}_{ij}$ leading to a spiral towards $\lim_{t \rightarrow \infty} \sigma_{ij}(t) \rightarrow 0$.

Inhomogeneous solution (G≠0)

The inhomogeneous solution of (7.9) with $G \neq 0$ and the initial condition $\sigma_{ij}(0) = 0$ is the integral over the homogeneous solutions in (7.10) weighted by the constant gain term G as

$$\sigma_{ij}(t) = G \int_0^t dt' e^{(-i\omega_{ij} - \bar{\Gamma}_{ij})(t-t')} = \frac{G}{-i\omega_{ij} - \bar{\Gamma}_{ij}} \left(e^{(-i\omega_{ij} - \bar{\Gamma}_{ij})t} - 1 \right). \quad (7.14)$$

In analogy to the homogeneous solution, we expect to find an oscillatory behavior related to ω_{ij} and damping related to $\bar{\Gamma}_{ij}$. In the further analysis we distinguish two extreme cases depending on the relative strength of ω_{ij} compared to $\bar{\Gamma}_{ij}$.

For $\omega_{ij} \gg \bar{\Gamma}_{ij}$ the oscillatory term dominates over damping and we can simplify the solution (7.14) by setting $\bar{\Gamma}_{ij} = 0$ to

$$\sigma_{ij}(t) = \frac{iG}{\omega_{ij}} (e^{-i\omega_{ij}t} - 1) \quad (7.15)$$

which results in a rotation of $\sigma_{ij}(t)$ in the complex plane as indicated in figure 7.9. The radius is determined by the absolute magnitude of the prefactor in

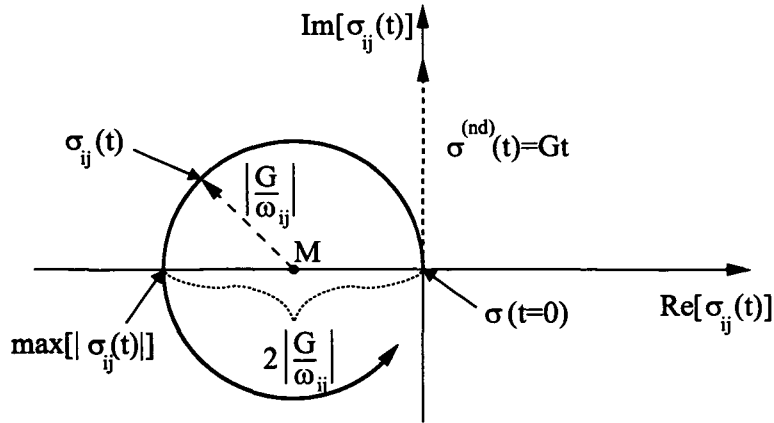


Figure 7.9: Schematic drawing of the inhomogeneous solution of $\sigma_{ij}(t)$ (7.14) in the complex plane with time as parameter for $\omega_{ij} \gg \bar{\Gamma}_{ij}$ with the initial condition $\sigma_{ij}(t=0) = 0$. Solid line: solution from equation (7.15) with G proportional to i with the center point denoted by M . Dashed line along imaginary axis: solution neglecting decay $\sigma^{(nd)}(t) = Gt$.

(7.15) as the ratio between gain and energy difference $|G/\omega_{ij}|$. The center point M is shifted by the last term in (7.15) by the length of this radius. This means that $\sigma_{ij}(t)$ evolves along a circle in the complex plane that goes through the origin. Consequently, at times that equal integer multiples of $T_{ij}^{2\pi}$ the coherence becomes zero again. The position of M with respect to the origin is determined by the phase of the prefactor in (7.15). In figure 7.9 we show $\sigma_{ij}(t)$ for G being purely imaginary. Combined with the i in the prefactor of (7.15) this results in a shift of the central point M towards the negative real axis.

An important consequence of this analysis is that the maximum of the coherence is bounded to

$$\max[|\sigma_{ij}(t)|] = 2 \left| \frac{G}{\omega_{ij}} \right| \quad (7.16)$$

regardless the fact that the source G is constantly feeding the coherence. A coherent superposition not affected by decay increases with time as $\sigma^{(nd)}(t) = Gt$ (figure 7.9). We can normalize $\sigma_{ij}(t)$ to the case without decay and obtain

$$\frac{\sigma_{ij}(t)}{\sigma^{(nd)}(t)} = \frac{1}{-i\omega_{ij}t} (e^{-i\omega_{ij}t} - 1) \quad (7.17)$$

and

$$\left| \frac{\sigma_{ij}(t)}{\sigma^{(nd)}(t)} \right| = \left(\frac{\pi t}{T_{ij}^{2\pi}} \right)^{-1} \left| \sin \left(\frac{\pi t}{T_{ij}^{2\pi}} \right) \right| \quad (7.18)$$

which decreases with time. Consequently, the coherence is reduced with respect to the non-decaying case. Therefore the restriction (7.16) can be interpreted as an effective decay of the coherence. Note that this decay mechanism is a feature of the inhomogeneous solution due to the interplay of a constant gain (G) with the complex term $i\omega_{ij}\sigma_{ij}(t)$ in the Lindblad master equation. Henceforth we will refer to this mechanism as “dephasing”.

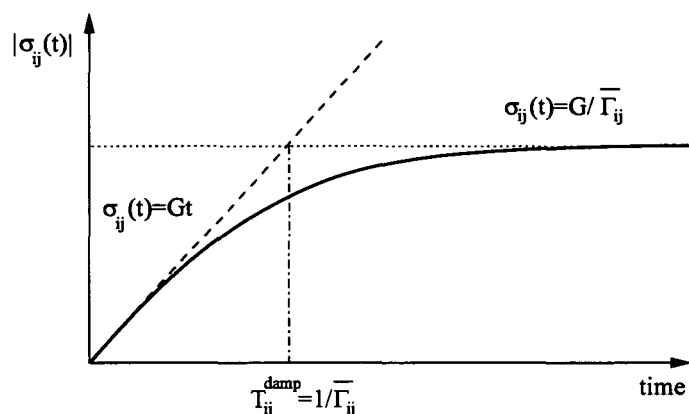


Figure 7.10: Schematic drawing of the inhomogeneous solution of the absolute value of $\sigma_{ij}(t)$ (7.14) for $\omega_{ij} \ll \bar{\Gamma}_{ij}$ as a function of time with the initial condition $\sigma_{ij}(t=0) = 0$. Solid line: solution from equation (7.19); dashed line: short time solution (7.21) neglecting decay proportional to Gt ; dotted line: asymptotic solution $G/\bar{\Gamma}_{ij}$ (7.22); dash-dotted line: crossing point corresponding to T_{ij}^{damp} .

For $\omega_{ij} \ll \bar{\Gamma}_{ij}$ in (7.14) the oscillatory term can be neglected ($\omega_{ij} = 0$) and the damping term governs the time evolution. This requirement is satisfied for coherences between degenerate and near-degenerate states. Thus we can approximate $-i\omega_{ij} - \bar{\Gamma}_{ij} \rightarrow -\bar{\Gamma}_{ij}$ in (7.14) and express the solution as

$$\sigma_{ij}(t) = \frac{G}{\bar{\Gamma}_{ij}} \left(1 - e^{-\bar{\Gamma}_{ij}t} \right). \quad (7.19)$$

To estimate the characteristic behavior of $\sigma_{ij}(t)$ we perform a Taylor expansion with respect to time t

$$1 - e^{-\bar{\Gamma}_{ij}t} = \bar{\Gamma}_{ij}t - \bar{\Gamma}_{ij}^2 t^2 + O(t^3). \quad (7.20)$$

On a short time scale $\sigma_{ij}(t)$ increases linearly with time

$$\lim_{t \rightarrow 0^+} \sigma_{ij}(t) = Gt, \quad (7.21)$$

while in the asymptotic limit of long times the exponential in (7.19) becomes zero and the coherence takes the constant value of

$$\lim_{t \rightarrow \infty} \sigma_{ij}(t) = \frac{G}{\bar{\Gamma}_{ij}}. \quad (7.22)$$

For the damping time T_{ij}^{damp} defined in (7.13) the two limits (equation (7.21) and (7.22)) meet as it is displayed in figure 7.10. At this time the second order in the Taylor expansion of the exponential in (7.20) starts to exceed the first order linear term. Consequently, at T_{ij}^{damp} the coherence $\sigma_{ij}(t)$ starts to be effectively damped. Relative to the ideal case of no decay we find

$$\frac{|\sigma_{ij}(t)|}{\sigma^{(\text{nd})}(t)} = \frac{1}{\bar{\Gamma}_{ij}t} \left(1 - e^{-\bar{\Gamma}_{ij}t}\right). \quad (7.23)$$

Thus $\sigma_{ij}(t)$ is effectively decreased. Hereafter we will refer to this mechanism as “damping”.

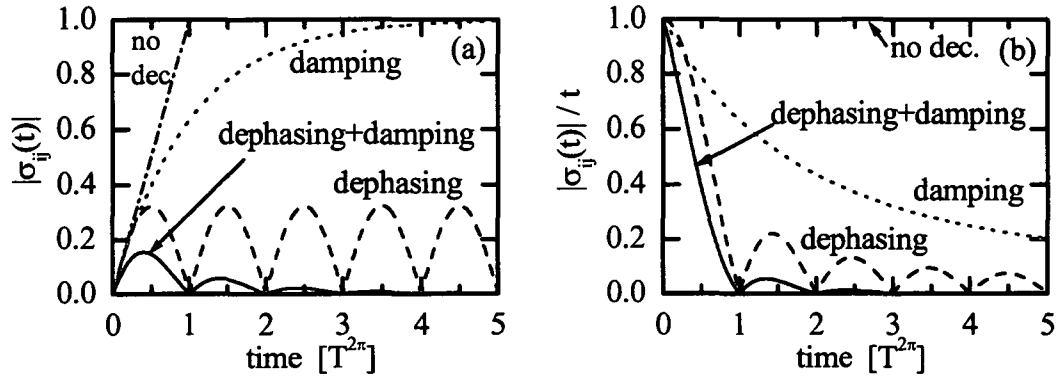


Figure 7.11: $\sigma_{ij}(t)$ solving the LME (7.9) as a function of time with the initial condition $\sigma_{ij}(t=0)=0$. The parameters are chosen as $G=1$, $\bar{\Gamma}_{ij}=1$ and $T_{ij}^{2\pi}=1$ and hence $T_{ij}^{\text{damp}}=1$ and $\omega_{ij}=2\pi$. (a) Absolute value of $\sigma_{ij}(t)$ (7.14) within different approximations: dash-dotted lines: no decoherence ($\sigma^{(\text{nd})}(t)=Gt$); dotted lines: decoherence by damping ($1-\exp(-t)$) (7.19); dashed lines: decoherence by dephasing ($|\sin(\pi t)|/\pi$) (7.15); solid lines: combined decoherence by dephasing and damping ($|\sin(\pi t)|\exp(-t)/\pi$) (7.14). (b) Solutions normalized to the case of no decoherence $|\sigma_{ij}(t)/\sigma^{(\text{nd})}(t)| = |\sigma_{ij}(t)|/t$.

Via this short analysis of the solution of the LME for one coherence we could identify two mechanisms of decoherence: dephasing and damping. For this model system we compare the solution of the LME (7.9) in different limits ($\sigma_{ij}(t=0)=0$) in figure 7.11.

n=2	2s _{1/2}	2p _{1/2}
2p _{3/2}	110	107
2p _{1/2}	4954	

n=3	3s _{1/2}	3p _{1/2}	3p _{3/2}	3d _{3/2}
3d _{5/2}	274	270	1118	1125
3d _{3/2}	363	355	178224	
3p _{3/2}	363	356		
3p _{1/2}	16547			

Table 7.1: Dephasing length $d_{\alpha\beta}^{2\pi}$ (7.24) in a.u. that a Kr³⁵⁺ ion traverses during the time $T_{\alpha\beta}^{2\pi} = 2\pi/|\omega_{\alpha\beta}|$ with a speed of 47 a.u. for intra-shell combinations of hydrogenic eigenstates with the unperturbed Hamiltonian specified in (5.65).

7.3.2 Numerical results for coherences

Although in the application to transport we are dealing with a highly coupled system that is strongly perturbed we nevertheless try to find characteristic features of the simple model presented in section 7.3.1. First we estimate the involved time scales. The dephasing time is given by the inverse energy spacing (7.12). For a transport problem it is more convenient to transform the dephasing time into a path length traversed by the projectile, i.e.

$$d_{\alpha\beta}^{2\pi} = v_p T_{\alpha\beta}^{2\pi} = \frac{2\pi v_p}{|\omega_{\alpha\beta}|}. \quad (7.24)$$

In table 7.1 we list values of $d^{2\pi}$ for the krypton projectile with a velocity of 47 a.u. for intra-shell states (α, β) .

The damping constant $\bar{\Gamma}_{ij}$ is defined in the simple model according to (7.7). The corresponding propagation length is

$$d^{\text{damp}} = \frac{v_p}{\bar{\Gamma}_{ij}} \approx \frac{v_p}{\frac{1}{2}(\Gamma_{ii} + \Gamma_{jj})} \quad (7.25)$$

with the decay operators of the two diagonal elements of the corresponding coherence σ_{ij} . For the dynamics in the non-unitary version of the QTMC we take Γ_{ii}^{p} for Γ_{ii} . In figure 6.2 we have shown that for core collisions Γ_{ii}^{p} resembles the decay rate of a free electron. This observation is state independent and applies also to electron-electron scattering (see figure 6.6). With these findings we can calculate the damping length as $d^{\text{damp}} \approx 500$ a.u. which is state independent too.

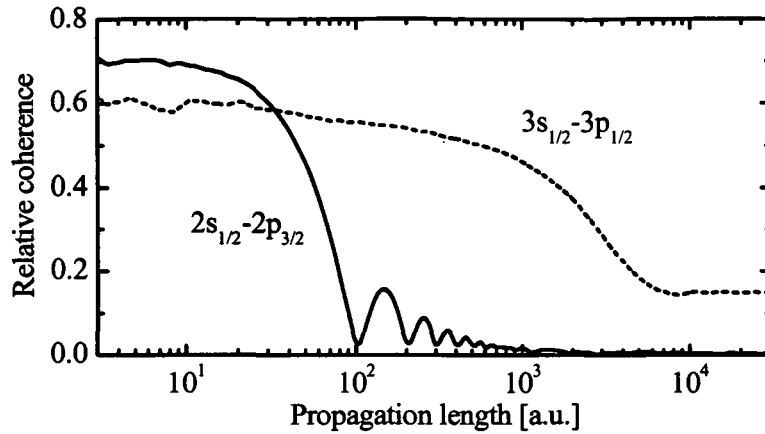


Figure 7.12: Relative coherence as a function of propagation length. Solid line: $|C_{2s_{1/2},2p_{3/2}}|$; dashed line: $|C_{3s_{1/2},3p_{1/2}}|$.

The main contribution to the population of excited states and also to coherences of excited states originates from the excitation of 1s. The gain term G in (7.9) is thus proportional to the excitation rate from 1s and is purely imaginary as expected for a single collision when the Born approximation holds.

The combination of $d_{ij}^{2\pi}$ and d_{ij}^{damp} for a certain coherence σ_{ij} and the range of investigated propagation lengths subdivide coherences into four groups classified by the energy spacing between the two coherent states. Inter-shell coherences decay very fast due to their very short dephasing length and are therefore unobservable in the experiment considered here. They are relevant on a short timescale where the Born-Markov approximation (see section 5.2) is not valid any more.

Coherences of states split by fine-structure decay slow enough to reach the time scale where the Born-Markov approximation is valid but fast compared to damping in further transport. They still decay in the single collision regime and we have the chance to observe dephasing before significant damping sets in. This corresponds to the limit discussed in equation (7.15). Figure 7.12 shows an example for dephasing of a fine-structure split coherence.

Coherences of states split by Lamb-shift have a longer dephasing path $d^{2\pi}$. These coherences do not get completely washed out by dephasing when multiple collisions and damping start contributing at longer propagation paths. In figure 7.12 we depict an example for this case in contrast to a coherence decaying by dephasing only. The $2s_{1/2}-2p_{3/2}$ is purely determined by dephasing as it is obvious by comparison with figure 7.11. The minima are located

at integer multiples of $d^{2\pi}$. The fact that it does not start at the value 1 for thin foils is the result of the different normalization in (5.69) and (5.69). For this case the simple model described in section 7.3.1 seems to reproduce the result of the complex system well. Differences are apparent in the second example shown in figure 7.12. The dephasing length for the $3s_{1/2}$ - $3p_{1/2}$ (compare table 7.1) is much longer than the damping length. The results can be approximately traced by equation (7.23) corresponding to decoherence by damping. However, two major differences can be observed. (i) The actual damping length seems to be approximately 1000 a.u. which is about a factor of two longer than predicted by the simple model in equation (7.25). (ii) The coherence is not entirely damped to zero but remains at a finite value. This indicates that the coherence populated by another source G that was not active at the beginning of the transport. In this case it is the excitation from $2s$ that starts contributing to $3s_{1/2}$ - $3p_{1/2}$.

The fourth group of coherences is between degenerate or near-degenerate states where $d^{2\pi}$ is very long and damping is the solely mechanism responsible for decoherence of these states. This corresponds to the limit discussed in equation (7.19). For a small subset of coherences damping is very weak allowing for a long lifetime for these coherences. The point to be noted is that most of the non-vanishing coherences in figure 7.7 and 7.8 survive for longer times than predicted by equation (7.24). The reason is that, as long as the primary source, the $1s$ ground state, is still populated, the excited-state coherences get replenished and a transient dynamical equilibrium is established for these coherences. In other words, decoherence and build-up of coherence compensate in these cases. In the following we discuss all these types of coherences (except for inter-shell coherences) in more detail.

Figure 7.7 and 7.8 do not present direct information on the phase of the density matrix element σ_{ij}^{NU} . We therefore display in figure 7.13, 7.14 and figure 7.15 the trajectories of a selected set of density matrix elements in the complex plane with snapshots taken at different propagation distances. While coherences shown in figure 7.13 and 7.14 are destroyed by dephasing, in figure 7.15 damping is the dominant decoherence mechanism. We investigate coherences split by fine-structure in figure 7.13 and 7.14 and such split by Lamb-shift in figure 7.15. For a better comparison we scale in figure 7.13 and 7.14 the propagation distance with the corresponding dephasing distance $d^{2\pi}$ for each coherence separately. Starting at the origin, the selected elements of the reduced density matrix $\sigma_{ij}^{NU}(d)$ (figure 7.13) evolve counterclockwise in the complex plane with increasing propagation path (compare figure 7.9). This subset has in common that the build-up of coherence already occurs in the single-collision regime. These elements approximately complete one circle after each multiple of $d^{2\pi}$. The shift, i.e. the fact that after 2π the

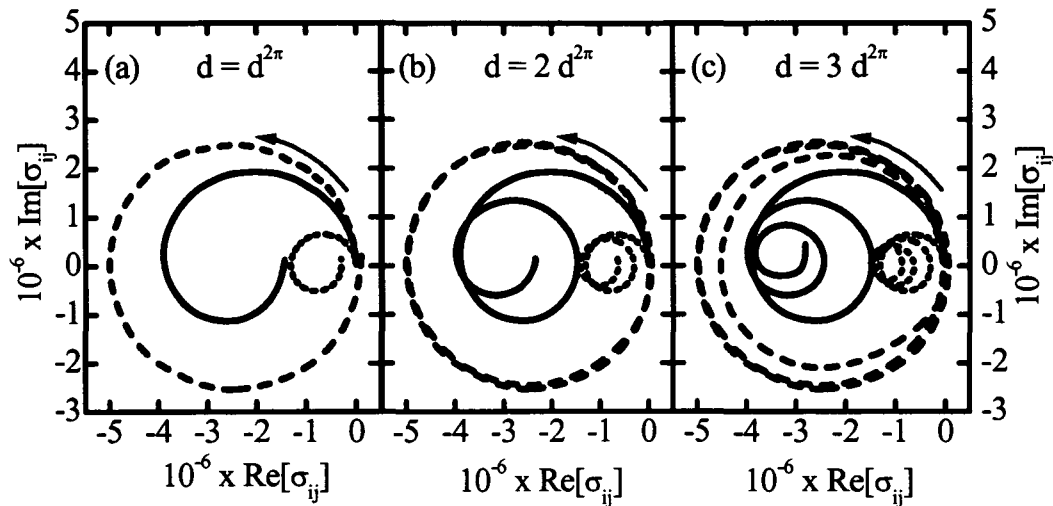


Figure 7.13: Evolution of selected elements of the density matrix σ_{ij}^{NU} of a Kr³⁵⁺ ion in transport through amorphous carbon at a velocity of $v_p = 47$ a.u. for different propagation lengths in the complex plane. The propagation length of each coherence has been chosen individually, such that in (a) it corresponds to the dephasing length shown in table 7.1; (b): $d=2 d^{2\pi}$; (c) $d=3 d^{2\pi}$. Solid lines: $\sigma_{3p_{3/2,3/2}, 3d_{5/2,3/2}}^{\text{NU}}$; dotted lines: $\sigma_{3p_{1/2,1/2}, 3d_{3/2,1/2}}^{\text{NU}}$; dashed lines: $\sigma_{2s_{1/2,1/2}, 2p_{3/2,1/2}}^{\text{NU}}$.

trajectory does not exactly return to its starting point, signifies the effect of multiple collisions and radiative decay during further transport. As we show in the same plot the coherences for different propagation lengths, the element $\sigma_{2s_{\frac{1}{2},\frac{1}{2}}, 2p_{\frac{3}{2},\frac{1}{2}}}^{\text{NU}}$ (dashed line in figure 7.13) with the shortest dephasing path $d^{2\pi}=100$ a.u. is least affected whereas $\sigma_{3p_{\frac{3}{2},\frac{3}{2}}, 3d_{\frac{5}{2},\frac{3}{2}}}^{\text{NU}}$ (solid line) with a ten times longer dephasing path is strongly perturbed. Multiple scattering and damping manifest themselves in a shift of the circle as well as in a shrinking radius of the rotation.

After a single rotation ($d=d^{2\pi}$) the relative coherence approaches the origin of the complex plane indicating a very fast decrease in coherence while still performing further revolutions. The relative coherence decays very fast because the populations as shown in figure 7.3 increase while the off-diagonal elements perform a circular motion (figure 7.13) that is bounded.

In figure 7.15 we selected those elements of $\sigma_{ij}^{\text{NU}}(d)$ with a long dephasing length $d^{2\pi}$ where multiple collisions dominate the build-up of coherence and decoherence. We selected four elements of $\sigma_{ij}^{\text{NU}}(d)$ that approach a non-

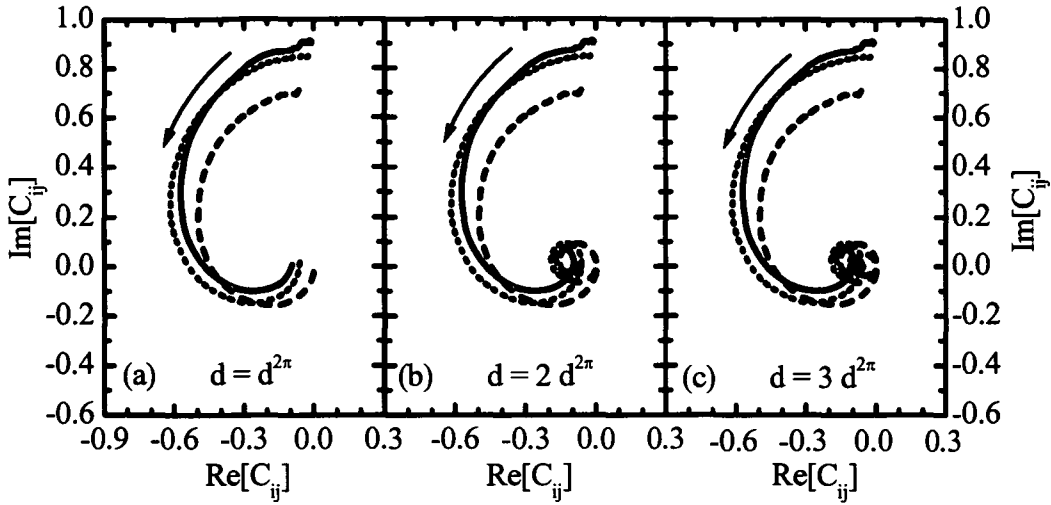


Figure 7.14: Evolution of selected elements of the density matrix σ_{ij}^{NU} of a Kr³⁵⁺ ion in transport through amorphous carbon at a velocity of $v_p = 47$ a.u. for different propagation lengths in the complex plane. We show the relative coherence C_{ij}^{NU} , i.e. the off-diagonal elements σ_{ij}^{NU} are normalized to the population of the involved states (σ_{ii}^{NU} and σ_{jj}^{NU} according to equation (5.69)). The propagation length of each coherence has been chosen individually, such that in (a) it corresponds to the dephasing length shown in table 7.1; (a) $d=d^{2\pi}$; (b) $d=2 d^{2\pi}$; (c) $d=3 d^{2\pi}$. Solid lines: $\sigma_{3p_{3/2,3/2},3d_{5/2,3/2}}^{NU}$; dotted lines: $\sigma_{3p_{1/2,1/2},3d_{3/2,1/2}}^{NU}$; dashed lines: $\sigma_{2s_{1/2,1/2},2p_{3/2,1/2}}^{NU}$.

vanishing (transient) equilibrium value of the relative coherence $|C_{ij}| \geq 0.1$ within the propagation distances studied. Starting at the origin (figure 7.15(a)) the coherences first evolve along circles of different radii (figure 7.15(b)). Note that in this figure (unlike figure 7.13 and 7.14) we have not rescaled the propagation path but show the density matrix for the identical propagation path in each plot ranging from $d=3 \times 10^2$ a.u. to $d=3 \times 10^4$. Therefore some elements with relatively short $d^{2\pi}$ succeed in almost completing one circle while others with a long $d^{2\pi}$ still evolve almost tangentially. Multiple collisions and radiative decay completely distort this circular motion for long propagation paths in figure 7.15(c). The long-time behavior of these elements of σ_{ij}^{NU} (d) mimics Brownian motion in the complex plane. Since these coherences are most sensitive to an accurate theoretical description, they provide a test for this approach.

It is important to note that the diagonal as well as the off-diagonal elements of σ_{ij}^{NU} are very sensitive to the competition between gain and loss.

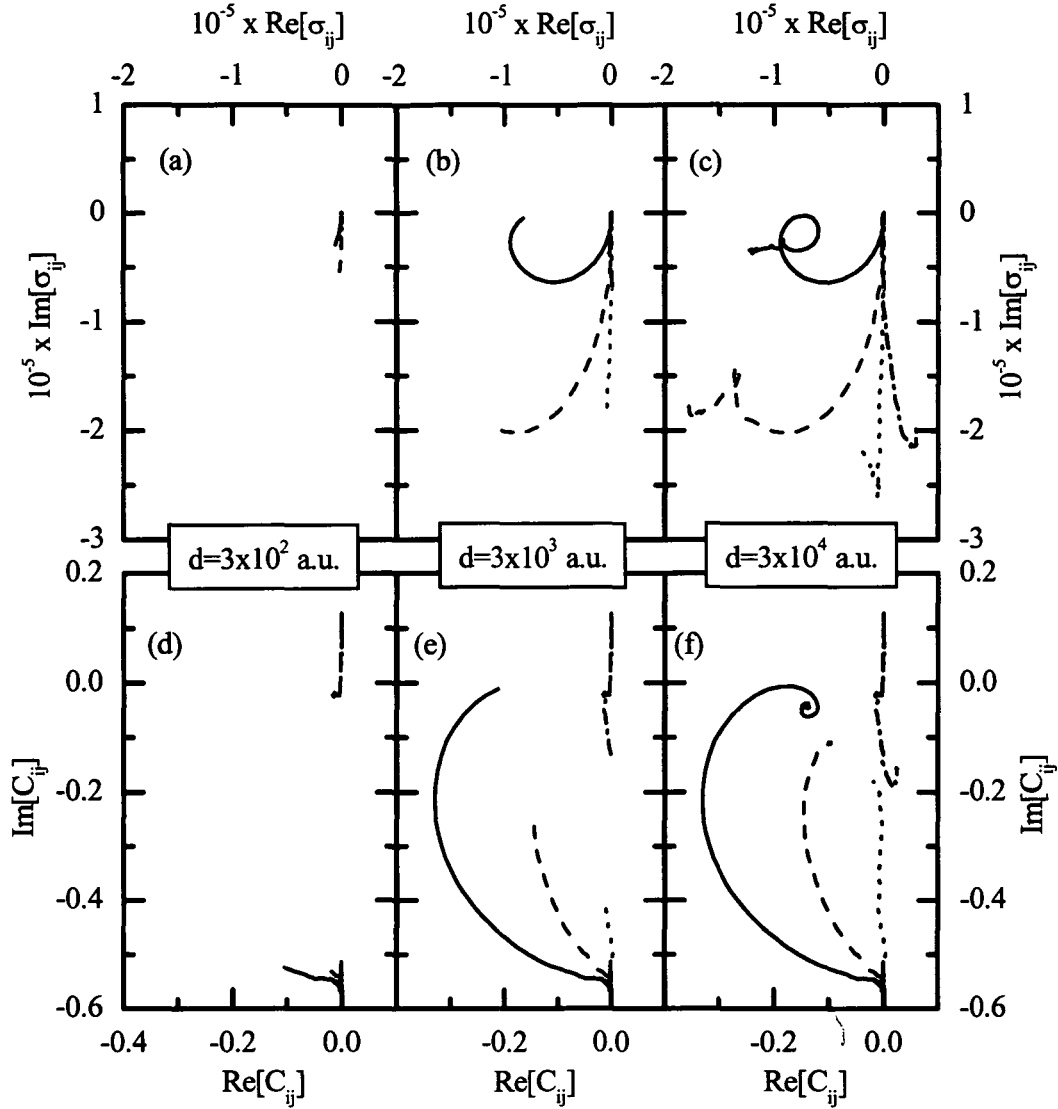


Figure 7.15: Evolution in the complex plane of selected elements of the density matrix σ_{ij}^{NU} of a Kr^{35+} ion in transport through amorphous carbon at a velocity of $v_p = 47$ a.u. for different propagation lengths. Upper row ((a), (b) and (c)) shows the off-diagonal elements of the density matrix σ_{ij}^{NU} while the lower row ((d), (e) and (f)) displays the relative coherences C_{ij} . Solid lines: $\sigma_{2s_{1/2,1/2},2p_{1/2,1/2}}^{NU}$; dashed lines: $\sigma_{3s_{1/2,1/2},3p_{1/2,1/2}}^{NU}$; dotted lines: $\sigma_{3p_{3/2,3/2},3d_{3/2,3/2}}^{NU}$; dot-dashed lines: $\sigma_{3p_{3/2,1/2},3d_{3/2,1/2}}^{NU}$. In (a-c) we show $\sigma_{2s_{1/2,1/2},2p_{1/2,1/2}}^{NU}/10$.

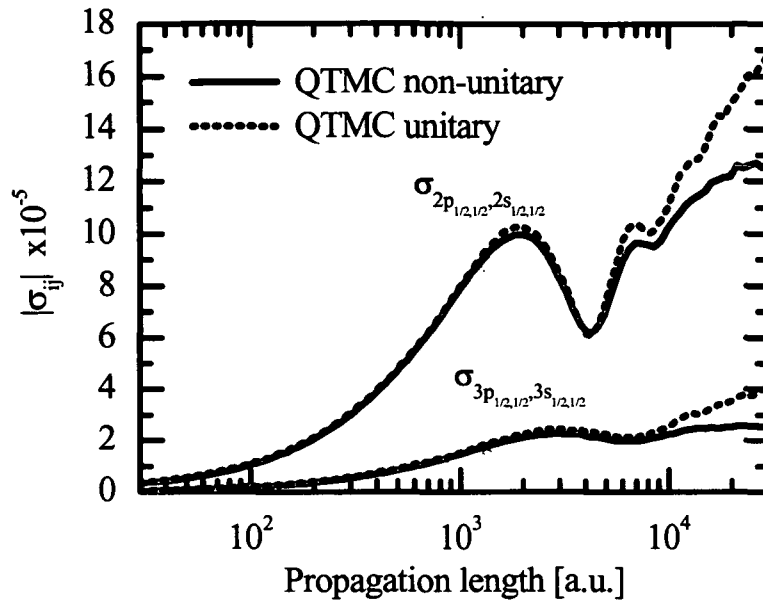


Figure 7.16: Comparison of selected coherences of a Kr^{35+} ion in transport through amorphous carbon at a velocity of $v_p = 47$ a.u. as a function of propagation length. We show the absolute magnitude $|\sigma_{ij}^{U,NU}|$ of coherences between s and p states for $n=2$ and $n=3$ obtained by a non-unitary QTMC (solid lines) and by a unitary QTMC simulation (dotted lines) with $n_{\max} = 4$.

It is the contribution from loss into the complement \mathbb{Q} that significantly changes σ_{ij}^{NU} in the region where a transient equilibrium persists. The diagonal elements of σ_{ii}^{NU} , the population probabilities, are clearly very different from a unitary σ_{ii}^U as discussed before. Likewise, the off-diagonal elements of $\sigma_{ij}^U(d)$ do not reach a transient equilibrium (figure 7.16) in contrast to those of $\sigma_{ij}^{NU}(d)$.

7.4 Comparison with experiment

We conclude this section by presenting a comparison with the experiment [Ver98] that originally stimulated our investigation. We consider the ratio between $3p_{1/2}$ and $3s_{1/2}$ which is sensitive to coherences that decay by damping (compare figure 7.16). The ratio of these populations can be expressed in terms of the intensity of emitted photons

$$\frac{I(3p_{1/2})}{I(3s_{1/2})} = 5.5855 \left(\frac{I(3p_{1/2} \rightarrow 2s_{1/2}) + I(3s_{1/2} \rightarrow 2p_{1/2})}{I(3s_{1/2} \rightarrow 2p_{3/2})} - 0.4361 \right) \quad (7.26)$$

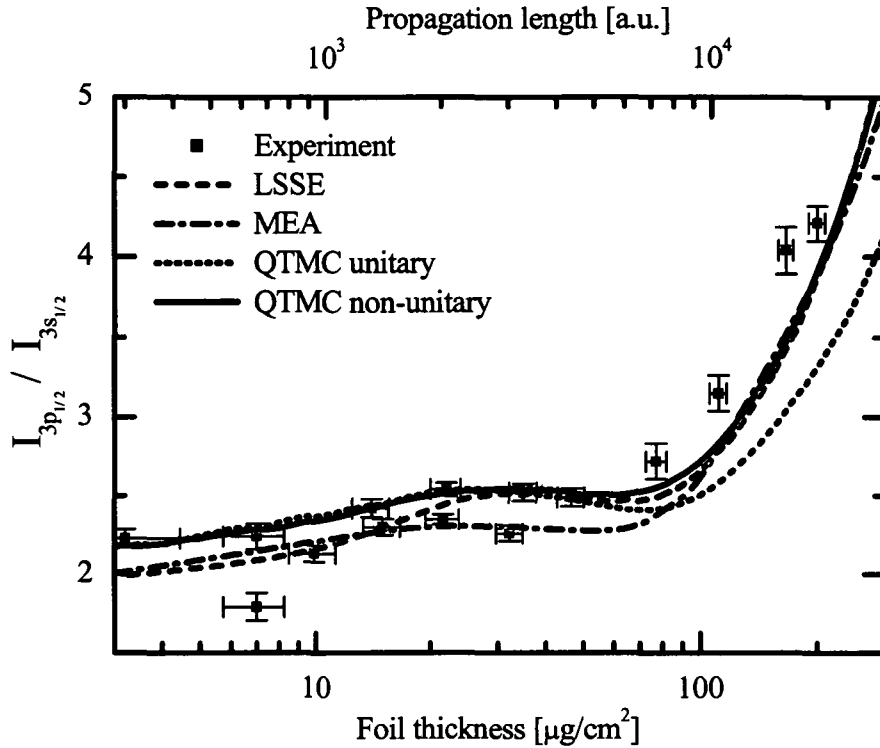


Figure 7.17: Relative line emission intensities $I_{3p_{1/2}}/I_{3s_{1/2}}$ resulting from the transmission of a $Kr^{35+}(1s)$ ion through amorphous carbon at a velocity of 47 a.u. as a function of target thickness. Symbols: experimental data from ref. [Ver98]; lines: theoretical calculations; dashed line: linear stochastic Schrödinger equation (LSSE) [Min02a]; dash-dotted line: master equation approach (MEA) [Ver01]; dotted line: unitary QTMC simulation; solid line: non-unitary QTMC simulation.

by considering the corresponding branching ratios.

There are two important details to be considered. First, the line intensities measured are integrated over the whole passage of the projectile through the foil and after exiting it. Therefore spatial information can only be obtained by repeating the measurement using targets of different thicknesses. Secondly, the contribution to a given Balmer line is not only determined by the population collisionally excited to the initial state of this radiative transition but also from all higher excited states feeding this state during the radiative cascade. In order to calculate the cascade contribution from $n > 4$ states, we extrapolate the quantum n, l, m distributions to higher n levels using scaling properties drawn from classical transport theory (CTT)(section

4.3). We apply the same extrapolation correction to both the unitary and non-unitary QTMC calculation.

In figure 7.17 we compare the experimental intensity ratio $I_{3p_{1/2}}/I_{3s_{1/2}}$ with results obtained by the non-unitary QTMC calculation. The non-unitary approach clearly improves the intensity ratio in the regime of multiple collisions for thicker targets and leads to much better agreement with the experimental findings than the unitary QTMC method. The non-unitary calculation agrees with the unitary calculation in the single collision regime and reproduces the experimental value in this limit. Overall, the QTMC method solving the NLSSE reproduces the measurements closest for short interaction times, while all theoretical calculations that account for ionization lead to the same results for thick targets. Only the unitary QTMC solution, which does not include ionization, underestimates the experimental data at large foil thicknesses. Consequently, the discrepancy observed in [Min03a] seems to be clarified.

7.5 Summary

We described the time evolution of the reduced density matrix of electronic degrees of freedom of a hydrogenic projectile by means of an open quantum system approach in the application to transport of a Kr³⁵⁺ ion through carbon. By describing the problem with the help of the non-unitary Lindblad master equation we could resolve a discrepancy with measurements that emerged in the description by a unitary Lindblad master equation. The good agreement with experimentally obtained intensity ratios of emitted photons underlines the need for a non-unitary treatment of this transport problem and indicates the validity of this approach for such a complex system. We find good agreement with experiment for all target thicknesses investigated. In comparison with other theoretical calculations we observe identical results for long propagation times with the master equation approach [Ver01] and also with the solution of the linear stochastic Schrödinger equation [Min02a].

We find that inclusion of loss processes via the non-unitary formulation leads to a modification of coherences and not just to a change of excited-state populations. Artificial pile-up of probability at high n is prevented as well as the overestimate of populations of states with large angular momentum.

We discussed the build-up of transient coherences in excitation. By means of a simple model we could identify characteristic features of the time evolution of coherences. While the fast dephasing of inter-shell coherences is beyond the scope of application of this description, dephasing of fine-structure split coherences could be discussed in contrast to damping of Lamb-shift split

and near-degenerate superpositions.

One conceptual short-coming of the formulation up to this point is the lack of a capture channel. While insignificant for the experimental data studied in this chapter, its inclusion is essential for further applications. In the next chapter we discuss the extension of the present method to account also for probability flux into the considered subsystem (i.e. electron capture). We apply it to the transport of initially bare projectiles where transient coherences are populated by electron capture.

Chapter 8

Open quantum system with a source

8.1 Introduction

In chapter 5 we have extended the strictly unitary Lindblad formalism and its quantum trajectory Monte Carlo solution by allowing for probability flux to flow into an unobserved complement. We have applied this method to a system, where the loss of probability (ionization of the electron) plays an essential role (chapter 7). In this chapter we go one step further and extend the non-unitary Lindblad formalism to additional source terms (such as electron capture) feeding probability flux into the observed system. This extension allows to apply the open quantum system approach to problems that exchange probability with the environment in both directions: loss and gain.

In section 8.2 we describe the modifications of the non-unitary Lindblad master equation including a probability source assigned to electron capture. To highlight various aspects of this approach and to show its validity we perform two numerical tests with a hydrogenic ion subject to radiative decay with a Hilbert space decomposed into a feeding part, a subspace and a complement (section 8.3). As an application we will describe a system where the initial state is formed by electron capture in chapter 9.

8.2 Source term in Lindblad master equation

We would like to use the Lindblad master equation (LME) to describe the time evolution of the density matrix of an open quantum system (OQS) that exchanges probability with the environment. In chapter 5.4 we have modified

the LME in such a way that it can account for probability flow out of the OQS. This became important for the transport of ions at longer propagation times where ionization started playing a role while capture could still be neglected. Ionization dominates over capture in fast projectiles, because capture cross sections fall off very fast with increasing projectile velocity. For transport of slower ions electron capture significantly contributes to the electronic population of the projectile. In order to be able to describe such systems within the OQS approach we have to modify the underlying LME and find the corresponding quantum trajectory Monte Carlo (QTMC) solution. For this purpose we include a source term in the master equation such that it describes the time evolution of the reduced density matrix under electron capture. While the extension of the unitary LME with a sink term led to modifications of the decay operators, the inclusion of a source has profound consequences on the Monte Carlo solution.

We start with the LME that describes the time evolution of the reduced density matrix $\sigma(t)$ of the subspace \mathbb{P}

$$\begin{aligned} \frac{d\sigma(t)}{dt} &= -i[H_S, \sigma(t)] - \frac{1}{2} [\Gamma^{\mathbb{P}\mathbb{P}}, \sigma(t)]_+ + \frac{1}{V} \sum_{\vec{k}} S^{\mathbb{P}}(\vec{k})\sigma(t)S^{\mathbb{P}\dagger}(\vec{k}) \\ &\quad - \frac{1}{2} [\Gamma^{\mathbb{P}\mathbb{Q}}, \sigma(t)]_+ \\ &= \{L\sigma(t)\} \end{aligned} \quad (8.1)$$

with transitions within the subspace described by $\Gamma^{\mathbb{P}\mathbb{P}}$ and transitions leading to probability flux outwards into the complement \mathbb{Q} described by $\Gamma^{\mathbb{P}\mathbb{Q}}$. To simplify the following discussion we abbreviate all terms in LME with a sink by $\{L\sigma(t)\}$.

The presence of a source of probability flux has two fundamental consequences on the dynamics of the OQS. The first is obvious, as a source creates probability within the considered subspace and thus populates $\sigma(t)$. We denote a source term representing a constant gain of probability as a rate F entering the LME. The gain is constant because the reservoir is considered as an infinitely large vendor. Quantifying the gain process in terms of state-to-state cross sections C per particle in the reservoir F is given by

$$F_{ij} = C_{ij}n_A v_p, \quad (8.2)$$

where the current of particles per unit time is expressed as a product of the number density of the target n_A and the projectile velocity in the rest frame of the target v_p . F represents a rate in units of inverse time. i and j denote states within the subspace \mathbb{P} .

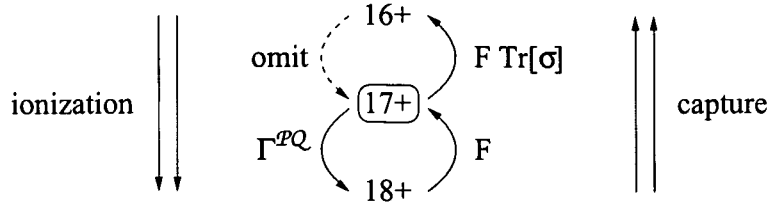


Figure 8.1: Schematic drawing of the argon charge states affected by electron capture and ionization. The corresponding components entering the Lindblad master equation are indicated.

The second consequence of a constant source is actually a loss term in the LME. This is at first glance particularly surprising, but becomes clear when we consider that the Hilbert space \mathbb{H}_S we deal with is a one-electron space. A two-electron state is not contained within \mathbb{H}_S . Therefore the capture of a second electron leads to a loss of probability in a one-electron Hilbert space. This loss is proportional to the probability of occupation of the one-electron state, which is determined by the trace over $\sigma(t)$, and by the probability for a second electron capture. In the particular case that the source is equally effective in populating the one-electron and the two-electron state, we can write this rate as $-F \text{Tr}[\sigma(t)]$. With these ingredients we can extend the LME in (8.1) by

$$\frac{d\sigma(t)}{dt} = \{L\sigma(t)\} + F(1 - \text{Tr}[\sigma(t)]). \quad (8.3)$$

Since $\text{Tr}[\sigma(t)] \leq 1$ the outgoing flux can never be larger than the incoming flow of probability. Consequently, the effectiveness of the source is reduced. The amount of reduction depends on the probability that has already flowed in. Since we approximate the driving force, i.e. electron capture, with the same rate for these two processes, the combination of them leads to populating $\sigma(t)$ according to F_{ij} . In the case the source and sink would affect $\sigma_{ij}(t)$ differently, we would see redistribution of states in $\sigma_{ij}(t)$.

Taking the example of transport of an initially bare argon projectile we can assign the terms to the following processes (see figure 8.1). The simulated subspace \mathbb{P} represents bound states of Ar^{17+} . Ionization described by $\Gamma^{\mathbb{P}\mathbb{Q}}$ in the LME in (8.1) corresponds to $\text{Ar}^{17+} \rightarrow \text{Ar}^{18+}$. F describes the electron capture channel transforming the Ar^{18+} ion into Ar^{17+} . The last term ($F\text{Tr}[\sigma(t)]$) describes additional capture, thus the process $\text{Ar}^{17+} \rightarrow \text{Ar}^{16+}$. In our simulation we explicitly describe the hydrogenic Hilbert space, i.e. Ar^{17+} . Ionization as well as second capture transfer the probability out of the described Hilbert space. While recapture of ionized electrons is very

unlikely, single ionization of Ar^{16+} would again contribute to Ar^{17+} . Since we do not explicitly treat the helium like Ar^{16+} we cannot account for $\text{Ar}^{16+} \rightarrow \text{Ar}^{17+}$ as well.

We approximately estimate capture cross sections for the second capture by the cross sections for the first capture. This approximation is reasonable due to the similar charge states ($18/17 \sim 1+0.06$) and due to the lack of a direct calculation of the corresponding cross sections.

Nonlinear stochastic Schrödinger equation

Before introducing the solution of the LME with a source (8.3) we consider the equation of motion of a quantum trajectory. It is governed by the nonlinear stochastic Schrödinger equation (NLSSE). The NLSSE solving the LME with a sink in (8.1) was determined as

$$\begin{aligned}
 |d\Psi^\eta(t)\rangle &= \left\{ -i H_S^\mathbb{P} dt - \frac{dt}{2} \left(\Gamma^\mathbb{P} - \langle \Gamma^{\mathbb{P}\mathbb{P}} \rangle_{t,\eta} \right) \right. \\
 &\quad \left. + \frac{1}{V} \sum_{\vec{k}} dN_{\vec{k}}^\eta(t) \left(\frac{S^\mathbb{P}(\vec{k})}{\sqrt{\langle \Gamma^{\mathbb{P}\mathbb{P}}(\vec{k}) \rangle_{t,\eta}}} - 1 \right) \right\} |\Psi^\eta\rangle \\
 &= \{M\} |\Psi^\eta(t)\rangle
 \end{aligned} \tag{8.4}$$

which we abbreviate by $\{M\} |\Psi^\eta\rangle$ in the further discussion.

Intuitively a source of probability is expected to add probability according to the rate F . While F is a two dimensional matrix, the wave vector is one-dimensional. To construct the source term for the NLSSE we first diagonalize C and reassemble it by means of the normalized eigenvectors X and eigenvalues ev

$$C_{nm} = \sum_k \sqrt{ev_k} X_{nk} \times X_{mk}^\dagger \sqrt{ev_k} = \sum_k |X_n(k)\rangle \langle X_m(k)| ev_k. \tag{8.5}$$

The NLSSE solving the LME with a source (8.3) can be constructed as

$$|d\Psi^\eta(t)\rangle = \{M\} |\Psi^\eta\rangle + \sum_k dN_k^{F,\eta}(t) |X(k)\rangle \tag{8.6}$$

with the Ito differential $dN_k^{F,\eta}(t)$ being one in an infinitesimally short time interval and otherwise zero. $dN_k^{F,\eta}(t)$ is one when a capture process occurs and a capture wave vector $|X(k)\rangle$ is assigned to $|\Psi^\eta\rangle$. This procedure is fundamentally different from scattering where probabilities are redistributed.

To determine $dN_k^{F,\eta}(t)$ we calculate the differential change of the reduced density matrix as

$$\begin{aligned} d\sigma^\eta(t) &= |d\Psi^\eta(t)\rangle\langle d\Psi^\eta(t)| \\ &= \{M\} |\Psi^\eta(t)\rangle\langle\Psi^\eta(t)| \{M\}^\dagger + \sum_{kk'} dN_k^{F,\eta}(t) |X(k)\rangle\langle X(k')| dN_{k'}^{F,\eta}(t) \end{aligned}$$

For the ensemble $d\sigma(t) = \sum_\eta |d\Psi^\eta(t)\rangle\langle d\Psi^\eta(t)|$ of a large number of trajectories η we find that the Ito differential is, on the average, determined by

$$\overline{dN_k^{F,\eta}(t)dN_{k'}^{F,\eta}(t)} = \overline{dN_k^{F,\eta}(t)}\delta_{kk'} = \delta_{kk'} dt n_A v_p ev_k (1 - Tr[\sigma(t)]) \quad (8.7)$$

leading to

$$d\sigma(t) = \{L\sigma(t)\} dt + n_A v_p (1 - Tr[\sigma(t)]) dt \sum_k |X(k)\rangle ev_k \langle X(k)|, \quad (8.8)$$

where we can identify C according to (8.5) and simplify to

$$\begin{aligned} d\sigma(t) &= \{L\sigma(t)\} dt + n_A v_p (1 - Tr[\sigma(t)]) dt C \\ &\quad \{L\sigma(t)\} dt + F (1 - Tr[\sigma(t)]) dt. \end{aligned} \quad (8.9)$$

This is exactly the LME we wanted to solve.

QTMC solution

After having introduced the NLSSE in (8.6) we would like to find a QTMC solution. For this purpose we decompose $\sigma(t)$ into single trajectories

$$\sigma(t) = \sum_\eta |\Psi^\eta(t)\rangle\langle\Psi^\eta(t)|, \quad (8.10)$$

where the time evolution of a wave vector is determined by the time evolution operator U as

$$|\Psi^\eta(t)\rangle = U^\eta(t)|0\rangle. \quad (8.11)$$

Initially, the projectile is bare ($|0\rangle$) so that the wave vector $|\Psi^\eta(t)\rangle$ gets populated only in the capture event when an eigenvector $|X(k)\rangle$ is assigned. We denote the time of this capture event by t_0 . Then $|\Psi^\eta(t)\rangle$ evolves according to the LME without a source (8.4). The second capture is accounted for in the reduced capture rate in (8.3). The corresponding time evolution operator is denoted by $U_{(H)}$. For a specific capture time t_0 and an eigenvector k we can describe a quantum trajectory by

$$|\Psi^\eta(t)\rangle = U_{(H)}^\eta(t - t_0)|X(k)\rangle. \quad (8.12)$$

Taking into account all eigenvectors $|X(k)\rangle$ and all capture times t_0 we have

$$|\Psi^\eta(t)\rangle = \sum_k \int_0^t dt_0 U_{(H)}^\eta(t-t_0) |X(k)\rangle \frac{dN_{\bar{k}}^{F,\eta}(t_0)}{dt_0}, \quad (8.13)$$

where we have transformed the integration over the Ito differential into an integration over the capture time t_0 . The reduced density matrix is then given by

$$\begin{aligned} \sigma(t) &= \sum_\eta \sum_{kk'} \int_0^t dt_0 U_{(H)}^\eta(t-t_0) |X(k)\rangle \langle X(k')| U_{(H)}^{\eta\dagger}(t-t_0) \\ &\quad \times \frac{dN_{\bar{k}}^{F,\eta}(t_0) dN_{\bar{k}'}^{F,\eta}(t_0)}{dt_0}, \end{aligned} \quad (8.14)$$

summing over an ensemble of stochastic realizations and taking the expectation value of the Ito differential. Consequently, we do not sample the stochastic variable of the source ($dN_{\bar{k}}^{F,\eta}(t_0)$) but integrate over time t_0 . The advantage is that fewer stochastic realizations η are necessary in order to obtain a converged result.

After rearranging summations and integration we obtain

$$\begin{aligned} \sigma(t) &= \int_0^t dt_0 n_A v_p (1 - \text{Tr}[\sigma(t_0)]) \\ &\quad \times \sum_\eta \sum_k U_{(H)}^\eta(t-t_0) |X(k)\rangle \langle X(k)| U_{(H)}^{\eta\dagger}(t-t_0). \end{aligned} \quad (8.15)$$

The bottom line corresponds to the solution of the LME without a source (8.1) with C as initial condition. We denote it by $\sigma^{(H)}(t)$. With this simplification the solution of the LME with a source (8.3) becomes

$$\sigma(t) = \int_0^t dt_0 n_A v_p (1 - \text{Tr}[\sigma(t_0)]) \sigma^{(H)}(t-t_0), \quad (8.16)$$

where $\sigma^{(H)}$ is determined by

$$\begin{aligned} \sigma^{(H)}(t) &= \sum_k \langle ev_k | \sum_\eta U_{(H)}^\eta(t) |X(k)\rangle \langle X(k)| U_{(H)}^{\eta\dagger}(t) \\ &= \sum_k \langle ev_k | \sigma^{(H)}(k, t). \end{aligned} \quad (8.17)$$

The trace of $\sigma(t)$ (8.16) becomes

$$\text{Tr}[\sigma(t)] = \int_0^t dt_0 n_A v_p (1 - \text{Tr}[\sigma(t_0)]) \text{Tr}[\sigma^{(H)}(t-t_0)], \quad (8.18)$$

which is an implicit equation for $Tr[\sigma(t)]$ that can be solved only numerically.

In summary, we have modified the Lindblad master equation such that it can account for electron capture. For this purpose we have introduced a source term that is directly related to the state-to-state capture cross sections. We have developed a QTMC solution for this modified Lindblad master equation. This solution is based on the solution of a reduced problem, namely the time evolution of a density matrix initially populated by a capture event and then propagated according to a LME without a source.

8.3 Application to radiative cascade

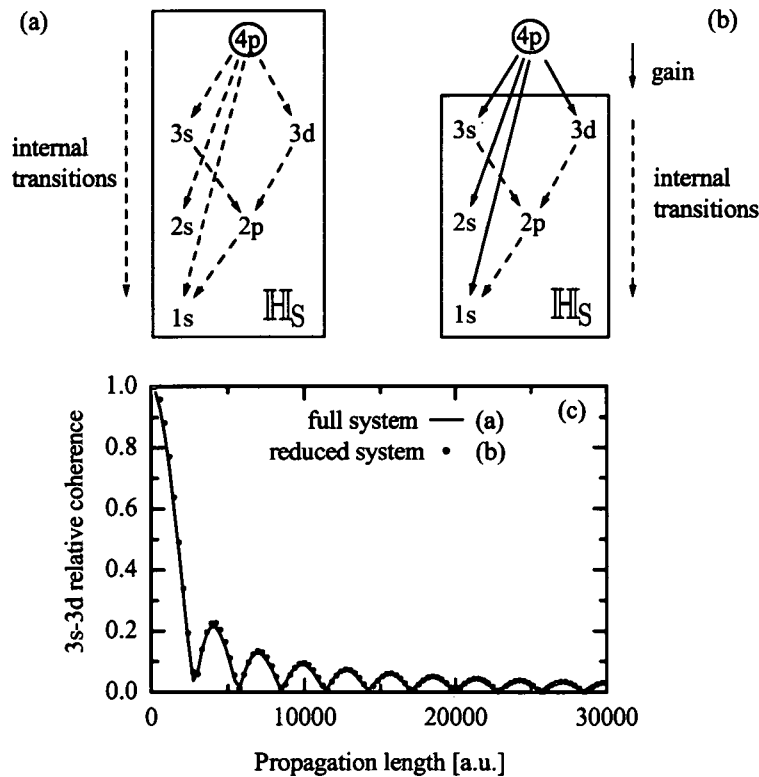


Figure 8.2: Schematic picture of the radiative cascade of a hydrogenic argon ion initially in the $4p_{3/2,1/2}$ state. (a): full system; (b): reduced system considering decay of the initial state as a source; (c): comparison of absolute magnitude of relative coherence between $3s_{1/2,1/2}$ and $3d_{3/2,1/2}$ as a function of propagation time: line: exact results; symbols: results of LME with source for the reduced system.

We first apply the newly developed method to a system where an exact solution is available against which we can test our numerical results. For this purpose we consider the cascade of a hydrogenic argon ion initially in an excited state radiatively decaying into the ground state. We focus on the case where the initial state is not included in the simulated subspace. The cascade electron therefore represents a gain of probability and the time evolution of the reduced density matrix of the subspace can be described by the LME including a source term (8.3). The source term F is determined by radiative transitions from the initial state. In contrast, for a Hilbert space H_S which spans over the initial and all states of the radiative decay cascade the time evolution is fully contained in the simulation and thus can be described by the unitary Lindblad master equation. The full system (figure 8.2(a)) serves as a test for the accuracy of the numerical results obtained for the reduced system. In section 8.3.1 we first analyze a system with a gain of probability and in section 8.3.2 we proceed to a system described by gain and loss.

8.3.1 Radiative cascade as source

For a first numerical test we reduce the size of the Hilbert space such that it contains only the final states of the radiative decay of the initial state but not the initial state itself (figure 8.2(b)). The transitions from the initial state have to be considered as gain into the reduced Hilbert space H'_S . The source term F entering the LME (8.3) is constructed by the transition operators $S_{ij}^{(r)}(\mathcal{J})$ describing radiative decay (see equation (3.31)) for the polarization directions $\mathcal{J} = x, y$, and z as

$$F_{ij}^{\text{casc}} = \sum_{\mathcal{J}}^{xyz} S_{\alpha i}^{(r)\dagger}(\mathcal{J}) S_{j\alpha}^{(r)}(\mathcal{J}) \quad (8.19)$$

with the initial state $\alpha = 4p_{3/2,1/2}$. Note that unlike the calculation for the decay operator $\Gamma_{ij}^{(r)} = \sum_{\nu} \sum_{\mathcal{J}} S_{i\nu}^{(r)\dagger}(\mathcal{J}) S_{\nu j}^{(r)}(\mathcal{J})$ the two inner indices are not equal. Equation (8.19) describes flux into the diagonal elements of the density matrix as well as build-up of coherences in the off-diagonal elements of F_{ij}^{casc} .

This model system does not feature a loss channel. Consequently the trace of $\sigma^{(H)}(t)$ is constant $Tr[\sigma^{(H)}(t)] = Tr[F^{\text{casc}}]$ simplifying the integral equation (8.18) to

$$Tr[\sigma(t)] = Tr[F^{\text{casc}}] \left(t - \int_0^t dt_0 Tr[\sigma(t_0)] \right) \quad (8.20)$$

The time evolution of the density matrix is calculated according to (8.16).

To test our approach we compare the absolute magnitude of relative coherence between 3s and 3d (figure 8.2(c)) that is built-up by direct radiative transition from the initial 4p state. The good agreement between the reduced and the full calculation verifies the validity of the method. The described feeding in the Lindblad formalism can also correctly reproduce the time evolution of the off-diagonal elements of the reduced density matrix.

8.3.2 Radiative cascade as source and sink

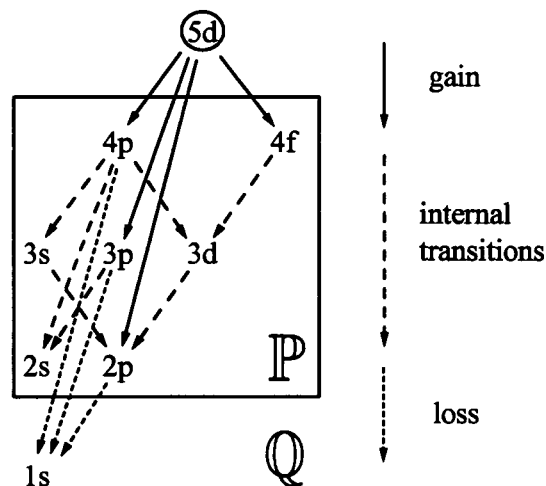


Figure 8.3: Outline of radiative cascade of a hydrogenic argon ion initially in the $5d_{3/2,1/2}$ state. Solid lines: gain of probability; long dashed lines: internal radiative transitions within the subspace \mathbb{P} ; short dashed lines: loss to the complement \mathbb{Q} .

In a second numerical test we consider the Lindblad master equation describing also loss of probability. The model system we analyze is an excited hydrogenic argon ion initially in the $5d_{3/2,1/2}$ state as shown in figure 8.3. We decompose the Hilbert space into three parts. (i) The first part contains the initial state and serves as a source of probability. (ii) The simulated subspace \mathbb{P} spans over the final states of direct radiative transitions from the initial state, i.e. all states within the shells $n=2-4$. (iii) The complement \mathbb{Q} not explicitly described is the ground state (1s). By this subdivision the radiative cascade enters the LME in three different ways. Decay of the initial state is described by the source term F^{casc} as defined in equation (8.19) with $\alpha = 5d_{3/2,1/2}$. Transitions within the subspace \mathbb{P} are accounted for by the transition operator $S^{\mathbb{P}}$ leading to the decay operator $\Gamma^{\mathbb{P}\mathbb{P}}$. Decay into the

1s ground state is described by $\Gamma^{\mathbb{P}\mathbb{Q}}$ in the LME. The time evolution of the density matrix is obtained as described in the previous section. The trace is determined by equation (8.20), while the individual elements are calculated according to (8.16). In combination with an exact calculation this system represents an ideal test for the generalized non-unitary LME. The exact results are obtained when \mathbb{P} spans over all states affected by the cascade including the initial state.

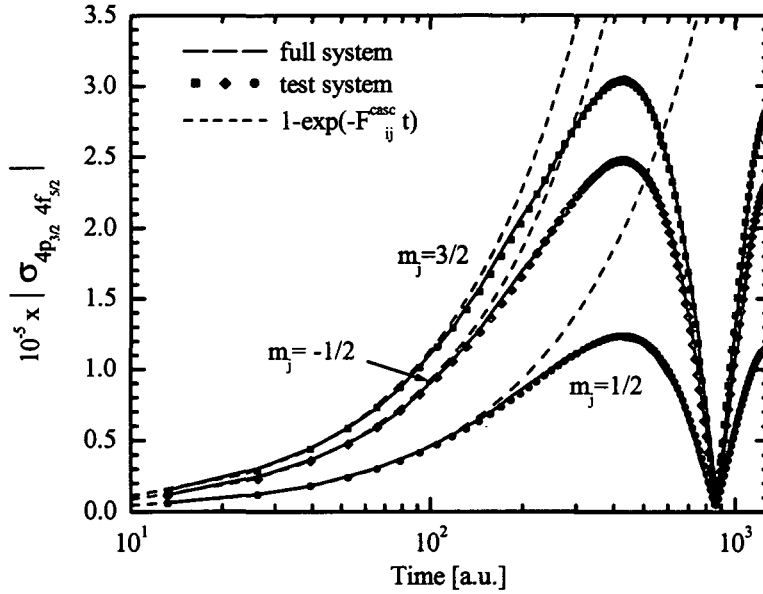


Figure 8.4: Absolute magnitude of coherence between $4p_{3/2, m_j}$ and $4f_{5/2, m_j}$ for $m_j = -1/2, 1/2$ and $3/2$ of argon populated by radiative decay from $5d_{3/2, 1/2}$. Solid lines: exact calculation; symbols: calculation according to the modified Lindblad master equation (8.3) for the system displayed in figure 8.3; dashed lines: exponential increase according to $1 - \exp(-F_{ij}^{\text{casc}} t)$.

To demonstrate the validity of the solution of the modified Lindblad master equation we consider the coherence between 4p and 4f. In figure 8.4 the coherence $4p_{3/2}-4f_{5/2}$ is depicted for different values of m_j . For short times the coherence increases exponentially according to $1 - \exp(-F_{ij}^{\text{casc}} t)$ with the corresponding gain rate F_{ij}^{casc} as indicated in figure 8.4. For longer times transitions within the subspace \mathbb{P} and also loss to \mathbb{Q} significantly modify the results as observed by the deviation from the simple exponential growth. The agreement between the exact calculation and the solution of the reduced system (figure 8.3) is given not only on the short time scale but also in the limit of long propagation times.

This first application of the LME with a source term shows that the solution (8.16) provides an accurate description of the time evolution of the reduced density matrix. For the radiative cascade we had the opportunity to compare with an exact solution. In the application to ion-solid transport we will have no exact results at hand to compare with. Therefore a verification of the method itself and its numerical implementation is a first step towards more complex problems.

8.4 Summary

In our aim to develop an open quantum system approach applicable to transport problems we have introduced a source term in the Lindblad master equation. This extension opens up a wide field of applications since most realistic open quantum systems do not exchange only energy with the environment but also probability flux. After having investigated the flow of flux out of the system in the first part of this thesis we now closed the cycle by considering also probability flux into the system.

After describing the modifications of the Lindblad master equation we have provided a solution by a Monte Carlo method. We have shown that this solution can be constructed by means of solutions of another problem. This is time evolution of the initial conditions determined by the source term and subsequently described by the non-unitary Lindblad master equation without a source.

As a first application we considered the radiative cascade from an excited state as feeding of deeply bound states. In comparison with an exact solution we could demonstrate the accuracy of our method. In the next chapter we will apply this method to the transport of excited states populated by electron capture.

Chapter 9

Application to Ar^{18+} transport

9.1 Introduction

In the previous chapter we have introduced the solution of an open quantum system with a source by means of the QTMC method. As an application we will describe in this chapter a system where the initial state is formed by electron capture while further system-reservoir interaction drives transitions within the system also leading to probability flux outwards. We focus on coherences produced by electron capture.

This study is motivated by recent measurements on excited state populations formed by electron capture in ion-solid transport. The experiment we compare with has been performed with the same setup as the experiments described in chapter 7 (for details see [Ver98, Lam97, Fou00] or figure 2.4 for a schematic picture). The collision system is a bare argon ion in transport through carbon at an energy of 13.6 MeV/amu that corresponds to a projectile velocity of $v_p = 23$ a.u.. The target thickness was varied between 2 and 200 $\mu\text{g}/\text{cm}^2$ corresponding to a propagation length from approx. 200 to 2×10^4 a.u. For this collision system the MFP for electron capture is approximately 4×10^4 a.u. which is longer than the thickest targets considered. Hence single collision conditions are fulfilled for the capture process for all propagation lengths.

The measured ratio between fine structure states $2p_{1/2}$ and $2p_{3/2}$

$$R_I = \frac{I(2p_{1/2} \rightarrow 1s_{1/2})}{I(2p_{3/2} \rightarrow 1s_{1/2})} \quad (9.1)$$

shows a significant solid state effect (figure 9.1). To exclude solid state effects also measurements with a CH_4 gas target instead of the solid carbon foil were performed. Calculations within the master equation approach (see section

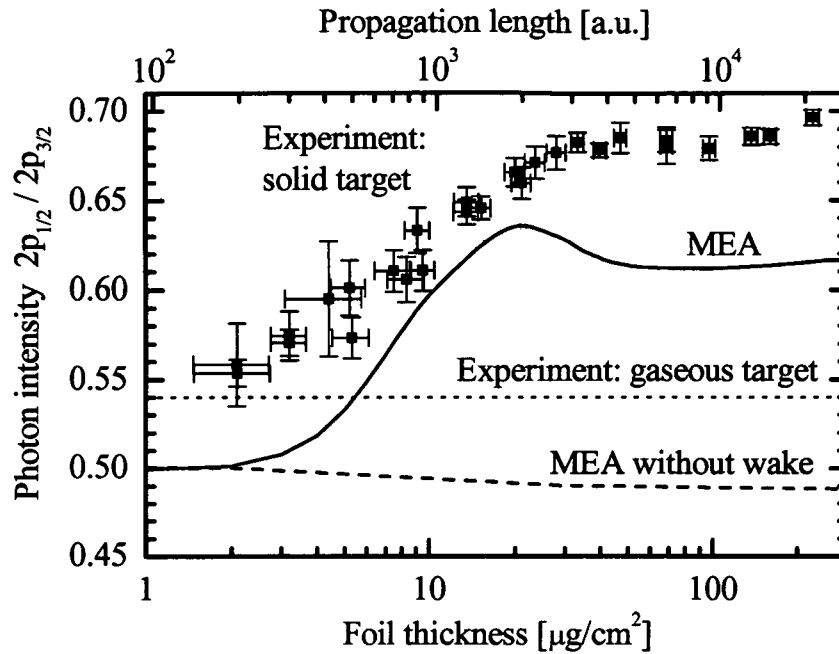


Figure 9.1: Ratio R_I between $2p_{1/2}$ and $2p_{3/2}$ as a function of foil thickness during transport of an Ar^{17+} ion through carbon ($v_p = 23$ a.u.) initially in the Ar^{18+} state. Symbols: experimental results for solid targets; dotted line: experimental results for gaseous CH_4 target as reference line; solid line: full MEA calculation ; dashed line: MEA calculation neglecting the wake field.

5.5.1) using CDW capture cross sections (section 3.4.2) can not fully reproduce these experimental findings. Results obtained by the same simulation with the wake field turned off show almost no solid state effect. The sensitivity to the wake field indicates a sensitivity to coherences during transport.

To resolve this issue we perform a simulation of this transport problem by means of the open quantum system approach developed in this thesis. In order to account for the build-up of excited states populations by electron capture we employ the non-unitary Lindblad master equation with a source term as described in chapter 8.2, where the source of probability is represented by electron capture.

In section 3.4 we have provided an overview over the available methods. We have found different capture cross sections resulting from different theoretical models. The comparison with measurements allows to test theoretical predictions for the electron capture process.

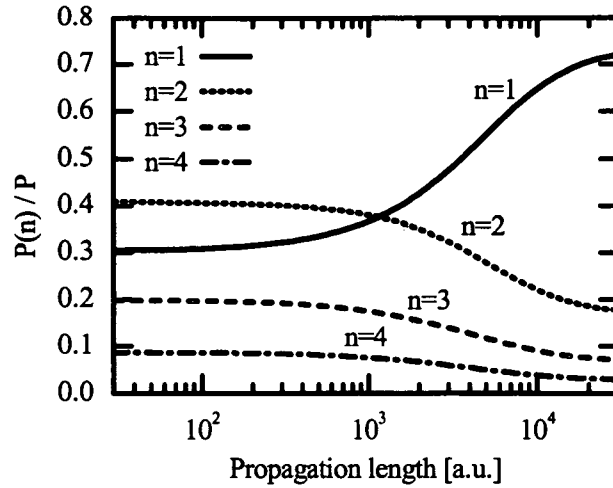


Figure 9.2: Evolution of relative shell populations of Ar^{17+} as a function of propagation length during transport of an initially bare argon ion through an amorphous carbon foil. The simulated shell populations are normalized to the overall charge state probability of Ar^{17+} .

9.2 Numerical simulation

At the entrance of the foil the initial state is a bare Ar^{18+} projectile while electron capture in the target populates the hydrogenic projectile states. In figure 8.1 we sketched the main processes changing the charge state. Electron capture also populates helium-like Ar^{16+} states. In our simulation we represent deeply bound one-electron projectile states with $n_{max}=4$. Therefore transitions to Ar^{16+} represent an effective loss of probability. The time evolution of the reduced density matrix is described by the Lindblad master equation (8.3). The electron capture cross sections enter the source term F_{ij} in (8.3) according to equation (8.2) where C_{ij} corresponds to the capture density matrix elements. We approximate second electron capture cross sections by the one-electron capture cross sections in order to include the source term in the Lindblad master equation as denoted in (8.3). The other terms in (8.3) accounting for core scattering, electron-electron interaction and radiative decay are equivalent to the ones used in chapter 7 for the transport of a krypton ion. Ionization is accounted for as well.

In section 8.2 we have presented a solution of (8.3). The method we proposed is to first solve the Lindblad master equation without a source (8.1) for an initial reduced density matrix given by the same cross sections that also enter the source term, i.e. $\sigma_{ij}^{(H)}(0) = C_{ij}$. In a second step we

obtain $\sigma_{ij}(t)$ as the solution of the Lindblad master equation with a source by solving numerically the integral in equation (8.16). As initial conditions we consider the electron capture density matrix resulting from the LTDSE calculation (section 3.4.3). Since these results are available only for $n \leq 3$ we take for $n=4$ values calculated by CDW (section 3.4.2). If not stated otherwise, we use this composed capture density matrix.

We investigate different aspects of the transition of $\sigma_{ij}(t)$ from a capture density matrix to a dynamical equilibrium determined by transport. First we discuss mixing of angular momentum and then focus on the build-up of coherences and decoherence by dephasing and damping. The relative shell populations are effectively modified by transport as shown in figure 9.2. In the single capture regime, or equivalently short propagation lengths, the relative populations are directly related to the cross sections in figure 3.5 where capture into $n=2$ is most dominant. In further transport excited states populations get either ionized or they radiatively decay into the ground state. Therefore the relative weight of $P(n=1)$ is increasing while $P(n>1)$ gets depleted during transport. The relation between $P(n=2)$, $P(n=3)$ and $P(n=4)$ remains almost constant (figure 9.2). At the longest propagation length considered (3×10^4 a.u.) an equilibrium seems to be established where the amount of captured probability distribution compensates mixing effects during transport. The long time limit is characterized by three components: feeding by capture, collisional excitation of the ground state and mixing by transport.

Considering relative populations within one shell (figure 9.3) we can investigate transport effects in more detail. According to figure 3.4, capture cross sections are largest for p-states and rapidly decrease for higher angular momenta. This general tendency is independent of the method applied to calculate the cross sections. On the other hand, transport tends to populate higher angular momentum states as is clearly seen in figure 9.3 at large propagation paths. This is due to the fact that collisions tend to align the angular momentum with the quantization axis, i.e. $m_l \rightarrow l$, while the wake potential is responsible for l-mixing by preserving m_l . Only the combination of both effects can be responsible for accessing all magnitudes and orientations of angular momenta [Rei00]. For the present collision system, the consequence is that in the limit of long propagation times the relative intra-shell probabilities are distributed proportionally to the magnitude of the angular momentum. In figure 9.3 we can observe a radical change of relative populations from single capture to equilibrium via a transient phase of dramatic mixing up to propagation lengths of $d \approx 2000$ a.u..

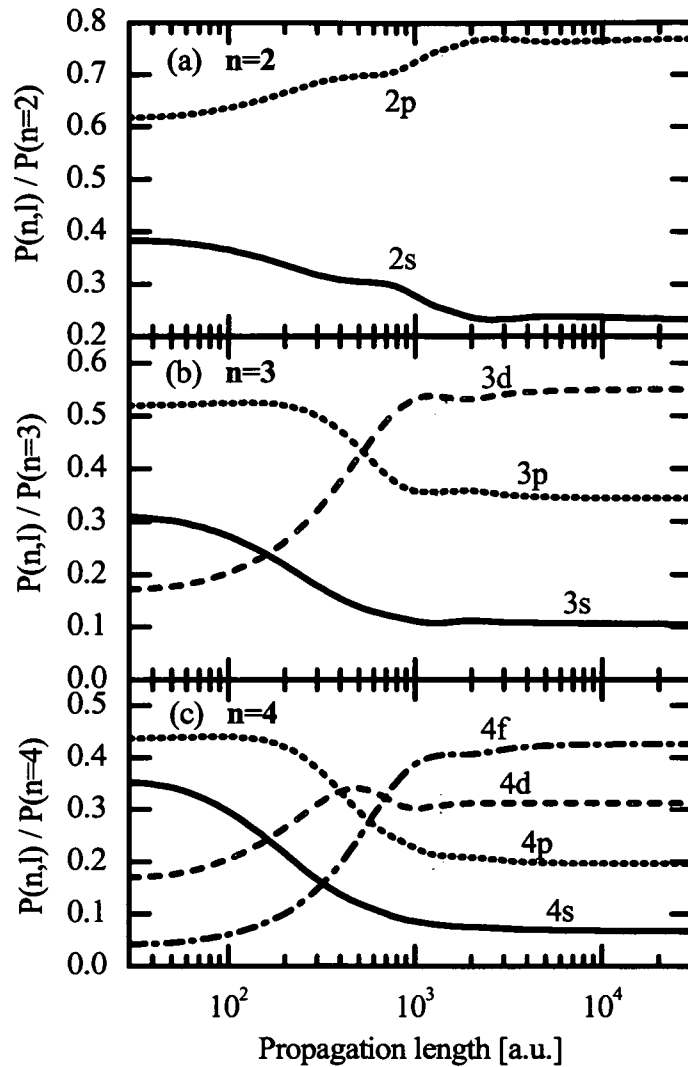


Figure 9.3: Evolution of relative populations of Ar^{17+} as a function of propagation length during transport of an initially bare argon ion through an amorphous carbon foil. The simulated populations are presented as a function of n and l . The results are normalized to the overall probability in the corresponding shell: (a) $P(n=2,l)$; (b) $P(n=3,l)$; and (c) $P(n=4,l)$.

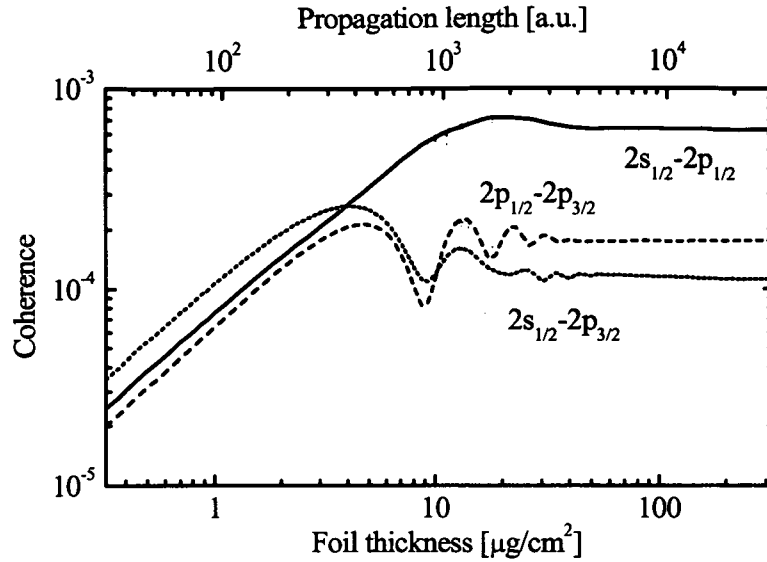


Figure 9.4: Coherence as a function of propagation length calculated with the QTMC method. Solid line: $|\sigma_{2s_{1/2}, 2p_{1/2}}|$; dotted line: $|\sigma_{2s_{1/2}, 2p_{3/2}}|$; dashed line: $|\sigma_{2p_{1/2}, 2p_{3/2}}|$.

9.2.1 Transient coherence

The reduced density matrix is populated by electron capture. Consequently coherences are the result of a steady build-up by the capture process. The analysis within the simple model of section 7.3.1 applies also to coherences populated by capture. In this case the gain term G represents the direct feeding by capture $G = F$. The damping rate $\bar{\Gamma}_{ij}$ determines the damping length to $d^{\text{damp}} \approx 300$ a.u. within the approximation of equation (7.25). In table 9.1 we list the dephasing lengths $d^{2\pi}$ for intra-shell coherences. In contrast to a krypton projectile with a velocity of 47 a.u. (section 7) for this collision system $d^{2\pi}$ is quite long. Only the fine structure in $n=2$ provides a dephasing length below 1000 a.u..

In figure 9.4 we depict coherences in $n=2$. Fine structure coherences first decay via dephasing (see also figure 7.11(a)). The minima of the oscillations are at the positions of integer multiples of $d^{2\pi}$ in agreement with the predicted values in table 9.1. The simple model fails to predict the behavior for longer propagation paths. The Lamb shift coherence between $2s_{1/2}$ and $2p_{1/2}$ is effectively damped. The comparison with figure 7.11(a) indicates a damping length of 1000 a.u. within the simple model. The fact that all coherences shown in figure 9.4 do not completely decay but remain at a constant value

n=2	$2s_{1/2}$	$2p_{1/2}$
$2p_{3/2}$	856	828
$2p_{1/2}$	2.5×10^4	

n=3	$3s_{1/2}$	$3p_{1/2}$	$3p_{3/2}$	$3d_{3/2}$
$3d_{5/2}$	2156	2103	8504	8471
$3d_{3/2}$	2893	2798	2×10^6	
$3p_{3/2}$	2889	2795		
$3p_{1/2}$	8.5×10^4			

Table 9.1: Dephasing length in a.u. for an Ar^{17+} ion with a speed of 23 a.u. during the time $T_{\alpha\beta}^{2\pi} = 2\pi/|\omega_{\alpha\beta}|$ for intra-shell coherences between hydrogenic eigenstates with the unperturbed Hamiltonian specified in (5.65).

indicates the build-up by an additional mechanism. This is the dynamical mixing of excited states in further transport.

To conclude, coherences are built-up linearly according to the capture density matrix until decoherence sets in establishing a dynamical equilibrium at long propagation lengths. The region of increasing coherences, i.e. for $d < 1000$ a.u., coincides with the region of dynamical mixing of populations and angular momentum diffusion.

9.3 Relativistic effects in electron capture

Up to this point we considered observables degenerate with respect to the electron spin. In order to test for relativistic effects we have to consider spin dependent observables. An excellent choice is to investigate the ratio of populations within a fine structure split manifold of a certain state. As we will see in section 9.3.1 this ratio has a fixed value in any non-relativistic theory and deviations can be attributed to spin dependent, i.e. relativistic, effects.

9.3.1 Predictions by non-relativistic theories

Most of the methods for obtaining electron capture cross sections discussed in this thesis neglect relativistic effects. The usage of these methods for the collision system considered here is justified by the relatively small projectile velocity of 23 a.u. ($\beta = v_p/c = 0.17$) and the low nuclear charge of the target atom. Therefore these approaches neglect the electron spin. When

we transform a capture density matrix from a basis without spin into a basis with spin using Clebsch-Gordan coefficients [Coh77] and equally weight the two spin states we obtain for

$$R = \frac{P(2p_{1/2})}{P(2p_{3/2})} \quad (9.2)$$

a value of exactly 1/2. This is due to the multiplicity of the degeneracy with respect to the projection of the total angular momentum j on the quantization axis. To be more specific, for $j=1/2$ m_j can take the two values $-1/2$ and $1/2$, while for $j=3/2$ four values of m_j are possible. This assumes a statistical distribution of orbital and total angular momentum orientation and transforms cross sections from the nl -basis to the nlj -basis as

$$\sigma(n, l, j) = \frac{1}{2} \frac{2j+1}{2l+1} \sigma(n, l). \quad (9.3)$$

Immediately after the charge transfer when the projectile is closest to the target atom all remaining electrons initially attached to the target atom are ionized. The residual carbon nucleus with the charge Z_T effectively modifies the captured electronic state as it departs from the collision region. An electric field enters the Hamiltonian as field strength times dipole operator. For $n=2$ an electric field mixes the s with the p states. The mixing strength between these states is thus determined as

$$M_{ij} = \frac{Z_T}{r^2(t)} \langle i|z|j \rangle. \quad (9.4)$$

The magnitude of the s - p dipole is 0.16 a.u. and for the $2s_{1/2}$ - $2p_{1/2}$ subset it is 0.096 a.u.. In figure 9.5 we plot the values of M for different target-projectile distances. We depict four positions of the projectile. In figure 9.5 (a) the projectile is still close to the target and thus M is very large. For distances shorter than 2 a.u. we find $M > \omega_{FS}$, where ω_{FS} is the energy spacing due to fine structure corrections. For M much larger than ω_{FS} the degeneracy in energy space of all states in $n=2$ results in complete mixing with respect to the angular momentum l neglecting the electron spin. The $2s$ - $2p$ -mixing does not modify the ratio R (9.2).

At a distance from 2 to 10 a.u. the mixing strength M is weaker than ω_{FS} but still stronger than ω_{LS} (ω_{LS} : Lamb shift). Under these conditions the degeneracy with respect to the spin is lifted and the Coulomb field of the remanent target ion effectively mixes the $2s_{1/2}$ with the $2p_{1/2}$ state (see figure 9.5(b) and 9.5(c)). At large distances, i.e. for weaker field strengths, $M \ll \omega_{LS}$ and thus too small to contribute (figure 9.5(d)). Therefore, the

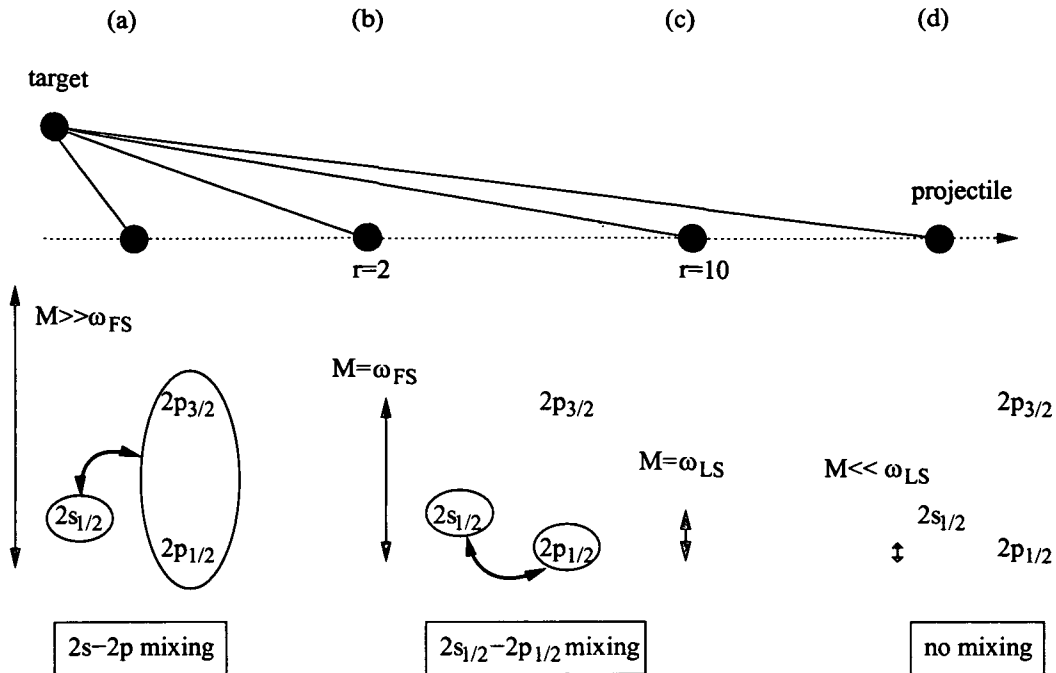


Figure 9.5: Post collision interaction for fine structure components in $n=2$ of Ar^{17+} with $v_p=23$ a.u. as a function of target-projectile distance r . (a) mixing strength M (9.4) larger than fine structure splitting ω_{FS} leading to $2s$ - $2p$ -mixing; (b) at a distance $r=2$ $M=\omega_{FS}$ and mixing of the subset $2s_{1/2}$ - $2p_{1/2}$ starts; (c) at a distance $r=10$ $M=\omega_{LS}$ and $2s_{1/2}$ - $2p_{1/2}$ -mixing weakens; (d) for longer distances mixing is not effective.

only region where the ratio R is effectively modified is between 2 and 10 a.u. of distance. The projectile passes through this region in a time interval of $1/3$ a.u.. In view of the long beat period $2\pi/\omega_{LS} \approx 10^3$ a.u. this interaction time is too short to produce a considerable effect.

To conclude, the prediction of non-relativistic approaches for electron capture (section 2.1) yields a ratio $R=1/2$ for the capture density matrix. The above estimate of the post collision interaction predicts a vanishingly short effective mixing time for the fine structure component thus confirming the scenario.

9.3.2 Comparison with experiment

The comparison of this prediction for R_I (equation (9.1)) with measurements in figure 9.6 reveals a difference. While the predicted value is 0.5 we

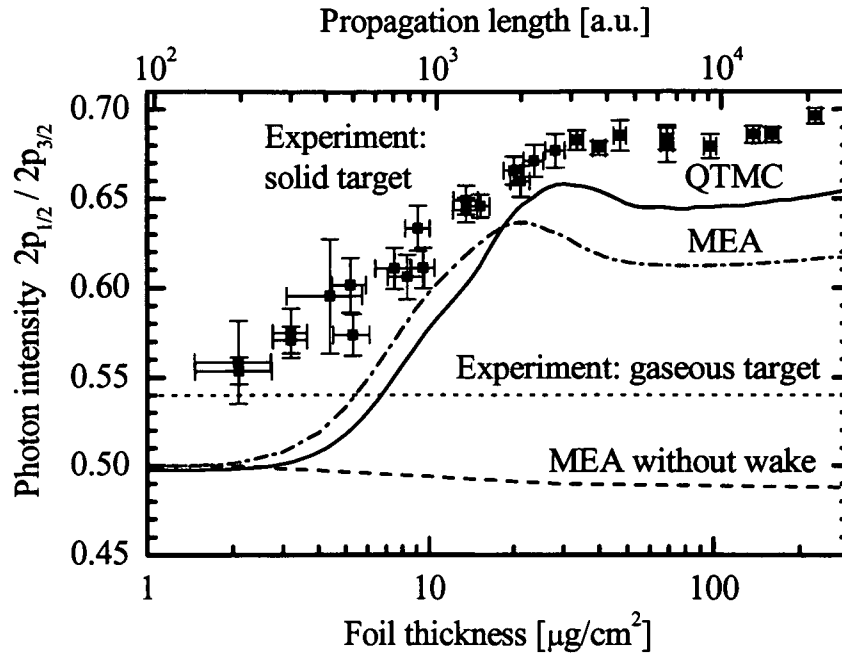


Figure 9.6: Ratio R_I between $2p_{1/2}$ and $2p_{3/2}$ as a function of foil thickness during transport of an Ar^{17+} ion through carbon ($v_p = 23$ a.u.) initially in the Ar^{18+} state. Symbols: experimental results for solid targets; dotted line: experimental results for gaseous CH_4 target as reference line; dash-dotted line: full MEA calculation; dashed line: MEA calculation neglecting wake field; solid line: QTMC calculation.

observe 0.54 in the single collision limit. This 8 % discrepancy is significant, i.e. exceeds the experimental uncertainty. Since the non-relativistic electron capture calculations for the ratio R_I deviate from the measurements in the single capture limit this discrepancy persists during transport.

Evaluating equation 3.49 for the considered collision system with the program of [Ich93] gives cross sections with the ratio $R=0.52$ [Eic05] (see table 3.3). This indicates that there is indeed a relativistic effect, however this effect is too small to explain the experimental ratio. To mimic the relativistic effect of mixing we can modify the capture density matrix σ^{LTDSE} in the spin-basis such that the ratio R is enhanced. This is achieved by shuffling probability from $2s_{1/2}$ to $2p_{1/2}$ in the same way as described by equation 9.4 until the ratio R has the value 0.52. This scheme is indicated in the inset of figure 9.7.

Figure 9.7 shows results of a simulation with this modified capture density matrix. The first observation is that although we used a density matrix

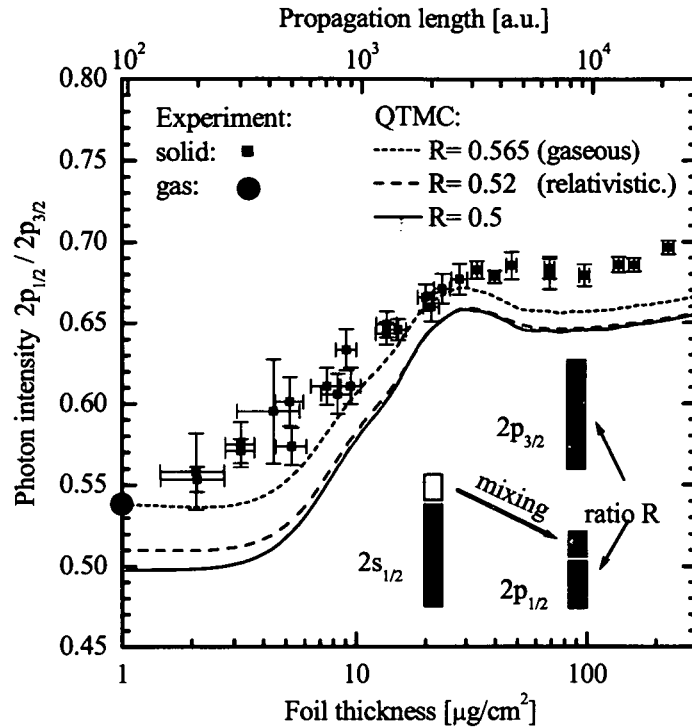


Figure 9.7: Ratio R_I between the $2p_{1/2}$ and $2p_{3/2}$ as a function of foil thickness during transport of an Ar^{17+} ion through carbon ($v_p = 23$ a.u.). Symbols: experimental results for solid and gaseous CH_4 targets; solid line: QTMC result using σ^{LTDSE} ; dotted line: modified σ^{LTDSE} as indicated in the inset to $R=0.565$ such that in the simulation we find $R_I=0.54$ in the single collision regime (thin foil); dashed line: setting $R=0.52$ in σ^{LTDSE} according to relativistic calculations.

with $R=0.52$ the ratio of emitted photon intensities R_I is only 0.51. The reason is the additional contribution by cascade electrons that has to be taken into account when comparing with measurements. With increasing propagation length the difference to a simulation with the unaltered σ^{LTDSE} almost disappears. This reveals that the relativistic effect predicted by the relativistic eikonal theory (section 3.4.4) is relevant in the single collision regime but gets washed out very quickly in dynamical mixing.

In figure 9.7 we also show results of a third simulation where we have changed the ratio R in σ^{LTDSE} such that in the single capture limit R_I resembles the gaseous value of $R_I=0.54$. In order to achieve this effect a shift of $R=0.565$ is necessary. In view of the arguments made in section 9.3.1 this high ratio is particularly surprising. We point out that this shift is not

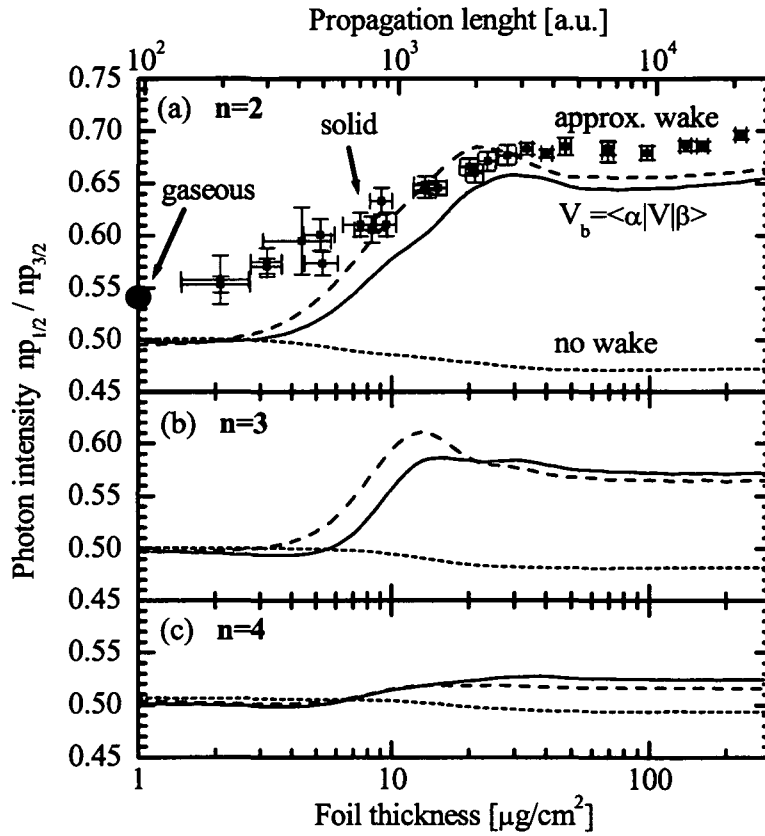


Figure 9.8: Ratio between the fine-structure split states $2p_{1/2}$ and $2p_{3/2}$ as a function of foil thickness determined by Lyman- $\alpha 1$ and Lyman- $\alpha 2$ photon intensities emitted during transport of a Ar^{17+} ion through carbon ($v_p = 23$ a.u.). Results for $n=2$ (a), $n=3$ (b), and $n=4$ (c) for different wake potential used in the full simulation within the QTMC method using σ^{LTDSE} . Solid lines: wake V_b calculated by boost operator (3.37); dashed lines: approximate wake according to Ponce [Roz99] (3.35); dotted lines: simulation neglecting wake potential; symbols: experimental results available for $n=2$ for solid and gaseous targets.

based on any physical effect and serves only as an estimate of the strength of a possible mixing effect following equation 9.4. In comparison with the experimental findings we observe that up to a propagation length of $d \sim 3000$ a.u. measured values for R_I can be explained by the calculation while for thicker targets further differences emerge.

The conclusions we can draw from the investigations shown in figure 9.7 are that the available cross sections do not fully comply with the measured ratio. Nevertheless, besides the 8 percent difference in the initial condition, the simulation follows the experimental data with an almost constant shift over three orders of magnitude of propagation length. This observation indicates that all other relevant aspects of the transport problem are contained within the simulation.

To underline this scenario we investigate the sensitivity of this observable as a function of the initial conditions and in dependence of transport effects. Since the $2p_{1/2}$ to $2p_{3/2}$ ratio is highly sensitive to the wake mixing of $2s_{1/2}$ with $2p_{1/2}$ we first discuss results obtained with different approximations of the wake effect and then proceed to the interdependence of R_I on the method used to calculate capture cross sections.

A simulation omitting the wake potential lead to an almost constant R_I while simulations accounting for the mixing by the wake result in an increased value of R_I with increasing propagation length. After propagation through ~ 3000 a.u. an equilibrium is reached. The asymptotic value deviates again from measurements by the same amount. The ratio R_I is sensitive to the field strength of the wake as we can observe in the comparison of the two approximations for the wake field compared in figure 9.8. The effect is most significant for $n=2$ and rapidly decrease for $n=3$ and $n=4$ as depicted in figure 9.8 (b) and (c), respectively.

In the calculations shown in figure 9.8 we used the LTDSE results for electron capture. In the next figure (figure 9.9) we depict results obtained by simulations using also other non-relativistic calculations to obtain electron capture cross sections. While results using σ^{CTMC} compare worse with measurements for thick foils, simulations using σ^{CDW} reproduce the experimental ratio R_I in the asymptotic limit well. For higher shells differences between the three calculations shown in figure 9.9 decrease.

Summarizing, the dependence of the ratio on the propagation length is reproduced by the QTMC result indicating that the discrepancy is produced rather in capture initial condition than in transport. A relativistic calculation of the electron capture within the eikonal approximation shows that relativistic dynamics can partly account for the shift of R_I . However, at least a ratio of $R=0.565$ in the electron capture density matrix is necessary in order to explain the data leaving the explanation of this effect partly unresolved.

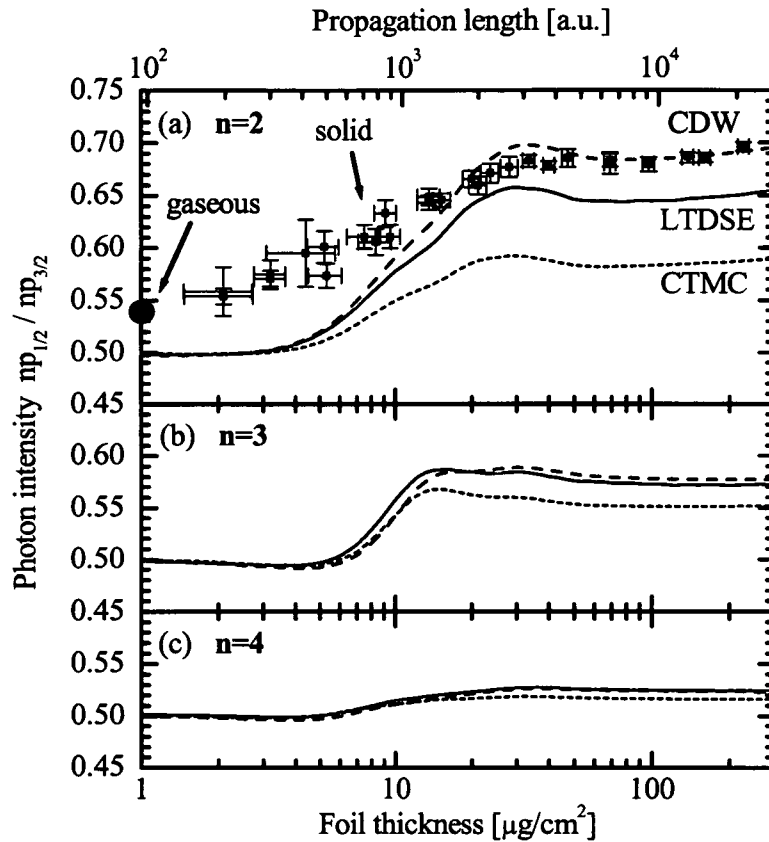


Figure 9.9: Ratio between the fine-structure states $2p_{1/2}$ and $2p_{3/2}$ as a function of foil thickness determined by Lyman- α 1 and Lyman- α 2 photon intensities emitted during transport of a Ar^{17+} ion through carbon ($v_p = 23$ a.u.). Results for $n=2$ (a), $n=3$ (b), and $n=4$ (c) for different capture density matrices used in the full simulation within the QTMC method. Symbols: experimental results; solid line: LTDSE; dashed line: CDW; dotted line: CTMC.

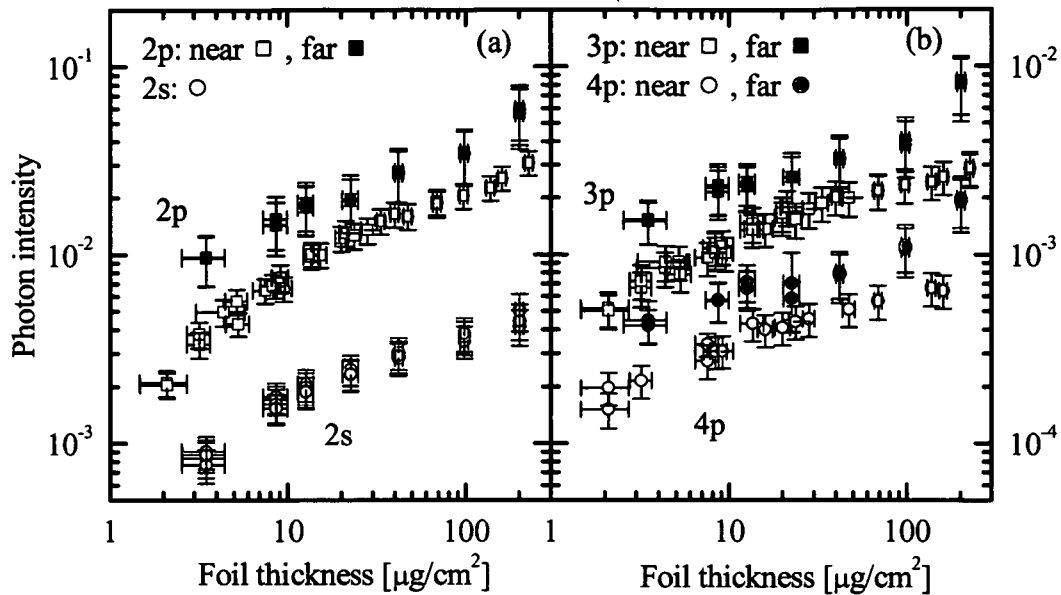


Figure 9.10: Experimental photon intensities as a function of foil thickness emitted by an Ar^{17+} projectile initially in the Ar^{18+} state in transmission through an amorphous carbon foil with a velocity of $v_p = 23$ a.u.. Closed symbols: experimental data obtained with the detector setup measuring photons emitted “far” after the foil; open symbols: data obtained by a recent detector setup optimized to measure photons emitted “near” the exit of the foil. (a): populations in $n=2$ from $2p \rightarrow 1s$ and the two-photon decay $2s \rightarrow 1s$; (b): np populations for $n=3$ and $n=4$ obtained from Lyman transitions $np \rightarrow 1s$.

9.4 Comparison of populations

The fine structure states discussed in the last section could be resolved for $n=2$. As is shown in figure 2.5 for higher shells ($n > 2$) the fine structure resolution in the photon spectrum is lost. The integrated peak intensity is closely related to the excited state population of the initial state of this transition. For example the 2p population can be traced by the $2p \rightarrow 1s$ Lyman $_{\alpha}$ transition. The population per ion is deduced from the measured photon intensities as $I(np) = I(np \rightarrow 1s)$. In a first measurement [Lam97] the acceptance area of the detectors was chosen such that it covered a longer distance after the target. The advantage of this choice is that states with longer lifetimes could be observed as well. On the other hand the difficult determination of detector efficiencies for photons emitted by states with short lifetimes introduces a systematic uncertainty to the results. In the following

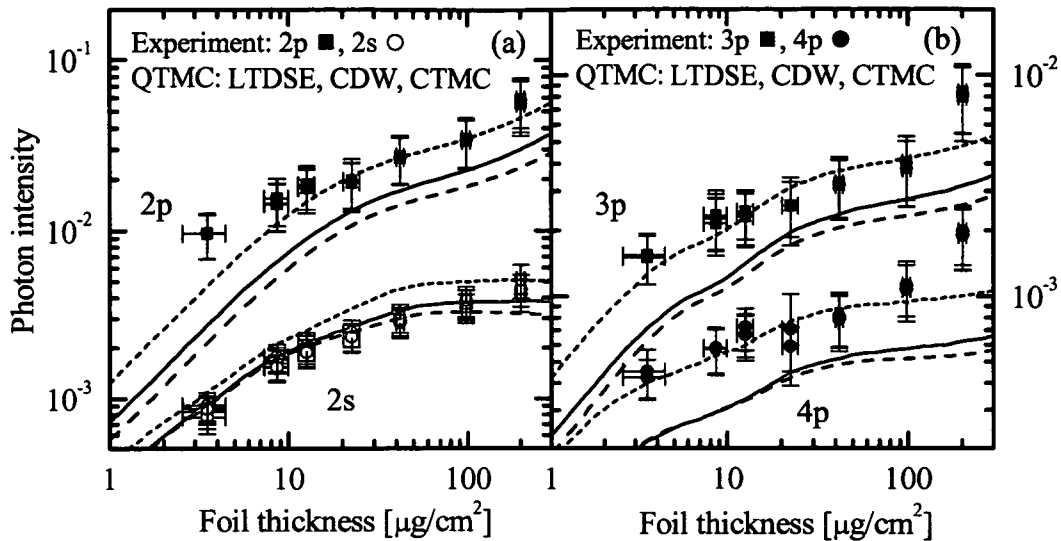


Figure 9.11: Populations obtained from absolute photon intensities emitted by an Ar^{17+} ion during transport through an amorphous carbon foil ($v_p = 23$ a.u.) as a function of foil thickness for $n=1,2$ (a) and $n=3,4$ (b). Symbols: experimental findings from detecting “far” photons; lines: results from full simulation within the QTMC method using different capture density matrices as input: solid lines: LTDSE; dotted lines: CDW; dashed: CTMC.

we refer to this first data set as “far”. The recent data was obtained with a setup optimized for fast decaying states in the region near the target. It will be labeled as “near”. In figure 9.10 we compare these two results for Lyman photon intensities from $n=2$ to $n=4$. It turned out that due to the uncertainty on detector efficiency for the “far” measurements of shortlived states the measurements of the “far” photons are slightly above the measurements of “near” photons, that are more accurate. Photons emitted by the metastable 2s state are measured with an extra detector.

To investigate the sensitivity of the populations to the initial conditions created by electron capture we have performed three otherwise identical simulations except using different capture density matrices obtained by the three different methods described in section 2.1. The comparison with the first measurements appear to suggest that cross sections obtained by CTMC (σ^{CTMC}) explain the data far better than the other methods (figure 9.11). This conclusion was very surprising because the LTDSE method is expected to be by far the most accurate solution available of the three body problem. Nevertheless, at a closer look the simulation using σ^{CTMC} could not explain all aspects of the measurements. It does not account for the thin foil mea-

surement of the 2p intensity as we see in the comparison (figure 9.11) and differences emerge for thick targets for 3p and 4p intensities as well. Attempts were made to resolve this issue and to improve the calculation but no attempt yielded a significant modification of the result. Meanwhile a new experiment was setup optimized to measure photons emitted from short-lived states. These results are discussed below.

9.4.1 Dependence on capture density matrix

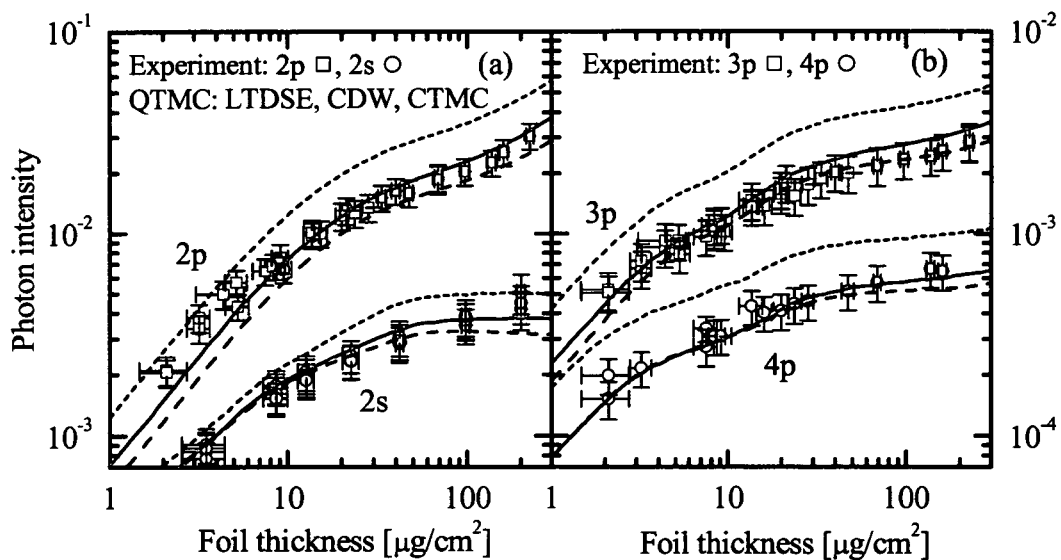


Figure 9.12: Populations obtained from absolute photon intensities emitted by an Ar^{17+} ion during transport through an amorphous carbon foil ($v_p = 23$ a.u.) as a function of foil thickness for $n=1,2$ (a) and $n=3,4$ (b). Symbols: experimental findings; lines: results from full simulation within the QTMC method using different capture density matrices as input: solid lines: LTDSE; dotted lines: CDW; dashed: CTMC.

The dependence of the emitted photon intensities on the electron capture density matrix is shown in figure 9.12. For thin foils the results reflect the initial capture cross sections shown in figure 3.4. Cross sections calculated by CTMC are higher and disagree with the experimental finding for 3p and 4p intensities. While being within the experimental resolution for 2s and 2p in the single collision regime, a discrepancy in transport is found.

Calculations with CDW (σ^{CDW}) and LTDSE (σ^{LTDSE}) cross sections can explain the experimental findings in all regions of interaction confirming the

precision of capture cross sections in the single capture regime, the description of the dynamical intermediate region and the asymptotic value. When looking closer we observe that σ^{LTDSE} reproduce the measurements slightly better than those obtained by CDW. When comparing the cross sections in section 3.4.5 we saw that while capture into 2s is equally effective, discrepancies for p cross section exist. Cross sections for electron capture into p states are smaller when calculated by CDW than those obtained by LTDSE. This small difference remains also during transport. As mentioned in section 3.4.3, capture cross sections were obtained with the LTDSE method for $n \leq 3$. For $n=4$ we have taken the results from CDW. Therefore the photon intensities for 4p are equal for short propagation paths in figure 9.12 (b) while a deviation emerges during transport.

9.4.2 Effect of wake field

The strength of the wake field determines the strength of the wake mixing of states. In figure 9.13 we investigate the effect of the wake field on the populations normalized with respect to the corresponding shell population. For this purpose we have performed three simulations differing only in the wake potential entering the system Hamiltonian. First we use the approximation by Ponce [Roz99] described by equation (3.35). Second we employ matrix elements obtained by evaluating the transition matrix elements of the wake potential in equation (3.37). The resulting field strength is a little bit smaller than the one used by Ponce. In the third simulation we have omitted the wake field completely.

Without a wake potential the mixing of states is the results of multiple collisions and radiative decay only. The mixing causes angular momentum diffusion towards higher angular momenta. The presence of an electric field amplifies this mixing for those states that are coupled by this field. Approximating the wake potential by a linear slope this means coupling dipole allowed transitions while the full wake potential leads also to higher order couplings. For $n=2$ the population of 2p is increased with increasing wake field strength at the expense of electron probability in 2s. Considering the photon intensities including contributions from cascade electrons this effect gets weaker but still can be observed as shown in figure 9.14 (a). The photon intensities emitted by 2s are more sensitive to the strength of the wake field mostly via the cascade contribution from the decay of $3p \rightarrow 2s$.

For $n=3$ the effect of the wake field on the p-populations is contrary to that for $n=2$. To be more specific, angular momentum diffusion leads to a strong increase of the state with the highest angular momentum. In the second shell the p state has this role while in the third shell it is the d state.

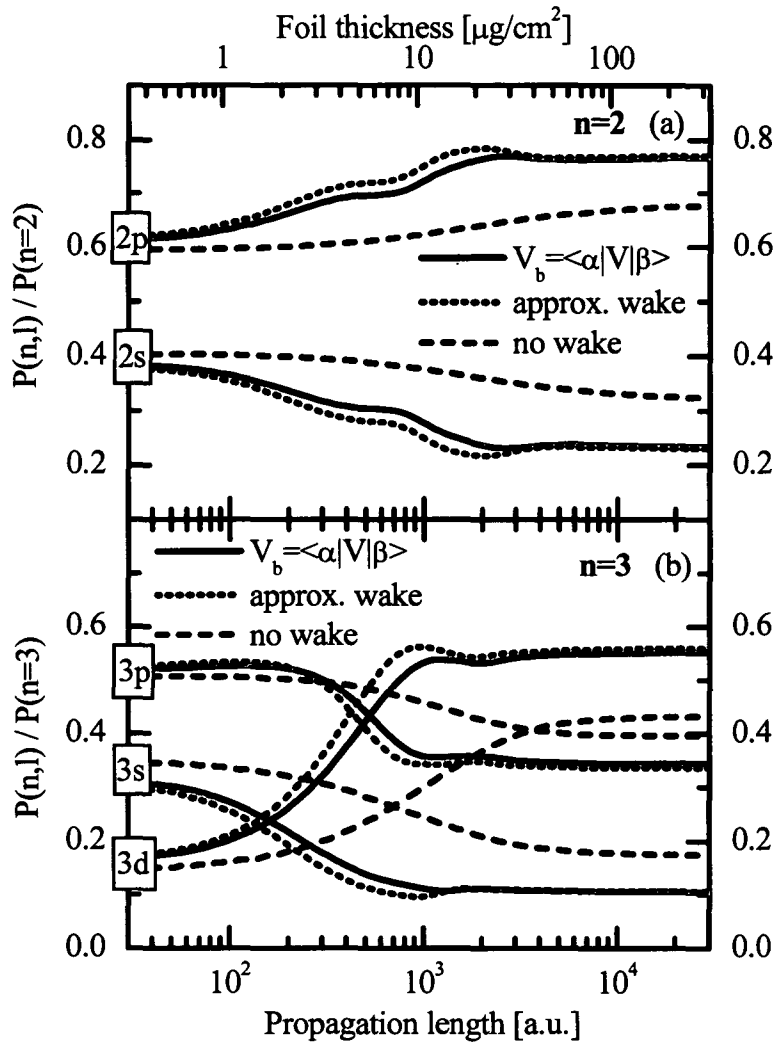


Figure 9.13: Evolution of relative populations of Ar^{17+} as a function of propagation length during transport of an initially bare argon ion through amorphous carbon. Populations are presented as a function of principal quantum number n and the angular momentum l and are normalized to overall probability in corresponding shell: (a) $P(n=2,l)$ for $n=2$; (b) $P(n=3,l)$ for $n=3$. Different wake potentials within the full QTMC calculation using σ^{LTDSE} . Solid lines: wake calculated by boost operator (3.37); dotted lines: approximation by Ponce [Roz99] (3.35); dashed lines: omitting wake.

Therefore the 3d population is increased with increasing field strength at the cost of 3s and 3p populations (see figure 9.13 (b)). For $n=4$ the picture is similar: population of 4p is decreasing with increasing field strength. This effect can be also observed in the photon intensities emitted from 3p and 4p.

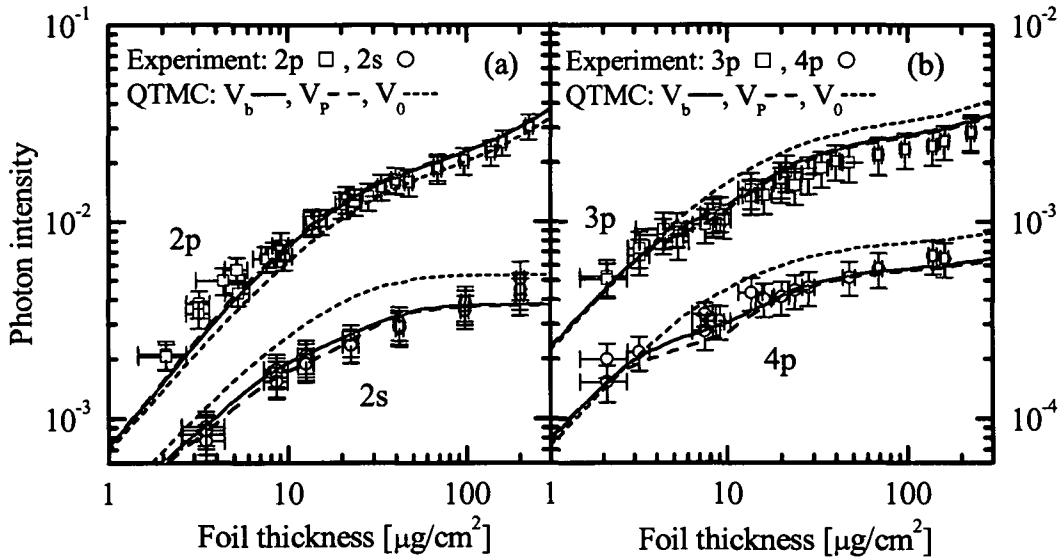


Figure 9.14: Populations obtained from absolute photon intensities emitted by an Ar^{17+} ion during transport through an amorphous carbon foil ($v_p=23$ a.u.) as a function of foil thickness for $n=2$ (a) and $n=3,4$ (b). Symbols: experimental results; lines: QTM results using LTDSE for capture and considering different wake potentials during transport: solid lines: wake V_b calculated by boost operator according to equation (3.37); dotted lines: wake V_P according to approximation by Ponce [Roz99] (see equation (3.35)); dashed lines: simulation neglecting wake potential ($V_0=0$).

Simulations with the two models used to describe the wake potential give identical results in the asymptotic region of long propagation paths. Difference in the populations can be observed in the intermediate region with respect to propagation length d . There mixing due to collisions and the wake field is most effective. For $d \approx 1000$ a.u. $= 10 \mu\text{g}/\text{cm}^2$ the difference is largest in populations and also in photon intensities. The comparison with measurements clearly indicates that the mixing by the wake plays an important role and that the two different models described in this work are accurate enough to explain the data. We are not able to decide which approach is more appropriate because of the uncertainty in the initial conditions and because the difference in photon intensities is smaller than the experimental resolution.

9.4.3 Comparison with alternative approaches

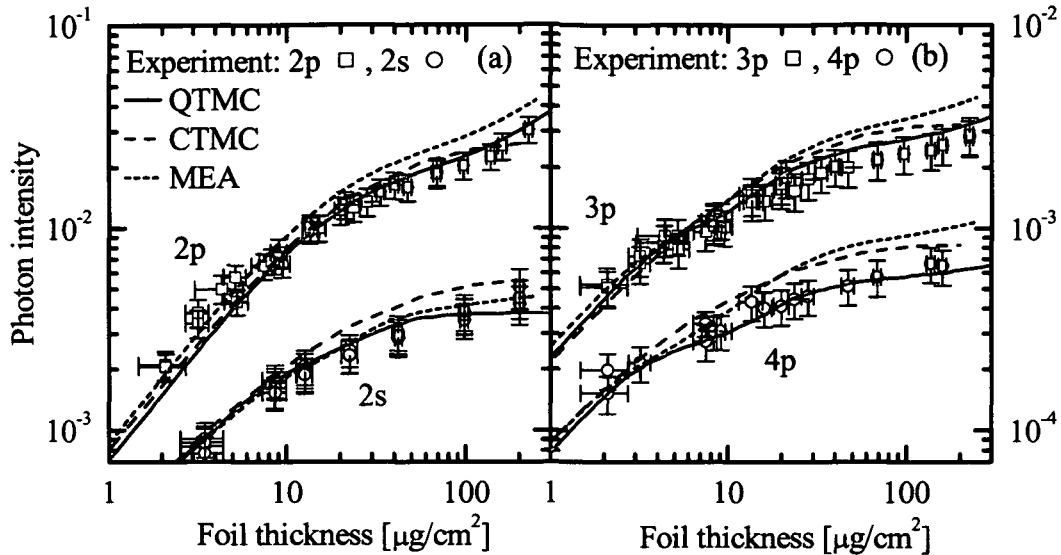


Figure 9.15: Populations obtained from absolute photon intensities emitted by an Ar^{17+} ion during transport through an amorphous carbon foil ($v_p = 23$ a.u.) as a function of foil thickness for $n=2$ (a) and $n=3,4$ (b). Symbols: experimental results; solid lines: QTMC results using LTDSE for capture; dashed lines: CTMC calculation using CDW for capture; dotted lines: MEA calculation using LTDSE for capture into $n \leq 3$ and CDW for capture into $n > 3$.

Results obtained by alternative approaches are compared with measurements of absolute populations in figure 9.15. We performed a calculation with the MEA (section 5.5.1)[Ver01] with the capture density matrix that we used within the QTMC calculation. This is we use for $n \leq$ LTDSE cross sections and results obtained by CDW otherwise. The MEA populations in figure 9.15 explain the data for thin foils while it overestimates the populations for longer propagation times. These differences in comparison of the QTMC solution seem to emerge in the dynamical mixing region starting at about $10 \mu\text{g}/\text{cm}^2$ indicating the consequence of the different treatment of the dynamics. Photon intensities deduced from a classical calculation that was discussed in section 4.3 are also shown for comparison in figure 9.15. The largest difference can be observed for the 3p and 4p intensities.

Unlike the in the QTMC method both alternative methods, MEA and CTMC, use collisional cross sections obtained in quasi-free electron approximation. The different description of the dynamics is decisive for the results

in the dynamical region. Overall, QTMC results explain the data more accurately than the other approaches.

9.5 Summary

We have presented an application of the newly developed open quantum system approach that allows to account for probability flux into the system as well as out of the system. The application we selected is the transport of an initially bare ion through a carbon foil. We investigated the solid state effect in populations created by electron capture. Due to the complexity of the three-body dynamics calculations of cross sections for populations as well as for coherences are still a challenging task. The resulting cross sections calculated by the non-relativistic quantum mechanical calculations are very similar. These are the CDW-PCI method and a recently implemented solution of the TDSE on a lattice. While these theories cannot account for the small relativistic effect observed in the fine structure manifold of 2p they could particularly explain measured populations of 2s and of p-states for $n \leq 4$.

The overall good agreement between theory and experiment demonstrates the accuracy of the calculation and underlines the validity of the chosen approach. The agreement in the single capture regime indicates the degree of precision of the non-relativistic quantum mechanical calculations (CDW and LTDSE) of electron capture cross section. The good agreement for intermediate propagation lengths confirm the dynamical mixing scenario. The fact that the calculation also renders the measured values in the asymptotic limit of very long interaction times demonstrates the accuracy of the calculated dynamical equilibrium between electron capture, dynamical mixing and ionization. For long propagation time the recent method explains measurements closed than alternative approaches.

Chapter 10

Summary and conclusions

In this thesis we have presented an open quantum system approach for ion-solid transport that is open with respect to energy as well as with respect to probability flux. The solution of the underlying quantum master equation by means of a quantum trajectory Monte Carlo method allows to address the problem of the passage of a hydrogenic ion through a solid including ionization and electron capture. For this purpose we extended the standard Lindblad formalism by overcoming the restrictions imposed by unitarity. We focused on two applications: the passage of a hydrogenic $\text{Kr}^{35+}(1s)$ and a bare Ar^{18+} ion through carbon foils. In the transport of a Kr^{35+} ion the attached electron is initially in the ground state and we can follow the dynamics in the subspace of deeply bound states including the loss channel. For the second application an initially bare argon projectile was used and the dynamics was followed in the framework of the combination of electron capture and ionization.

We discussed the role of different collision mechanisms and their signature in the spectra of emitted convoy electrons within classical transport theory and their role in the production of coherence within the present open quantum system approach. In our analysis we focused on the creation and destruction of transient coherences as a result of the dynamical mixing by electron-core and electron-electron collisions, radiative decay, wake field and electron capture. While for krypton ($1s$) violent core collisions are the major driving force for the population of coherent superpositions of excited states, in the argon transport we can observe a gradual shift from first creating coherences by electron capture to excitation from lower lying states in later stages.

For the krypton transport we could resolve discrepancies of a previous unitary calculation with measurements confirming the accuracy of the recent non-unitary method. In the second application we studied the role of elec-

tron capture during transport. We compared different methods for calculating electron capture cross sections and found good agreement with measured populations for non-relativistic quantum mechanical descriptions of the capture channel. Capture cross sections calculated within a classical framework could not be confirmed by experiment. Furthermore we found that a description of capture by a solution of the time dependent Schrödinger equation on a lattice compares best with measurements. The agreement with measured populations is good over three orders of magnitude of propagation length confirming the accuracy of capture cross sections in the single collision regime, i.e. for the thinnest targets. The dynamical scenario for intermediate propagation lengths was confirmed as well as the accurate balance between ionization and capture for large interaction times. The experimentally resolved relativistic effect in the 2p fine structure manifold could only partly be explained in the framework of the relativistic eikonal approximation for electron capture.

In general, the presented open quantum system approach provides an improved explanation of the measurements compared to previous classical and quantum transport theories. Finally we would like to point out that the Lindblad equation and its Monte Carlo solution are universal and can be adapted to describe the coherent dynamics of a wide range of atomic systems that are strongly perturbed by their environment. The generalization presented in this thesis overcomes the restriction of the Lindblad master equation to unitary evolution making it an attractive alternative for a large number of problems.

Bibliography

- [Abr66] R. Abrines and I.C. Percival, *Classical theory of charge transfer and ionization of hydrogen atoms by protons*; Proc. Phys. Soc. **88**, 861 (1966).
- [Arb99] D. G. Arbó, C. O. Reinhold, P. Kürpick, S. Yoshida and J. Burgdörfer, *Quantum transport theory for atomic states through solids*; Phys. Rev. A **60**, 1091-1102 (1999).
- [Arb00] D. G. Arbó, C. O. Reinhold, S. Yoshida and J. Burgdörfer, *Quantum evolution of atomic states during transmission through solids*; Nucl. Inst. & Methods Phys. Res. B, **164-165**, 495-503 (2000).
- [Ash79] J. Ashley, C. Tung, and R. Ritchie, *Electron inelastic mean free paths and energy losses in solids , : I. Aluminum metal*; Surf. Sci. **81**, 409 (1979); C. Martin, E. Arakawa, T. Callcott, and J. Ashley, *J. Electron Spectroscopy Relat. Phenom.* **35**, 307 (1985); J. Ashley, J. Cowan, R. Ritchie, V.E. Anderson, and J. Hoelzel, *Stragglng and plasmon excitation in the energy loss spectra of electrons transmitted through carbon*; Thin Films **60**, 361 (1979); J. Ashley, *J. Electron Spectrosc. Relat. Phenom.* **28**, 177 (1982).
- [Bec84] R. L. Becker and A. D. MacKellar, *Theoretical initial l dependence of ion-Rydberg-atom collision cross sections*; J. Phys. B **17**, 3923 (1984).
- [Bet77] H. Bethe and F. Salpeter, *Quantum Mechanics of One- and Two-Electron Atoms*, (Plenum, NY, 1977).
- [Bra83] B. H. Bransden and C. J. Joachain, *Physics of Atoms and Molecules* (Longman Scientific and Technical, Harlow, 1983).
- [Bre82] M. Breinig, S. B. Elston, S. Hultdt, L. Liljeby, C. R. Vane, S. D. Berry, G. A. Glass, M. Schauer, I. A. Sellin, G. D. Alton, S. Datz, S. Overbury, R. Laubert, and M. Suter, *Experiments concerning electron capture and loss to the continuum and convoy electron production by*

- highly ionized projectiles in the 0.7 - 8.5-MeV/u range transversing the rare gases, polycrystalline solids, and axial channels in gold*; Phys. Rev. A **25**, 3015 (1982).
- [Bro97] I. N. Bronstein, K. A. Semendjajew, G. Musiol, and H. Mühlig, *Taschenbuch der Mathematik*; (1997), Frankfurt am Main, page 958, equation 45.
- [Bur81a] J. Burgdörfer, *Theorie kohärenter Zustände in Wasserstoff nach schnellen Ion-Atom-Stößen*; PhD thesis (1981).
- [Bur81b] J. Burgdörfer, *Influence of the linear Stark effect on electron capture into fully stripped ions*; Phys. Rev. A. **24**, 1756 (1981).
- [Bur83a] J. Burgdörfer, M. Breinig, S. B. Elston, and I. A. Sellin, *Calculation of electron-loss-to-continuum cusps: An algebraic approach*; Phys. Rev. A **28**, 3277 (1983).
- [Bur83b] J. Burgdörfer, *Group Theoretical Classification of Angular Momentum Coherences in Hydrogen*; Z. Phys. A **309**, 285 (1983).
- [Bur84] J. Burgdörfer, and L. J. Dubé, *Multiple-Scattering Approach to Coherent Excitation in Electron-Capture Collisions*; Phys. Rev. Lett. **52**, 2225 (1984).
- [Bur85] J. Burgdörfer, and L. J. Dubé, *Population of Rydberg states by electron capture in fast-ion-atom collisions*; Phys. Rev. A **31**, 634-640 (1985).
- [Bur86] J. Burgdörfer, *Statistical multipoles for cusp electrons and Rydberg electrons*; Phys. Rev. A **33**, 1578-1589 (1986).
- [Bur88] J. Burgdörfer and C. Bottcher, *Production of High-Angular-Momentum Rydberg States by Stochastic Collisions*; Phys. Rev. Lett. **61**, 2917 (1988).
- [Bur90a] J. Burgdörfer and J. Gibbons, *Electron transport in the presence of a Coulomb field*; Phys. Rev. A **42**, 1206 (1990).
- [Car93] H. J. Carmichael, *Quantum trajectory theory for cascaded open systems*; Phys. Rev. Lett. **70**, 2273 (1993).
- [Che64] I. M. Cheshire, Proc. Phys. Soc. **84**, 89-98 (1964).

- [Cle74] E. Clementy, and C. Roetti, *Roothaan-Hartree-Fock atomic wave-functions; basis functions and their coefficients for ground and certain excited states of neutral and ionized atoms, $Z \leq 54$* ; Atomic Data and Nuclear Data Tables **14**, 177-478 (1974).
- [Coh77] C. Cohen-Tannoudji, B. Diu, F. Laloe, *Quantum Mechanics, Vol 2*; New York, Wiley (1977).
- [Dal92] J. Dalibard, Y Castin, and K. Mølmer, *Wave-function approach to dissipative processes in quantum optics*; Phys. Rev. Lett., **68**, 580 (1992).
- [Dre76] F. Drepper and J. Briggs, *Doubly differential cross sections for electron-loss in ion-atom collisions*; J. Phys. B **9**, 2063 (1976).
- [Dum92] R. Dum, P. Zoller, and H. Ritsch, *Monte Carlo simulation of the atomic master equation for spontaneous emission*; Phys. Rev. A **45**, 4879 (1992).
- [Ech79] P. M. Echenique, R. H. Ritchie, and W. Brandt, *Spatial excitation patterns induced by swift ions in condensed matter*; Phys. Rev. B **20** 2567 (1979).
- [Ech86] P. M. Echenique, W. Brandt, and R. H. Ritchie, *Self-consistent wake binding energies*; Phys. Rev. B **33**, 43 (1986).
- [Eic85] J. Eichler, *Relativistic eikonal theory of electron capture*; Phys. Rev. A **32**, 112 (1990).
- [Eic90] J. Eichler, Phys. Rep. **193**, 165 (1990).
- [Eic05] J. Eichler, *private communication* (2005).
- [Els85] S. B. Elston, S. D. Berry, J. Burgdörfer, I. A. Sellin, M. Breinig, R. DeSerio, C. E. Gonzalez-Lepera, L. Liljeby, K. -O. Groeneveld, D. Hofmann, P. Koschar, and I. B. E. Nemirovsky, *Observation of Quadrupole and Hexadecapole Moments of the Electronic Charge Cloud Produced in Electron-Loss Collisions*; Phys. Rev. Lett. **55**, 2281 (1985).
- [Fou00] C. Fourment, *Transport d'ions hydrogénoïdes rapides dans les solides: mise en évidence de l'écrantage dynamique*; PhD thesis (2000).
- [Gar99] C. W. Gardiner and P. Zoller, *Quantum Noise*, (Springer, Berlin, 1999).

- [Ger96] B. Gervais, C. O. Reinhold, and J. Burgdörfer, *Simulation of excited-state formation of hydrogen in transmission of relativistic H⁻ ions through thin foils*; Phys. Rev. A **53**, 3189 (1996).
- [Gib91] J. P. Gibbons, S. B. Elston, K. Kimura, R. DeSerio, I. A. Sellin, J. Burgdörfer, J. P. Grandin, A. Cassimi, X. Husson, L. Liljeby, and M. Druetta, *Observation of rapid evolution of convoy electron angular distributions*; Phys. Rev. Lett. **67**, 481 (1991).
- [Gul96] M. S. Gulley, P. B. Keating, H. C. Bryant, E. P. MacKerrow, W. A. Miller, D. C. Rislove, S. Cohen, J. B. Donahue, D. H. Fitzgerald, S. C. Frankle, D. J. Funk, R. L. Hutson, R. J. Macek, M. A. Plum, N. G. Stanciu, O. B. van Dyck, C. A. Wilkinson, and C. W. Planner, *Measurement of H⁻, H⁰, and H⁺ yields produced by foil stripping of 800-MeV H⁻ ions*; Phys. Rev. A **53**, 3201 (1996).
- [Ich93] A. Ichihara, T. Shirai, and J. Eichler, *Cross sections for electron capture in relativistic atomic collisions*; Atomic Data and Nuclear Data Tables **55**, 63-79 (1993).
- [Ino71] M. Inokuti, *Inelastic Collisions of Fast Charged Particles with Atoms and Molecules - The Bethe Theory Revisited*; Rev. Mod. Phys. **43**, 297 (1971).
- [Joh85] W. R. Johnson and G. Soff, *The lamb shift in hydrogen-like atoms, $1 \leq Z \leq 110$* ; At. Data Nucl. Data Tables **33**, 405 (1985).
- [Kle02] U. Kleinekathofer, I. Kondov, and M. Schreiber, *Stochastic unraveling of time-local quantum master equations beyond the Lindblad class*; Phys. Rev. E **66**, 037701 (2002).
- [Kon03] I. Kondov, U. Kleinekathofer, and M. Schreiber, *Stochastic unraveling of Redfield master equations and its application to electron transfer problems*; J. Chem. Phys. **119**, 6635 (2003).
- [Kur98] P. Kürpick, C. O. Reinhold, J. Burgdörfer, and B. Gervais, *Excited-state subshell population of hydrogen atoms after transmission of relativistic H⁻ ions through thin foils*; Phys. Rev. A **58**, 2183 (1998).
- [Lam97] E. Lamour, *Production et transport des états excités du projectile en interaction ion-solide*; PhD thesis (2000).
- [Lam05] E. Lamour, *private communication*.

- [Lin76a] G. Lindblad, *Commun. Math. Phys.* **48**, 119 (1976).
- [Lin76b] G. Lindblad, *Rep. Mod. Phys.* **10**, 393 (1976).
- [Luc80] M. Lucas, W. Streckelmacher, J. Macek, and J. Potter, *Charge transfer to continuum and high Rydberg states in proton-carbon-foil collisions*; *J. Phys. B* **13**, 4833 (1980).
- [Mel92] M. Melles, *Quantenmechanik des instantan gestoßenen Wasserstoffatoms*; Diploma Thesis (1992).
- [Mel93] M. Melles, C. O. Reinhold, J. Burgdörfer, *Classical and quantum dynamics of the impulsively driven hydrogen atom*; *Nucl. Instr. and Meth. B* **79**, 109-113 (1993).
- [Men90] L. Meng, C. O. Reinhold, and R. E. Olson, *Subshell electron capture in collisions of fully stripped ions with He and H₂ at intermediate energies*; *Phys. Rev. A* **42**, 5286 (1990).
- [Mes86] A. Messiah, *Quantum Mechanics, Volume 2*, North-Holland Publishing Company (1961): equation (C.56).
- [Min02a] T. Minami, C. O. Reinhold, M. Seliger, J. Burgdörfer, C. Fourment, E. Lamour, J.-P. Rozet, D. Vernhet, and B. Gervais, *Quantum transport of the internal state of Kr³⁵⁺ ions through amorphous carbon foils*; *Phys. Rev. A* **65**, 032901 (2002).
- [Min02b] T. Minami, C. O. Reinhold, M. Seliger, J. Burgdörfer, C. Fourment, J.-P. Rozet, B. Gervais, D. Vernhet, *Evidence of collisional coherences in the transport of hydrogenic krypton through amorphous carbon foils*; *Nucl. Instr. and Meth. B* **193**, 79-84 (2002).
- [Min03a] T. Minami, C. O. Reinhold, and J. Burgdörfer, *Quantum-trajectory Monte Carlo method for internal-state evolution of fast ions traversing amorphous solids*; *Phys. Rev. A* **67**, 022902 (2003).
- [Min04a] T. Minami, C. O. Reinhold, D. R. Schultz, and M. S. Pindzola, *Coherence parameters for charge transfer in collisions of protons with helium calculated using a hybrid numerical approach*; *J. Phys. B* **37**, 4025 (2004).
- [Min04b] T. Minami, *private communication*.
- [Mol93] K. Mølmer, Y. Castin, and J. Dalibard, *Monte Carlo wave-function method in quantum optics*; *J. Opt. Soc. Am. B* **10**, 524 (1993).

- [Ols77] R.E. Olson and A. Salop, *Charge-transfer and impact-ionization cross sections for fully and partially stripped positive ions colliding with atomic hydrogen*; Phys. Rev. A **16**, 531 (1977).
- [Pal98] V. G. Pal'chikov, *Relativistic Transition Probabilities and Oscillator Strengths in Hydrogen-like Atoms*; Physica Scripta, **57**, 581 (1998).
- [Per75] I.C. Percival and D. Richards, *The theory of collisions between charged particles and highly excited atoms*; Adv. At. Mol. Phys. **11**, 1 (1975)
- [Pre86] W. H. Press, S. A. Teukolsky, W. T. Vetterling, and B. P. Flannery, *Numerical Recipes in Fortran 77, The Art of Scientific Computing*; Cambridge University Press (1986).
- [Pin89] D. Pines and P. Nozieres, *Theory of Quantum Liquids*; (Addison-Wesley, Reading, 1989).
- [Rei92] C. O. Reinhold, J. Burgdörfer, J. Kemmler, and P. Koschar, *Simulation of convoy-electron emission*; Phys. Rev. A **45**, R2655 (1992).
- [Rei00] C. O. Reinhold, D. G. Arbó, J. Burgdörfer, B. Gervais, E. Lamour, D. Vernhet and J.-P. Rozet, *Enhanced population of high- l states due to the interplay between multiple scattering and dynamical screening in ion-solid collisions*; J. Phys. B, **33**, L111 (2000).
- [Rei04] C. O. Reinhold, *private communication*.
- [Roz99] J.-P. Rozet, D. Vernhet, I. Bailly-Despiney, C. Fourment, L. J. Dubé, *Dynamical substate mixing of fast ions in solids: a density matrix approach*; J. Phys. B **32**, 4677 (1999).
- [Sch92] D. R. Schultz, C. O. Reinhold, R. E. Olson, and D. G. Seely, *Differential cross sections for state-selective electron capture in 25-100-keV proton-helium collisions*; Phys. Rev. A **46**, 275 (1992).
- [Sel01] M. Seliger, K. Tökési, C. O. Reinhold, J. Burgdörfer, Y. Takabayashi, T. Ito, K. Komaki, T. Azuma and Y. Yamazaki, *Relativistic electron transport through carbon foils*; Physica Scripta **T92**, 211-213 (2001).
- [Sel03] M. Seliger, K. Tökési, C. O. Reinhold, J. Burgdörfer, *Highly transverse velocity distribution of convoy electrons emitted by highly charged ions*; Nucl. Instr. Meth. B **205**, 830 (2003).

- [Sel05a] M. Seliger, C. O. Reinhold, T. Minami, and J. Burgdörfer, *Non-unitary master equation for the internal state of ions traversing solids*; Nucl. Instr. and Meth. B **230**, 7-11 (2005).
- [Sel05b] M. Seliger, C. O. Reinhold, T. Minami, and J. Burgdörfer, *Non-unitary quantum trajectory Monte Carlo method for open quantum systems*; to appear in Phys. Rev. A **71** (May 2005).
- [Sel05c] M. Seliger, C. O. Reinhold, T. Minami, D. R. Schultz, S. Yoshida, J. Burgdörfer, E. Lamour, J.-P. Rozet and D. Vernhet, *Production and transport of electronic states in fast ions penetrating solids*; in preparation, 2005.
- [Sza93] G. Szabó, J. Wang, and J. Burgdörfer, *Ellipsoidal angular distribution of electrons emitted from Rydberg atoms*; Phys. Rev. A **48**, R3414 (1993).
- [Tak99a] Y. Takabayashi, T. Ito, T. Azuma, K. Komaki, Y. Yamazaki, H. Tawara, M. Torikoshi, A. Kitagawa, E. Takada, and T. Murakami, *Convoy electron production in 390 MeV/u Ar17+ ion collisions with thin foils*; Abstract book of 21st ICPEAC, 730 (1999).
- [Tak99b] Y. Takabayashi, T. Ito, T. Azuma, K. Komaki, Y. Yamazaki, H. Tawara, M. Torikoshi, A. Kitagawa, E. Takada, and T. Murakami, *Convoy Electron Production and Ionization in 390 MeV/u Ar17+ Ion Collisions with Thin Foils*; Physica Scripta **T80B**, 249 (1999).
- [Tak03] Y. Takabayashi, T. Ito, T. Azuma, K. Komaki, Y. Yamazaki, H. Tawara, E. Takada, T. Murakami, M. Seliger, K. Tökési, C. O. Reinhold, J. Burgdörfer, *Excited-state evolution probed by convoy electron emission in relativistic heavy ion collisions*; Phys. Rev. A **68**, 042703 (2003).
- [Ver98] D. Vernhet, J.-P. Rozet, I. Bailly-Despiney, C. Stephan, A. Cassimit, J.-P. Grandin and L. J. Dubé, *Observation of dynamical substate mixing of fast ions in solids*; J. Phys. B, **31**, 117 (1998).
- [Ver01] D. Vernhet, C. Fourment, E. Lamour, J.-P. Rozet, B. Gervais, L. J. Dubé, F. Martin, T. Minami, C. O. Reinhold, M. Seliger and J. Burgdörfer, *Transport of Kr35+ inner-shells through solid carbon foils*; Physica Scripta, **T92**, 233-236 (2001).
- [Wil72] M. W. Williams, and E. T. Arakawa, *Optical properties of glassy carbon from 0 to 82 eV*; J. Appl. Phys., **43** 3460 (1972).

- [Yos99] S. Yoshida, S. Watanabe, C. O. Reinhold, and J. Burgdörfer, *Reflection-free propagation of wave packets*; Phys. Rev. A **60**, 1113 (1999).

List of Figures

2.1	Wake potential of a bare argon ion in carbon	8
2.2	Schematic picture of electron capture	9
2.3	Experimental setup for convoy electron measurements	10
2.4	Experimental setup for Ar ¹⁸⁺ projectiles	11
2.5	Spectrum of emitted photons from Ar ¹⁷⁺	12
2.6	Experimental photon intensities (2p _{1/2} → 1s)/(2p _{3/2} → 1s)	14
2.7	Experimental photon intensities 2p → 1s and 2s → 1s	14
3.1	Momentum transfer distribution in free electron scattering	22
3.2	Stark map of wake field for n=2, 3	28
3.3	Schematic picture of LTDSE	35
3.4	Electron capture cross section for Ar ¹⁸⁺ + C → (Ar ¹⁷⁺)* + C ¹⁺	39
3.5	Electron capture cross section into different shells	41
4.1	Random walk along a Kepler orbit	43
4.2	CTMC populations of transport of Ar ¹⁷⁺ through carbon	45
4.3	Convoy emission process within a classical transport theory	47
4.4	Outgoing fractions of Ar ¹⁷⁺ and Ar ¹⁸⁺ ions	48
4.5	Velocity distribution of emitted electrons	50
4.6	Comparison of CEP with experimental findings	51
5.1	Example quantum trajectory	63
5.2	Schematic picture of the open quantum system	64
5.3	Schematic picture of decomposition of H_S into \mathbb{P} and \mathbb{Q}	67
5.4	Radiative decay test model for non-unitary QTMC	73
6.1	Correction terms $D_\alpha^{(c)}$ and $M_{\alpha\alpha}^{(c)}$ for core scattering	82
6.2	Core scattering decay rates for Ar ¹⁷⁺	83
6.3	Effective intra-shell core scattering decay rates for Ar ¹⁷⁺	84
6.4	Effective decay rates of s-states for Ar ¹⁷⁺ for high n	85
6.5	Integrand of $M_{\alpha\beta}^{(e)}$ for electron-electron interaction	89
6.6	Decay rates for electron-electron collisions of Ar ¹⁷⁺	90

6.7	Effective electron-electron decay rates of s-states for Ar ¹⁷⁺ . . .	91
7.1	Experimental photon intensities and other approaches	94
7.2	Charge state fraction of a Kr ³⁵⁺ (1s) ion in transport	95
7.3	Excited states populations of Kr ³⁵⁺	98
7.4	Shell population ratios of a Kr ³⁵⁺ ion	99
7.5	Relative populations of Kr ³⁵⁺ states	100
7.6	Evolution of selected populations and coherences of a Kr ³⁵⁺ .	101
7.7	Reduced density matrix $\sigma^{(NU)}$ of a Kr ³⁵⁺ ion	103
7.8	Relative coherences $ C_{ij}^{NU}(d) $ of a Kr ³⁵⁺ ion	104
7.9	Inhomogeneous solution $\omega_{ij} > \bar{\Gamma}_{ij}$	107
7.10	Inhomogeneous solution for $\omega_{ij} \ll \bar{\Gamma}_{ij}$	108
7.11	Result of simple model for coherence	109
7.12	Relevant regions of decoherence: dephasing and damping . . .	111
7.13	Dephasing of elements of the density matrix σ_{ij}^{NU} of a Kr ³⁵⁺ ion	113
7.14	Dephasing of elements of the density matrix σ_{ij}^{NU} of a Kr ³⁵⁺ ion	114
7.15	Damping of elements of the density matrix σ_{ij}^{NU} of a Kr ³⁵⁺ ion	115
7.16	Effect of loss onto coherences	116
7.17	Photon intensities, experiment and theory	117
8.1	Argon charge states affected by electron capture and ionization	122
8.2	Numerical test for gain using radiative decay from 4p _{3/2,1/2} . .	126
8.3	Scheme of radiative cascade from 5d _{3/2,1/2}	128
8.4	Coherence in radiative cascade from 5d _{3/2,1/2}	129
9.1	Ratio R_I between 2p _{1/2} and 2p _{3/2} and MEA	132
9.2	Relative shell populations of Ar ¹⁷⁺	133
9.3	Relative nl populations of Ar ¹⁷⁺	135
9.4	Transient coherence in argon	136
9.5	PCI for fine structure components in n=2 of Ar ¹⁷⁺	139
9.6	Ratio R_I between 2p _{1/2} and 2p _{3/2}	140
9.7	Photon ratio 2p _{1/2} /2p _{3/2} for different P(2p _{1/2})/P(2p _{3/2})	141
9.8	np _{1/2} /np _{3/2} for different wake potentials	142
9.9	np _{1/2} /np _{3/2} for different capture density matrices	144
9.10	Experimental photon intensities measured by different setups .	145
9.11	Photon intensities (“far”) from Ar ¹⁷⁺ and QTMC with σ^{CTMC}	146
9.12	Experimental and theoretical photon intensities from Ar ¹⁷⁺ . .	147
9.13	Wake effect on relative nl populations of Ar ¹⁷⁺	149
9.14	Photon intensities from Ar ¹⁷⁺ for different wake potentials . .	150
9.15	Populations of photon intensities emitted by an Ar ¹⁷⁺ ion . . .	151

List of Tables

3.1	Lamb-shift parameter Λ for argon and krypton	17
3.2	Eigen energies of hydrogenic argon	17
3.3	Relativistic 2p capture cross sections for an $\text{Ar}^{18+} \rightarrow \text{C}$	37
3.4	Electron capture cross section for an $\text{Ar}^{18+} \rightarrow \text{C}$	38
3.5	Coherences of electron capture cross section for an $\text{Ar}^{18+} \rightarrow \text{C}$	41
6.1	$D_{\alpha}^{(c)}$ for core scattering	81
6.2	$D_{\alpha}^{(e)}$ for electron-electron interaction	87
7.1	Dephasing length $d^{2\pi}$ for krypton	110
9.1	Dephasing length $d^{2\pi}$ for argon	137

Acknowledgments

I would like to take the opportunity to thank all the people who have helped me to complete this thesis by providing stimulation, inspiration and motivation. To begin with I would like to thank my advisor and promoter *Joachim Burgdörfer* who contributed enormously to the genesis of this doctorate in terms of intellectual input, support and encouragement. He inspired my work towards science since my first steps as an unexperienced student. I wish to express my sincere gratitude to my second advisor *Carlos O. Reinhold* who, although far away, always found time for discussions and in particular I would like to thank him for his hospitality in Knoxville and Oak Ridge National Laboratory. I am furthermore thankful to *Tatsuya Minami* for teaching me how to use the QTMC program and for calculating appropriate electron capture cross sections for us.

I am indebted to our French collaborators *Dominique Vernhet*, *Emily Lamour*, and *Jean-Pierre Rozet* for the stimulating collaboration and especially for their hospitality at their new institute. I am grateful to *Dominique Vernhet* for reading the thesis and for her willingness to serve as assessor of my thesis and to travel to Vienna for the defense. My first steps in science were closely accompanied by *Karoly Tökési* who introduced me into the world of relativistic CTMC calculations. I am also thankful for his hospitality in Debrecen. I thank *Jörg Eichler* for advise on relativistic electron capture and *Akira Ichihara* for providing us with relativistic electron capture cross sections.

I was fortunate to work in a pleasant and stimulating (intellectually and culinary) *group*. (So long, and thanks for all the chocolate.) I especially thank my colleagues *Christoph Lemell*, *Shuhei Yoshida* and *Ludger Wirtz* for help on solving all sorts of computer problems. A smooth and unbureaucratic operation of the institute combined with an up-to-date equipment rounded off the picture.

I am much obliged to my girlfriend *Maria Hörndl* (who is also member of Joachim's research group) who made me a happy person and gave me the extra strength to get things done. She also managed to gently correct

my English into something readers may actually understand. I owe special thanks to my *family* for moral support. Last but not least, I want to thank all my *friends*, especially the members of the “First Viennese Physical Society”, for their support in all sorts of things also in the world beyond physics. The Austrian Science Fund (“Fonds zur Förderung der Wissenschaftlichen Forschung”) and the EU provided *financial support*.

Marek Seliger

Institute for Theoretical Physics
Vienna University of Technology
Wiedner Hauptstrasse 8-10/136
A-1040 Vienna, Austria
phone: +43 1 58801-136 27, fax: +43 1 58801-136 99
marek@concord.itp.tuwien.ac.at
<http://dollywood.itp.tuwien.ac.at/~marek/>

PERSONAL DATA

Date and place of birth: November 15th 1975 in Praha, Czech Republic

Nationality: Austrian

Private address: Rienöblgasse 15/12, A-1040 Vienna, Austria

EDUCATION

10/2001 - 06/2005: PhD in physics
at the Institute for Theoretical Physics at the Vienna University of Technology (Vienna UT)
Title: Open Quantum System Approach to Transient Coherence in Ion-Solid Transport
Advisor: Prof. Joachim Burgdörfer (Vienna) and Prof. Carlos O. Reinhold (Oak Ridge)

10/1995 - 06/2001: Study of physics at the Vienna University of Technology
Master degree in physics, passed with distinction
Diploma thesis at the Institute for Theoretical Physics at the Vienna UT
Title: Classical and Quantum Transport; advisor: Prof. Joachim Burgdörfer

09/1987 - 06/1995: Grammar school in Austria

EMPLOYMENT, INTERNSHIPS AND TEACHING EXPERIENCE

10/2001 - 06/2005: PhD student in physics at the Vienna University of Technology
supported by the Austrian Science Fund (FWF) and EU

10/1997 - 01/2001: Teaching assistant (tutor) at the Vienna University of Technology
under-graduate physics exercises, laboratory course

07-09/2001: Internship at the NA-48 experiment at CERN, Geneva, Switzerland
improving monitoring system and instructing students for support of data taking

07-08/2000: Internship at the NA-48 experiment at CERN, Geneva, Switzerland
supporting analysis of $K_S \rightarrow \gamma\gamma$ decay, support of data taking

07-08/1999: Internship at the NA-48 experiment at CERN, Geneva, Switzerland
support of data taking, attending CERN summer-student lectures

02/1999 Internship at Siemens, Vienna, Austria
programming in the group for electrical power network solutions

07-08/1996-1998: Summer jobs as youth tutor at Ferienhort am Wolfgangsee, Austria

SCIENTIFIC PUBLICATIONS

Quantum transport theory

Production and transport of electronic states in fast ions penetrating solids

Marek Seliger, Carlos O. Reinhold, Tatsuya Minami, David R. Schultz, Shuhei Yoshida, Joachim Burgdörfer, Emily Lamour, Jean-Pierre Rozet and Dominique Vernhet; in preparation, 2005.

Non-unitary quantum trajectory Monte Carlo method for open quantum systems

Marek Seliger, Carlos O. Reinhold, Tatsuya Minami, and Joachim Burgdörfer; accepted to appear in Phys. Rev. A in June 2005.

Non-unitary master equation for the internal state of ions traversing solids

Marek Seliger, Carlos O. Reinhold, Tatsuya Minami, and Joachim Burgdörfer; Nucl. Instr. and Meth. B 230, 7-11 (2005).

Quantum Monte Carlo method for open quantum systems

Marek Seliger, Carlos O. Reinhold, Tatsuya Minami, and Joachim Burgdörfer; Tagungsband der 25. Tagung ueber Energiereiche Atomare Stöße (02/2004).

Quantum transport of the internal state of Kr^{35+} ions through amorphous carbon foils

T. Minami, C. O. Reinhold, M. Seliger, J. Burgdörfer, C. Fourment, E. Lamour, J.-P. Rozet, D. Vernhet, B. Gervais; Phys. Rev. A 65, 032901 (2002).

Evidence of collisional coherences in the transport of hydrogenic krypton through amorphous carbon foils

T. Minami, C. O. Reinhold, M. Seliger, J. Burgdörfer, C. Fourment, J.-P. Rozet, B. Gervais, D. Vernhet; Nucl. Instr. and Meth. B 193, 79-84 (2002).

Transport of Kr^{35+} inner-shells through solid carbon foils

D. Vernhet, C. Fourment, E. Lamour, J.-P. Rozet, B. Gervais, L. J. Dubé, F. Martin, T. Minami, C. O. Reinhold, M. Seliger, J. Burgdörfer; Physica Scripta, T92, 233-236 (2001).

Classical transport theory

Excited-state evolution probed by convoy electron emission in relativistic heavy ion collisions

Y. Takabayashi, T. Ito, T. Azuma, K. Komaki, Y. Yamazaki, H. Tawara, E. Takada, T. Murakami, M. Seliger, K. Tökési, C. O. Reinhold, J. Burgdörfer; Phys. Rev. A 68, 042703 (2003).

Highly transverse velocity distribution of convoy electrons emitted by highly charged ions

M. Seliger, K. Tökési, C. O. Reinhold, J. Burgdörfer; Nucl. Instr. and Meth. B 205, 830-834 (2003).

Relativistic electron transport through carbon foils

M. Seliger, K. Tökési, C. O. Reinhold, J. Burgdörfer, Y. Takabayashi, T. Ito, K. Komaki, T. Azuma, Y. Yamazaki; Physica Scripta, T92, 211-213 (2001).

EN ROUTE ON BEHALF OF SCIENCE

- 07/2005: Poster at the XXIV International Conference on Photonic, Electronic and Atomic Collisions (ICPEAC), Rosario, Argentina
- 01/2005: Visit at the Institut de NanoSciences de Paris, Universités Paris 6 et 7, France
- 11/2004: Talk at the Intern. Workshop on Atomic Physics (ATOM 2004), Dresden, Germany
- 07/2004: Poster at the 21st Intern. Conf. on Atomic Collisions in Solids (ICACS), Genova, Italy
- 02/2004: Talk at the 25. Tagung über Energiereiche Atomare Stöße (EAS), Riezlern, Austria
- 01/2004: Seminar-talk at the Institute of Nuclear Research of the Hungarian Academy of Sciences (ATOMKI), Debrecen, Hungary
- 11/2003: Talk at the Austrian - Hungarian Workshop on charged-particle transport through nanostructures and solids, ATOMKI, Debrecen, Hungary
- 05/2003: Talk at the NIPNET HITRAP IONCATCHER 2nd Annual Joint Collaboration Meeting, La Londe-les-Maures, Var, France
- 09/2002: Poster at the 11th International Conference on Highly Charged Ions (HCI), Caen, France
- 04/2001: Talk at the 7th ECAMP and DPG spring meeting, Berlin, Germany
- 02/2000: Visit at Oak Ridge National Laboratory and University of Tennessee, Knoxville, USA

SCHOLARSHIPS/AWARDS

- Furtherance scholarship** of the Vienna University of Technology, 2001
- Achievement scholarship** of the Vienna University of Technology, 2001

LANGUAGES

- Native speaker:** German and Czech
- Fluently:** English
- Basic knowledge:** French

COMPUTATIONAL SKILLS

- Programming:** languages (Fortran, C, Pascal),
object oriented (C++, lectures by Prof. Purgathofer),
functional (Mathematica, lecture by Dr. Reiner)
- Operating systems:** Linux, Windows
- Software:** Mathematica, MS Office, LaTeX, Gnuplot, Origin, HTML, etc.

PERSONAL INTERESTS BEYOND PHYSICS

- Hiking, mountaineering, skiing and traveling